Identification and Characterization of Genes with Unknown Function on

Plasmodium falciparum

Chromosome 4

- Dissertation -

With the aim of achieving a doctoral degree at the Faculty of

Mathematics, Informatics and Natural Sciences

Department of Biology

University of Hamburg

submitted by

Yangyang Guo

Hamburg, 2025

Ich versichere, dass dieses gebundene Exemplar der Dissertation und das in elektronischer Form eingereichte Dissertationsexemplar (über den Docata-Upload) und das bei der Fakultät (zuständiges Studienbüro bzw. Promotionsbüro Physik) zur Archivierung eingereichte gedruckte gebundene Exemplar der Dissertationsschrift identisch sind.

I, the undersigned, declare that this bound copy of the dissertation and the dissertation submitted in electronic form (via the Docata upload) and the printed bound copy of the dissertation submitted to the faculty (responsible Academic Office or the Doctoral Office Physics) forarchiving are identical.

Hamburg, den 11.07.2025

Ort, Datum

Unterschrift

Day of oral defence: 12.09.2025

1. Dissertation reviewer: Dr. Tobias Spielmann

2. Dissertation reviewer: Prof. Dr. Tim Gilberger

Member of the examination committee: PhD Hannah Michaela Behrens

Chair of the examination committee: Prof. Dr. Julia Kehr

Eidesstattliche Versicherung

Hiermit versichere ich an Eides statt, die vorliegende Dissertationsschrift selbst

verfasst und keine anderen als die angegebenen Hilfsmittel und Quellen benutzt zu

haben.

Sofern im Zuge der Erstellung der vorliegenden Dissertationsschrift generative

Künstliche Intelligenz (gKI) basierte elektronische Hilfsmittel verwendet wurden,

versichere ich, dass meine eigene Leistung im Vordergrund stand und dass eine

vollständige Dokumentation aller verwendeten Hilfsmittel gemäß der Guten

wissenschaftlichen Praxis vorliegt. Ich trage die Verantwortung für eventuell durch

die gKI generierte fehlerhafte oder verzerrte Inhalte, fehlerhafte Referenzen, Verstöße

gegen das Datenschutz- und Urheberrecht oder Plagiate.

Affidavit

I hereby declare and affirm that this doctoral dissertation is my own work and that I

have not used any aids and sources other than those indicated.

If electronic resources based on generative artificial intelligence (gAI) were used in

the course of writing this dissertation, I confirm that my own work was the main and

value-adding contribution and that complete documentation of all resources used is

available in accordance with good scientific practice. I am responsible for any

erroneous or distorted content, incorrect references, violations of data protection and

copyright law or plagiarism that may have been generated by the gAI.

Hamburg, den 11.07.2025

Ort, Datum

Unterschrift

i

Language certificate

I am a native speaker, have read the present PhD thesis and hereby confirm that it complies with the rules of the English language.

Mittel Liberach, 21.07.25

City, Date Signature

Summary

Malaria remains one of the most significant infectious diseases globally, with Plasmodium falciparum responsible for the majority of severe cases and deaths. Despite being extensively studied, more than 2,600 of the \sim 5,400 protein-coding genes in P. falciparum remain annotated as "unknown function" or "putative" in PlasmoDB, reflecting major gaps in understanding of parasite biology and developing drugs and vaccine. This thesis contributes to addressing this challenge by functionally investigating a systematically selected subset of unknown genes from P. falciparum chromosome 4.

We selected 44 candidate genes (here designated Y1-Y44) with unknown functional, based on combined bioinformatic filtering using BLAST, HHPred, and MotifScan. Genes with known or predictable domains were excluded. The final set comprised what we considered to be all non-secretory proteins without homology outside Apicomplexa encoded on that chromosome. For all genes plasmids were generated for genome modification of the parasites to fuse the endogenous candidate gene with the sequence encoding GFP and FKBP by using the Selection-Linked Integration system. With this approach 33 stable integrant lines were successfully generated.

Subcellular localization of Candidates was analyzed by live-cell fluorescence microscopy across different stages of the intraerythrocytic cycle. This showed that 15 candidates localized to the nucleus, representing the most frequent localization category. Additional localizations included five candidates in the mitochondrion, two in the Golgi apparatus, one likely at the inner membrane complex (IMC), and several with diffuse cytoplasmic or unclear patterns. Six candidates showed no detectable signal using

single-copy GFP tagging, but a signal could be observed for one of them (Y29) using a 7×GFP array, revealing nuclear localization.

To assess gene function, 31 knock sideways lines were generated using rapaloginducible mislocalization. Knock sideways constructs included Lyn-based (plasma membrane mislocalization) and NLS-based (nuclear mislocalization) mislocalization, depending on native localization of the candidate analyzed. Growth phenotypes were quantified in flow cytometry-based five-day assays. Six candidates showed a severe reduction in parasite growth upon mislocalization (<20% growth of control), indicating a high importance for blood-stage survival. Of these, Y2 localized to the inner membrane complex (IMC), was only expressed ring and late stage, and its conditional mislocalization caused severe growth inhibition suggesting a role in parasite daughter cell formation or invasion. Y9 localized to the Golgi and its essentiality implied a potentially important role at vesicular trafficking in P. falciparum. Y24 and Y29 (the protein successfully visualized using a 7×GFP tag) showed a nuclear localization, pointing to an important function in nuclear processes for these proteins. Fourteen other candidates showed moderate (20-50%) or mild (50-80%) growth reduction, suggesting an intermediate importance for parasite growth. Seven candidates were classified as dispensable under standard in vitro conditions, and for four mitochondrial candidates (Y3, Y8, Y15, and Y18), KS was unsuccessful due to methodological limitations, particularly in targeting proteins localized to mitochondria.

Comparison with prior chromosome 3 screens confirmed a trend that there is an overrepresentation of nuclear proteins among unknown proteins, reinforcing the notion that *P. falciparum* possesses a diverged nuclear proteome with numerous parasite-specific proteins and functions. Several nuclear proteins showed focal patterns indicative of subnuclear structures, such as kinetochores or chromatin-associated complexes. Notably, three candidates (Y21, Y22, Y38) were recently annotated as

AKiT (Apicomplexan-specific kinetochore) proteins, but remain poorly characterized in *P. falciparum*. Both Y21 and Y38 displayed a single intense GFP focus per nucleus and were here shown to overlap with tubulin, indicating they are kinetochore proteins in *P. falciparum*. In contrast, Y22 was present in multiple punctate within each nucleus, lacking the singular, strongly concentrated focus observed in Y21 and Y38.

It should be noted that while GFP-based tagging and FKBP-FRB based mislocalization are powerful tools for studying protein localization and function, they are not without limitations. Low expression levels, transient localization patterns, or steric hindrance introduced by the tag may result in undetectable signals or mislocalization that does not reflect the protein's native distribution. Similarly, the knock sideways system depends on accessibility and the competence of the target to be effectively mislocalized, which may not be achievable for all proteins, particularly those in organelles such mitochondria. These limitations were considered in data interpretation throughout this study.

In summary, this work uses a functional screening pipeline for uncharacterized *P. falciparum* genes, combining SLI-based tagging, subcellular localization, conditional inactivation, and phenotypic readouts. It successfully identifies multiple essential proteins, expands our understanding of parasite cell biology and highlights novel potential targets for antimalarial intervention. Future work should focus on mechanistic characterization of essential hits and exploration of their potential as therapeutic targets.

Zusammenfassung

Malaria gehört nach wie vor zu den bedeutendsten Infektionskrankheiten weltweit, wobei *Plasmodium falciparum* für die meisten schweren Krankheitsverläufe und Todesfälle verantwortlich ist. Trotz intensiver Forschung sind über 2.600 der rund 5.400 protein-codierenden Gene in *P. falciparum* in PlasmoDB weiterhin als "unbekannte Funktion" oder "vermutet" annotiert. Dies verdeutlicht erhebliche Wissenslücken im Verständnis der Parasitenbiologie und erschwert die Entwicklung neuer Medikamente und Impfstoffe. Diese Dissertation leistet einen Beitrag zur Schließung dieser Lücken durch die funktionelle Untersuchung einer systematisch ausgewählten Untergruppe unbekannter Gene auf Chromosom 4 von *P. falciparum*.

Es wurden 44 Kandidatengene (hier als Y1-Y44 bezeichnet) mit unbekannter Funktion ausgewählt, basierend auf einer kombinierten bioinformatischen Filterung unter Verwendung von BLAST, HHPred und MotifScan. Gene mit bekannten oder vorhersehbaren Domänen wurden ausgeschlossen. Der endgültige Gen-Satz umfasste ausschließlich nicht-sekretorische Proteine ohne Homologie außerhalb der Apicomplexa, die auf diesem Chromosom kodiert sind. Für alle Gene wurden Plasmide zur genomischen Modifikation des Parasiten generiert, um das endogene Kandidatengen mit Sequenzen für GFP und FKBP mithilfe des Selection-Linked Integration (SLI)-Systems zu fusionieren. Auf diese Weise konnten 33 stabile Integrantenlinien erfolgreich erzeugt werden.

Die subzelluläre Lokalisation wurde mittels Lebendzell-Fluoreszenzmikroskopie über verschiedene Stadien des erythrozytären Entwicklungszyklus hinweg analysiert. Dabei zeigten 15 Kandidaten eine nukleäre Lokalisation - dies war die häufigste Kategorie. Weitere Lokalisationen umfassten fünf Kandidaten in den Mitochondrien, zwei im Golgi-Apparat, einen vermutlich an der Inneren Membrankomplex (IMC) sowie

mehrere mit diffuser zytoplasmatischer oder unklarer Lokalisation. Bei sechs Kandidaten konnte mit einfacher GFP-Markierung kein Signal nachgewiesen werden, jedoch konnte bei einem (Y29) mithilfe eines 7×GFP-Tags eine nukleäre Lokalisation sichtbar gemacht werden.

Zur Funktionsanalyse wurden für 31 Kandidaten Knock sideways Linien erzeugt, in denen die Proteine mittels Rapalog-induzierter Fehl-Lokalisation inaktiviert wurden. Je nach nativer Lokalisation kamen entweder Lyn-basierte (Plasmamembran) oder NLSbasierte (Zellkern) Zielstrukturen zum Einsatz. Wachstumsphänotypen wurden in Durchflusszytometrie-basierten Fünf-Tages-Assays quantifiziert. Sechs Kandidaten zeigten bei Fehl-Lokalisation ein stark vermindertes Parasitenwachstum (<20% im Vergleich zur Kontrolle), was auf eine essenzielle Rolle für das Überleben im Blutstadium hinweist. Darunter war Y2, welches an der IMC lokalisiert war, nur in späten Stadien exprimiert wurde und vermutlich an der Tochterzellbildung oder Invasion beteiligt ist. Y9 war im Golgi lokalisiert und dessen Essenzialität deutet auf eine wichtige Rolle im vesikulären Transport hin. Y24 und Y29 (nur sichtbar mit 7×GFP) zeigten eine nukleäre Lokalisation und weisen auf essenzielle Funktionen im Zellkern hin. Weitere 13 Kandidaten führten zu moderaten (20-50%) oder leichten (50-Wachstumshemmungen, eine Relevanz 80%) was auf mittlere Parasitenwachstum schließen lässt. Sieben Kandidaten wurden unter Standardbedingungen als verzichtbar eingestuft. Für vier mitochondrial lokalisierte Kandidaten (Y3, Y8, Y15 und Y18) war die Knock sideways Strategie aufgrund methodischer Einschränkungen - insbesondere bei der Umlenkung mitochondrialer Proteine - nicht erfolgreich.

Ein Vergleich mit früheren Chromosom-3-Screenings bestätigte den Trend einer Überrepräsentation nukleärer Proteine unter den unbekannten Genprodukten. Dies unterstützt die Annahme, dass *P. falciparum* über ein stark divergentes nukleäres

Proteom mit zahlreichen parasitenspezifischen Proteinen und Funktionen verfügt. Mehrere nukleäre Proteine zeigten fokale Muster, die auf subnukleäre Strukturen wie Kinetochoren oder chromatinassoziierte Komplexe hindeuten. Bemerkenswert ist, dass drei Kandidaten (Y21, Y22, Y38) kürzlich als AKiT-Proteine (Apicomplexaspezifische Kinetochore) annotiert wurden, jedoch in *P. falciparum* bislang kaum charakterisiert sind. Y21 und Y38 zeigten je einen einzelnen intensiven GFP-Fokus pro Zellkern und kolokalisierten mit Tubulin, was ihre Funktion als Kinetochor-Proteine in *P. falciparum* nahelegt. Im Gegensatz dazu zeigte Y22 mehrere punktförmige Signale pro Zellkern ohne die starke Fokussierung von Y21 und Y38.

Es sei darauf hingewiesen, dass GFP-Markierung und FKBP-FRB-abhängige Fehl-Lokalisation zwar leistungsstarke Werkzeuge zur Untersuchung von Proteinlokalisation und -funktion sind, aber auch Einschränkungen aufweisen. Geringe Expression, transiente oder hochdynamische Lokalisationen sowie sterische Hinderung durch den Tag können zu nicht detektierbaren oder irreführenden Signalen führen. Ebenso ist die Knock sideways-Methode abhängig von der Zugänglichkeit und Umlenkbarkeit des Zielproteins, was insbesondere bei Organellproteinen wie mitochondrialen eine Herausforderung darstellt. Diese Einschränkungen wurden bei der Interpretation der Ergebnisse berücksichtigt.

Zusammenfassend stellt diese Arbeit eine funktionelle Screening-Pipeline für uncharakterisierte Gene von *P. falciparum* vor, die SLI-basierte Markierung, subzelluläre Lokalisation, konditionelle Inaktivierung und phänotypische Auswertung kombiniert. Sie identifiziert erfolgreich mehrere essenzielle Proteine, erweitert das Verständnis der Zellbiologie des Parasiten und weist auf neue potenzielle Ziele für antimalariale Interventionen hin. Zukünftige Arbeiten sollten sich auf die mechanistische Charakterisierung essenzieller Kandidaten und deren therapeutisches Potenzial konzentrieren

Contents

Eidesstattliche Versicherung	i
Affidavit	i
Language certificate	ii
Summary	iii
Zusammenfassung	vi
Contents	ix
1. Introduction	1
1.1 Malaria and Plasmodium parasites	1
1.2 Organelles of Plasmodium parasites	11
1.3 Plasmodium falciparum Genome	27
1.4 Aims	32
2. Materials and Methods	34
2.1 Materials	34
2.2 Methods	45
3. Results	59
3.1 Overview of Chromosome 4 in <i>Plasmodium falciparum</i>	59
3.2 Characterization of Y1 (PF3D7_0403600)	64
3.3 Characterization of Y2 (PF3D7_0404000)	67
3.4 Characterization of Y3 (PF3D7_0404200)	72
3.5 Characterization of Y4 (PF3D7_0404300)	75
3.6 Characterization of Y5 (PF3D7_0405500)	78
3.7 Characterization of Y6 (PF3D7_0406000)	82

3.8 Characterization of Y7 (PF3D7_0406500)	84
3.9 Characterization of Y8 (PF3D7_0406600)	88
3.10 Characterization of Y9 (PF3D7_0406700)	91
3.11 Characterization of Y11 (PF3D7_0407400)	97
3.12 Characterization of Y13 (PF3D7_0407700)	101
3.13 Characterization of Y14 (PF3D7_0408000)	104
3.14 Characterization of Y15 (PF3D7_0408100)	107
3.15 Characterization of Y17 (PF3D7_0408300)	112
3.16 Characterization of Y18 (PF3D7_0408400)	115
3.17 Characterization of Y20 (PF3D7_0410500)	118
3.18 Characterization of Y21 (PF3D7_0410800)	120
3.19 Characterization of Y22 (PF3D7_0410900)	124
3.20 Characterization of Y23 (PF3D7_0411000)	127
3.21 Characterization of Y24 (PF3D7_0411300)	131
3.22 Characterization of Y25 (PF3D7_0411800)	137
3.23 Characterization of Y28 (PF3D7_0415200)	138
3.24 Characterization of Y29 (PF3D7_0416900)	141
3.25 Characterization of Y30 (PF3D7_0417600)	145
3.26 Characterization of Y32 (PF3D7_0417900)	147
3.27 Characterization of Y33 (PF3D7_0418300)	149
3.28 Characterization of Y34 (PF3D7_0418900)	153
3.29 Characterization of Y35 (PF3D7_0419000)	155
3.30 Characterization of Y38 (PF3D7_0420600)	159
3.31 Characterization of Y41 (PF3D7_0422600)	163
3.32 Characterization of Y42 (PF3D7_0423000)	166
3.33 Characterization of Y43 (PF3D7_0423200)	168
3.34 Characterization of Y44 (PF3D7_0423600)	172

Contents

4. Discussion	177
4.1 Selection of candidates, localizations, function	177
4.2 Nuclear-Localized Candidates	184
4.3 Mitochondrial Candidates	190
4.4 Golgi Candidates	193
4.5 Undetectable Candidates	195
4.6 Comparison of the results from this screen with published high	throughput sets
	199
4.7 Challenges	203
5. Conclusion	206
6. References	207
Appendix	226
Appendix 1 - Integration check Primers	226
Appendix 2 - Homology Region Primers	229
Appendix 3 - Y43 (PF3D7_0423200) recodonization	236
Appendix 4 - Schematic of SLI strategy.	237
Acknowledgement	238

1. Introduction

1.1 Malaria and Plasmodium parasites

Malaria is an ancient infectious disease that can be traced back more than 3,000 years in human history (Carter et al., 2002). Despite the availability of effective antimalarial drugs, including artemisinin-based combination treatments (ACTs), malaria remains a major public health burden, particularly in sub-Saharan Africa, Southeast Asia, and parts of South America (WHO, 2022). The disease is caused by protozoan parasites of the genus Plasmodium, which are transmitted to humans through the bite of infected Anopheles mosquitoes.

1.1.1 The role of *Plasmodium falciparum* in malaria

Malaria is caused by protozoan parasites of the genus Plasmodium, with five species known to infect humans: *Plasmodium falciparum*, *Plasmodium vivax*, *Plasmodium ovale*, *Plasmodium malariae*, and *Plasmodium knowlesi* (White, 2017). Main characteristics of these Plasmodium species are listed in Table 1.

Table 1. The comparison table of human-infecting Plasmodium species

	P. falciparum	P. vivax	P. ovale	P. malariae	P. knowlesi
Geography	Africa, Southeast Asia, South America	Asia, South America, Africa	Sub-Saharan Africa, Southeast Asia, Western Pacific	Worldwide	Southeast Asia
Severity	Most severe	Moderate	Moderate	Mild	Severe
Incubation Period	7-14 days	10-18 days	12-20 days	18-40 days	9-12 days

Introduction

Replication Cycle	Asynchronous	Tertian (48h)	Tertian (48h)	Quartan (72h)	24h (synchrony unclear)
Relapse Potential	No	Yes	Yes	No	No
Infected Erythrocyte	All RBC	Reticulocytes	Reticulocytes	Older RBCs	All RBC
Morphology	Multiple rings	amoeboid trophozoites	Oval-shaped RBCs	Band-form trophozoite	Malariae- like, compact

Table 1 illustrates that *Plasmodium falciparum* is the most virulent species, responsible for the

majority of severe malaria cases and associated deaths worldwide (WHO, 2022). Its high pathogenicity stems from its ability to rapidly multiply in human red blood cells (RBCs) and its capacity to sequester in major organs of the host, leading to life-threatening complications such as cerebral malaria, severe anemia, and multi-organ dysfunction (Miller et al., 2002; Rowe et al., 2009; Smith et al., 2013). These characteristics make P. falciparum the most critical target for malaria research and intervention efforts (Cowman et al., 2016; White, 2017). The clinical symptoms of P. falciparum malaria typically begin with nonspecific symptoms such as fever, chills, headache, and muscle pain, which result from the rupture of infected RBCs and the subsequent release of toxic parasitic byproducts (Gazzinelli et al., 2014). Unlike P. vivax, P. ovale, and P. malariae, which exhibit synchronous 48-hour or 72-hour replication cycles in the host that lead to synchronous fever attacks, P. falciparum lacks highly synchronized schizogony, leading to more irregular fever patterns (Table 1). In a few cases, gastrointestinal symptoms, including nausea, vomiting, and diarrhea, may also occur. The most severe form of the disease, cerebral malaria, is characterized by altered mental status, seizures, and coma, resulting from the sequestration of infected RBCs in the microvasculature of the brain (Miller et al., 2002). If left untreated, cerebral malaria can lead to neurological damage or death, particularly in young children under 5 years old and pregnant women in endemic regions (Miller et al., 2002; WHO, 2022). Repeated exposure leads to a "semi-immunity" which strongly reduces the risk of severe disease, but naïve individuals remain at risk of severe disease and fatal outcomes (Langhorne et al., 2008)

One of the major factors contributing to the virulence of *P. falciparum* is its ability to cytoadhere to the vascular endothelium, a process that enables infected RBCs to evade clearance by the spleen (Miller et al., 2002; Smith et al., 2013). This cytoadherence is mediated by *P. falciparum* erythrocyte membrane protein 1 (*Pf*EMP1), a highly variable protein encoded by the *var* gene family (Baruch et al., 1995; Fidock et al., 2008; Su et al., 1995). *Pf*EMP1 binds to endothelial receptors such as intercellular adhesion molecule 1 (ICAM-1) and CD36, leading to sequestration of infected RBCs in vital organs, including the brain, lungs, and placenta (Rowe et al., 2009). The functional versatility of *Pf*EMP1 comes at a cost, as increased antigenic variation enhances immune evasion but may reduce binding affinity to specific endothelial receptors - a trade-off critical to parasite survival (Lavstsen et al., 2012).

Another critical factor in *P. falciparum*'s pathogenicity is its ability to undergo antigenic variation. The *var* gene family, which encodes *Pf*EMP1, enables the parasite to frequently switch surface antigens, preventing the host immune system from mounting an effective response. This continuous antigenic variation complicates vaccine development, as immune recognition of the parasite is constantly changing (Bachmann et al., 2019; Kraemer et al., 2007; Kyes et al., 2007; Scherf et al., 2008).

Due to its wide distribution in areas with limited health care resources, its high mortality rate, immune evasion, and increasing drug resistance, *P. falciparum* remains the most significant challenge in global malaria control (WHO, 2022). Understanding its biology, particularly the molecular mechanisms of its virulence and survival strategies, is essential for the development of new antimalarial drugs and vaccine interventions. Research efforts focusing on identifying novel drug targets, enhancing vaccine efficacy, and improving vector control strategies with the aim to achieve long-term malaria elimination would be highly beneficial. Several

international initiatives have been launched to combat malaria, including the Roll Back Malaria Partnership and the WHO Global Technical Strategy for Malaria 2016-2030, which outlines a roadmap towards elimination. However, recent assessments indicate that progress has stalled in many high-burden countries due to challenges such as drug resistance, funding gaps, and health system limitations (WHO, 2022)

1.1.2 Malaria Epidemiology and Global Burden

According to the World Malaria Report 2022 (WHO 2022), an estimated 247 million malaria cases occurred globally in 2021, leading to approximately 619,000 deaths. Despite ongoing control efforts, malaria continues to be one of the heaviest public health and economic burden, especially in low-income countries. Africa bears the highest malaria burden, accounting for 95% of all malaria deaths, with children under five years old comprising approximately 80% of all fatalities. Four countries—Nigeria, the Democratic Republic of the Congo, Uganda, and Mozambique—collectively contribute to more than 50% of global malaria deaths (WHO, 2022).

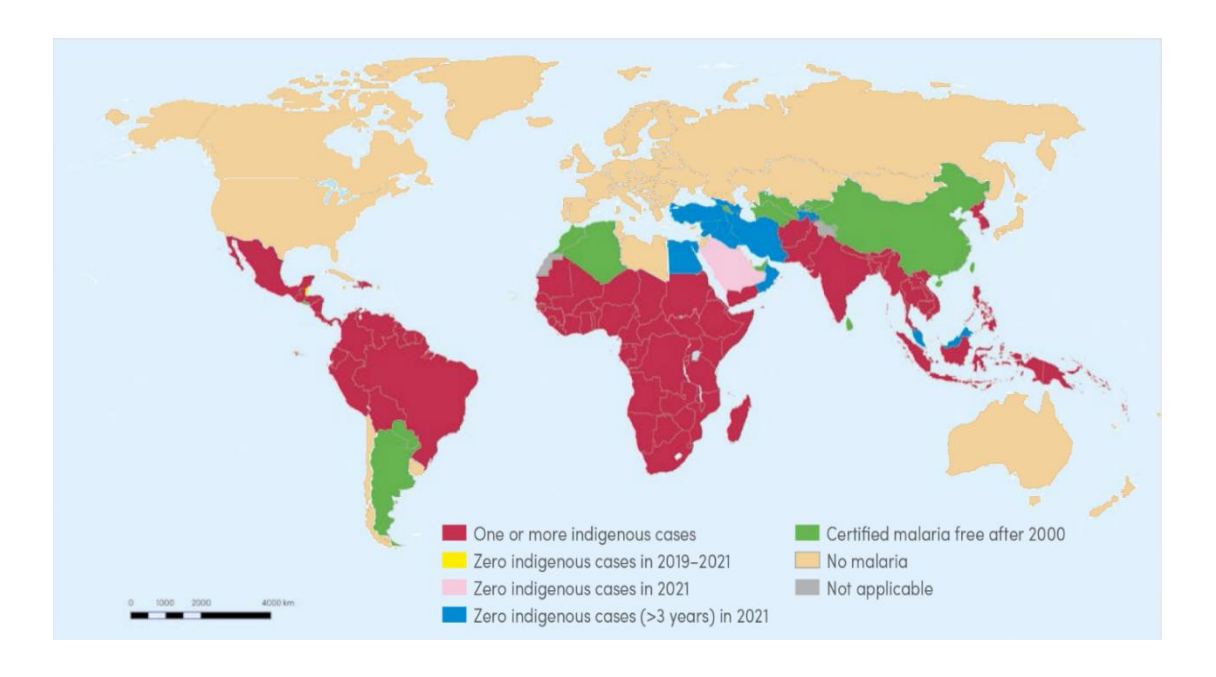


Figure 1. Global Malaria Distribution (WHO, 2022).

Outside of Africa, malaria remains endemic in Southeast Asia, South America, and the Western Pacific. In Southeast Asia, *Plasmodium vivax* accounts for 65% of infections, particularly in India, Myanmar, and Indonesia (Howes et al., 2016). In South America, the highest transmission occurs in the Amazon Basin, with *Plasmodium vivax* responsible for 75% of cases in Brazil, Colombia, and Venezuela (WHO, 2022). The Western Pacific, especially Papua New Guinea and the Solomon Islands, continues to experience fluctuating malaria transmission due to seasonal and environmental factors.

Several countries have successfully eliminated malaria through sustained public health efforts. Between 2000 and 2021, 21 countries achieved WHO malaria-free certification, including China (2021), El Salvador (2021), Algeria (2019), and Sri Lanka (2016) (WHO, 2022) (Figure 1). These achievements demonstrate that with the correct combination of interventions, malaria elimination is possible even in historically endemic regions. However, most of these countries had lower malaria endemicity compared to the highest-burden regions, where elimination remains far more challenging. Hence, the path to global eradication remains difficult due to persistent challenges, including drug resistance, insecticide resistance, and climate change.

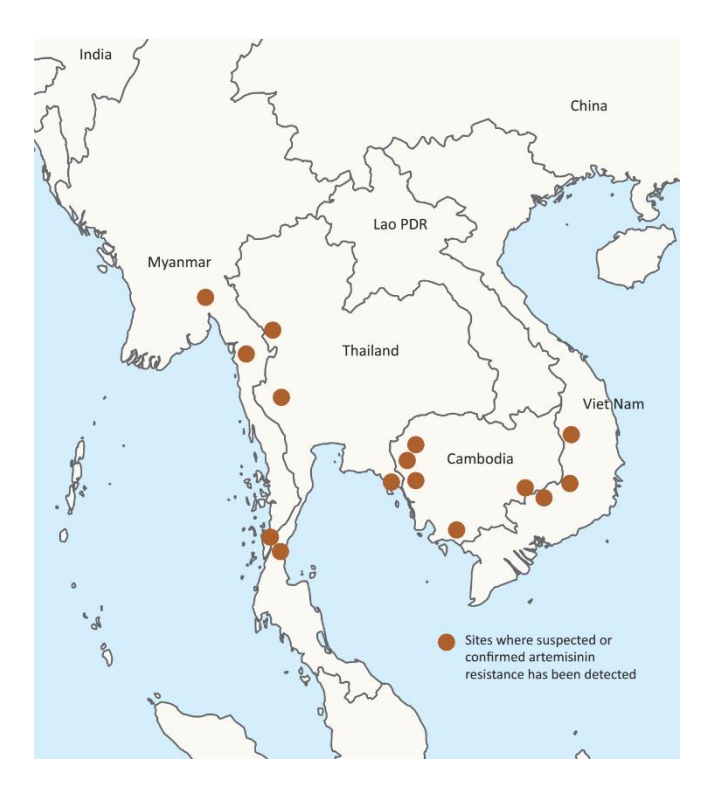


Figure 2. Artemisinin resistance in Southeast Asia (Corbel et al., 2013).

One of the most pressing threats to malaria control is the emergence of artemisinin resistance in P. falciparum, particularly in Southeast Asia (Figure 2). Studies have shown that resistance to artemisinin-based therapies is associated with mutations in the kelch13 gene, raising concerns about the efficacy of current treatment regimens (Behrens et al., 2021). In addition, widespread resistance to pyrethroid insecticides among Anopheles mosquitoes threatens the effectiveness of Insecticide-Treated Nets (ITNs) and Indoor Residual Spraying (IRS) programs, potentially leading to increased malaria transmission

(Hemingway et al., 2016). Climate change is also altering malaria epidemiology by expanding transmission zones, with rising temperatures and shifting rainfall patterns creating favorable conditions for mosquito breeding in previously malaria-free areas (Caminade et al., 2014).

1.1.3 Life cycle and host

The life cycle of *Plasmodium falciparum* parasites is complex, involving both human and mosquito hosts (Cox, 2010). This two-host system allows the parasite to develop, multiply, and spread efficiently (Figure 3). Understanding the different stages of the life cycle is important for malaria prevention and treatment, as each stage presents unique challenges and potential drug targets (White, 2017).

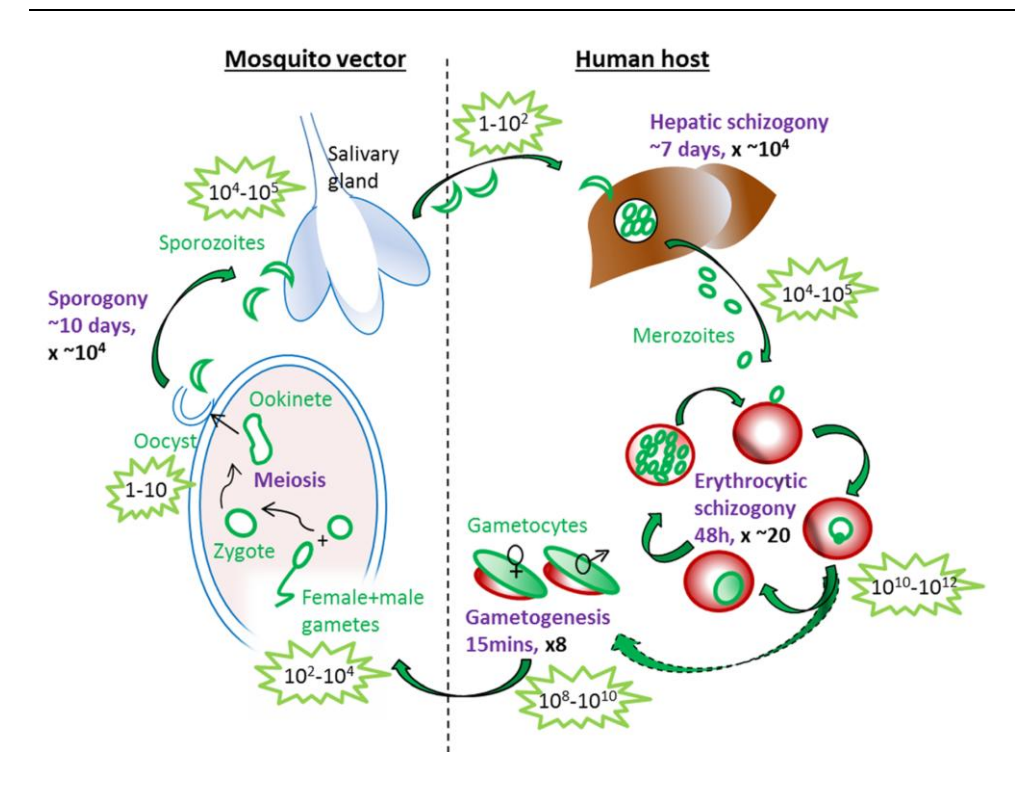


Figure 3. The life cycle of *Plasmodium falciparum* (Matthews et al., 2018).

Malaria infection starts with an infected female *Anopheles* mosquito injecting sporozoites into the skin while it bites (Kebaier et al., 2009). The sporozoites, which are highly motile, actively move through the dermis before entering the bloodstream, primarily via blood capillaries, although a small fraction may enter lymphatic vessels and be diverted to lymph nodes (Amino et al., 2007; Hopp et al., 2015). Once in circulation, sporozoites migrate to the liver, reaching hepatocytes within minutes (Mota et al., 2001). This transition from skin to liver is facilitated by the parasite's ability to move through host cells via a process known as gliding motility, which enables rapid dissemination (Dvorin et al., 2010).

In the liver stage, sporozoites invade hepatocytes and form a parasitophorous vacuole, which shields them from intracellular degradation pathways and allows safe development inside the host cell (Mota et al., 2001; Prado et al., 2015; Silvie et al., 2003). Over the course of 7 to 10 days, the parasites undergo exo-erythrocytic schizogony, during which they grow and divide to form thousands of merozoites (Miller et al., 2014). Unlike *P. vivax* and *P. ovale*, *P. falciparum* cannot form hypnozoites, meaning there is no latent liver stage (Rossati et al.,

2016). Once fully developed, the merozoites are released from the hepatocytes in so called merosomes (host cell plasma membrane bounded packets of merozoites) and enter the bloodstream. The merosomes rupture and release the merozoites, marking the beginning of the cycle inside RBC (Sturm et al., 2006).

1.1.3.1 Asexual intraerythrocytic cycle

Upon release, merozoites rapidly invade human RBCs and start the asexual intraerythrocytic cycle (Figure 4).

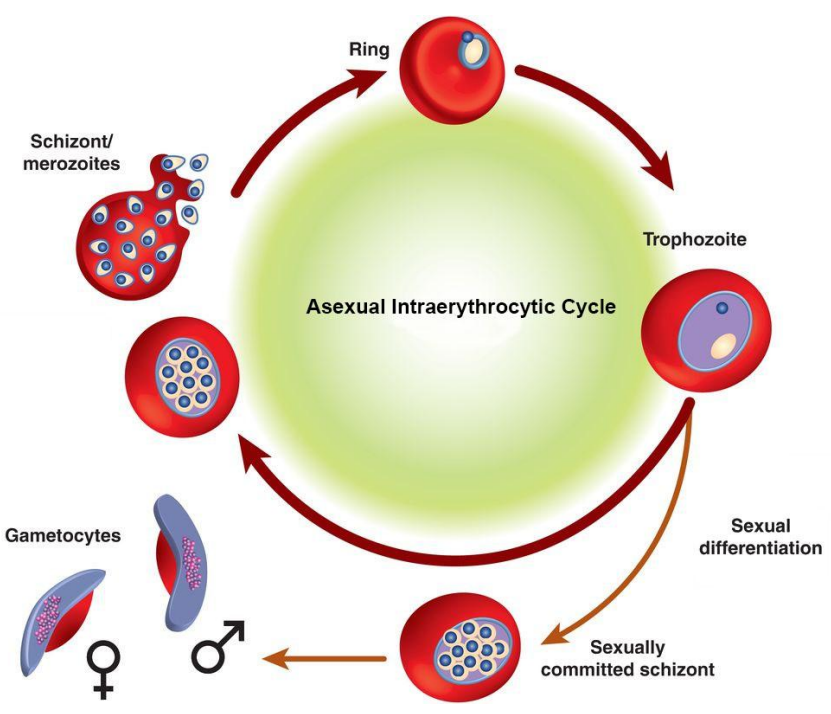


Figure 4. The asexual intraerythrocytic cycle of *Plasmodium falciparum* (modified from Cortes et al., 2017).

Within RBCs, *P. falciparum* progresses through different developmental stages (Grüring et al., 2011). The ring stage is the earliest phase, where the young parasites establish themselves inside the RBC (Solebo et al., 2023). In the following trophozoite stage, the parasite rapidly grows, actively digests hemoglobin and accumulates hemozoin pigment, a crystalline byproduct. In the schizont stage, nuclear division produces 16-32 new merozoites, which eventually lead to rupture of the RBC and release of the merozoites, starting a new cycle (Milner, 2018). Unlike *P. vivax*, which preferentially infects reticulocytes, *P. falciparum*

invades RBC irrespective of age, leading to higher parasitemia and much severer disease outcomes (Galinski et al., 2013). The progression through the intraerythrocytic cycle follows a tightly regulated gene expression program, as shown by transcriptome analyses from merozoite invasion to schizont rupture (Bozdech et al., 2003). A summary of these erythrocytic stages, including their morphological characteristics and metabolic activity, is provided in Table 2.

Table 2. Summary of *P. falciparum* erythrocytic stages

Stage	Characteristics	Metabolic Activity	Morphology
Merozoite	Infects RBCs	Very short-lived, rapid invasion	Small, oval, dense chromatin, 1 nucleus
Ring	Establishment in RBC	Low	Ring-shaped, invisible vacuole, 1 nucleus
Trophozoite	Growth and hemoglobin digestion	High	Enlarged, dark pigment, 1 ~2 nuclei
Schizont	Merozoite generation	Peak DNA replication	Large, multiple nuclei
Segmenter	Prepares for RBC rupture	Final processing	Well-defined merozoites, 16-32 nuclei

A subset of intraerythrocytic parasites differentiates into gametocytes, the sexual transmission stages, at least in part in response to environmental and host cues (Brancucci et al., 2017). Only about 0.1% to 10% of asexual parasites develop into gametocytes (Bruce et al., 1990). These gametocytes mature over 10-12 days and stay in the bone marrow and spleen before entering the blood circulation (Cortes et al., 2017). Staying in deep tissues enhances their survival and transmission efficiency while avoiding premature immune clearance (Baker, 2010).

1.1.3.2 Development and Transmission in the Mosquito Host

When a mosquito takes a blood meal from an infected human, it ingests mature gametocytes, which enter the mosquito's digestive tract where they end up in the midgut (Keleta et al., 2021). Within minutes, the gametocytes differentiate into male and female gametes. Male gametes (microgametes) are small, motile, and numerous, while female gametes (macrogametes) are large, non-motile, and few (Sinden et al., 1978). The male microgamete is flagellated and fertilizes the female macrogamete, resulting in the formation of a zygote (Arredondo et al., 2017).

The zygote develops into a motile ookinete, which penetrates the mosquito midgut epithelium and embeds itself in the basal lamina of the midgut wall. Here, it differentiates into an oocyst, undergoing sporogony, a rapid replication process in which thousands of sporozoites are formed over 10-14 days (Nacer et al., 2008). After their release from oocysts, sporozoites disseminate through the mosquito hemocoel and a proportion eventually invade the salivary glands, enabling transmission during the next blood meal (Aly et al., 2009; Frischknecht et al., 2017). From this point, the mosquito becomes infectious and can transmit malaria upon biting a new human host and a new life cycle starts (Meibalan et al., 2017).

In the mosquito, the parasite modifies the vector's metabolism and immune pathways to ensure its own survival and increase transmission (Rossati et al., 2016). The parasite also alters the composition of the mosquito's gut microbiota, creating a good environment for its development (Hopp et al., 2012).

1.1.3.3 Regulation of Developmental Progression

The life cycle of *Plasmodium falciparum* is highly dynamic, involving multiple unconventional replication strategies and precise regulatory mechanisms that control parasite development in both human and mosquito hosts. Unlike classical eukaryotic organisms, *P. falciparum* conducts asynchronous nuclear replication through schizogony in both liver and blood stages, as well as meiosis during gametogenesis in the mosquito vector (Klaus et al.,

2022). These processes require precise molecular regulation to ensure the parasite's survival, transmission, and immune evasion.

Schizogony and sporogony enable *P. falciparum* to produce 16-32 merozoites per erythrocytic cycle and thousands of liver and mosquito-stage progeny from individual replication events. The cell cycle of *Plasmodium falciparum* parasites lacks a conventional G2 phase, with nuclear replication occurring asynchronously before a final coordinated division. In erythrocytic schizogony, chromatin decondensation begins at ~30 hours post-invasion, and the first round of nuclear division is completed by ~32 hpi, followed by asynchronous replication until coordinated merozoite culminating in cytokinesis and segmentation to form synchronized daughter merozoites (Grüring et al., 2011). During gametogenesis, male gametocytes undergo three rapid rounds of nuclear division followed by exflagellation, producing eight motile microgametes within approximately 15 minutes. This process differs both in speed and mechanism from schizogony and is regulated by distinct signaling pathways (Guttery et al., 2012).

The life cycle of *Plasmodium falciparum* involves highly specialized adaptations at each stage, ensuring survival, transmission, and immune evasion (Cowman et al., 2016; Talman et al., 2010). Key malaria control strategies include vaccines such as RTS,S/AS01, which target the sporozoite stage (Laurens, 2018), antimalarial drugs designed to inhibit intraerythrocytic replication (Burrows et al., 2017; White et al., 2014; White, 2017), and vector control measures aimed at reducing mosquito populations (Bhatt et al., 2015; Hemingway et al., 2016). A deeper understanding of the parasite's biology, immune evasion strategies, and transmission dynamics is essential for developing new interventions to combat malaria (Draper et al., 2018; Florens et al., 2002; Travassos et al., 2015).

1.2 Organelles of Plasmodium parasites

Plasmodium falciparum, as a single cell organism, must carry out nearly all vital biological functions within a single cell. That requires a highly specialized and precisely coordinated network of organelles systems that fulfil distinct roles essential for parasite survival and proliferation. The structure, function, and dynamics of these organelles significantly change during the different developmental stages of the parasite's life cycle, adapting to the varying host environments. Organelles affected by this are for instance the food vacuole (Goldberg et al., 1990); specific parasite-induced organelles in the host red blood cell (Wickham et al., 2001); the apicoplast which disappears during the gametocyte stage (Van Dooren et al., 2013), the inner membrane complex and invasion organelles which are in various combinations only formed in the invasive zoite stages (Kono et al., 2012; Lal et al., 2009). Given that this thesis focuses mainly on the intraerythrocytic stage of *P. falciparum*, the following sections (1.2.1 to 1.2.4) will provide a detailed overview of the major organelles during this stage.

During the intraerythrocytic stage of *Plasmodium falciparum*, in addition to nucleus (details in section 1.2.1) and common eukaryotic organelles such as the mitochondrion (details in section 1.2.3), endoplasmic reticulum, and Golgi apparatus (details in section 1.2.2), the parasite possesses several specialized organelles that are crucial for its survival and proliferation within red blood cells (Figure 5). Among these are Maurer's clefts, parasite-induced membranous structures within the host RBC cytoplasm that facilitate the export and trafficking of virulence proteins like *Pf*EMP1 (Spycher et al., 2008). Another essential modification is the formation of knobs, electron-dense protrusions on the iRBC surface

dependent on the parasite protein KAHRP, which anchor *Pf*EMP1 on the cell surface and are necessary for cytoadhesion (Crabb et al., 1997).

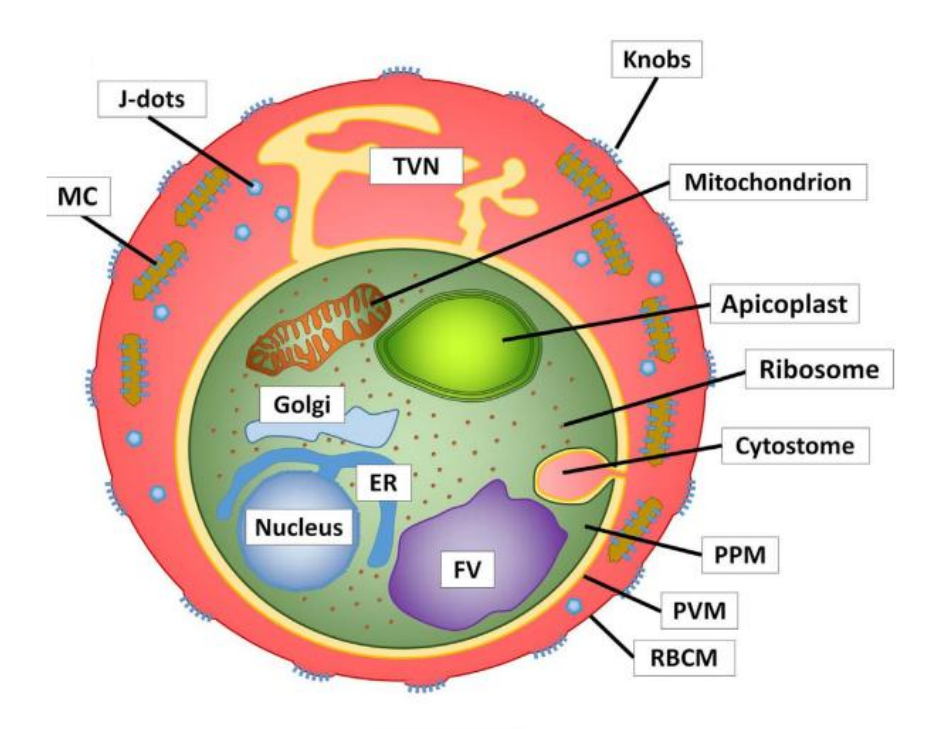


Figure 5. Intracellular organelles of trophozoite stage (Flammersfeld et al., 2018).

Once rupture of the host cell, released merozoites exhibit additional specialized structures such as the subpellicular microtubules, which maintain their shape, and the inner membrane complex (IMC) (Figure 6). The specialized invasion organelles in *P. falciparum*—namely the micronemes, rhoptries, and dense granules—are localized at the apical end of the merozoite (Figure 6). These organelles are discharged during erythrocyte invasion, delivering proteins required for attachment, entry, and establishment of the parasitophorous vacuole (Bannister et al., 2000; Cowman et al., 2017). The specialized invasion organelles are the so-called micronemes, rhoptries, and dense granules (Figure 6), located at the apical tip of the invasive zoite stages such as merozoites. These organelles are discharged in a regulated sequence to mediate invasion of host cells, a process powered by an actin-myosin motor anchored to the inner membrane complex (see section 1.2.4 for details) (Cowman et al., 2016; Meissner et al., 2013).

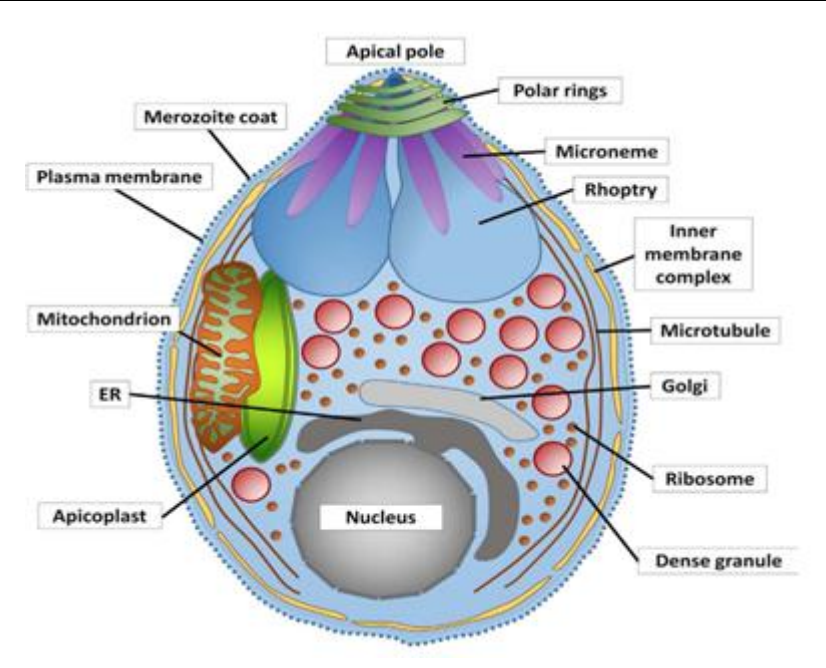


Figure 6. Organelles of merozoite stage (Flammersfeld et al., 2018).

1.2.1 Nucleus

The nucleus of *Plasmodium falciparum* parasites exhibits several highly divergent features compared to higher eukaryotic nuclei (Meissner et al., 2013). These differences are particularly pronounced in mitotic division, kinetochore organization, and nuclear pore complex (NPC) architecture. Unlike typical eukaryotes, which undergo open mitosis with synchronized chromosome segregation, *P. falciparum* employs an asynchronous nuclear division process without nuclear envelope breakdown. Additionally, Apicomplexan kinetochore proteins show minimal conservation with their eukaryotic counterparts (van Hooff et al., 2017), and the nuclear transport machinery, while exhibiting compositional differences in the NPC, appears to retain functional compatibility with classical NLS-dependent import (e.g., as exploited in experimental systems) (Chen et al., 2015). Together, these features reflect the highly specialized nature of the *P. falciparum* nucleus and underscore its potential as a target for antimalarial interventions (Klaus et al., 2022).

In higher eukaryotes, mitosis is tightly regulated and follows a synchronous progression through prophase, metaphase, anaphase, and telophase. This process involves nuclear envelope breakdown (open mitosis) and the formation of a mitotic spindle that segregates chromosomes into daughter cells (Francia et al., 2014). Furthermore, the parasite undergoes multiple rounds of asynchronous nuclear replication, producing multinucleated schizonts in the asexual blood stage (Klaus et al., 2022).

An outstanding feature of *P. falciparum* mitosis is the absence of a strict checkpoint system (Ganter et al., 2017; Gerald et al., 2011). In higher eukaryotes, mitotic checkpoints regulate progression, ensuring that DNA replication is completed before chromosome segregation begins. However, in *P. falciparum* parasites, individual nuclei within a schizont divide asynchronously, meaning that nuclei within the same parasite may exist at different stages of mitosis simultaneously (Heinberg et al., 2022). This unusual nuclear cycle is thought to maximize replication efficiency, allowing the parasite to rapidly expand its population within red blood cells. Another key difference is the lack of canonical centrosomes in *P. falciparum*. While higher eukaryotic cells rely on centrosomes to organize the mitotic spindle, *P. falciparum* utilizes centriolar plaques, a unique structure that anchors microtubules and directs nuclear division (Wittayacom et al., 2010). These centriolar plaques are embedded within the nuclear envelope, reinforcing the closed mitosis system (Gerald et al., 2011; Simon, 2022).

1.2.1.1 Kinetochore

The kinetochore, a protein complex that assembles on centromeres to mediate chromosome attachment to the spindle, is highly conserved in most eukaryotes. In metazoans and yeast, kinetochore proteins such as Ndc80, Mis12, and Spc105 form the KMN network, a well-characterized structure that ensures accurate chromosome segregation (Cheeseman et al., 2008). In *Plasmodium falciparum* and other Apicomplexans, kinetochore components are highly divergent, with many canonical proteins either absent or showing extreme sequence

divergence (Heinberg et al., 2022). Nevertheless, recent experimental studies have revealed that core kinetochore functions are preserved through structurally and functionally conserved, yet divergent, components. For example, *Pf*NDC80 localizes to discrete foci during mitosis in *P. falciparum*, and its depletion leads to spindle abnormalities and defective chromosome segregation, highlighting its essential role in mitotic progression (Zeeshan et al., 2020a). Similarly, super-resolution imaging and proximity labeling in *P. berghei* uncovered an atypical but functional NDC80 complex architecture that links centromeres to spindle microtubules (Brusini et al., 2022). Additionally, a gene-by-gene functional screen of chromosome 3 in *P. falciparum* identified several nuclear-localized proteins associated with DNA replication and mitosis, supporting the presence of a divergent but operational kinetochore network (Kimmel et al., 2023).

Recent proteomic studies identified a set of Apicomplexan-specific kinetochore proteins, many of which lack direct homologs in yeast or humans (Klaus et al., 2022). These proteins are thought to be essential for chromosome segregation, yet they function within an unconventional kinetochore architecture. Unlike in higher eukaryotes, where kinetochores assemble dynamically at each mitotic cycle, in *P. falciparum*, kinetochore components appear to be constitutively associated with centromeres, possibly reflecting the parasite's unique replication cycle (Heinberg et al., 2022).

Furthermore, the spindle architecture of *P. falciparum* differs significantly from that of higher eukaryotes. While typical eukaryotic spindles align chromosomes along a single mitotic plate, *P. falciparum* organizes its chromosomes in a dispersed manner, possibly due to the constraints of closed mitosis (Wittayacom et al., 2010). These adaptations suggest that kinetochore function in *P. falciparum* is tailored to support its divergent replication strategies, including asynchronous nuclear cycles during asexual stages and the extremely rapid divisions during microgamete formation, where eight nuclei are produced within approximately 30 minutes

(Fang et al., 2017; Sinden et al., 1976). These unique dynamics highlight the kinetochore as a potentially druggable structure.

1.2.1.2 Nuclear pore complex

The nuclear pore complex (NPC) is responsible for mediating nucleocytoplasmic transport, allowing for the regulated exchange of mRNA, proteins, and signaling molecules between the nucleus and the cytoplasm. In higher eukaryotes, NPCs are massive structures composed of ~30 different nucleoporins (Nups) that form a highly symmetric, ring-like scaffold (Wittayacom et al., 2010).

In contrast to model eukaryotes, the nuclear pore complex (NPC) of *Plasmodium falciparum* is structurally divergent, reflecting adaptations to its intracellular lifestyle (Heinberg et al., 2022). Although comparatively fewer nucleoporins (Nups) have been identified in *P. falciparum*, this may be due to limitations in detecting highly divergent sequences rather than a truly reduced NPC composition (Dahan-Pasternak et al., 2013). Supporting this, studies in *P. berghei* have revealed additional NPC components, suggesting that similar proteins may be present but remain unrecognized in *P. falciparum* (Kehrer et al., 2018). Moreover, while NPCs in higher eukaryotes typically exhibit eightfold symmetry, cryo-electron microscopy analyses indicate that *P. falciparum* NPCs may adopt an irregular structure, potentially related to the parasite's compact nuclear architecture (Wittayacom et al., 2010).

Another notable feature is the link between nuclear pores and gene regulation in *P. falciparum*. In human cells, nuclear pore proteins have been implicated in chromatin organization and transcriptional regulation. Similarly, in *P. falciparum*, certain nucleoporins appear to interact with *var* gene loci, suggesting that nuclear transport and antigenic variation may be functionally coupled (Heinberg et al., 2022).

The *P. falciparum* nucleus is highly specialized and divergent from classical eukaryotic models, particularly in its mitotic regulation, kinetochore organization, and nuclear transport mechanisms. Unlike higher eukaryotes, *P. falciparum* undergoes closed mitosis with asynchronous nuclear divisions, facilitating rapid parasite proliferation. While some kinetochore components, such as NDC80, are conserved, many are highly divergent or Apicomplexan-specific in sequence, forming an unconventional machinery for chromosome segregation. In parallel, the nuclear pore complex exhibits structural and compositional adaptations that support selective, parasite-specific nuclear transport. Together, these features highlight potential vulnerabilities for antimalarial intervention.

1.2.2 **Golgi**

The Golgi apparatus serves as the central pivot for protein modification, sorting, and secretion in eukaryotic cells (Hellerschmied et al., 2019). In *Plasmodium falciparum* parasites, the Golgi complex exhibits significant structural and functional adaptations to accommodate its intracellular lifestyle. Unlike the stacked, ribbon-like Golgi apparatus observed in mammalian cells, Plasmodium falciparum harbors a simplified, unstacked Golgi that exists as dispersed mini-stacks throughout the cytoplasm and remains closely associated with the endoplasmic reticulum (Struck et al., 2005; Van Wye et al., 1996). The Golgi is spatially and functionally divided into cis-, medial-, and trans-Golgi compartments, but it lacks a well-defined Golgi ribbon structure and appears as a single, perinuclear compartment during early blood-stage development (Struck et al., 2005; Van Dooren et al., 2005). The cis-Golgi, identified via the Plasmodium falciparum Endoplasmic Reticulum Retention Defective-2 (PfERD2) receptor, interacts with the ER and is involved in vesicular trafficking, whereas the trans-Golgi is demarcated by PfRab6 and directs proteins towards their final destinations (Elmendorf et al., 1993; Van Wye et al., 1996). Unlike the stacked cisternae observed in *Toxoplasma gondii* and mammalian cells, the Plasmodium Golgi remains minimally organized (Struck et al., 2005; Van Dooren et al., 2005).

Protein trafficking in P. falciparum is highly specialized, relying on unique signals for efficient sorting. In most eukaryotic cells, vesicle budding and protein trafficking follow a canonical route, whereby proteins synthesized in the endoplasmic reticulum (ER) are transported to the Golgi apparatus, and subsequently sorted to the plasma membrane or endosomal/lysosomal compartments (Bonifacino et al., 2004), but evidence in P. falciparum suggests specialized Golgi-derived direct sorting pathways. For example, one study identified a Golgi-to-endosome pathway involving retromer and Rab7, and others report Golgi involvement in trafficking proteins directly to the apicoplast (Krai et al., 2014). As in other eukaryotes, ER-to-Golgi transport in Plasmodium falciparum relies on Coat Protein Complex II (COPII)-mediated vesicle budding. In this parasite, the small GTPase PfRab6 has been implicated in directing vesicle fusion with the cis-Golgi, suggesting its functional role in Golgi trafficking (Ben-Rached et al., 2013; Quevillon et al., 2003; Tawk et al., 2011). The trans-Golgi network directs proteins primarily via clathrin-coated vesicles to target destinations such as the apicoplast, food vacuole, or Maurer's clefts (Joiner et al., 2002; Przyborski et al., 2005). In contrast, COPImediated vesicles function in retrograde transport from the Golgi to the ER or between Golgi compartments (Cancino et al., 2013; Shima et al., 1999). Additionally, the Golgi is essential for default secretion of proteins into the parasitophorous vacuole (PV). From there, some proteins remain in the PV, others are inserted into the parasitophorous vacuole membrane (PVM), and a subset are exported across the PVM into the host red blood cell. Within the host cell, exported proteins can localize to various compartments, including Maurer's clefts, the RBC membrane, or knobs, though the precise sorting mechanisms remain incompletely understood (Beck et al., 2021; Elsworth et al., 2014).

Due to its essential role in protein trafficking, the Golgi has been proposed as a potential antimalarial drug target (Gulati et al., 2015; McNamara et al., 2013). For instance, Plasmodium phosphatidylinositol 4-kinase (*Pf*PI4K)—localized at Golgi/ER membranes—has been validated as the target of aminopyridine inhibitors such as MMV390048. These compounds

trigger potent schizonticidal activity in vitro and have progressed into clinical trials (McNamara et al., 2013). More recently, imidazolopiperazines (IZPs), identified via phenotypic screening, were found to disrupt ER-to-Golgi protein trafficking and block establishment of new permeation pathways, leading to parasite death—highlighting ER/Golgi processes as exploitable vulnerabilities (LaMonte et al., 2020).

The Golgi and trans-Golgi network in *P. falciparum* exhibit a simplified, unstacked architecture that may reflect adaptation to the parasite's intracellular lifestyle. While the functional consequences of this organization are not fully understood, it likely supports efficient protein trafficking required for survival within host erythrocytes (Struck et al., 2005; Van Dooren et al., 2005). Understanding its molecular architecture and trafficking mechanisms may reveal novel drug targets to disrupt malaria pathogenesis.

1.2.3 Mitochondrion

The mitochondrion of *Plasmodium falciparum* exhibits significant differences from those of higher eukaryotes and even other protozoans, showing the parasite's adaptation to an intracellular parasitic lifestyle. While most eukaryotes rely on oxidative phosphorylation for ATP generation, *P. falciparum* mitochondria have evolved specialized functions, including pyrimidine biosynthesis, iron-sulfur cluster formation, and electron transport-dependent redox balance (Falekun et al., 2021; MacRae et al., 2013; Vaidya et al., 2008). Recent studies have highlighted the unique dynamics of mitochondrial division, inheritance, and regulation, providing insights into potential drug targets.

Unlike mammalian cells, which contain multiple mitochondria per cell, *P. falciparum* maintains a single, highly dynamic mitochondrion that undergoes extensive morphological changes throughout its life cycle (Van Dooren et al., 2005). During schizogony, this mitochondrion elongates and branches, later undergoing asymmetric fission to be distributed

among developing merozoites. In gametocytes, the mitochondrion becomes highly elongated and interconnected, forming a branched network that persists until transmission to the mosquito vector (Verhoef et al., 2024).

1.2.3.1 Electron transport chain and metabolites

The mitochondrial electron transport chain (ETC) in *P. falciparum* is highly divergent from that of mammalian cells, lacking classical Complex III and IV (Smith et al., 2024). Instead, the parasite relies on Complex II (succinate dehydrogenase) and an alternative oxidase (AOX) to maintain redox homeostasis and electron flow (Vaidya, 2023). Notably, mitochondrial ATP production is minimal in asexual blood stages, with *P. falciparum* primarily relying on glycolysis for energy. However, detailed metabolomic and genetic studies have shown that the mitochondrial TCA cycle remains active, particularly via glutamine-fueled oxidation, and is essential for sexual development and redox balance (Cobbold et al., 2013; MacRae et al., 2013). However, dihydroorotate dehydrogenase (DHODH), an essential enzyme in pyrimidine biosynthesis, is dependent on the mitochondrial ETC, making it a validated drug target (Phillips et al., 2015).

1.2.3.2 Organelle tethering

Recent research highlights the physical tethering of the mitochondrion and apicoplast and ER throughout the intraerythrocytic cycle, suggesting coordinated division and metabolic exchange (Van Dooren et al., 2005). Emerging evidence indicates that the *P. falciparum* mitochondrion physically contacts other organelles via membrane tethering: recent work first documented stable ER-mitochondria contact via *Pf*PSS-defined ER protrusions (Anwar et al., 2022); also electron microscopy and fluorescence imaging studies have demonstrated that the single branched mitochondrion remains apposed to the apicoplast throughout asexual blood-stage development, suggesting coordinated inheritance and potential metabolite exchange

(Ramesh et al., 2023; Van Dooren et al., 2005). In *Toxoplasma gondii*, mitochondrial-ER tethering has been shown to involve conserved tethering complexes (Ovciarikova et al., 2017), and recent studies in *P. falciparum* have suggested similar proximity using proximity labeling and imaging-based approaches (Bertiaux et al., 2021; Birnbaum etal., 2020). These organelle interactions are hypothesized to support metabolic crosstalk and organelle segregation during schizogony, although the molecular components of tethering in *P. falciparum* remain incompletely defined.

While core mitochondrial functions such as electron transport and ATP synthesis are conserved in *Plasmodium falciparum*, complexome profiling has revealed a markedly divergent composition of respiratory complexes, characterized by multiple lineage-specific subunits and the absence of classical supercomplex assembly (van Esveld et al., 2021). These structural features, together with strong stage-dependent modulation of complex abundance, underscore the unique regulatory and evolutionary adaptations of the parasite mitochondrion. Although it contributes minimally to ATP production, the mitochondrion is indispensable for pyrimidine biosynthesis, electron transport, and redox homeostasis. Recent studies have demonstrated that small-molecule inhibitors targeting *Pf*DHODH, mitochondrial ribosomes, and redox-regulating enzymes exhibit potent activity against both asexual blood stages and gametocytes, offering promising avenues for malaria transmission blocking (Phillips et al., 2015). Ongoing research into mitochondrial dynamics, protein import pathways, and stage-specific metabolic rewiring continues to uncover novel vulnerabilities, reinforcing the mitochondrion making it an increasingly important target in antimalarial drug discovery.

1.2.4 Apicoplast

The apicoplast, a non-photosynthetic plastid found in *Plasmodium falciparum*, is an essential organelle that plays a pivotal role in parasite survival. It originated through secondary endosymbiosis and retains a distinct four-membrane structure (Lemgruber et al., 2013).

Comparative genomic studies have shown significant genetic diversity in apicoplast sequences among *P. falciparum* isolates, particularly in regions such as the China-Myanmar border, indicating an ancient evolutionary history and potential adaptation mechanisms (Tian et al., 2024).

1.2.4.1 Metabolic functions

This plastid houses several metabolic pathways crucial for the parasite's intracellular life cycle. One of the most important is the Type II fatty acid synthesis (FAS-II) pathway, which differs from the mammalian FAS-I pathway, making it a prime drug target (Ralph et al., 2004). The apicoplast is also responsible for isoprenoid biosynthesis via the methylerythritol phosphate (MEP) pathway, which provides essential precursors for numerous cellular processes, including protein prenylation and tRNA modification (Guggisberg et al., 2014; Yeh et al., 2011). Another critical function is the synthesis of iron-sulfur (Fe-S) clusters, which serve as cofactors for various enzymes. The cysteine desulfurase *SufS*, localized in the apicoplast, plays a dual role in Fe-S cluster assembly and tRNA thiolation, highlighting its essential function in parasite survival (Swift et al., 2023). In addition, while *Plasmodium* primarily scavenges heme from its host, the apicoplast contributes to heme biosynthesis, particularly during the early developmental stages, further emphasizing its metabolic significance (Mamudu et al., 2024).

1.2.4.2 Organelle Dynamics and Division

Throughout the *P. falciparum* life cycle, the apicoplast undergoes extensive morphological changes, closely following the parasite's replication cycle. During schizogony, it must be accurately segregated into daughter merozoites. Research has shown that the dynamin-related protein *Pf*Dyn2 is required for the division of both the apicoplast and mitochondrion, suggesting a shared fission mechanism between these two essential organelles (Morano et al., 2024).

1.2.4.3 Antibiotics and the "Delayed Death" Phenomenon

Due to its bacterial ancestry, the apicoplast is highly susceptible to antibiotics and other small-molecule inhibitors that target prokaryotic-like pathways. One well-characterized class of apicoplast-targeting drugs is antibiotics such as clindamycin and doxycycline, which disrupt protein translation in the organelle, leading to the so-called "delayed death" phenotype (Dahl et al., 2008; Dahl et al., 2006). This delayed effect occurs because the apicoplast is essential for progeny parasites but is not required for immediate survival in the first cycle of drug exposure (Ralph et al., 2004). One promising drug target within the apicoplast is its DNA replication machinery. The organelle contains a single DNA polymerase (apPol), which has been identified as a vulnerable component of apicoplast maintenance (Kaur et al., 2022). Small-molecule inhibitors have been developed to selectively target apPol, impairing apicoplast genome replication and leading to parasite death (Kumari et al., 2022). Recent high-throughput screening efforts have identified several compounds with potent activity against apPol, highlighting its potential as an antimalarial target (Kaur et al., 2022).

In addition to these established drug targets, novel chemical entities are being explored for their antiplasmodial effects on the apicoplast. One such compound class, 2-phenoxy-3-trichloromethylquinoxalines, has been found to rapidly disrupt apicoplast function, leading to parasite death within a single replication cycle (Amrane et al., 2021). Unlike traditional antibiotics, these compounds do not exhibit delayed death effects, making them particularly attractive for therapeutic development. Further studies on their mechanism of action have revealed that they interfere with multiple apicoplast-related processes, including DNA replication and metabolic functions (Amrane et al., 2021). Overall, the apicoplast seems to be a viable drug target.

1.2.5 Food Vacuole

The food vacuole (FV) in *Plasmodium falciparum* is a specialized acidic organelle central to hemoglobin degradation, nutrient acquisition, and drug action. During the intraerythrocytic stage, the parasite internalizes host hemoglobin through cytostomes, which subsequently fuse to form the FV. Within this compartment, a cascade of proteases, including falcipains and plasmepsins, degrades hemoglobin to release amino acids, essential for parasite growth and survival (Banerjee et al., 2002; Gluzman et al., 1994). The heme component, which is toxic to the parasite, is detoxified into insoluble hemozoin, a process targeted by several antimalarial drugs (Sherman, 1977). The FV membrane harbors critical transporters such as the P. falciparum chloroquine resistance transporter (PfCRT), which alters drug accumulation within the vacuole, and the multidrug resistance protein PfMDR1, implicated in modulating sensitivity to multiple antimalarials, including mefloquine and artemisinin derivatives (Fidock et al., 2000; Sidhu et al., 2002). Additionally, one study have examined FV appearance and PfCRT trafficking dynamics during blood-stage development (Ehlgen et al., 2012). Notably, mutations in PfCRT not only mediate chloroquine resistance but also influence FV morphology, leading to its enlargement and altered sensitivity to quinoline antimalarials (Pulcini et al., 2015). The trafficking of essential proteases to the digestive vacuole (DV) relies on pathways distinct from PTEX. For example, plasmepsin II (PM2) is internalized via cytostomal endocytosis and sorted to the DV, independent of PTEX. While PTEX exports virulence proteins across the parasitophorous vacuole, DV proteases use classical endocytic and secretory routes (Klemba et al., 2004).

The FV remains a primary target for antimalarial intervention, with drugs like chloroquine and quinine acting by disrupting heme detoxification (Bohórquez et al., 2012). However, emerging resistance of the parasite has complicated treatment strategies, necessitating alternative approaches. Recent studies suggest that autophagy-related proteins, such as *Pf*ATG18, play a role in FV dynamics and parasite survival under stress conditions (Agrawal et al., 2020). Additionally, nitric oxide-derived species have been detected within the FV, indicating

potential redox regulation mechanisms that could be exploited for novel therapeutic strategies (Ostera et al., 2008). The FV's interaction with the host environment also extends beyond nutrient acquisition, as its membrane proteins influence drug resistance and metabolic adaptation (Ehlgen et al., 2012). Advances in imaging and inducible expression systems have allowed deeper investigation into FV biogenesis, revealing that multiple pre-FV compartments—such as haemoglobin-containing vesicles and *Pf*CRT-positive nascent vacuoles—form during ring and early trophozoite stages and subsequently merge to establish the mature digestive vacuole (Bakar et al., 2010; Ehlgen et al., 2012). Given its indispensable role in parasite survival and susceptibility to multiple drug classes, the FV remains a key focus for antimalarial drug development, with ongoing efforts aimed at targeting its proteolytic machinery, transporters, and heme detoxification pathways.

1.2.6 The Inner Membrane Complex (IMC)

The inner membrane complex (IMC) is a highly structured organelle in *Plasmodium falciparum*, located beneath the plasma membrane of the invasive forms of the parasites, in blood stages the merozoites. The inner membrane complex (IMC) in *Plasmodium falciparum* is a defining feature of the invasive stages (merozoites, ookinetes, sporozoites), forming a flattened double-membrane system beneath the plasma membrane and serving as a scaffold for glideosome assembly. It houses a family of intermediate filament-like proteins, alveolins, which are conserved across the alveolates and reinforce cell shape (Gould et al., 2008). Evolutionary and architectural studies demonstrate that the IMC architecture varies dynamically between asexual and sexual stages and contains Plasmodium-specific components necessary for merozoite morphogenesis and gametocyte development (Kono et al., 2012). It consists of flattened vesicles supported by a protein-rich cytoskeletal network, functioning as a scaffold for cellular shape, stability, and motility (Harding et al., 2014). During the asexual cycle, the IMC is assembled in late schizogony and plays a crucial role in merozoite formation, egress and invasion. Key components of the IMC, such as glideosome-

associated proteins (GAPs) and alveolins, coordinate the parasite's ability to undergo segmentation and invasion, ensuring the rapid propagation of *P. falciparum* within the host (Harding et al., 2019). Given its role in maintaining cellular architecture and facilitating asexual proliferation, disruptions in IMC formation or function can severely impair parasite replication, indirectly influencing downstream developmental pathways, including gametocytogenesis.

Emerging evidence suggests that the IMC is not only a structural component of asexual stages but also a key determinant of gametocyte and maturation (Gould et al., 2008). Additionally, the IMC is closely linked to the regulation of intracellular signaling pathways that control cell differentiation. PfPKG, a cGMP-dependent kinase essential for gametocyte activation, plays a role in early cellular remodeling including IMC disassembly during exflagellation—but direct mechanistic links between PfPKG activity and IMC structural integrity or gametocyte commitment have not yet been demonstrated (McRobert et al., 2008). Furthermore, alveolins and microtubule-associated proteins that stabilize the IMC are also involved in cytoskeletal rearrangements required for gametocyte development (Dearnley et al., 2012). This suggests that any perturbation in IMC dynamics during asexual replication may compromise the structural and regulatory environment necessary for gametocyte emergence. The IMC is essential for *Plasmodium falciparum* egress and invasion, serving as a structural scaffold in merozoites. Inhibiting IMC components can thus block blood-stage propagation, making it an attractive and parasite-specific drug target. In addition, the IMC plays a critical role during gametocyte development, especially in shaping cell morphology and supporting rigidity in later stages. Although it does not influence the initial commitment decisions, IMC structures are absent at that point-targeting IMC in developing gametocytes could impair parasite transmission, offering a second stage-specific therapeutic window.

1.3 Plasmodium falciparum Genome

The Plasmodium falciparum genome, first sequenced in 2002, remains a fascinating subject due to its high A-T richness (~80%), compact size (~23 Mb), and a large number of hypothetical genes with unknown functions (Gardner et al., 2002). To illustrate the genome architecture of *Plasmodium falciparum*, a schematic overview of its 14 chromosomes is presented in Figure 7. The genome comprises 14 linear chromosomes, each with a conserved gene-dense core (green) and variable subtelomeric regions (yellow) (Conway, 2015). Despite significant advances in genome annotation and functional studies, a considerable proportion of the genome remains uncharacterized (Figure 8), with many genes lacking homologs outside the Plasmodium genus (Birnbaum et al., 2017; Oberstaller et al., 2021). These unknown genes, particularly those located in subtelomeric regions, are critical to understanding parasite survival, immune evasion, and drug resistance mechanisms. While the functional relevance of unannotated genes has increasingly been addressed through high-throughput reverse genetics, several landmark genome-wide screens have greatly expanded our understanding of essential gene sets in Plasmodium. These include the PlasmoGEM barseq-based screening approach applied to *P. berghei* (Bushell et al., 2017; Gomes et al., 2022; Kenthirapalan et al., 2016; Modrzynska et al., 2017), as well as transposon-based saturation mutagenesis screens using piggyBac in P. falciparum and P. knowlesi (Toenhake et al., 2018; Zhang et al., 2018).

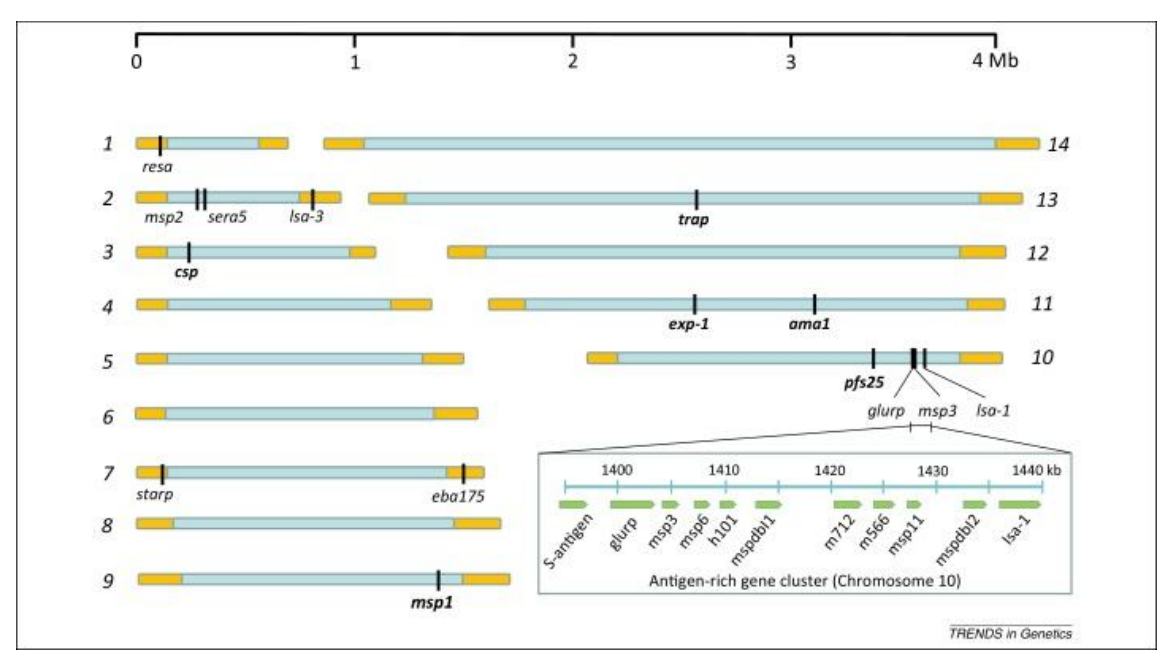


Figure 7. Haploid *Plasmodium falciparum* genome containing 14 chromosomes (Conway et al., 2015).

Among the chromosomes studied, chromosome 3 has yielded particularly rich insights, with recent targeted studies uncovering novel regulators of nuclear organization, mitosis, and parasite-specific cell division mechanisms. While a comprehensive analysis of these findings will follow below, foundational studies from our group (Schmitt, 2020; Kimmel, 2024; Kimmel et al., 2023) have been instrumental in resolving the spatial-functional map of this genomic region.

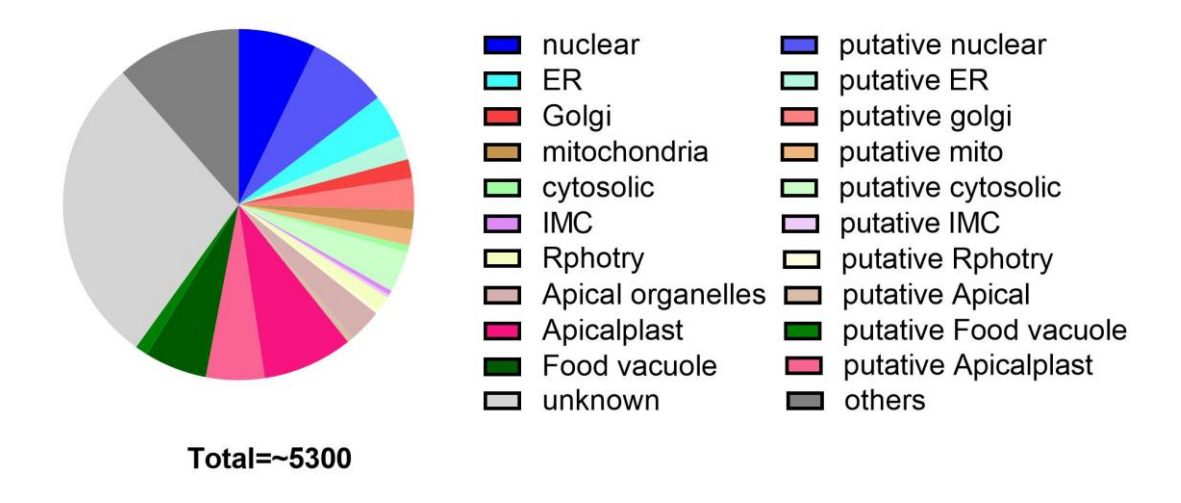


Figure 8. Subcellular localization predictions of P. falciparum proteins (Data from PlasmoDB).

The 14 chromosomes of *P. falciparum* encode ~5,300 predicted genes, with more than 60% classified as hypothetical proteins (Gardner et al., 2002). The genome lacks many conserved transcription factors, metabolic regulators, and checkpoint proteins found in other eukaryotes, suggesting that the parasite has evolved highly divergent regulatory mechanisms (Coulson et al., 2004). Subcellular localization predictions for the whole *P. falciparum* proteins reveal that a substantial fraction localizes to the nucleus, ER, mitochondria, and apicoplast, with a large proportion remaining uncharacterized (Figure 8), underscoring the need for systematic functional annotation of parasite-specific pathways. The gene families responsible for antigenic variation—*var*, rifin, and stevor—are clustered in subtelomeric regions, allowing rapid adaptation to immune pressure (Otto et al., 2018).

One of the major challenges in studying *P. falciparum* gene function is the essential nature of many unknown genes, making them difficult to knock out using traditional genetic tools. Advances in CRISPR-Cas9 editing, PiggyBac mutagenesis, and barcoded knockout libraries have enabled systematic large-scale functional screens, identifying genes essential for parasite growth and survival (Zhang et al., 2018; Bushell et al., 2017; Ghorbal et al., 2014). Despite these efforts, many genes remain functionally uncharacterized, particularly those involved in nuclear organization, vesicular trafficking, and host-cell remodeling.

The study of *Plasmodium falciparum* chromosome 3 has provided significant insights into the unknown genes within the parasite's genome (Schmitt 2020; Kimmel 2024; Kimmel et al., 2023). This chromosome-wide screen of all genes encoding non-secretory proteins without apparent similarity to proteins of known function, demonstrated that a substantial proportion of these unknown genes encode nuclear proteins, which suggests that the nucleus is a hotspot for parasite-specific biological processes. The identification of these nuclear proteins highlights potential vulnerabilities in *P. falciparum* that may serve as drug targets.

For the analysis of chromosome 3, a gene-by-gene screen was done. Of the intitial 249 candidate genes on chromosome 3 filters were applied to remove proteins with a signal peptide or transmembrane domain, function analysis, resulting in 33 genes for further investigation (Schmitt 2020; Kimmel 2024; Kimmel et al., 2023). In order to analyse these genes, selection linked integration (SLI, Birnbaum et al., 2017) was used to obtain parasite cell lines where the respective genes were modified in a way that the expressed protein received a multi-purpose tag containing FKBP domains and GFP. This tag permits to study the location (via GFP), the function (using knock sideways using the FKBP domain) and DiQ-BioID (Birnbaum and Scharf, 2020; Kimmel et al., 2022) for proxiome studies. The results showed that several of these genes play essential roles in DNA replication and mitosis, suggesting their involvement in fundamental parasite survival mechanisms. Similar to chromosome 3, a substantial proportion of genes on chromosome 4 remain uncharacterized in terms of subcellular localization, with the "unknown" category representing the largest single group (Figure 9).

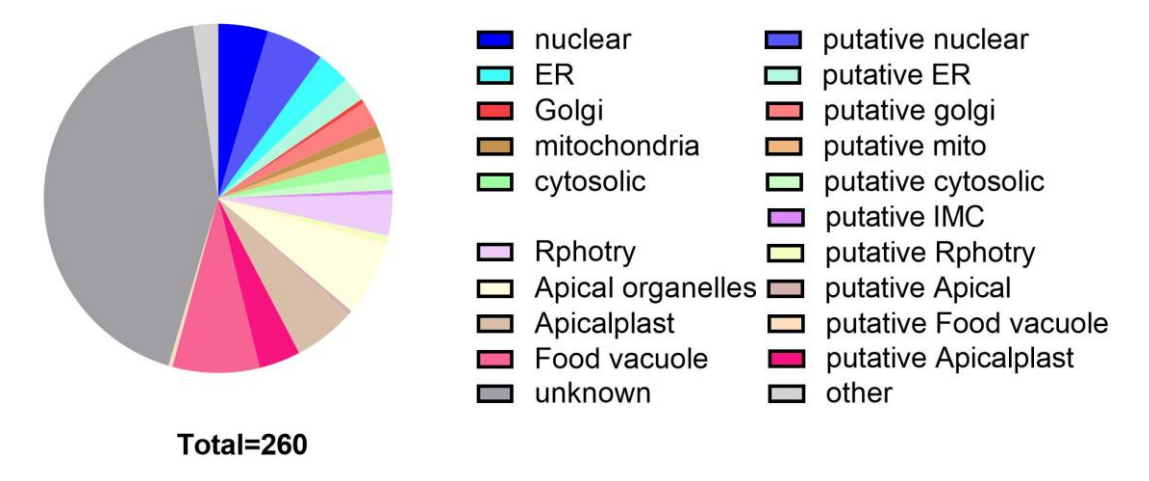


Figure 9. The subcellular distribution of chromosome 4 (Date from PlasmoDB).

Overall, advances in gene-editing techniques and medium as well as large-scale screening approaches will be instrumental in further elucidating the biological significance of unknown proteins of the parasite, ultimately contributing to the identification of novel therapeutic targets against malaria.

1.4 Aims

The *Plasmodium falciparum* genome contains a large number of genes with unknown functions, many of which are specific to the parasite and have no homologs in model organisms. So far, open screens have been conducted for some of the genes on chromosome 1 (Schmidt 2017) and chromosome 2 (Birnbaum et al., 2017) and comprehensively chromosome 3 (Schmitt 2020; Kimmel et al., 2023). The logic next step in the quest to elucidate the unknown biology of the parasite are the genes on chromosome 4 to further close the gap in our understanding of malaria parasite biology. While genome-wide studies have helped define essential genes, the precise localization and function of many chromosome 4 proteins remain unclear (Figure 8). Identifying their roles could uncover novel parasite-specific pathways and highlight potential drug targets.

This study aims to investigate unknown genes on chromosome 4 using SLI approach that combines genetic tagging, functional screening, and localization studies. The specific objectives are:

- (i) Determining the subcellular localization of unknown proteins encoded on chromosome 4 to predict their potential roles in parasite physiology.
- (ii) Assessing the essentiality of these genes in the asexual blood stage to identify those critical for parasite survival.
- (iii) Functionally characterizing selected essential genes through targeted genetic manipulation to define the biological process they are involved in.
- (iv) Creating a genetically modified parasite strain collection that can be used for further functional studies by the research community.

By focusing on chromosome 4, this study aims to contribute to a more comprehensive understanding of parasite-specific biological processes, uncover new regulatory mechanisms, and provide valuable insights that may guide future malaria intervention strategies.

2. Materials and Methods

2.1 Materials

2.1.1 Technical Devices

Table 3. List of Technical Devices

Device	Manufacturer	Model
Flow cytometer	BD Biosciences	LSR II
Culture incubator	Thermo Scientific	Heracell VIOS 160i
Nucleofector	Lonza	Nucleofector II
Centrifuge	Eppendorf	5810 R
NanoDrop spectrophotometer	Thermo Fisher	NanoDrop One
Gel documentation system	Peqlab	Fusion FX
Confocal microscope	Leica	SP8
Fluorescence microscope	Zeiss	Axio Observer
Electrophoresis chamber	Bio-Rad	Mini-Sub Cell GT
-80 °C Freezer	Thermo Fisher	Forma 900 series

2.1.2 Chemicals

Table 4. List of Chemicals

Chemical	Supplier	Catalog Number
RPMI 1640 medium	Thermo Fisher	11875093
Albumax II	Gibco	11021029
D-Sorbitol	Sigma-Aldrich	S1876
Hypoxanthine	Sigma-Aldrich	H9636

Glucose	Merck	G8270
HEPES	Sigma-Aldrich	H3375
NaHCO ₃	Sigma-Aldrich	S5761
Gentamycin	Gibco	15750060
WR99210	Jacobus Pharmaceuticals	WR99210
Blasticidin S	InvivoGen	ant-bl-1
G418 sulfate	InvivoGen	ant-gn-5
Saponin	Sigma-Aldrich	47036
Mitotracker	Thermo Fisher	M7512
TRIzol reagent	Invitrogen	15596026
Paraformaldehyde	Electron Microscopy Sciences	15710
Glutaraldehyde	Electron Microscopy Sciences	16020
DAPI	Sigma-Aldrich	D9542
Hoechst 33342	Thermo Fisher	H3570
DHE	Thermo Fisher	D11347

2.1.3 Labware and Disposables

Table 5. List of Labware and Disposables

Item	Supplier	Catalog Number
1.5 mL tubes	Eppendorf	0030120086
2.0 mL tubes	Eppendorf	0030120094
15 mL Falcon tubes	Corning	430052
50 mL Falcon tubes	Corning	430828
10 cm Petri dishes	Greiner Bio-One	664160
6-well culture plates	Corning	3516

Serological pipettes (1-25 mL)	Falcon	Various
Glass Pasteur pipettes	Sigma-Aldrich	P0413
Sterile pipette tips (filter)	Sarstedt	70.760.002
PCR tubes and strips	Biozym	320500
Microscope slides	Thermo Fisher	12-550-15
Coverslips	VWR	630-2183
Electroporation cuvettes (0.2 cm)	Bio-Rad	1652086
Cell strainer (40 μm)	Falcon	352340
Hemocytometer	Marienfeld	0640030

2.1.4 Kits

Table 6. List of Kits

Kit	Supplier	Catalog Number
NucleoSpin Gel and PCR Clean-up	Macherey-Nagel	740609.50
RNeasy Mini Kit	Qiagen	74104
Plasmid MiniPrep Kit	Zymo Research	D4054
Plasmid MidiPrep Kit	Qiagen	12143
TRIzol Reagent	Invitrogen	15596026
SuperSignal West Pico PLUS	Thermo Fisher	34580
ECL Prime Kit	GE Healthcare	RPN2232
Qubit RNA Assay Kit	Thermo Fisher	Q32852
NEBNext Ultra II RNA Kit	NEB	E7770

2.1.5 Enzymes and Polymerases

Table 7. List of Enzymes and Polymerases

Name	Application	Supplier	Catalog No.
T4 DNA ligase	Ligation of DNA fragments	New England Biolabs	M0202S
Phusion High-Fidelity DNA Polymerase	High-fidelity PCR amplification	New England Biolabs	M0530S
FIREPol DNA Polymerase	Routine PCR	Solis BioDyne	01-02- 00500
Taq DNA Ligase	Ligation of adjacent DNA ends at high temp	New England Biolabs	M0208S
Proteinase K	Protein digestion in DNA/RNA extraction	Qiagen	19131

2.1.6 Antibodies and Fluorescent Dyes

Table 8. List of Antibodies and Fluorescent Dyes

Antibody / Dye	Туре	Application	Dilution	Supplier	Catalog Number
Anti- GFP	Rabbit polyclonal	WB / IFA	1:1000	Abcam	ab290
Anti-HA	Mouse monoclonal	WB / IFA	1:2000	Sigma-Aldrich	H3663
Anti- EXP2	Rabbit polyclonal	IFA	1:500	BEI Resources	NR- 45753
Anti-BiP	Rabbit polyclonal	WB	1:1000	Santa Cruz Biotechnology	sc- 13968
Anti- rabbit HRP	Goat polyclonal	WB	1:5000	Cell Signaling	7074
Anti- mouse HRP	Goat polyclonal	WB	1:5000	Cell Signaling	7076

Alexa Fluor 488 anti- rabbit	Goat polyclonal	IFA	1:1000	Thermo Fisher	A11008
Alexa Fluor 594 anti- mouse	Goat polyclonal	IFA	1:1000	Thermo Fisher	A11005
DAPI	-	Nuclear stain	1 μg/mL	Sigma-Aldrich	D9542
Hoechst 33342	-	DNA stain	1 μg/mL	Thermo Fisher	H3570
DHE	-	PPM stain	5 μg/mL	Thermo Fisher	D11347

2.1.7 Biological Material

Table 9. List of Biological Material

Material	Type / Purpose	Supplier / Source	Catalog No. / Reference
P. falciparum 3D7	Parasite line for transfection	BEI Resources	MRA-102
Human O+ erythrocytes	Host cells for parasite culture	Blood Bank (UKE)	n/a
E. coli XL10-Gold	Bacterial strain for cloning	Agilent Technologies	200314
LB	E. coli culture medium	Sigma-Aldrich	L3022
LB agar	Solid culture medium	Sigma-Aldrich	L2897
Ampicillin	Selection antibiotic (<i>E. coli</i>)	AppliChem	A0839,1000

2.1.8 Plasmids

Table 10. List of Plasmids

Plasmid	Backbone	Application	Resistance Marker	Source / Reference
pSLI-TGD	pDC2	Endogenous gene tagging	hDHFR, NeoR	(Birnbaum et al., 2017)
pSLI- sandwich-N	pDC2	Knock sideways system	hDHFR, BSDR	(Birnbaum et al., 2017)
7xGFP	pDC2	Enhanced signal	BSDR	(Birnbaum et al., 2017)
Miniturbo-C	pDC2	BioID C-terminal tagging	BSDR	(Birnbaum et al., 2017)
Minitubro-N	pDC2	Endogenous GFP tagging	hDHFR, NeoR	(Birnbaum et al., 2017)
N-terminal sandwich	pL6	Integration reporter	BSDR	(Ghorbal et al., 2014)
Lyn/NLS	pARL	Constitutive expression	hDHFR	(Adjalley et al., 2011)

2.1.9 Software and Databases

Table 11. List of Software and Databases

Software / Database	Purpose	Versio n	Source / Website
GraphPad Prism	Statistical analysis and graphing	9.0	GraphPad Software
ImageJ / Fiji	Image processing	2.3.0	https://imagej.net

PlasmoDB	Parasite genome annotation	Releas e 60	https://plasmodb.org
SnapGene	Plasmid annotation and cloning design	v6.0	GSL Biotech
ApE	Free plasmid visualization	Latest	https://jorgensen.biology.utah.edu/wayned/ape/
Microsoft Office	Documentatio n and spreadsheets	2019	Microsoft
CorelDRA W	Figure layout	2018	Corel Corporation
FACSDiva	Flow cytometry acquisition software	8.0	BD Biosciences

2.1.10 5% Sorbitol Solution

50 g of D-Sorbitol (Sigma, S1876-500g) was dissolved in 1 L of distilled water. The solution was sterile filtered using 2×500 mL Stericups and stored at 4 °C

2.1.11 10× LB Medium

200 g of LB-Medium powder (Roth, X964.3) was dissolved in 1 L of ultrapure water. The solution was stirred at room temperature, stored refrigerated overnight, and autoclaved the next day before use.

2.1.12 50× TAE Buffer (pH 8.5)

242.28 g Tris base and 18.61 g Na₂EDTA·2H₂O were dissolved in 800 mL distilled water. Then, 60.05 g glacial acetic acid was added carefully while wearing safety goggles. The pH was adjusted to 8.5, and the final volume was brought up to 1 L. The buffer was stored at room temperature.

2.1.13 Ampicillin Stock

5 g Ampicillin (AppliChem, A6352,0025) was dissolved in 50 mL distilled water, sterile-filtered, and aliquoted (2 mL/tube) for storage at -20 °C. For LB medium, 500 μ L of this stock was added to 500 mL of LB to yield a final concentration of 100 μ g/mL.

2.1.14 Blasticidin S (BSD)

50 mg Blasticidin S (Invitrogen, R21001) was dissolved in 1 mL water, followed by 9 mL Ampuwa water. The solution was mixed thoroughly, sterile-filtered through a 0.2 μ m filter, and aliquoted (100 μ L/tube). Stocks were stored at -80 °C. A working concentration of 2.5 μ g/mL was obtained by adding 2.5 μ L of stock to 5 mL culture.

2.1.15 dNTP Mix (2.5 mM each)

To prepare a 2.5 mM dNTP mix, 250 μ L each of 100 mM dATP, dCTP, dGTP, and dTTP (Roth, K039.1) were combined in 9 mL distilled water to a total of 10 mL. The mix was aliquoted in 150 μ L portions and stored at -20 °C.

2.1.16 DSM1

A 187.5 mM stock was prepared by dissolving 0.258 g DSM1 in 5 mL 100% DMSO, aliquoted (1 mL) and stored at -80 °C. A working solution of 3.75 mM was prepared by mixing 100 μ L of stock with 4.75 mL DMSO and 250 μ L PBS, sterile-filtered, aliquoted, and stored at -80 °C. To achieve a final concentration of 0.9 μ M in culture, 1.2 μ L of the working solution was added to 5 mL of parasite culture.

2.1.17 Human O⁺ Erythrocytes:

O⁺ erythrocytes were ordered weekly from the UKE blood bank (liefer-transmed@uke.de). Upon receipt, the bag was disinfected and aliquoted into 50 mL Falcon tubes (~20 mL/tube). Samples were stored at 4 °C and used within 7 days. Records were maintained under ethics approval (AG Spielmann, BNITM).

2.1.18 FACS Solutions

To prepare the Hoechst 33342 working solution, dissolve 4.5 mg powder in 1 mL DMSO to obtain a 4.5 mg/mL stock. For the working dilution, mix 100 μ L of the stock with 900 μ L DMSO to yield 0.5 mg/mL.

DHE was prepared similarly by dissolving 5 mg in 1 mL DMSO (5 mg/mL stock), followed by 1:10 dilution to 0.5 mg/mL.

All stock and working solutions were aliquoted ($100 \,\mu\text{L}$) and stored in the general freezer in room 213 south.

2.1.19 FACS Stop Solution

Prepared by adding $0.5~\mathrm{mL}$ glutaral dehyde to $40~\mathrm{mL}$ RPMI medium. Stored at $4~\mathrm{^{\circ}C}$ for up to one week.

2.1.20 10% Giemsa Staining Solution

Prepared fresh every Monday, Wednesday, and Friday by diluting Giemsa stock solution 1:10 in tap water (e.g., 30 mL stock + 270 mL H₂O). Used solution was discarded in the designated Giemsa waste container under the sink in the cell culture room. Methanol was refilled as needed for slide fixation.

2.1.21 LB Agar Plates (Ampicillin)

To prepare LB agar, weigh 17.5 g LB-Agar (Lennox, Roth) into each of eight 500 mL glass bottles. Once autoclaved, agar was cooled to ~60 °C, and 500 μL ampicillin (100 mg/mL) was added per bottle before pouring. Plates were stored at 4 °C in sealed, labeled plastic bags.

2.1.22 MFS Freezing Solution

Prepared by dissolving 37.8 g D-sorbitol and 8.1 g NaCl in 350 mL glycerol. The volume was adjusted to 1 L with distilled water. The solution was sterile-filtered using 2×500 mL Stericups and stored at 4 °C.

2.1.23 MTS Thawing Solution

Prepared by dissolving 35 g NaCl in 1 L distilled water (3.5% NaCl), followed by sterile filtration. Stored at 4 °C

2.1.24 G418 (Neomycin)

Stock solution was prepared at 50 mg/mL by dissolving G418 disulfate salt (Sigma A1720) in cold sterile RPMI medium. For a 25 g batch, 25 g powder was first dissolved in 100 mL RPMI, then filled up to 500 mL, sterile-filtered, and aliquoted (1.7 mL in 2 mL tubes). Working concentration in culture was 400 µg/mL (i.e., 40 µL per 5 mL culture). Aliquots were stored at -20 °C. Once thawed, they were kept at 4 °C and used within a few days.

2.1.25 Percoll Solutions

To make 90% Percoll, 27.7 mL 10× PBS was added to 250 mL Percoll (GE Healthcare No. 17-0891-02).

For 250 mL of each gradient:

60% Percoll: 10 g sorbitol + 167.5 mL 90% Percoll + 82.5 mL RPMI

80% Percoll: 10 g sorbitol + 222.5 mL 90% Percoll + 27.5 mL RPMI

40% Percoll: 10 g sorbitol + 110 mL 90% Percoll + 140 mL RPMI

Solutions were sterile-filtered under a hood using 0.2 µm filters and stored in 50 mL Falcon tubes at 4 °C (valid for 6 weeks).

2.1.26 Rapalog (Clontech #635055, 5 mg)

Stock solution was made by dissolving 5 mg Rapalog in 983 μ L 100% ethanol (5 mM), then diluted with 8.85 mL ethanol to reach 0.5 mM. Aliquoted into 1 mL tubes and stored in a brown Falcon tube at -20 °C.

For working solution, one aliquot was diluted with 19 mL RPMI complete medium and filtered to make 25 μ M final. Usage was 20 μ L per 2 mL culture (final 250 nM). Working aliquots were shared and used quickly due to limited stability.

2.1.27 RPMI 1640 Complete Medium Preparation (Based on Applichem A1538,9010)

Complete culture medium for *Plasmodium falciparum* was prepared by dissolving the following components in 2.5 L of distilled water: 160 g RPMI 1640 powder, 10 g sodium bicarbonate, and 20 g glucose monohydrate. Separately, 50 g of Albumax II was dissolved in another 2.5 L of distilled water. The two solutions were combined to yield a total volume of 5 L.

Subsequently, 0.272 g of hypoxanthine was dissolved in 8 mL of 1 N NaOH and added to the medium. Gentamycin was added to a final concentration of 20 μ g/mL (i.e., 5 mL of a 200 mg/5 mL solution). The pH was adjusted to 7.2 using 10 N NaOH. The mixture

was split equally into two 2.5 L containers and each was topped up to 5 L with distilled water.

The complete medium was sterile-filtered using large-neck Stericups and subsequently aliquoted into sterile 2 L glass bottles, then further dispensed into labeled 250 mL green-cap bottles. Four bottles were incubated overnight at 37 °C to verify sterility.

2.1.28 WR99210

A 20 mM WR99210 stock solution in DMSO was stored at -80 °C. For preparation of a working solution, 10 μL of the stock was added to 10 mL of complete RPMI medium (1:1000 dilution), resulting in a final concentration of 20 μM.

The working solution was sterile-filtered using a 0.2 μm syringe filter and aliquoted into 100 μL portions for storage at -80 °C.

For use in parasite cultures, the working concentration was 3 nM, achieved by adding $0.75 \,\mu\text{L}$ of the working solution to 5 mL of culture.

2.2 Methods

2.2.1 Parasite Culture

Plasmodium falciparum 3D7 parasites were cultured in vitro following standard protocols with specific modifications for consistency and optimal growth. Parasites were maintained in human O⁺ erythrocytes at a hematocrit of 2-5% in RPMI 1640 complete medium supplemented with 25 mM HEPES, 2 mM L-glutamine, 0.2 mM hypoxanthine, 0.5% (w/v) Albumax II, 12 mM NaHCO₃, 6 mM glucose, and 0.4 mM gentamicin. Cultures were incubated at 37 °C in a low-oxygen environment (5% O₂, 5% CO₂, and 90% N₂). Medium was replaced daily or every other day depending on

parasitemia. Cultures below 1% parasitemia could be fed every second day. If feeding was postponed for two days, parasitemia was diluted to ≤0.05% to avoid overgrowth. Cultures exceeding 5-10% parasitemia were diluted to maintain healthy growth. For high-density cultures used in harvests, cultures were fed twice a day, and the medium volume was increased up to 15 mL per 10 mL dish to prevent nutrient depletion.

Parasitemia and parasite morphology were monitored daily via Giemsa-stained thin blood smears. Smears were prepared from the "tongue" region of the slide, where red blood cells are well-distributed and flat. Parasites showing signs of pyknosis or abnormal morphology were considered nonviable, and the cultures were discarded unless working with poorly adapted or nutrient-limited lines.

Synchronized cultures were obtained via 5% sorbitol treatment, typically performed twice in one cycle with an interval of 8-10 hours. Highly synchronous stages were generated using Percoll purification followed by sorbitol lysis after a defined invasion window (based on protocols adapted from Grüring et al., 2011). To avoid excessive physiological perturbation, synchronization was conducted one cycle prior to experimental time points when appropriate.

Care was taken to avoid stage shifting by extended room temperature exposure. Parasites were maintained strictly at 37 °C, and experimental manipulation was performed with minimal time outside of the incubator. No experiments involving temperature shifting were included in this thesis.

Smears from harvested cultures were archived for future reference. For important time points, multiple smears were prepared, with one stained immediately and others fixed in methanol and stored unstained for later use. Slides intended for long-term preservation were mounted under coverslips after enhanced Giemsa staining.

To preserve consistency, a single blood batch was used throughout each experiment. This avoided the appearance of dual growth populations which could complicate interpretation.

2.2.2 Synchronization and Parasite Preparation

For schizont-stage enrichment, a 60% Percoll density gradient was prepared by adding 4 mL of Percoll solution into a 15 mL Falcon tube. Parasite cultures were gently mixed and carefully layered on top of the Percoll using a pipette, ensuring minimal disturbance of the interface. The gradient was centrifuged at 2000 × g for 6 minutes at room temperature without brake.

After centrifugation, the upper medium layer was discarded. The enriched schizont band, located at the interface between the medium and Percoll, was carefully collected using a sterile Pasteur glass pipette and transferred to a new 15 mL Falcon tube. The collected fraction was then diluted with complete culture medium up to a total volume of $14 \, \text{mL}$ and centrifuged at $4000 \times \text{g}$ for 2 minutes. The resulting pellet containing purified schizonts was immediately used for downstream applications such as transfection.

2.2.3 DNA Assembly by Gibson Cloning

DNA fragments with overlapping homologous regions (15-40 bp) were assembled using Gibson Assembly. Fragments were generated by PCR and purified using the PCR Clean-up Kit (Macherey-Nagel). DNA concentrations were measured using a NanoDrop spectrophotometer and adjusted to 0.1-0.5 pmol per fragment for assembly.

Reactions were incubated at 50 °C for 60 minutes. Assembled products were either directly used for transformation into chemically competent E. coli (XL10-Gold) or stored at -20 °C for future use.

Positive clones were screened by colony PCR and Sanger sequencing.

2.2.4 DNA Ligation Using T4 DNA Ligase

DNA ligation was performed using T4 DNA ligase (New England Biolabs) to insert restriction-digested DNA fragments into compatible plasmid backbones. Vector and insert DNA fragments were purified using the NucleoSpin Gel and PCR Clean-up Kit (Macherey-Nagel) and quantified by NanoDrop.

Reactions were incubated at room temperature for 2 hours or overnight at 16 °C. Ligated products were transformed into chemically competent E. coli XL10-Gold cells using the standard heat-shock protocol and plated on LB agar plates containing 100 μg/mL ampicillin.

Positive clones were screened by colony PCR and Sanger sequencing.

2.2.5 E. coli Transformation and Plasmid Preparation

Chemically competent *E. coli* XL10-Gold cells stored at -80 °C were thawed on ice. For transformation, plasmid DNA was gently mixed with 100 µL of competent cells and incubated on ice for 20 minutes. The mixture was then heat-shocked at 42 °C for 30 seconds and immediately transferred back to ice for 1-3 minutes.

Following heat shock, 1 mL of antibiotic-free LB medium was added, and the cells were incubated at 37 °C with shaking at 800 rpm for 30 minutes to allow recovery. After centrifugation, 900 μ L of the supernatant was discarded. The remaining 100 μ L was resuspended and spread evenly on LB agar plates containing 100 μ g/mL ampicillin using sterile glass beads. Plates were incubated overnight at 37 °C.

Plasmids were extracted from overnight cultures of single colonies using commercial miniprep or midiprep kits depending on the required yield.

2.2.6 Transfection and Selection of P. falciparum

Schizont-stage *Plasmodium falciparum* 3D7 parasites were enriched using a 60% Percoll gradient and pelleted by centrifugation. For transfection, the parasite pellet was resuspended in 90 µL of TB buffer. Fifty micrograms of linearized plasmid DNA, dissolved in 10 µL TE buffer, was added to the suspension and gently mixed.

The 100 μ L DNA-parasite mixture was transferred to a certified electroporation cuvette, and electroporation was performed using the Amaxa Nucleofector II system with program U-033. Immediately following electroporation, the sample was transferred into a 1.5 mL microcentrifuge tube containing 300 μ L of packed human erythrocytes and 200 μ L of pre-warmed RPMI complete medium. The mixture was incubated at 37 °C with shaking at 800 rpm for 30 to 60 minutes to facilitate parasite recovery and invasion.

Following recovery, the full suspension was transferred to 5 mL of fresh medium culture in a 5 mL Petri dish and maintained under standard culturing conditions. Drug selection was initiated 24-48 hours post-transfection. In the case of selection-linked integration (SLI), parasites were initially cultured with WR99210 to enrich episomal plasmids, followed by selection with G418 to promote genomic integration. WR was withdrawn during G418 selection.

Parasites typically reappeared within 1 to 4 weeks. Correct genomic integration was confirmed by diagnostic PCR across integration junctions and by absence of the wild-type allele. Successfully modified lines were maintained under continuous drug pressure and used for downstream assays.

2.2.7 Preparation of Chemically Competent E. coli XL10-Gold Cells

Chemically ultra-competent Escherichia coli XL10-Gold cells were prepared following the modified Inoue method. Transformation buffer was prepared by dissolving 3 g/L PIPES (10 mM), 2.2 g/L CaCl₂·2H₂O (15 mM), and 18.6 g/L KCl (250 mM) in ~800 mL deionized water. The pH was adjusted to 6.7 using KOH. Subsequently, 10.9 g/L MnCl₂·4H₂O (55 mM) was added, and the solution was adjusted to 1 L with deionized water, sterile filtered, aliquoted (50 mL), and stored at -20 °C.

SOB medium was prepared by dissolving 20 g tryptone, 5 g yeast extract, and 0.5 g NaCl in 950 mL deionized water. After complete dissolution, 10 mL of 250 mM KCl was added. The pH was adjusted to 7.0 with 5 N NaOH, the volume adjusted to 1 L, and the solution was autoclaved. Just before use, 5 mL of sterile 2 M MgCl₂ was added.

To begin the preparation, 10 mL LB medium containing 34 µg/mL chloramphenicol was inoculated with XL10-Gold glycerol stock and grown overnight at 37 °C with shaking (lid loosely closed). The following day, 200 mL SOB medium was inoculated with 5 mL overnight culture and incubated at 18 °C and 160 rpm for 20-24 hours until OD600 reached 0.45-0.6. Additional backup cultures were prepared in parallel (2 × 200 mL with 2.5 mL inoculum each).

Once the target OD was reached, the cultures were cooled on ice and divided into 15 mL Falcon tubes (4 tubes per 200 mL). Cells were pelleted by centrifugation at 3000 × g for 15 minutes at 4 °C. After discarding the supernatant, tubes were briefly inverted on absorbent paper to remove residual medium.

Each pellet was gently resuspended in 20 mL of ice-cold transformation buffer and incubated on ice for 10 minutes, followed by a second centrifugation (3000 × g, 15 minutes, 4 °C). Pellets were then resuspended in a total of 16 mL ice-cold

transformation buffer (4 mL per pellet, pooled). While gently swirling the suspension, 1.2 mL DMSO was added dropwise. The suspension was transferred to a pre-cooled small beaker.

Aliquots of $100 \,\mu\text{L}$ were immediately dispensed into pre-chilled microcentrifuge tubes, frozen in a dry ice-ethanol bath, and transferred to a -80 °C freezer. Throughout the entire process, care was taken to avoid temperature fluctuations. Competency of each batch was tested using a standard plasmid transformation assay.

2.2.8 Immunofluorescence Assay (IFA)

Thin smears of parasite-infected (parasitemia \sim 5%) erythrocytes were prepared on 10-well multiwell slides (8 mm diameter per well). To prepare smears, parasite cultures (typically 50-500 μ L) were centrifuged at 2000 g 30s, the supernatant was removed, and the pellet was washed three times with 1× PBS. After a second centrifugation, the cells were diluted to 1-2% hematocrit and 2-5 μ L of suspension was added to each well. The volume was adjusted such that the surface of the well was uniformly wetted, but not overloaded with cells. Slides were left to air-dry at room temperature.

For fixation, slides were placed in a 50 mL Falcon tube containing 100% acetone and incubated at room temperature for 30 minutes. Slides were then removed and allowed to air-dry. Slides could be stored at this stage.

For immunostaining, wells were first rehydrated with $\sim \! 50\,\mu L$ of $1\times$ PBS per well and incubated in a humid chamber. Wells were then washed three times with $1\times$ PBS using a vacuum pump with a modified 1 mL pipette tip for aspiration. Care was taken not to touch the well surface during washing. Clean $1\times$ PBS from a dedicated IFA-use Falcon tube was used.

Primary antibodies (diluted 1:10 000 depending on the antibody) were applied in 20 μ L of 3% BSA in 1× PBS containing ampicillin, and incubated for overnight at 4 °C in a humid chamber. Wells were washed five times with 1× PBS as described above.

Secondary antibodies (diluted 1:2000) were applied in 3% BSA/1× PBS/ 1 μ g/mL Hoester, and incubated for 1 hour at room temperature in the humid chamber. A final wash was performed (5× with 1× PBS), and the slides were mounted with PBS-buffered glycerol or antifade mounting medium. Coverslips were sealed with nail polish and stored at 4 °C in the dark until imaging.

2.2.9 Conditional Mislocalization (Knock Sideways)

The knock sideways (KS) approach was used to conditionally mislocalize endogenously expressed proteins in *Plasmodium falciparum* using the FKBP-FRB* heterodimerization system. Genes of interest were tagged at the endogenous locus with a C-terminal GFP-2×FKBP-GFP tag via selection-linked integration (SLI) using the pSLI-sandwich plasmid backbone. Constructs were verified by diagnostic PCR and sequencing.

To drive subcellular mislocalization upon rapalog addition, mislocalizer plasmids expressing mCherry-FRB* fusions were used. Two types of mislocalizers were employed: one targeting the nucleus via a nuclear localization signal (NLS), and the other targeting the plasma membrane using a Lyn-derived signal anchor.

Parasites expressing both the FKBP-tagged target gene and FRB-mislocalizer were split into two parallel cultures. One culture was treated with 250 nM rapalog (AP21967, Clontech), and the other served as an untreated control.

After 16-24 hours of rapalog treatment, live-cell fluorescence microscopy was performed to assess situation of mislocalization. GFP fluorescence was monitored for

redistribution from the original subcellular site (e.g., cytosol or nucleus) to either the nucleus (NLS mislocalizer) or plasma membrane (Lyn mislocalizer). Images were acquired using a Zeiss Axio Observer microscope equipped with a 63× oil objective and analyzed with Fiji/ImageJ to evaluate mislocalization efficiency.

Functional consequences of KS induction were assessed by measuring parasite growth and development over 5 days using daily flow cytometry. Any stage-specific accumulation or growth arrest was interpreted as indicative of an essential function for the mislocalized protein.

2.2.10 Flow Cytometry Analysis

For each sample, a staining mix was prepared containing $18 \mu L$ of RPMI 1640 medium, $1 \mu L$ of Hoechst working solution, and $1 \mu L$ of DHE working solution. Twenty microliters of parasite culture were added to this mix and incubated for 20 minutes at room temperature in the dark.

After staining, $400\,\mu\text{L}$ of ice-cold FACS stop solution ($40\,\text{mL}$ RPMI + $0.5\,\text{mL}$ glutaraldehyde) was added to each sample to fix the cells. Samples were kept on ice and vortexed immediately before acquisition.

Prior to sample measurement, the instrument was prepared by sequentially running: 10 minutes CLEAN solution (high speed), 10 minutes RINSE solution (high speed), 10 minutes distilled water (high speed).

FACSDiva software was launched during the wash cycles (login: BDIS). Instrument connection and user preset settings were confirmed. Samples were acquired with medium or low flow rate, and 100,000 events were collected per sample.

After measurements, the system was cleaned by repeating the CLEAN, RINSE, and WASH cycles (5 minutes each), then switched to STANDBY mode with low speed. All dyes and waste were disposed of according to safety regulations.

2.2.11 Freezing and Thawing of *Plasmodium falciparum*

For long-term storage, *Plasmodium falciparum* cultures at the late ring and ~5% parasitemia were cryopreserved. Parasite-infected red blood cells were pelleted by centrifugation at 3000 g for 3 minutes. The pellet was resuspended 1mL MFS buffer. The luqid were transferred into cryovials, frozen at -80 °C for middle long-term preservation and stored in liquid nitrogen for long-term preservation.

Frozen parasite stocks were rapidly thawed in a 37 °C water bath. The thawed suspension was transferred to a tube and centrifuged at 3000 g for 3 minutes. The supernatant was discarded, and the pellet was gently resuspended in 1 mL of prewarmed MTS buffer. After a second centrifugation at 3000 g for 3 minutes, the pellet was washed once with complete RPMI medium.

The cell suspension was transferred into a 5 mL culture dish containing fresh human O⁺ erythrocytes. Cultures were incubated under standard conditions. Drug selection was withheld for the first 24-48 hours to facilitate parasite recovery and reinvasion, and subsequently reintroduced according to the selection marker.

Parasite viability was assessed daily by Giemsa-stained thin smears.

2.2.12 Parasite Stage Assay

To monitor the intraerythrocytic development of *Plasmodium falciparum*, Giemsastained thin smears were prepared at defined time points from synchronous cultures. At each time point, 1-2 μL of parasite culture was applied to a clean glass slide, air-dried,

fixed in methanol for 1-2 minutes, and stained with 10% Giemsa solution (prepared in tap water) for 10 minutes. After staining, slides were rinsed with water, dried, and stored for microscopy.

Parasite stages were quantified by light microscopy under a 100× oil immersion objective. At least 300 infected red blood cells (iRBCs) were counted per sample. Parasites were morphologically classified as rings, trophozoites, or schizonts. Gametocytes and other atypical forms, if present, were recorded separately.

The proportion of each stage was calculated as a percentage of the total iRBCs counted. Counts were performed in duplicate or triplicate per condition, and mean values were used for analysis. Whenever possible, slide counting was done in a blinded fashion to minimize observer bias.

Stage distribution curves were generated to evaluate the synchrony and timing of parasite progression under different experimental conditions.

2.2.13 Live Cell Microscopy

Live *Plasmodium falciparum*-infected red blood cells were imaged to monitor subcellular localization and morphology under physiological conditions. Parasite cultures were harvested at the desired time point and gently washed once in pre-warmed complete RPMI medium. Cells were resuspended in medium at 2% hematocrit and transferred to a glass-bottom dish (Ibidi μ-Dish 35 mm, high Glass Bottom).

Cells were allowed to settle for 5-10 minutes at 37 °C before imaging. Imaging was performed on fluorescence microscope equipped with a 63×/ 100× oil immersion objective. Parasite structures labeled with GFP, mCherry, or other fluorescent proteins were visualized using appropriate excitation and emission filters. For nuclear

visualization, live cells were incubated with $1 \mu g/mL$ Hoechst 33342 for 10 minutes before to imaging.

2.2.14 E. coli Culture and Plasmid Purification

Chemically competent Escherichia coli XL10-Gold cells were transformed with plasmid DNA using the standard heat-shock method. Transformed cells were spread onto LB agar plates containing $100 \, \mu g/mL$ ampicillin and incubated overnight at $37 \, ^{\circ}C$. Single colonies were picked and grown in $5 \, mL$ of LB medium with ampicillin ($100 \, \mu g/mL$) at $37 \, ^{\circ}C$ with shaking at $800 \, rpm$ for overnight.

For miniprep plasmid extraction, 2 mL of the overnight culture was processed using the NucleoSpin Plasmid Miniprep Kit (Macherey-Nagel), following the manufacturer's instructions. DNA was eluted in $30\text{--}50\,\mu\text{L}$ of sterile nuclease-free water or elution buffer and stored at -20 °C.

For midiprep-scale purification, 200 mL of overnight E. coli culture was inoculated from a single colony and grown under the same conditions. Plasmid DNA was isolated using the Qiagen Plasmid Plus Midi Kit or the ZymoPURE II Plasmid Midiprep Kit according to the supplier's protocol. Eluted DNA was quantified using a NanoDrop spectrophotometer and either used immediately or stored at -20 °C.

All media were prepared with autoclaved LB broth (Lennox formulation) and supplemented with the appropriate antibiotic. Sterile technique was maintained throughout all procedures.

2.2.15 DNA Precipitation

For ethanol precipitation of plasmid or PCR-derived DNA, 1/10 volume of 3 M sodium acetate (pH 5.2) was added to the DNA solution, followed by 2.5 volumes of cold 100%

ethanol. The mixture was vortexed briefly and incubated at -20 °C for at least 1 hour or overnight. DNA was pelleted by centrifugation at 15,000 × g for 30 minutes at 4 °C, washed once with 70% ethanol, and centrifuged again for 10 minutes. The pellet was air-dried and resuspended in nuclease-free water or TE buffer.

2.2.16 Sequencing of Plasmid DNA

Plasmid DNA was sequenced using Sanger sequencing. DNA templates were prepared using miniprep or midiprep kits and quantified by NanoDrop. For each reaction, 300-500 ng of plasmid DNA and 5 pmol of sequencing primer were submitted in a total volume of 10 µL to a commercial provider (e.g., Eurofins Genomics, Macrogen). Sequencing was performed using standard BigDye Terminator chemistry and capillary electrophoresis. Raw chromatograms were analyzed using SnapGene Viewer or ApE.

2.2.17 Agarose Gel Electrophoresis

DNA samples were analyzed by agarose gel electrophoresis using 1-2% agarose gels prepared in $1\times$ TAE buffer. Gels were cast with SYBR Safe DNA stain or ethidium bromide for visualization. DNA loading dye (6×) was mixed with samples before loading, and 5 μ L of DNA ladder (Thermo Scientific GeneRuler) was included as a size reference. Electrophoresis was carried out at 80-120 V for 30-60 minutes depending on gel size. Gels were visualized using a gel documentation system (Peqlab Fusion FX).

2.2.18 Genomic DNA Isolation

Genomic DNA from *Plasmodium falciparum*-infected red blood cells was extracted using the phenol-chloroform method or commercial kits (e.g., DNeasy Blood & Tissue Kit, Qiagen). Briefly, parasites were released from infected erythrocytes by 0.1% saponin treatment in PBS and washed twice in cold PBS. The pellet was resuspended in 200 μL of lysis buffer containing proteinase K and incubated at 56 °C for 5 minutes.

DNA was purified according to the kit protocol. Final DNA was eluted in 20-50 μL of nuclease-free water and quantified by NanoDrop.

3. Results

3.1 Overview of Chromosome 4 in *Plasmodium falciparum*

The goal of this project was to conduct a global screen of all unknown genes on Plasmodium falciparum chromosome 4 (CHR4). In total, there are 261 predicted genes located on this chromosome. Due to the limitation of the experimental method used, we first excluded genes with transmembrane domains and signal peptides, because these proteins are not suitable for the knock sideways approach (Birnbaum et al., 2017). After this step, 175 genes remained. From these 175 genes, 92 genes were annotated as "unknown or putative" in the PlasmoDB database (Release 55). We then used the amino acid sequences encoded in these genes and conducted **BLAST** (https://blast.ncbi.nlm.nih.gov/Blast.cgi), Motif scan (https://myhits.sib.swiss/cgibin/PFSCAN) and HHPred (https://toolkit.tuebingen.mpg.de/tools/hhpred) analyses to assess whether any of them contained regions with similarity to domains of known function of proteins from other organisms. This led to further exclusion of genes for which the protein sequence indicated a plausible function and finally resulted in 44 genes as our candidates for further study (Figure 10). One of them, PF3D7 0420000, had at the time this project was started already being worked on by others in the lab, and was therefore excluded from analysis in this work. Therefore, we focused on the remaining 43 genes which constitute all that encode unknown, non-secretory proteins on chromosome 4 and were named Y1 to Y44 (Table 12) For comparison, a similar strategy for chromosome 3 resulted in 33 out of 249 (13% total) (Kimmel et al., 2023) whereas this selected resulted in 44 out of 261 genes (17%). From an initial list of 44 candidates, parasite lines for analysis (for localization and knock sideways functional analysis of the candidate) were successfully obtained for 33. The successful genome modification in these lines was confirmed with diagnostic PCR (Figure 11).

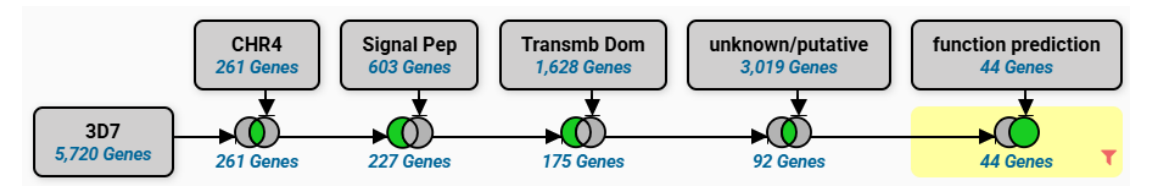


Figure 10. The summary of gene selection procedure. The gray boxes represent filter criteria applied sequentially in PlasmoDB (Release 55), while the green/gray overlapping circles indicate the intersection with the previous step's gene set. The numbers below each circle denote the number of genes retained after applying each filter. Starting from all 5,720 annotated genes in the 3D7 genome, filters were applied for chromosome 4 location (CHR4, 261 genes), presence of a signal peptide (Signal Pep, 227 genes), transmembrane domains (Transmb Dom, 175 genes), and lack of functional annotation (unknown function or putative, 92 genes), after removal of manual prediction of plausible function (see main text), resulting in 44 final target candidates.

Table 12. Candidates list for functional analysis. The table shows the candidates which were selected for functional investigation. HR, homology region; bp, base pairs.

assigned as	Gene ID	transcript length (bp)	HR length(bp)
Y1	PF3D7_0403600	3435	1017 bp
Y2	PF3D7_0404000	1234	418 bp
Y3	PF3D7_0404200	1231	628 bp
Y4	PF3D7_0404300	2615	1022 bp
Y5	PF3D7_0405500	675	934 bp
Y6	PF3D7_0406000	2470	669 bp
Y7	PF3D7_0406500	11445	998 bp
Y8	PF3D7_0406600	420	414 bp
Y9	PF3D7_0406700	2906	894 bp
Y10	PF3D7_0406900	5256	1117 bp
Y11	PF3D7_0407400	1215	291 bp
Y12	PF3D7_0407600	3639	738 bp
Y13	PF3D7_0407700	6121	815 bp

Results

Y14	PF3D7_0408000	668	513 bp
Y15	PF3D7_0408100	4881	807 bp
Y16	PF3D7_0408200	2122	984 bp
Y17	PF3D7_0408300	1749	960 bp
Y18	PF3D7_0408400	2470	1065 bp
Y19	PF3D7_0409000	8235	951 bp
Y20	PF3D7_0410500	642	522 bp
Y21	PF3D7_0410800	5023	1152 bp
Y22	PF3D7_0410900	3873	1005 bp
Y23	PF3D7_0411000	5092	879 bp
Y24	PF3D7_0411300	2744	873 bp
Y25	PF3D7_0411800	7141	972 bp
Y26	PF3D7_0414400	993	825 bp
Y27	PF3D7_0414800	1787	567 bp
Y28	PF3D7_0415200	7684	831 bp
Y29	PF3D7_0416900	8359	974 bp
Y30	PF3D7_0417600	2560	870 bp
Y31	PF3D7_0417700	1542	813 bp
Y32	PF3D7_0417900	2378	888 bp
Y33	PF3D7_0418300	5993	969 bp
Y34	PF3D7_0418900	2016	1013 bp
Y35	PF3D7_0419000	1323	731 bp
Y36	PF3D7_0419100	1772	859 bp
Y38	PF3D7_0420600	2127	960 bp
Y39	PF3D7_0421700	5811	1003 bp
Y40	PF3D7_0421800	255	252 bp
Y41	PF3D7_0422600	887	375 bp

Results

Y42	PF3D7_0423000	1374	759 bp
Y43	PF3D7_0423200	853	562 bp
Y44	PF3D7_0423600	5305	897 bp

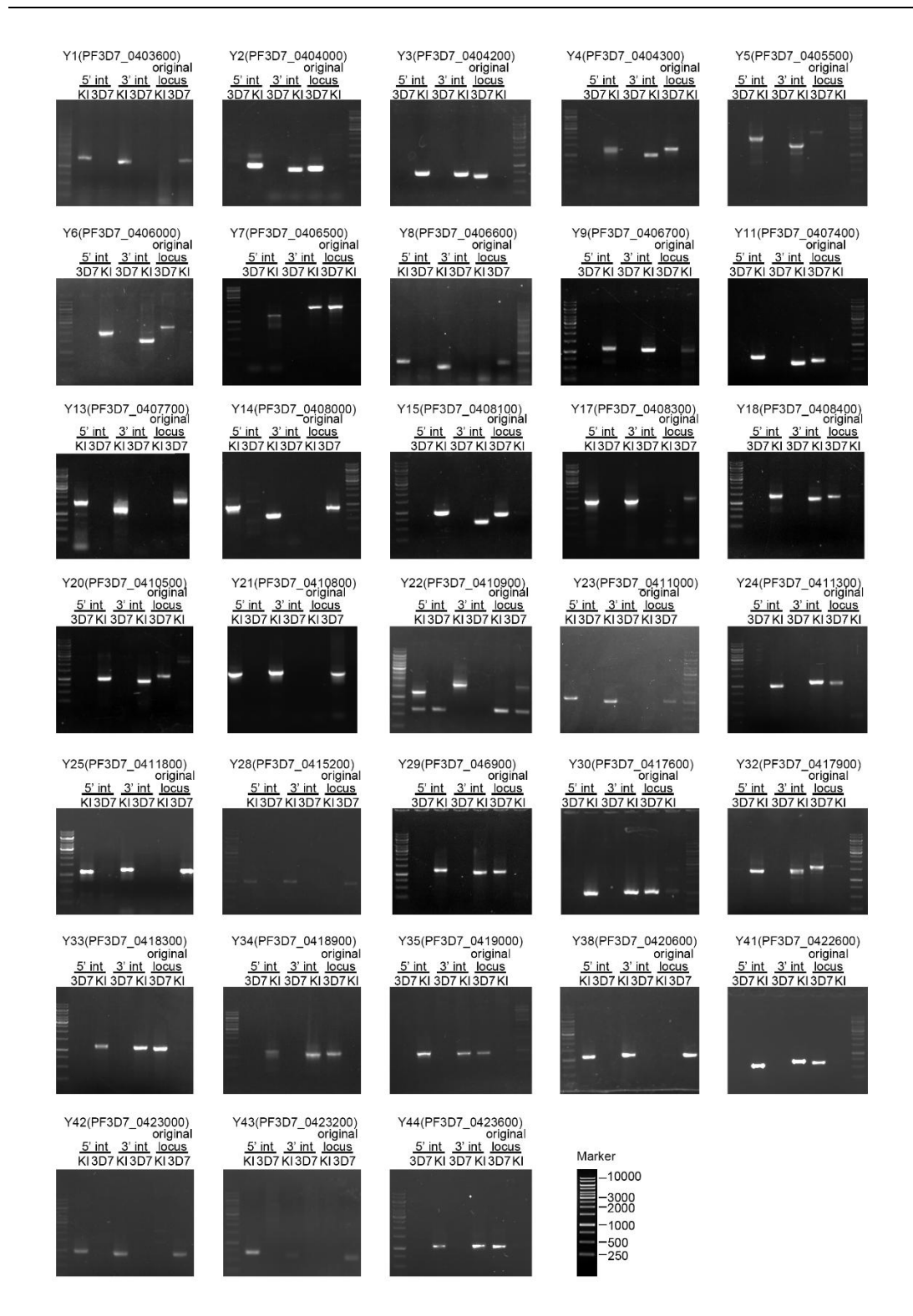


Figure 11. PCR diagnostics to confirm correct integration of the plasmid into the desired region of the genome. PCR products from genomic parasite DNA of the cell lines (indicated by candidates-IDs are shown above the agarose gels) were applied and separated using agarose gel electrophoresis. Primers used were positioned as indicated in Appendix I demonstrating a PCR product across 5' and 3' integration junction indicated by bands in lanes labelled 5' int and 3' int, as well as absence of original

locus ('original locus'). No band at the lane labeled with 'original locus' confirms that no parasites with wild type locus remained in the corresponding cell line. The original locus band with the 3D7 DNA serves as control that the primer pair can detect the locus. Marker), 1kb DNA, size of bands indicated in bp; knock-in cell line (KI), wild type parasite line (3D7).

3.2 Characterization of Y1 (PF3D7 0403600)

The candidate Y1 (GeneID: PF3D7_0403600) is annotated in PlasmoDB as a conserved Plasmodium protein with unknown function. *In silico* searches (HHPred, blast and MotifScan) did not detect significant similarities to known domains.

In order to localize and functionally analyze Y1, the corresponding gene was modified using SLI (Birnbaum et al., 2017) so that the endogenous Y1 becomes fused with the multipurpose sandwich tag (2xFKBP-GFP-2xFKBP). Correct integration into the genome was confirmed by PCR across the 5'- and 3'- integration junctions and absence of original locus (Figure 11). Fluorescence microscopy with the Y1-2xFKBP-GFP-2xFKBP^{endo} parasites showed that this protein is localized in the nucleus (Figure11), with expression restricted to the trophozoite and schizont stages. No signal was observed during the ring stage and the signal intensity declined during the schizont stage (Figure 12).

In order to assess the importance of Y1 for the parasite, the Y1-2xFKBP-GFP-2xFKBP^{endo} cell line was transfected with an episomal plasmid mediating expression of the Lyn mislocalizer, permitting conditional inactivation using knock sideways. Representative live-cell microscopy confirmed that Y1-GFP efficiently mislocalized to cytoplasm upon rapalog treatment in the majority of parasites, consistent with full knock sideways, while a minority showed partial mislocalization (Figure 13A). Mislocalization efficiency was determined by fluorescence microscopy 24 h after induction and indicated that >90% of cells showed full mislocalization of Y1 (no GFP fluorescence detected in the nucleus by microscopy) (Figure 13B). Growth curves

revealed only minimal differences between rapalog-treated (inactivated Y1) and control parasites (Figure 13C-D)

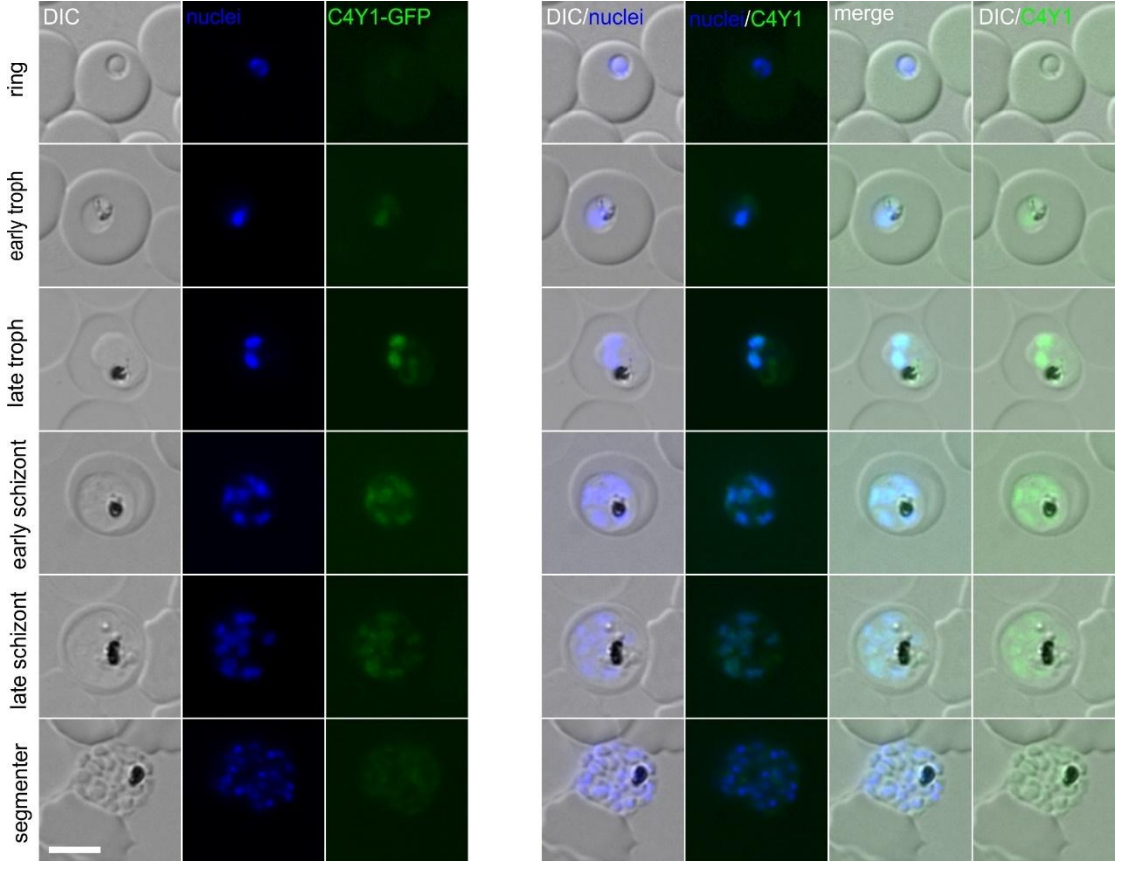


Figure 12. Localization of endogenously tagged candidate Y1 (PF3D7_0403600). Representative live cell fluorescence microscopy images of knock-in cell line Y1-2xFKBP-GFP-2xFKBP ('GFP'). The stages are indicated on the left of the panel. Representative images from 3 independent imaging sessions, each with at least 7 inspected fields of view. Parasite nuclei were stained with Hoechst33342. Scale bar 5 μm, DIC, differential interference contrast; merge, overlay of DIC, GFP and nuclei.

indicating that Y1 mislocalization does not affect parasite growth under standard *in vitro* conditions, and Y1 can therefore be considered dispensable for asexual blood stage development of the parasite.

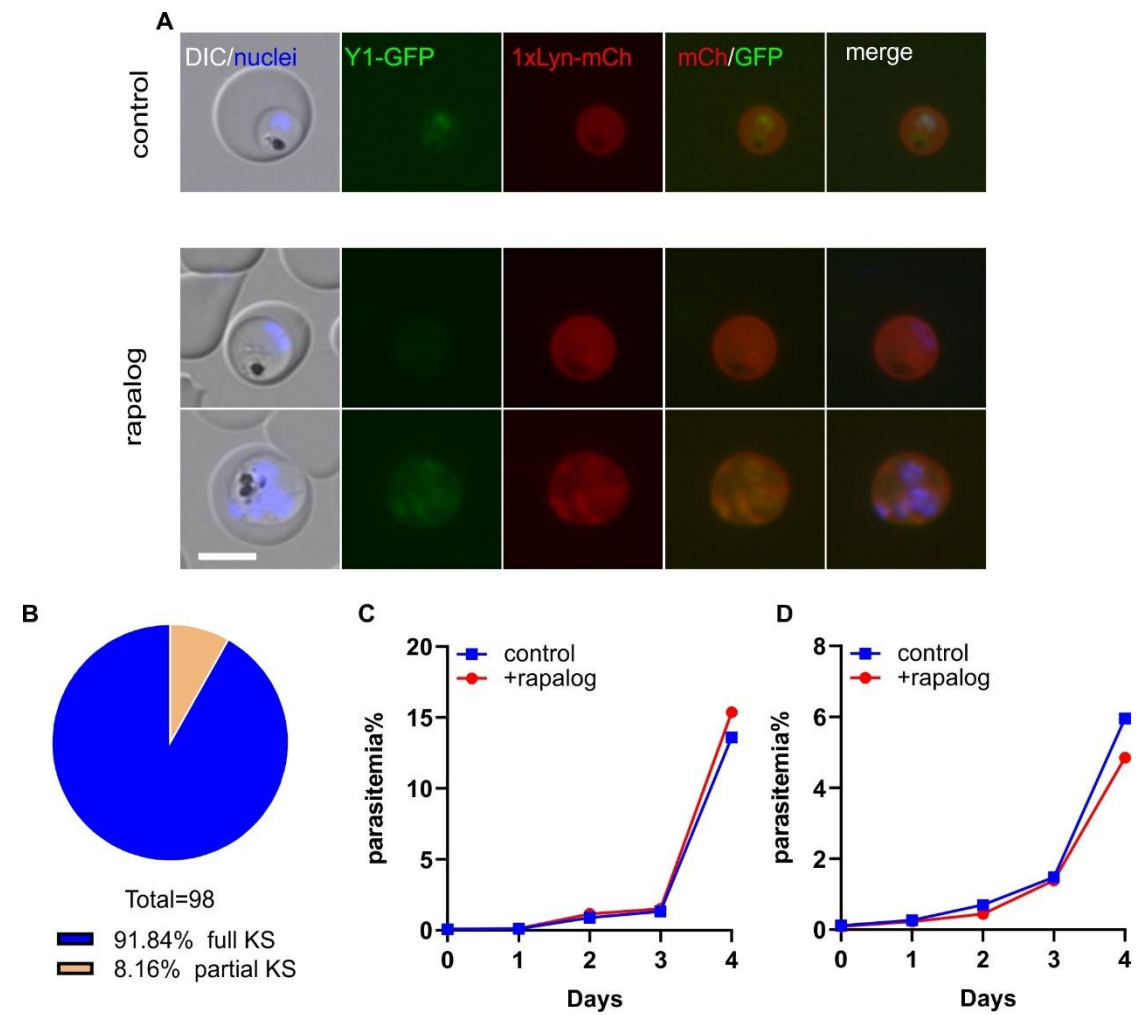


Figure 13. Knock sideways analysis of endogenous Y1 (PF3D7_0403600) tagged with 2xFKBP-GFP-2xFKBP. A) Representative live cell images of knock-in cell line Y1-2xFKBP-GFP-2xFKBP ('GFP') with an episomally expressed Lyn-FRB-mCherry mislocalizer. Representative images from 3 independent imaging sessions with at least 7 inspected fields of view. The top row shows a parasite with full KS (complete GFP mislocalization, "full KS" in (B)), while the bottom row shows a parasite with partial KS (incomplete GFP mislocalization. "partial KS" in (B)). The cell culture was split into two dishes: one served as control without rapalog (control), and the other grown in the presence of 250 nM rapalog. The samples for live cell imaging were taken 24 h post addition of rapalog. Scale bar, 5 μm, DIC, differential interference contrast, mCh, mCherry, merge, overlay of GFP, mCh and nuclei. B) Pie chart shows quantification of knock sideways efficiency based on GFP localization following rapalog treatment. Quantification of knock sideways efficiency for Y1, based on the same experiments shown in (B). A total of 98 parasites were scored across 5 independent imaging sessions. KS status was evaluated 24 hours after rapalog addition. C-D) Growth curve of the Y1 knock sideways. Parasite growth was assessed by flow cytometry in the presence (rapalog, functional inactivation of Y1) or absence (control) of rapalog. Two independent replicates (both shown).

3.3 Characterization of Y2 (PF3D7 0404000)

Y2 (Gene ID: PF3D7_0404000) encodes a very small protein with only 99 amino acids. It is annotated in PlasmoDB as a conserved Plasmodium protein with unknown function. BLAST, Motifscan and HHPred analysis did not showed any similarity to known domains.

The alphfold 3 (DeepMind, 2024) protein structure prediction indicates that the protein consists mainly of one α -helix (Figure 14). In order to localize and functionally analyze Y2, the corresponding gene was modified using SLI (Birnbaum et al., 2017) so that the endogenous Y2 becomes fused with the multipurpose sandwich tag (2xFKBP-GFP-2xFKBP). Correct integration into the genome was confirmed by PCR across the 5'and 3'- integration junctions and by absence of the wild-type locus (Figure 11). Fluorescence microscopy of the Y2-2xFKBP-GFP-2xFKBP^{endo} parasite line revealed that the GFP signal was expressed in rings, late schizonts and segmenters (Figure 15). No signal was detected during the trophozoite stage, and only some parasites exhibited GFP signal during the ring stage. The Y2-GFP signal showed a pattern highly reminiscent of the inner membrane complex (IMC) with circular structures on the apical side of the forming merozoites in schizonts and a signal in the periphery of the nascent merozoites in segmenters (Figure 15). Based on this observation, we performed colocalization with an IMC marker. For this we episomally expressed IMC1- mCherryyDHODH in the Y2-2xFKBP-GFP-2xFKBP^{endo} parasites (Mesen-Ramirez et al., 2025). Since Y2 is only expressed at late stages, its fluorescence signal overlaps with that of the IMC marker during these stages. However, as the parasite PPM also adopts an IMClike pattern in late schizonts and segmenters, we cannot definitively conclude that Y2 localizes to the IMC (Figure 16).



Figure 14. AlphaFold-predicted structure of candidate Y2 (PF3D7_0404000). The structure was predicted using AlphaFold3 and visualized with standard confidence coloring.

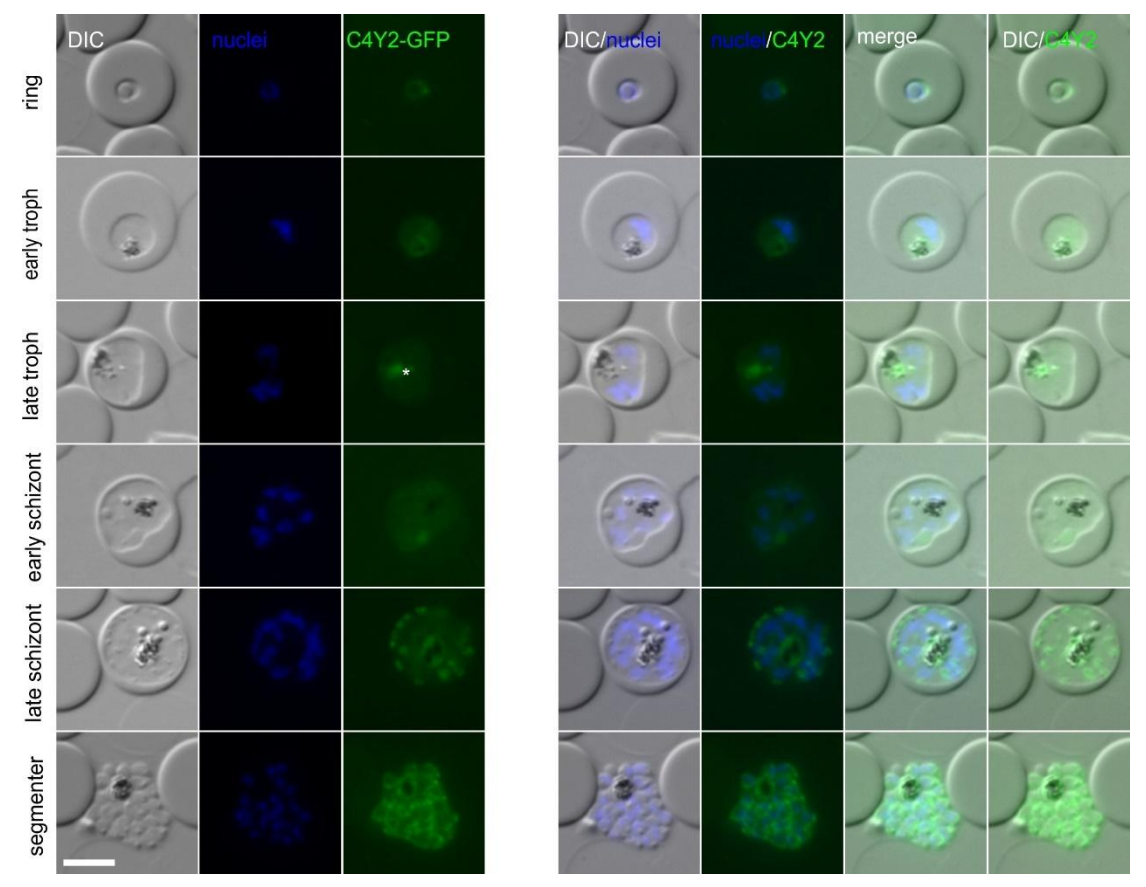


Figure 15. Localization of endogenously tagged candidate Y2 (PF3D7_0404000). Representative live cell fluorescence microscopy images of knock-in cell line Y2-2xFKBP-GFP-2xFKBP ('GFP'). The stages are indicated on the left of the panel. Representative images from 3 independent imaging sessions each with at least 7 inspected fields of view. The weak green signal observed in the trophozoite stage (marked with an asterisk) is likely due to autofluorescence rather than Y2-GFP expression. Parasite nuclei were stained with Hoechst33342. Scale bar 5 μ m, DIC, differential interference contrast; merge, overlay of DIC, GFP and nuclei.

To assess the expression pattern of Y2 specifically during the ring stage, we tightly synchronized parasites to obtain a 0-4 hpi population and performed live-cell imaging at both 0-4 hpi and 4-8 hpi. In both synchronized populations, approximately half of

the parasites showed detectable GFP signal, while the rest were negative (Figure 17). This indicates that the detection of Y2 in only some cells is not due to differences in stage but that Y2 is detectable only in a portion of the population, regardless of the exact ring-stage timing. Such variation may reflect cell-to-cell differences in protein expression levels or stability.

In order to assess the importance of Y2, the Y2-2xFKBP-GFP-2xFKBP^{endo} cell line was transfected with an episomal plasmid mediating expression of the NLS mislocalizer, allowing conditional inactivation through the knock sideways system. Representative live-cell microscopy showed efficient mislocalization of Y2-GFP to the nucleus upon rapalog treatment, consistent with full knock sideways in the majority of parasites (Figure 18A). Mislocalization efficiency was evaluated by fluorescence microscopy 24 h after rapalog addition, and quantification revealed that over 90% of parasites exhibited complete mislocalization, with no residual GFP signal at the original site (Figure 18B).

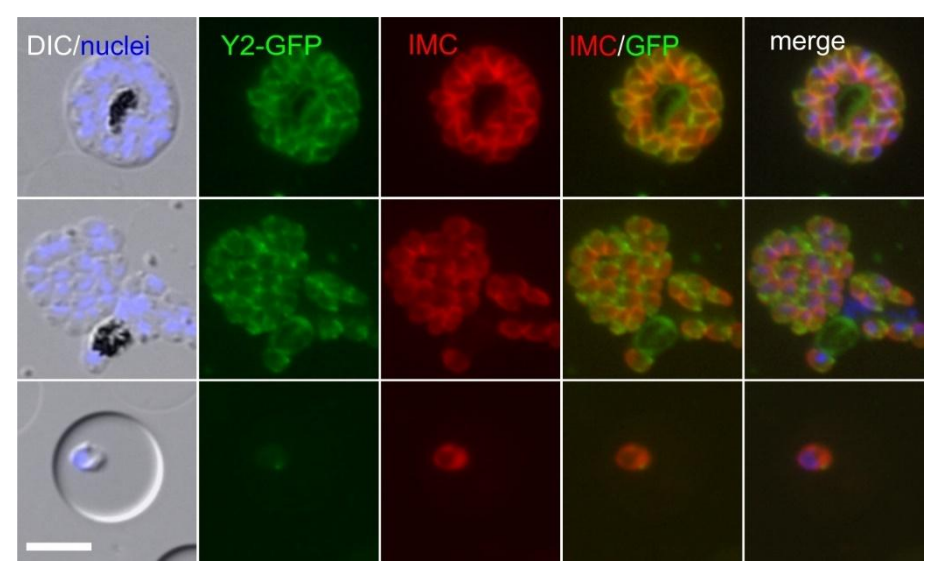


Figure 16. Fluorescence microscopy images of endogenously tagged Y2 (PF3D7_0404000) and IMC1-mCherry-yDHODH^{epi} colocalized. Representative images of parasites expressing GFP-tagged Y2 (green) and IMC marker (red). Representative images from 3 independent imaging sessions each with at least 7 inspected fields of view. Parasite nuclei were stained with Hoechst33342. Scale bar 5 μm, DIC, differential interference contrast; merge, overlay of DIC, GFP and nuclei.

blood-stage development, likely contributing to late-stage processes such as segmentation or merozoite invasion due to its predominant expression in late stages and IMC-like localization.

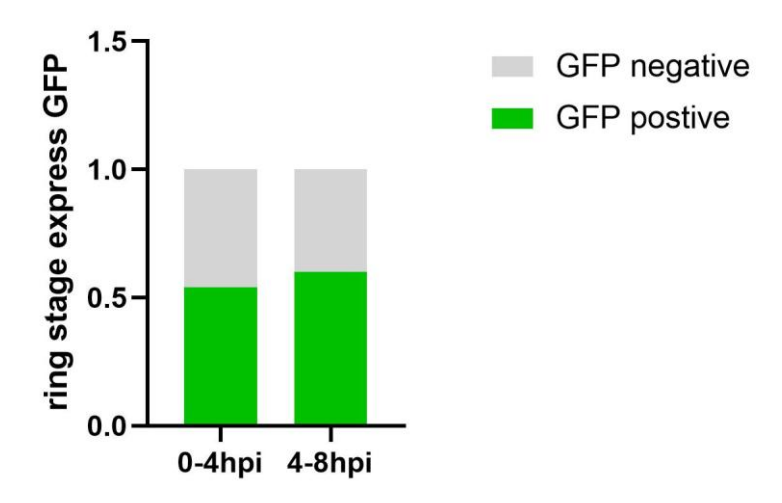


Figure 17. Quantification of Y2-GFP expression in ring-stage parasites. The proportion of parasites expressing detectable GFP signal (green) versus no detectable signal (grey) in tightly synchronized populations collected at 0-4 hpi and 4-8 hpi.

To characterize the role of Y2 in the intraerythrocytic developmental cycle of *Plasmodium falciparum*, we performed a stage-specific assay using the NLS-based mislocalization system under rapalog treatment to functionally inactivate Y2. Parasites were synchronized at 10-18 hpi and monitored for 5 days across more than two developmental cycles. During the early stages (10-32 hpi), no differences were observed between the control and Y2-NLS-KS parasites, consistent with the lack of detectable Y2 expression at this time. However, starting from 48-56 hpi, parasitemia in the control group increased markedly, reflecting successful egress and invasion, while parasites with rapalog showed a delayed late stage developmentt (Figure 19) and only produced about quarter the number of ring-stage parasites compared to controls (Figure 19, 58-66 hpi). These defects became more pronounced in the second cycle, with an accumulation of late stage parasites when the control already produced new rings and an even more pronounced reduction in rings produced in the plus rapalog conditions

(96-104 hpi and 106-114 hpi), indicating a defect in merozoite formation, egress or invasion (Figure 19).

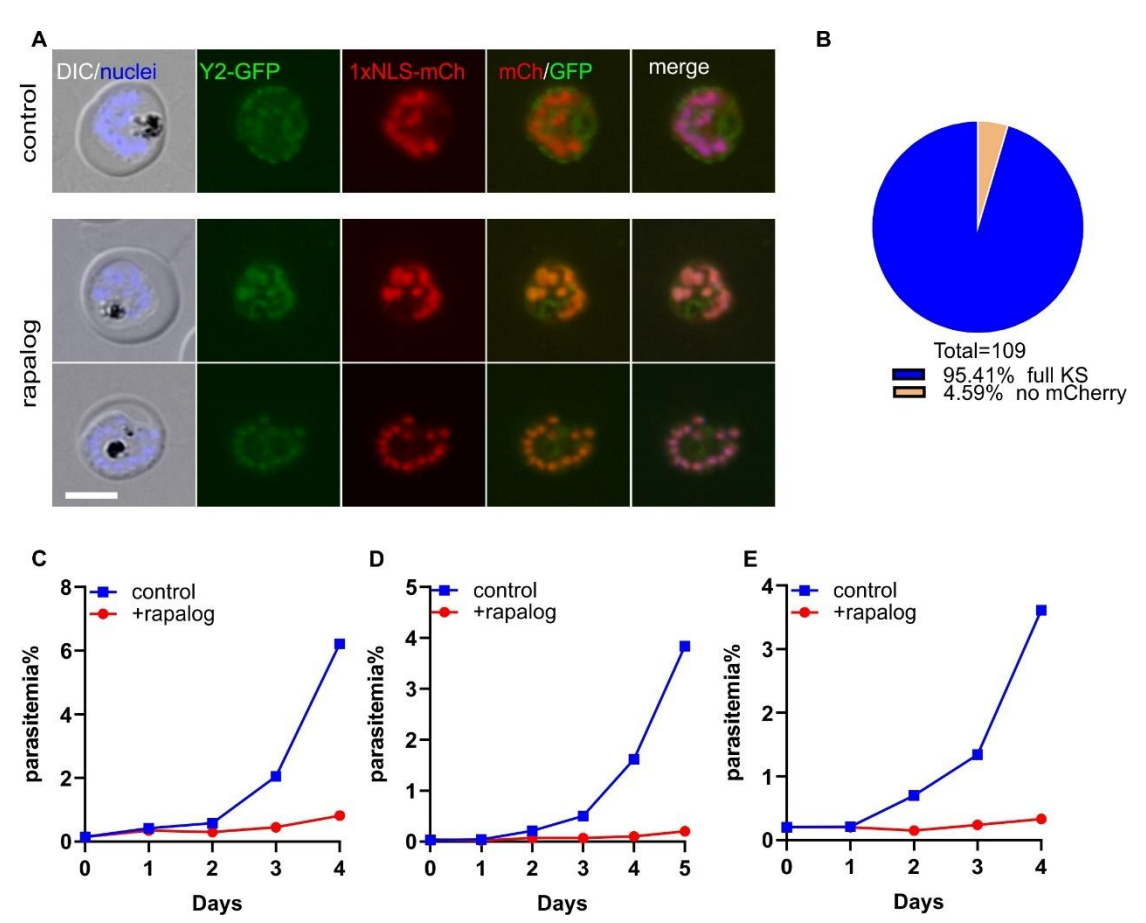


Figure 18. Knock sideways analysis of endogenous Y2 (PF3D7_0404000) tagged with 2xFKBP-GFP-2xFKBP. A) Representative live cell images of knock-in cell line Y2-2xFKBP-GFP-2xFKBP ('GFP') with an episomally expressed NLS-FRB-mCherry mislocalizer. Representative images from 3 independent imaging sessions with at least 7 inspected fields of view. Both two rows of "rapalog" show parasites with full KS (complete GFP mislocalization, "full KS" in (B)). The cell culture was split into two dishes: one served as control without rapalog (control), and the other grown in the presence of 250 nM rapalog. The samples for live cell imaging were taken 24 h post addition of rapalog. Scale bar, 5 μm, DIC, differential interference contrast, mCh, mCherry, merge, overlay of GFP, mCh and nuclei. B) Pie chart shows quantification of knock sideways efficiency based on GFP localization following rapalog treatment. Quantification of knock sideways efficiency for Y2 is based on the same experiments shown in (A). A total of 109 parasites were scored across 5 independent imaging sessions. KS status was evaluated 24 hours after rapalog addition.C-E) Growth curve of the Y2 knock sideways. Parasite growth was assessed by flow cytometry in the presence (rapalog) or absence (control) of rapalog. Three independent replicates (all shown).

Taken together, these results indicate that Y2 is important for efficient schizont egress and subsequent merozoite invasion.

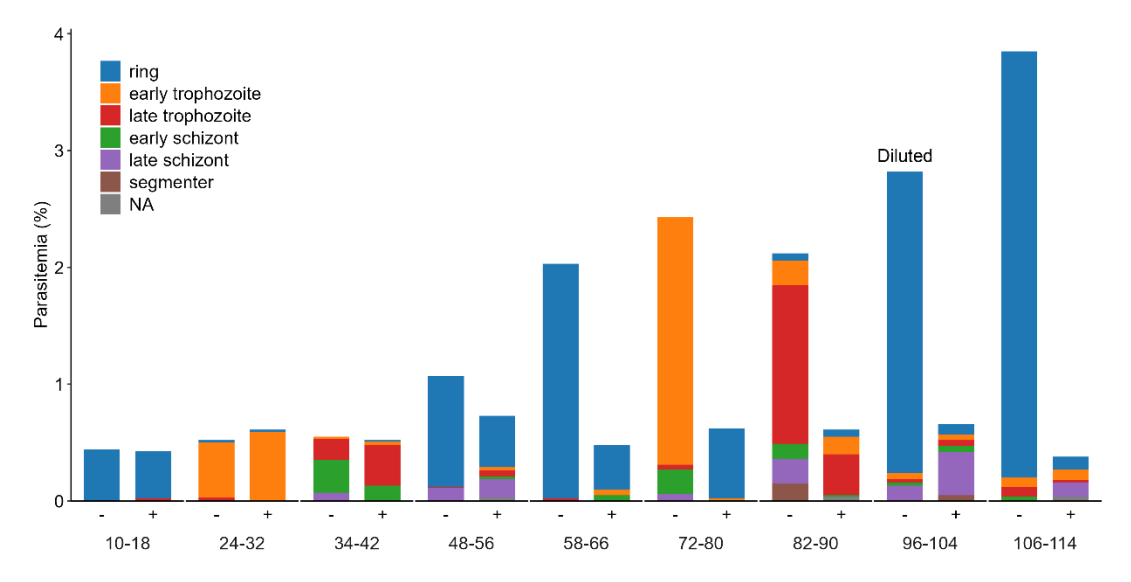


Figure 19. Stage assay of Y2-NLS knock sideways parasites following rapalog treatment. Synchronized parasites (0-8 h age window based on two subsequent synchronisations 10 h apart) expressing a knock sideways version of Y2 were treated with rapalog whit the first synchronization and parasite stages were monitored every 10 or 14 hours in 5 days over two intraerythrocytic developmental cycles at the indicated parasite age. Diluted: the parasitemia shown is based on diluted samples (1:10), without extrapolation to original culture density. Parasitemia (%) and the distribution of parasite stages were quantified by Giemsa-stained blood smears. Data shown are representative of two independent biological replicates.

3.4 Characterization of Y3 (PF3D7 0404200)

Y3 (Gene ID: PF3D7_0404200) is annotated in PlasmoDB as a conserved Plasmodium protein with unknown function. BLAST, Motifscan and HHPred analysis did not show any similarity to known domains.

In order to localize and functionally analyze Y3, the corresponding gene was modified using SLI (Birnbaum et al., 2017) so that the endogenous Y3 becomes fused with the multipurpose sandwich tag (2xFKBP-GFP-2xFKBP). Correct integration into the genome was confirmed by PCR across the 5'- and 3'- integration junctions and absence of the wild-type locus (Figure 11). Fluorescence microscopy of Y3-2xFKBP-GFP-2xFKBP^{endo} parasites revealed a signal throughout the asexual blood-stage cycle

(Figure 20). In rings the GFP signal was in a focal accumulation while in trophozoites the GFP signal was observed as a continuous thread-like structure (Figure 20), typical of the parasite's single branched mitochondrion (Kimmel et al., 2023), and was clearly visible in ring, trophozoite, and schizont stages, indicating constitutive expression of Y3. To confirm mitochondrial localization, we performed co-localization with MitoTracker, which showed overlap between the Y3-GFP signal and the mitochondrial stain (Figure 21).

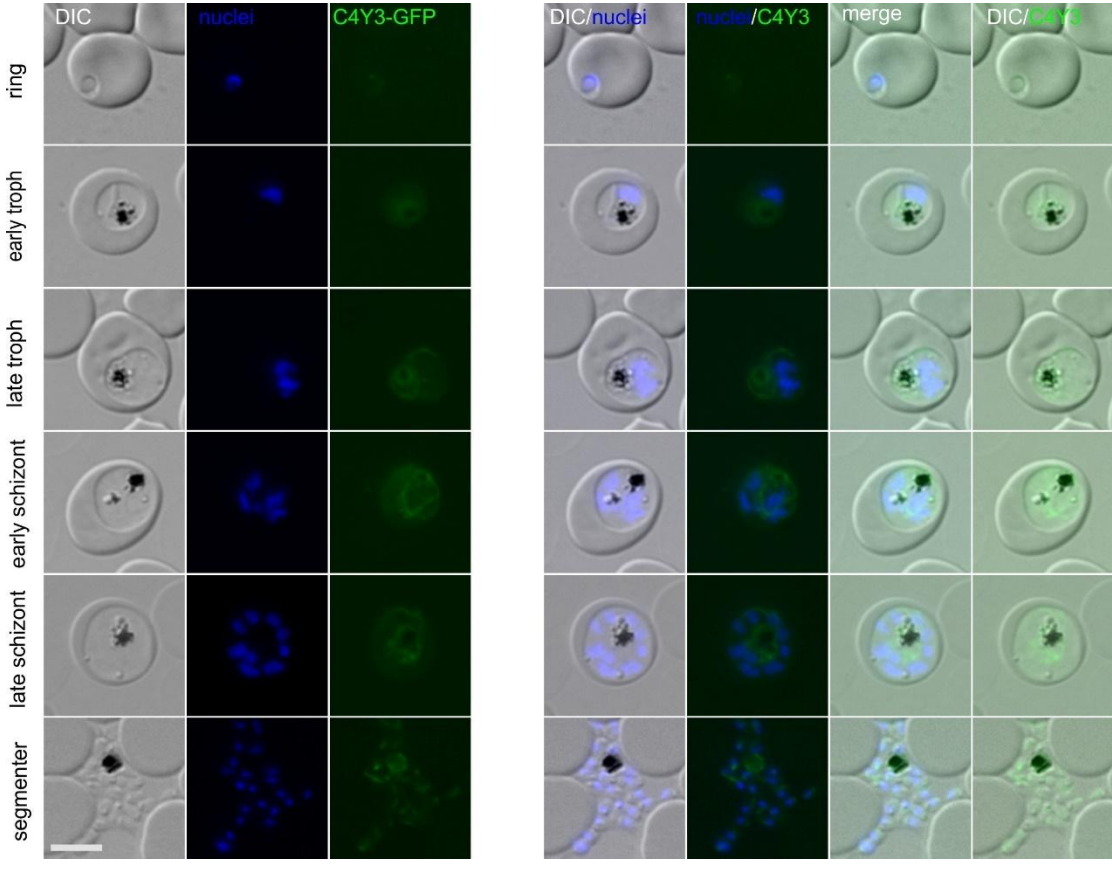


Figure 20. Localization of endogenously tagged candidate Y3 (PF3D7_0404200). Representative live cell fluorescence microscopy images of knock-in cell line Y3-2xFKBP-GFP-2xFKBP ('GFP'). The stages are indicated on the left of the panel. Representative images from 3 independent imaging sessions each with at least 7 inspected fields of view. Arrow marks the Y3-GFP signal in a trophozoite near the food vacuole. Parasite nuclei were stained with Hoechst33342. Scale bar 5 μm, DIC, differential interference contrast; merge, overlay of DIC, GFP and nuclei. Arrow highlight Y3 signal in the early trophozoite.

To investigate the functional relevance of Y3, the Y3-2xFKBP-GFP-2xFKBP^{endo} cell line was transfected with an episomal plasmid expressing the NLS mislocalizer to enable conditional inactivation via knock sideways. However, live-cell microscopy revealed that upon rapalog treatment, Y3-GFP remained associated with its native filamentous structure, and no mislocalization to the nucleus was observed (Figure 22), indicating that mislocalization away from the mitochondrion was unsuccessful. As the knock sideways failed, Y3 could not be functionally assessed. This most likely was due to limited accessibility of the FKBP-GFP fusion protein within the mitochondrial compartment and alternative approaches such as DiCre-mediated conditional knockout will be required to determine the essentiality of Y3. However, due to time constraints, we were not able to generate the DiCre line during this study.

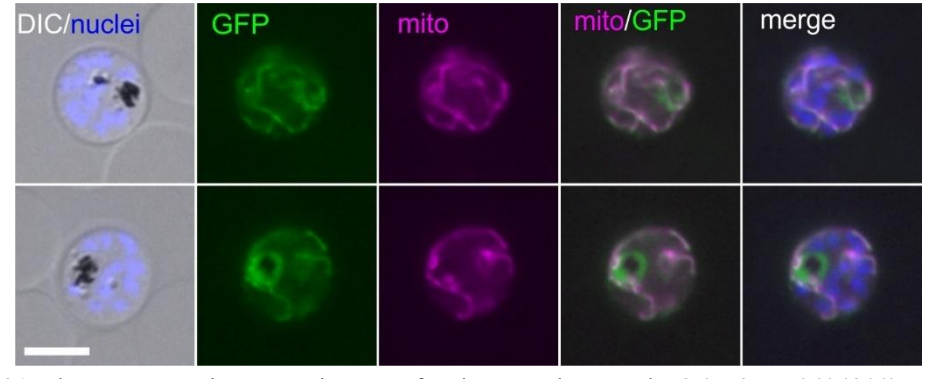


Figure 21. Fluorescence microscopy images of endogenously tagged Y3 (PF3D7_0404200) stained with MitoTrackerTM Red CMXRos. Representative images of parasites expressing GFP-tagged Y3 (green), counterstained with Mitotracker (purple). Representative images from 3 independent imaging sessions with at least 7 inspected fields of view. Parasite nuclei were stained with Hoechst33342. Scale bar 5 μm, DIC, differential interference contrast; merge, overlay of DIC, GFP and nuclei.

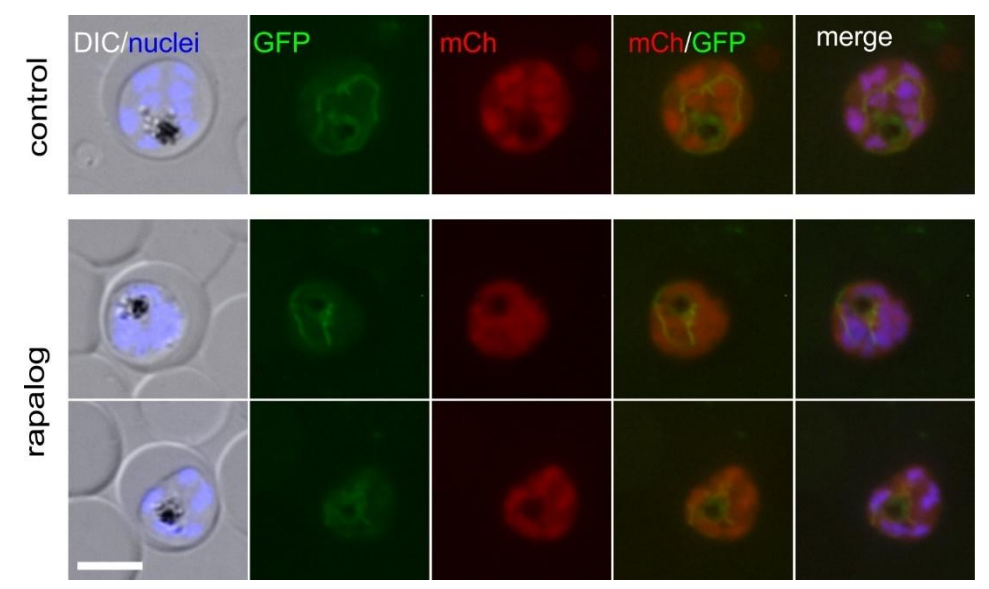


Figure 22. Knock sideways of endogenously tagged Y3 (PF3D7_0404200). Representative live cell images of knock-in cell line Y3-2xFKBP-GFP-2xFKBP ('GFP') with an episomally expressed NLS-FRB-mCherry mislocalizer. The cell culture was split into two dishes: one served as control without rapalog (control), and the other grown in the presence of 250 nM rapalog (rapalog) to induce the knock sideways. The samples for live cell imaging were taken 24 h post addition of rapalog. Representative images from 3 independent imaging sessions with at least 7 inspected fields of view. Parasite nuclei were stained with Hoechst33342. Scale bar, 5 μm, DIC, differential interference contrast, mCh, mCherry, merge, overlay of GFP, mCh and nuclei.

3.5 Characterization of Y4 (PF3D7 0404300)

Y4 (Gene ID: PF3D7_0404300) is annotated as putative Ran-binding protein in PlasmoDB. BLAST and Motifscan did not show any significant similarity, but HHPred analysis identified a RanBP1 domain with high confidence (Probability: 98.79;

E-value: 6.9e-9), which is often associated with nucleocytoplasmic transport or ribosome assembly (Bischoff et al., 1995; Koyama and Matsuura, 2010).

In order to localize and functionally analyze Y4, the corresponding gene was modified using SLI (Birnbaum et al., 2017) so that the endogenous Y4 becomes fused with the multipurpose sandwich tag (2xFKBP-GFP-2xFKBP). Correct integration into the genome was confirmed by PCR across the 5'- and 3'- integration junctions and by the absence of the wild-type locus (Figure 11). Live-cell fluorescence microscopy of Y4-2xFKBP-GFP-2xFKBP^{endo} parasites revealed a nuclear localization across all asexual

stages (Figure 23). The signal was diffusely distributed throughout the nucleus, without clear subnuclear foci except for schizont stages that showed some more confined signal that frequently appeared not to encompassed the entire nucleus (Figure 23).

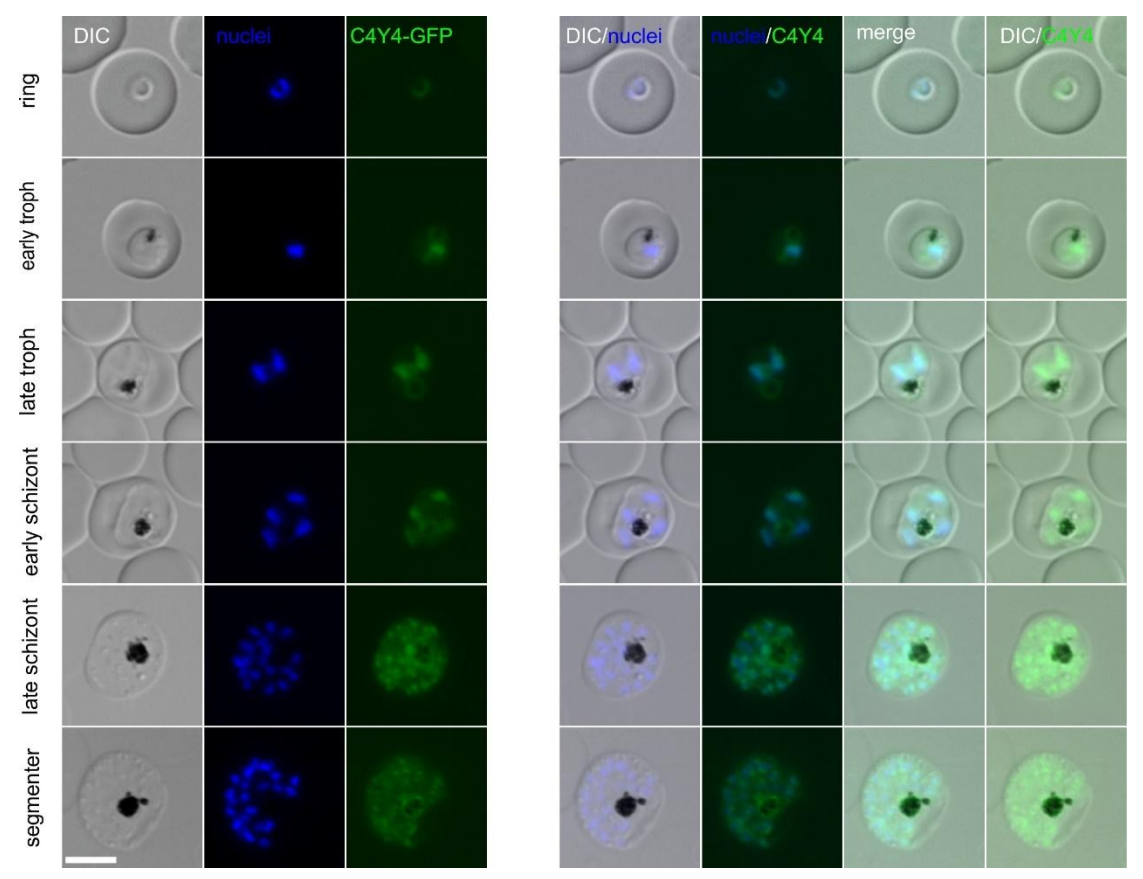


Figure 23. Localization of endogenously tagged candidate Y4 (PF3D7_0404300). Representative live cell fluorescence microscopy images of knock-in cell line Y4-2xFKBP-GFP-2xFKBP ('GFP'). The stages are indicated on the left of the panel. Representative images from 3 independent imaging sessions with at least 7 inspected fields of view. Parasite nuclei were stained with Hoechst33342. Scale bar 5 μ m, DIC, differential interference contrast; merge, overlay of DIC, GFP and nuclei.

To evaluate the functional importance of Y4, the Y4-2xFKBP-GFP-2xFKBP^{endo} cell line was transfected with an episomal plasmid expressing the Lyn mislocalizer, enabling conditional inactivation via the knock sideways system. Upon rapalog treatment, Y4-GFP efficiently mislocalized from the nucleus to the plasma membrane in the majority of parasites, as shown by live-cell fluorescence microscopy (Figure 24A). Mislocalization efficiency was quantified 24 hours after induction and revealed

that over 80% of parasites exhibited full mislocalization, defined by the complete absence of nuclear GFP signal (Figure 24B).

Despite efficient mislocalization, only a mild reduction in parasite growth was observed between rapalog-treated and control cultures across 3 independent biological replicates (Figure 24C-E). The final parasitemia in the rapalog-treated parasites in the three replicates was 76.98%, 62.96%, and 65.39% of the control, respectively. These results suggests that Y4 is required for optimal parasite growth during the asexual blood stage,

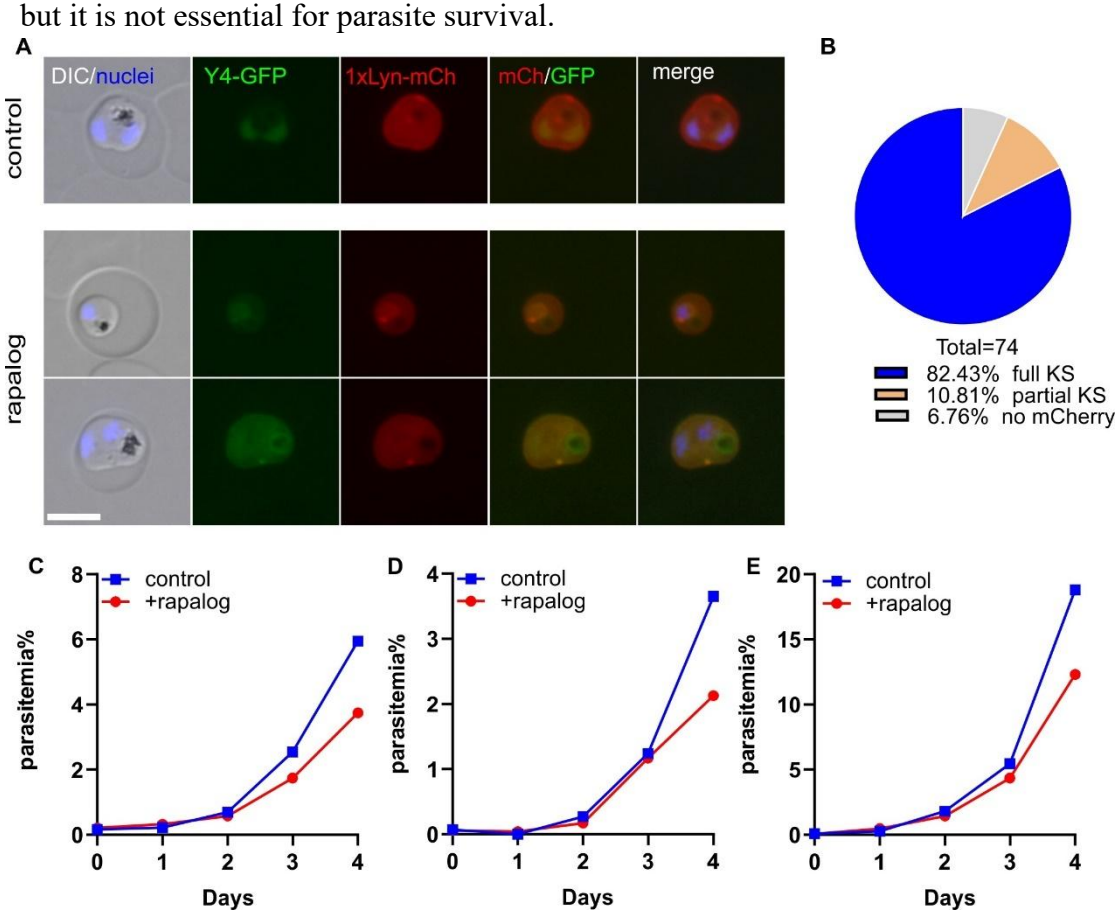


Figure 24. Knock sideways analysis of endogenous Y4 (PF3D7_0404300) tagged with 2xFKBP-GFP-2xFKBP. A) Representative live cell images of knock-in cell line Y4-2xFKBP-GFP-2xFKBP ('GFP') with an episomally expressed Lyn-FRB-mCherry mislocalizer. Representative images from 3 independent imaging sessions with at least 7 inspected fields of view. The top row shows a parasite with full KS (complete GFP mislocalization, "full KS" in (B)), while the bottom row shows a parasite with partial KS (incomplete GFP mislocalization. "partial KS" in (B)). The cell culture was split into two dishes: one served as control without rapalog (control), and the other grown in the presence of 250 nM rapalog. The samples for live cell imaging were taken 24 h post addition of rapalog. Scale bar, 5 μm,

DIC, differential interference contrast, mCh, mCherry, merge, overlay of GFP, mCh and nuclei. B) Pie chart shows quantification of knock sideways efficiency based on GFP localization following rapalog treatment. Quantification of knock sideways efficiency for Y4, based on the same experiments shown in (A). A total of 74 parasites were scored across 3 independent imaging sessions. KS status was evaluated 24 hours after rapalog addition. C-E) Growth curve of the Y4 knock sideways. Parasite growth was assessed by flow cytometry in the presence (rapalog) or absence (control) of rapalog. Three independent replicates (all shown).

3.6 Characterization of Y5 (PF3D7_0405500)

Y5 (Gene ID: PF3D7_0405500) is annotated as a conserved Plasmodium protein with unknown function in Plasmodb. BLAST, Motifscan and HHPred analysis did not showed any similarity to known domains.

To investigate the subcellular localization of Y5, the endogenous gene was modified using the SLI system (Birnbaum et al., 2017) to fuse it with a sequence encoding a 2xFKBP-GFP-2xFKBP tag. Correct genomic integration was confirmed by PCR across both integration junctions and the absence of the wild-type locus (Figure 11). Live-cell fluorescence microscopy of Y5-2xFKBP-GFP-2xFKBP^{endo} parasites revealed a nuclear localization throughout the asexual blood-stage cycle (Figure 25). In ring-stage and early trophozoites, Y5-GFP displayed a diffuse signal within the nucleus, indicating a general nuclear distribution. However, during late trophozoite and schizont stages, Y5-GFP formed distinct puncta positioned near the nuclear periphery, suggesting transient recruitment to subnuclear regions or complexes. These foci disappeared upon completion of nuclear division, and the signal turned into a more distributed pattern that however only partially matched the DNA, suggesting that also in segmented parasites, Y5 was in a subnuclear region.

The prominent peripheral focus during the late trophozoite and schizont stages often did not overlap with the Hoechst-stained DNA, but coinciding with periods of active nuclear division. In order to assess whether this was due to a localization of Y5 to a

spindle-related structures, we performed co-localization experiments with tubulin, but the strong peripheral GFP foci did not overlap with microtubule signal in the nucleus (Figure 26), suggesting that Y5 is not directly associated with spindle microtubules. Given its perinuclear accumulation, we next Y5 is not in fact located at the Golgi and performed co-localization with GRASP, a marker for the cis-Golgi. As expected, no overlap was observed between Y5-GFP and GRASP signal was observed (Figure 27). Together, these results suggest that Y5 localizes to distinct nuclear envelope-adjacent regions that are not part of the spindle.

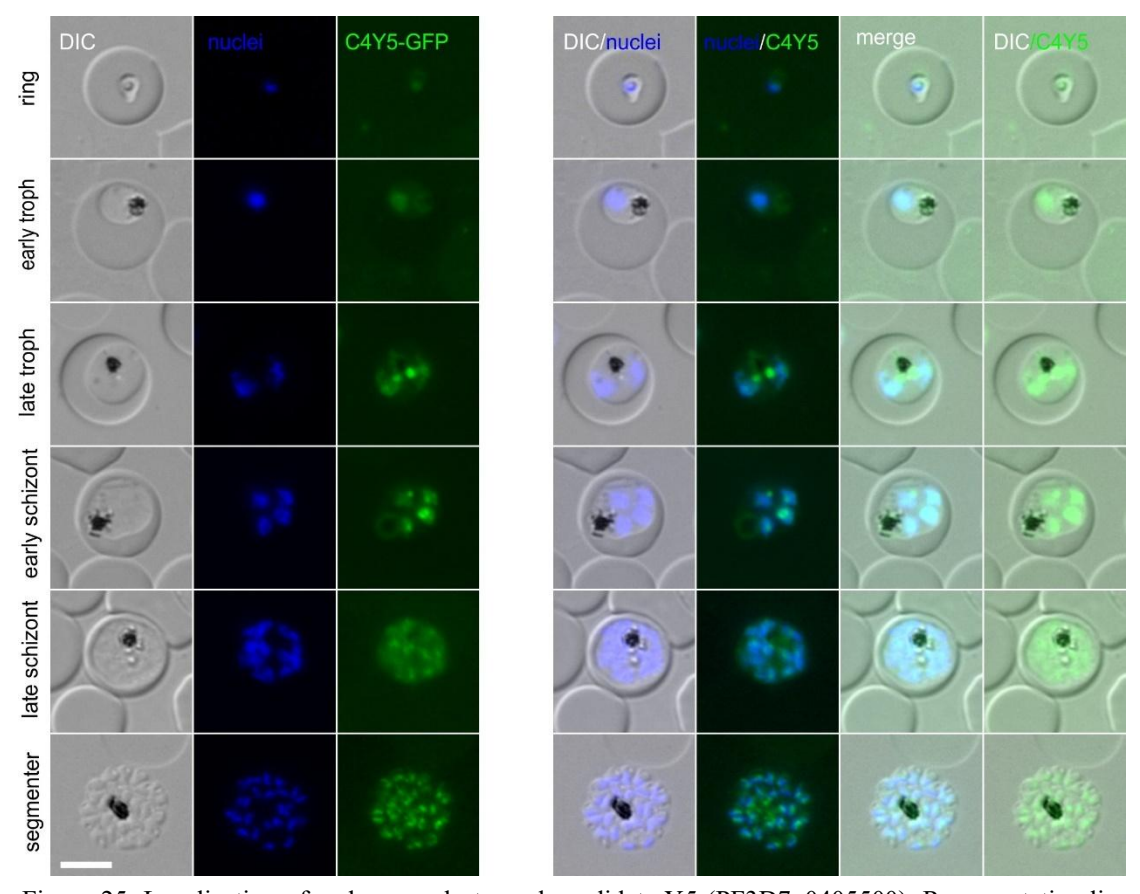


Figure 25. Localization of endogenously tagged candidate Y5 (PF3D7_0405500). Representative live cell fluorescence microscopy images of knock-in cell line Y5-2xFKBP-GFP-2xFKBP ('GFP'). The stages are indicated on the left of the panel. Representative images from 3 independent imaging sessions with at least 7 inspected fields of view. Parasite nuclei were stained with Hoechst33342. Scale bar 5 μ m, DIC, differential interference contrast; merge, overlay of DIC, GFP and nuclei.

To evaluate the functional importance of Y5, the Y5-2xFKBP-GFP-2xFKBP^{endo} cell line was transfected with an episomal plasmid expressing the Lyn mislocalizer, enabling conditional inactivation via the knock sideways system. Upon rapalog treatment, live-cell microscopy showed redistribution of Y5-GFP from the nuclear periphery to the plasma membrane in most parasites (Figure 28A). Quantification after 24 hours of rapa treatment revealed that only 60% of cells exhibited full mislocalization, while 15% showed partial relocalization, and 17% displayed a combination of partial and recruitment of the mislocalizer to Y5 ("reverse mislocalization") patterns (defined as mixed KS) (Figure 28B).

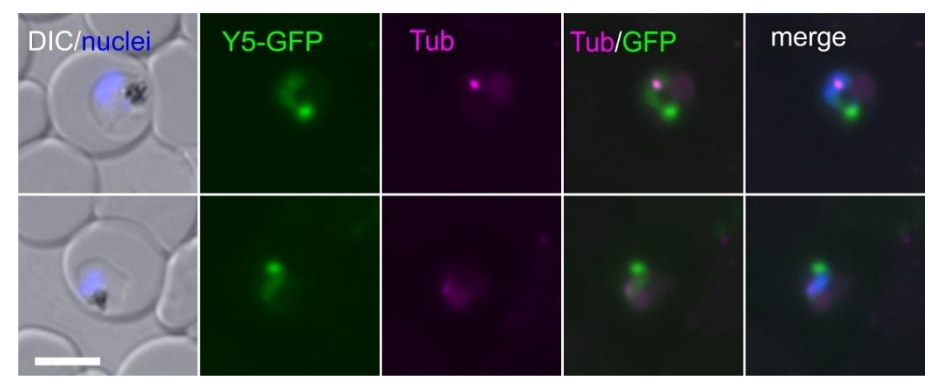


Figure 26. Y5 (PF3D7_0405500) co-localization with Tubulin. Representative live cell images of knockin cell line of Y5-2xFKBP-GFP-2xFKBP (green) with staining TubulinTrackerTM deep red (purple). Representative images from 3 independent imaging sessions with at least 7 inspected fields of view. Parasite nuclei were stained with Hoechst33342. Scale bar 5 μm, DIC, differential interference contrast; merge, overlay of Tub, GFP and nuclei.

Growth curve analysis revealed a reduction in parasite proliferation following Y5 mislocalization across three independent experiments. Final parasitemia in the rapalog-treated groups was 59.01%, 24.44%, and 76.96% of the corresponding controls, respectively (Figure 28C-E). Although the degree of growth inhibition varied, all replicates consistently showed reduced proliferation, indicating that Y5 contributes to asexual blood-stage development. The moderate and variable phenotype may reflect

incomplete inactivation due to suboptimal KS efficiency, or a function that is required only during specific developmental windows.

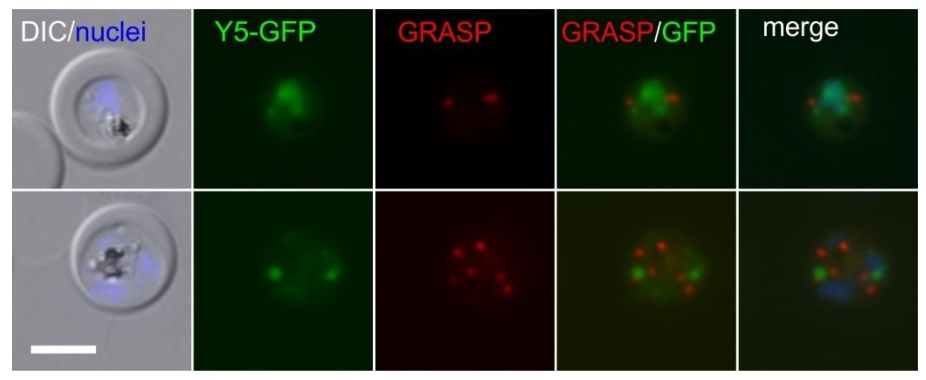


Figure 27. Y5 (PF3D7_0405500) co-localization with GRASP. Representative live cell images of knockin cell line of Y5-2xFKBP-GFP-2xFKBP (green) with episomally expressed GRASP-mCherry (red). Representative images from 3 independent imaging sessions with at least 7 inspected fields of view. Parasite nuclei were stained with Hoechst33342. Scale bar 5 μ m, DIC, differential interference contrast; merge, overlay of mCh, GFP and nuclei.

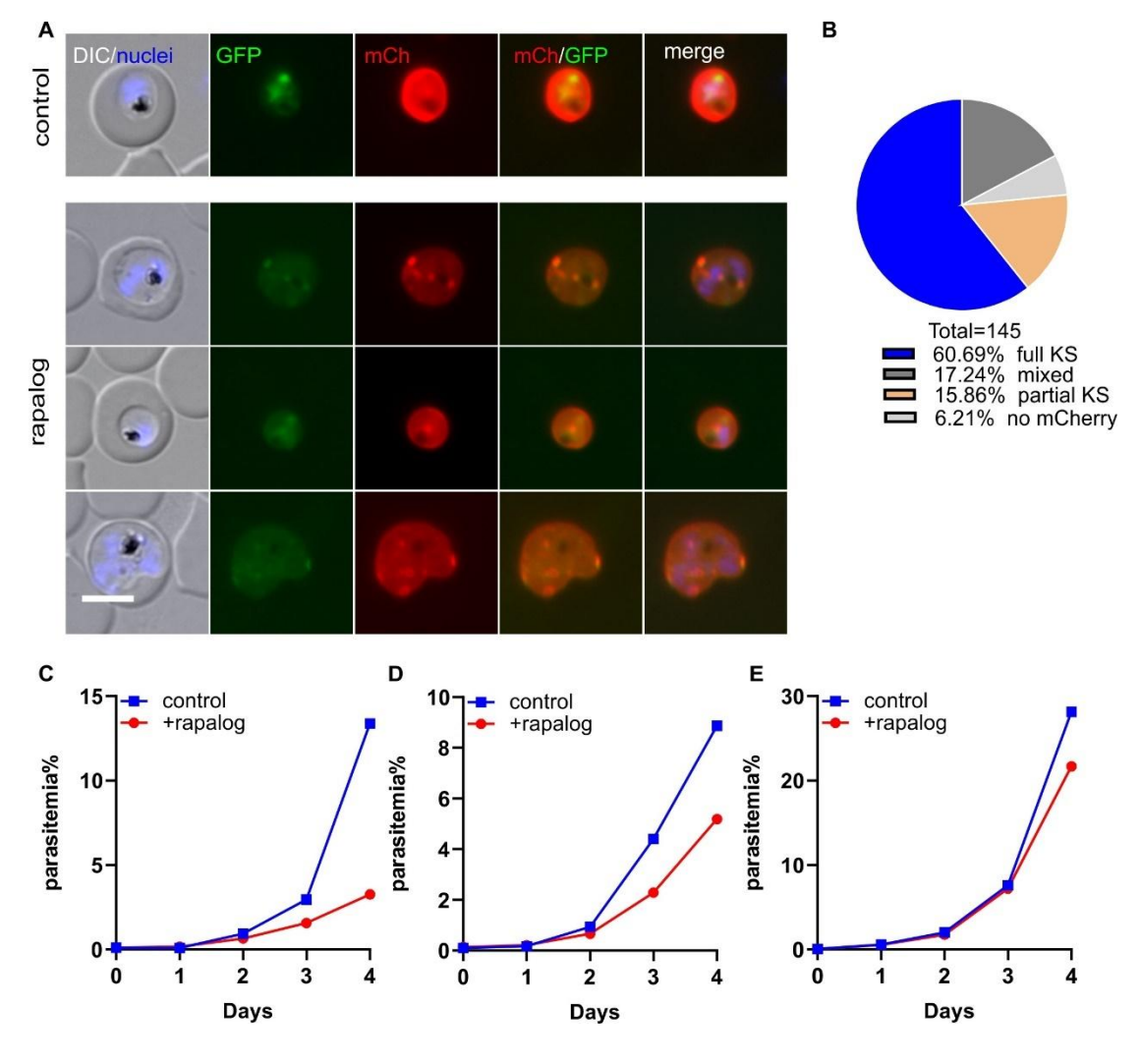


Figure 28. Knock sideways analysis of endogenous Y5 (PF3D7 0405500) tagged with 2xFKBP-GFP-2xFKBP. A) Representative live cell images of knock-in cell line Y5-2xFKBP-GFP-2xFKBP ('GFP') with an episomally expressed Lyn-FRB-mCherry mislocalizer. Representative images from 3 independent imaging sessions with at least 7 inspected fields of view. The middle row shows a parasite with full KS (complete GFP mislocalization, "full KS" in (B)), while the top row shows a parasite with partial KS (incomplete GFP mislocalization. "partial KS" in (B)); the bottom row shows a parasite with mixed KS (incomplete and reverse GFP mislocalization. "mixed KS" in (B)). The cell culture was split into two dishes: one served as control without rapalog (control), and the other grown in the presence of 250 nM rapalog. The samples for live cell imaging were taken 24 h post addition of rapalog. Scale bar, 5 μm, DIC, differential interference contrast, mCh, mCherry, merge, overlay of GFP, mCh and nuclei. B) Pie chart shows quantification of knock sideways efficiency based on GFP localization following rapalog treatment. Quantification of knock sideways efficiency for Y5, based on the same experiments shown in (A). A total of 145 parasites were scored across 6 independent imaging sessions. KS status was evaluated 24 hours after rapalog addition. C-E) Growth curves of the Y5 knock sideways. Parasite growth was assessed by flow cytometry in the presence (rapalog) or absence (control) of rapalog. Three independent replicates (all shown).

Overall, Y5 is a nuclear protein with an unknown subnuclear localization. Although its mislocalization led to a moderate decrease in parasite growth, it is likely only needed for efficient growth but not fully essential for asexual blood-stage development.

3.7 Characterization of Y6 (PF3D7_0406000)

Y6 (Gene ID: PF3D7_0405500) is annotated as a conserved Plasmodium protein with unknown function. BLAST, Motifscan and HHPred analysis did not showed any similarity to known domains.

In order to localize Y6, the corresponding gene was modified using SLI (Birnbaum et al., 2017) to generate a parasite line in which the endogenous gene is fused to a sequence encoding 2xFKBP-GFP-2xFKBP. Correct genomic integration was confirmed by PCR across both the 5' and 3' integration junctions and by absence of the wild-type locus (Figure 11). Y6 localized to the nucleus, often as punctate foci (Figure 29). Colocalization experiments with tubulin revealed that although Y6-GFP puncta did only rarely full overlap with the tubulin foci, they were consistently partially overlapping or

adjacent to the tubulin-positive structures (Figure 30), suggesting that Y6 may localize to a subnuclear region near or associated with mitotic spindles. FACS-based growth assays from three independent experiments showed 24.02%, 64.02%, and 36.67% growth reduction (Figure 31).

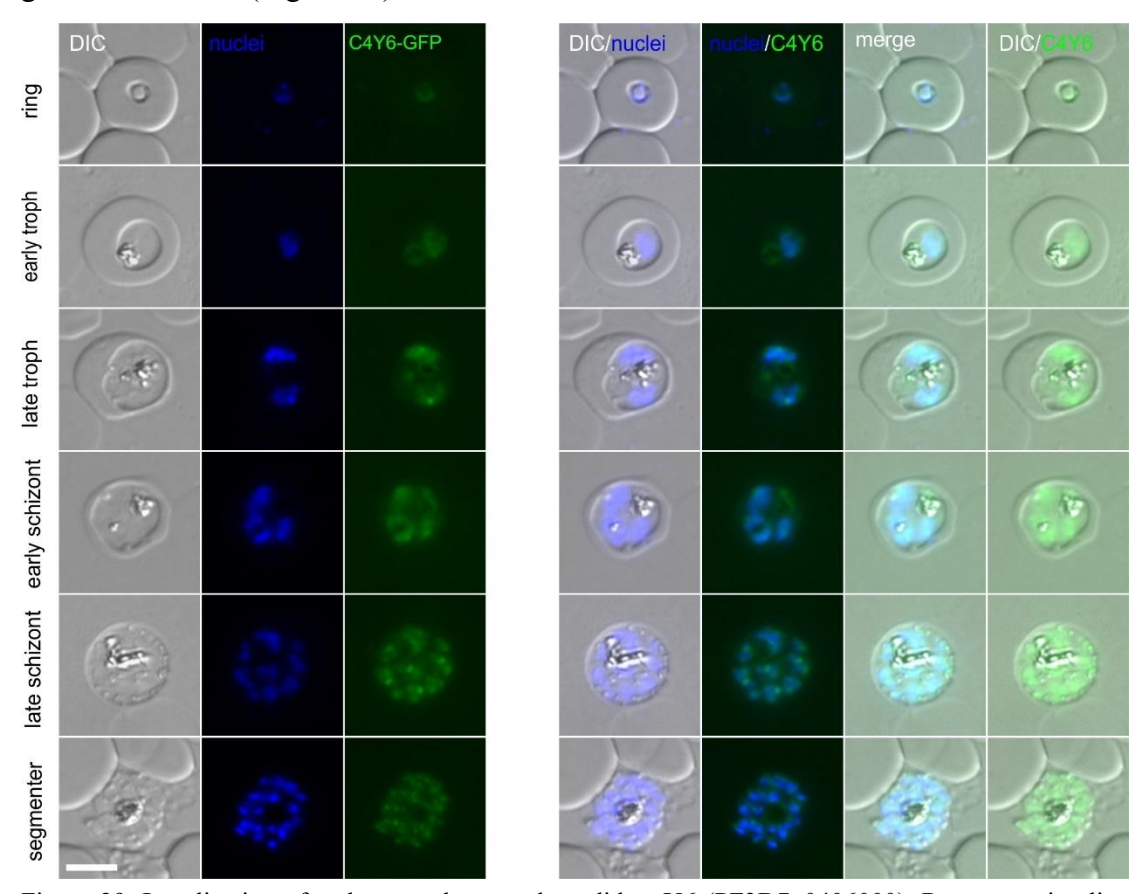


Figure 29. Localization of endogenously tagged candidate Y6 (PF3D7_0406000). Representative live cell fluorescence microscopy images of knock-in cell line Y6-2xFKBP-GFP-2xFKBP ('GFP'). The stages are indicated on the left of the panel. Representative images from 3 independent imaging sessions with at least 7 inspected fields of view. Parasite nuclei were stained with Hoechst33342. Scale bar 5 μ m, DIC, differential interference contrast; merge, overlay of DIC, GFP and nuclei.

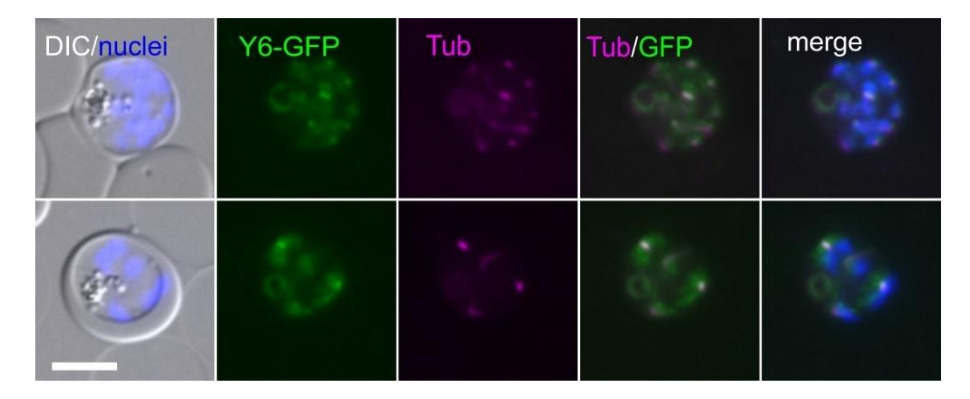


Figure 30. Y6 (PF3D7_0406000) co-localization with Tubulin. Representative live cell images of knockin cell line of Y6-2xFKBP-GFP-2xFKBP (green) with staining TubulinTrackerTM deep red (purple). Representative images from 3 independent imaging sessions with at least 7 inspected fields of view. Parasite nuclei were stained with Hoechst33342. Scale bar 5 μm, DIC, differential interference contrast; merge, overlay of Tub, GFP and nuclei.

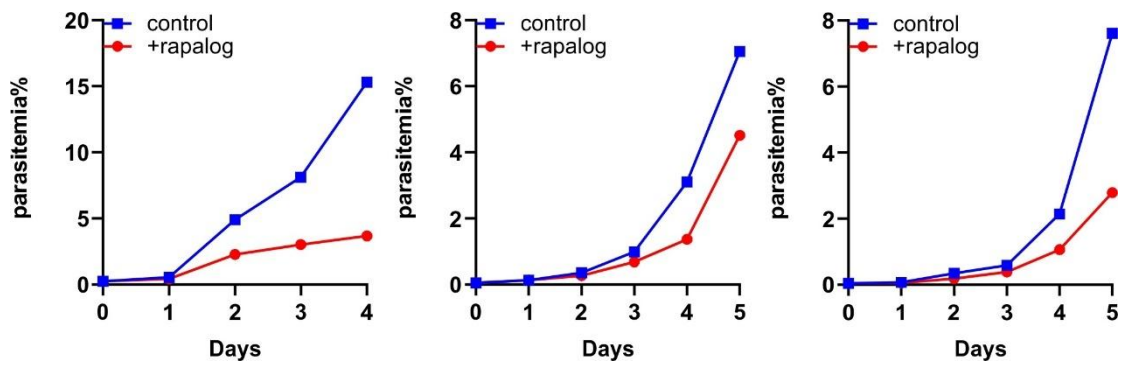


Figure 31. Growth curves of the Y6 knock sideways. Parasite growth was assessed by flow cytometry in the presence (rapalog) or absence (control) of rapalog. Three independent replicates (all shown).

These results indicate that Y6 is a nuclear protein with a punctate subnuclear distribution, potentially associated with the mitotic machinery.

3.8 Characterization of Y7 (PF3D7 0406500)

Y7 (Gene ID: PF3D7_0406500) is annotated in PlasmoDB as a putative NYN domain-containing protein, and in NF54 it is annotated as "NYN domain-containing protein" without the "putative" label. However, this appears to reflect annotation style differences rather than experimental confirmation, as no published literature or domain validation is available in UniProt, PDB, or PubMed to support the presence of a functional NYN domain. Additionally, HHPred analysis did not identify a NYN domain or other nuclease-related features.

To investigate the localization of Y7, we generated a Y7-2xFKBP-GFP-2xFKBP^{endo} cell line using the SLI system (Birnbaum et al., 2017). Correct genomic integration was confirmed by PCR at both 5' and 3' junctions and by the absence of the wild-type locus (Figure 11). However, live-cell fluorescence microscopy of the resulting parasite line failed to detect any GFP signal under standard imaging conditions across the asexual

blood-stage cycle (Figure 32), indicating very low expression levels. The filamentous structures seen in later stages (Figure 32, arrows) are likely due to autofluorescence as they are also seen in 3D7 parasites using similarly high exposure levels. Consistently, transcriptome data from synchronized parasites showed that Y7 mRNA is expressed at low levels throughout intraerythrocytic development (Otto et al., 2010).

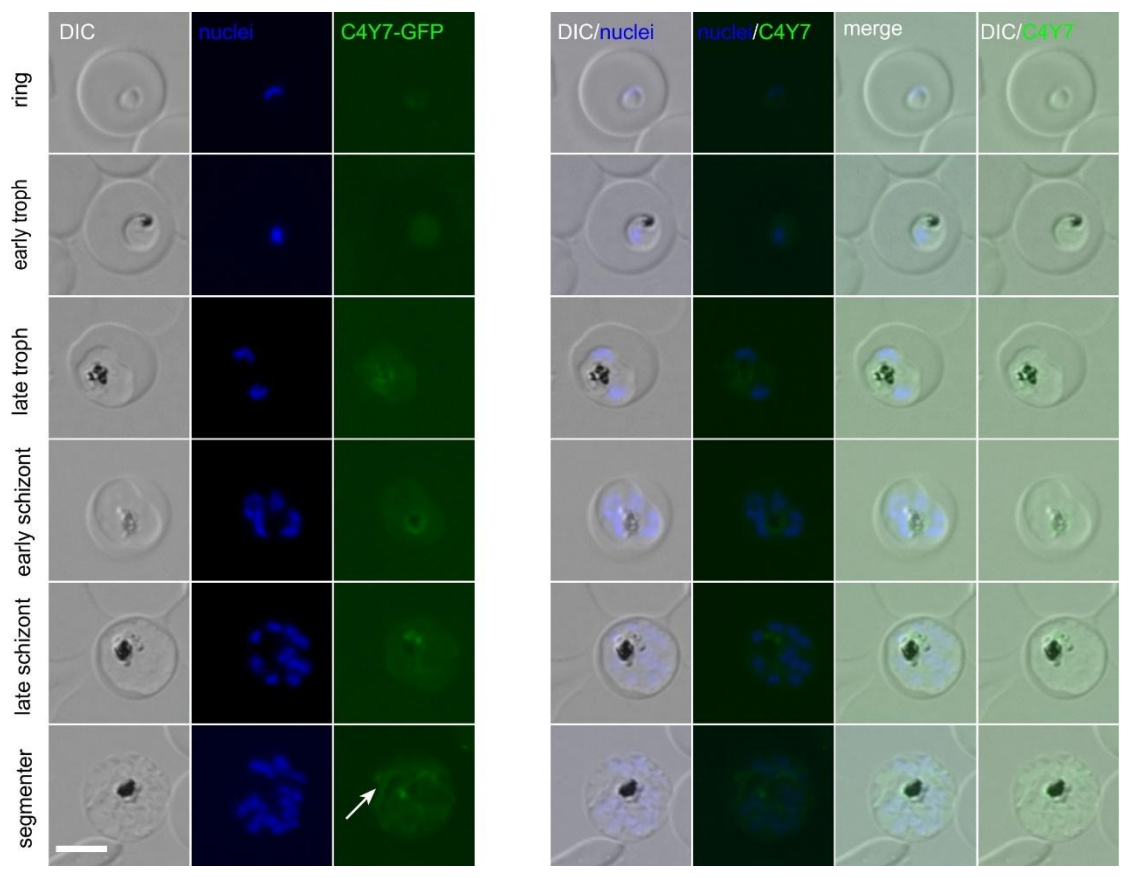


Figure 32. Attempted localization of endogenously tagged candidate Y7 (PF3D7_0406500). Representative live cell fluorescence microscopy images of knock-in cell line Y7-2xFKBP-GFP-2xFKBP ('GFP'). The stages are indicated on the left of the panel. Representative images from 3 independent imaging sessions with at least 7 inspected fields of view. Parasite nuclei were stained with Hoechst33342. Scale bar 5 μ m, DIC, differential interference contrast; merge, overlay of DIC, GFP and nuclei. Arrows show likely autofluorescence also detected in parental 3D7 parasites when imaged at similar exposure times.

Although Y7 was undetectable by fluorescence microscopy using standard GFP tagging and live cell fluorescence microscopy, we performed knock sideways experiments to investigate its functional relevance. The Y7-2xFKBP-GFP-2xFKBP^{endo} cell line was transfected with episomal plasmids expressing either Lyn-FRB-mCherry (Figure 33A) or NLS-FRB-mCherry (Figure 34 A) mislocalizers. Due to the absence of detectable Y7-GFP fluorescence, it was not possible to quantify mislocalization efficiency. Upon rapalog induction, Lyn-mediated mislocalization to the parasite plasma membrane, which mainly targets proteins from the nucleus, had no effect on parasite proliferation, with final parasitemia remaining at 98.93%, 96.37%, and 101.41% of the control across three biological replicates (Figure 33B-D). In contrast, NLS-based mislocalization, which transports the target proteins into the nucleus, consistently impaired growth, with treated parasites reaching only 46.98%, 57.20%, and 56.16% of control parasitemia (Figure 34B-D). This outcome indicates that Y7 functions in the cytoplasm, and that its

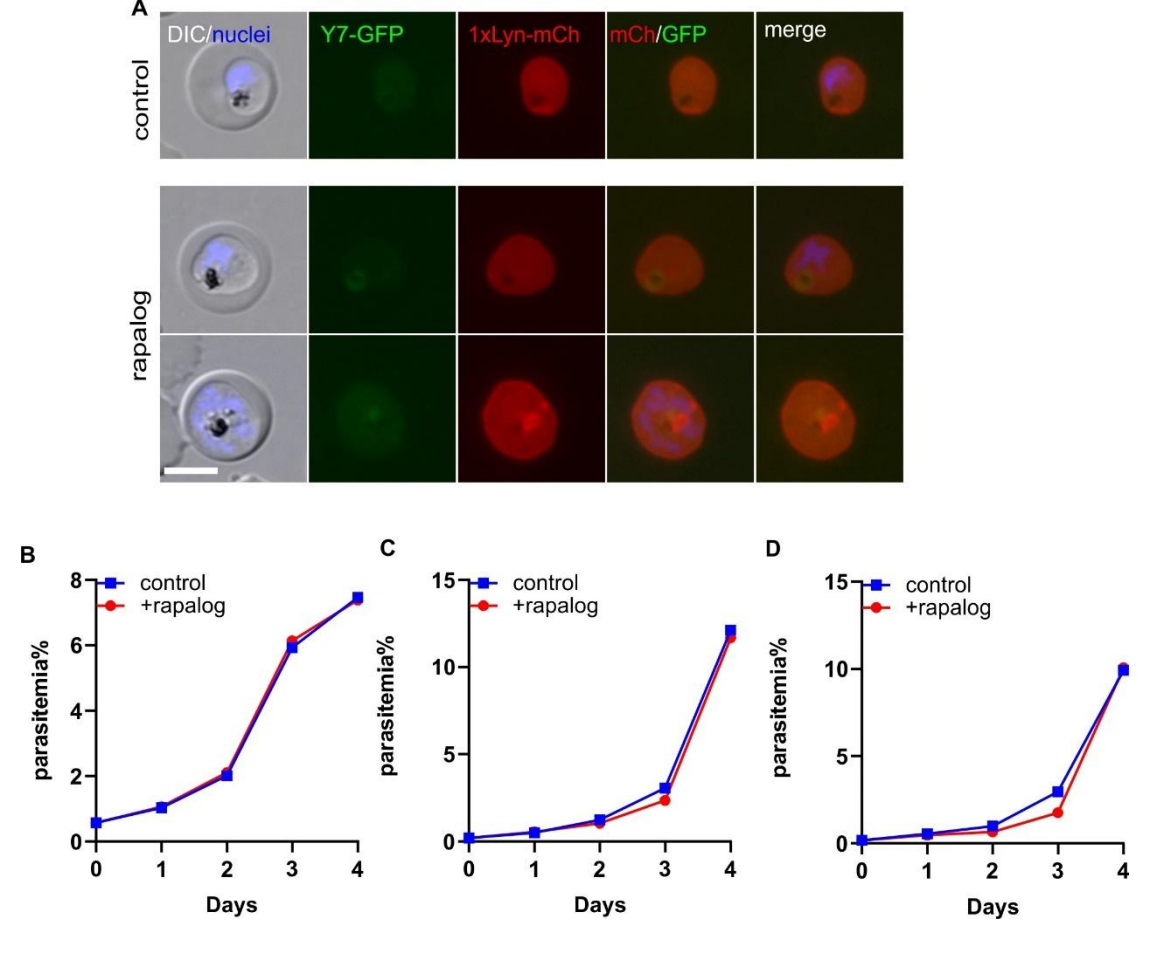


Figure 33. Knock sideways analysis of endogenous Y7 (PF3D7_0406500) tagged with 2xFKBP-GFP-2xFKBP. A) Representative live cell images of knock-in cell line Y7-2xFKBP-GFP-2xFKBP ('GFP') with an episomally expressed Lyn-FRB-mCherry mislocalizer. Representative images from 3 independent imaging sessions with at least 7 inspected fields of view. The cell culture was split into two dishes: one served as control without rapalog (control), and the other grown in the presence of 250 nM rapalog. The samples for live cell imaging were taken 24 h post addition of rapalog. Scale bar, 5 μm, DIC, differential interference contrast, mCh, mCherry, merge, overlay of GFP, mCh and nuclei. B-D) Growth curve of the Y7-Lyn knock sideways. Parasite growth was assessed by flow cytometry in the presence (rapalog) or absence (control) of rapalog. Three independent replicates (all shown).

forced removal to the nucleus ablates the function of Y7. These findings evidence for a cytoplasmic localization of Y7 and an important function of this protein.

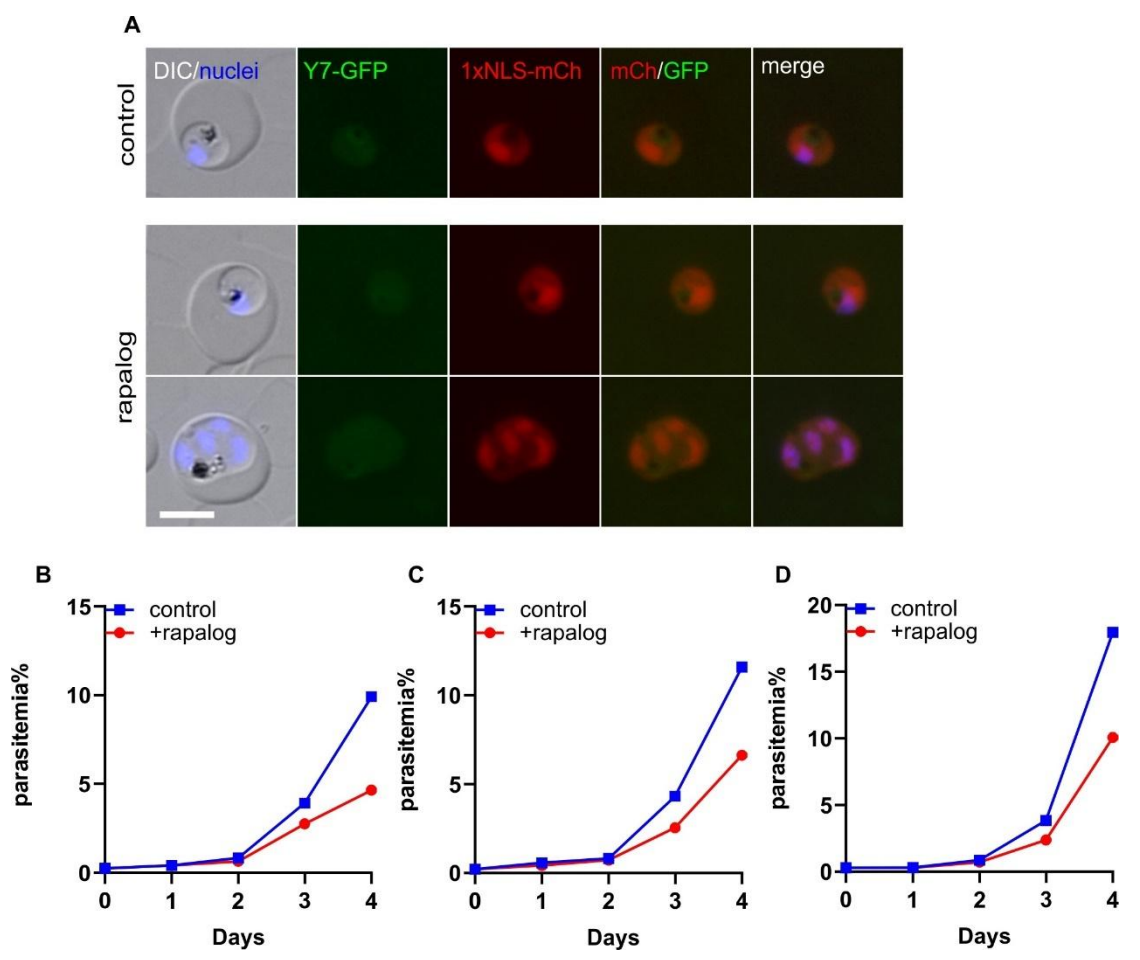


Figure 34. Knock sideways analysis of endogenous Y7 (PF3D7_0406500) tagged with 2xFKBP-GFP-2xFKBP. A) Representative live cell images of knock-in cell line Y7-2xFKBP-GFP-2xFKBP ('GFP') with an episomally expressed NLS-FRB-mCherry mislocalizer. Representative images from 3 independent imaging sessions with at least 7 inspected fields of view. The cell culture was split into two dishes: one served as control without rapalog (control), and the other grown in the presence of 250 nM

rapalog. The samples for live cell imaging were taken 24 h post addition of rapalog. Scale bar, 5 μm, DIC, differential interference contrast, mCh, mCherry, merge, overlay of GFP, mCh and nuclei. B-D) Growth curve of the Y7-NLS knock sideways. Parasite growth was assessed by flow cytometry in the presence (rapalog) or absence (control) of rapalog. Three independent replicates (all shown).

3.9 Characterization of Y8 (PF3D7 0406600)

Y8 (Gene ID: PF3D7_0406600) is annotated as a conserved Plasmodium protein with unknown function. BLAST and Motifscan analysis did not identify homologs with known function outside the *Plasmodium* genus. However, HHPred revealed a strong match (probability: 100%; E-value: 6.4e–43) to a mitochondrial ribosomal protein, mS156, from *Toxoplasma gondii*, suggesting that Y8 may play a role in mitochondrial translation or rRNA-associated processes. The similarity covered 125 out of 139 amino acids of Y8, indicating a high-confidence alignment and supporting a functional relevance of this homology.

To investigate the localization and potential function of Y8, the endogenous gene was tagged using the SLI system (Birnbaum et al., 2017) with a 2xFKBP-GFP-2xFKBP tag at the C-terminus. Correct genomic integration was confirmed by PCR amplification across the 5' and 3' integration junctions and loss of the wild-type locus (Figure 11). Live-cell fluorescence microscopy of the Y8-2xFKBP-GFP-2xFKBP^{endo} parasite line revealed a distinct filamentous and branched GFP signal that resembled a localization typical for mitochondrial proteins (Figure 35). The signal was visible across all asexual blood-stage forms, including rings, trophozoites, and schizonts, indicating constitutive expression of Y8. A mitochondrial localization would be in line with the HHPred predictions indicating homology to *T. gondii* mS156, a mitochondrial ribosomal protein.

To further confirm mitochondrial localization, we performed co-localization with MitoTracker. The Y8-GFP signal showed complete overlap with MitoTracker staining (Figure 36), confirming the mitochondrial residency of Y8.

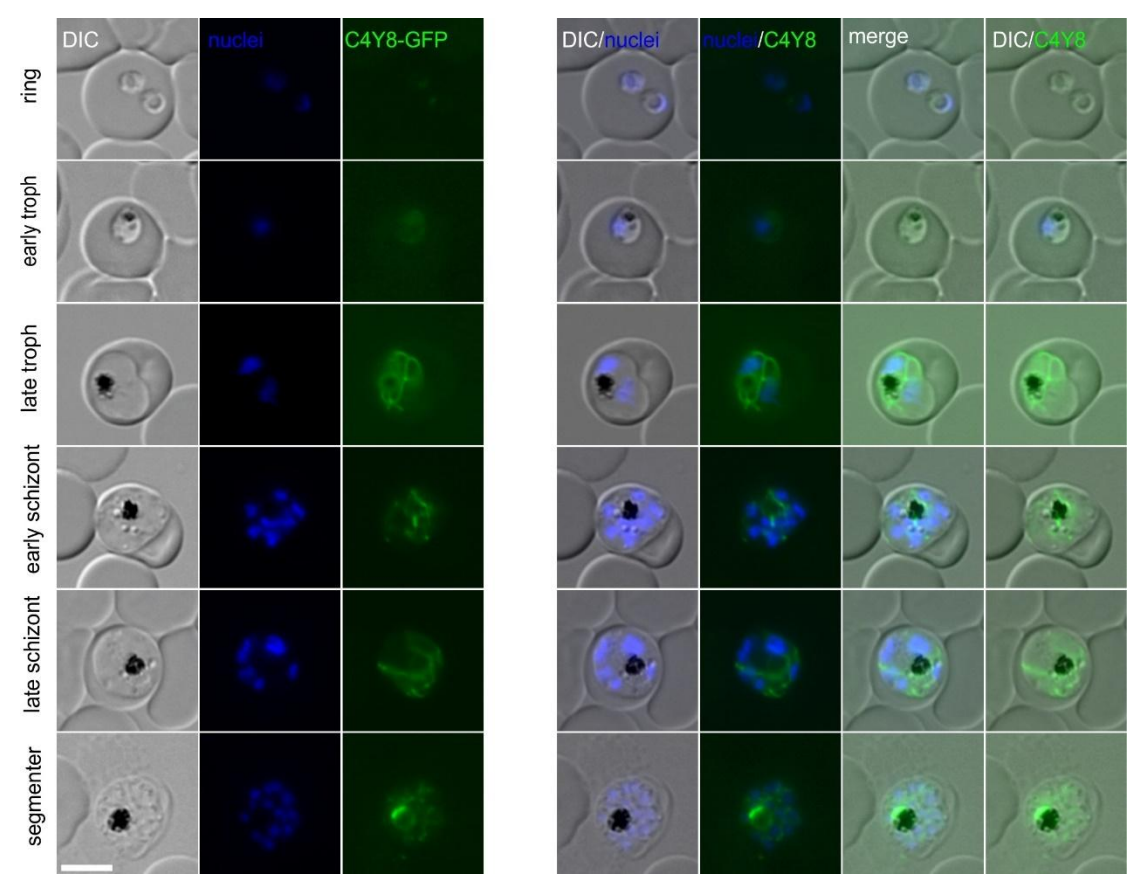


Figure 35. Localization of endogenously tagged candidate Y8 (PF3D7_0406600). Representative live cell fluorescence microscopy images of knock-in cell line Y8-2xFKBP-GFP-2xFKBP ('GFP'). The stages are indicated on the left of the panel. Representative images from 3 independent imaging sessions with at least 7 inspected fields of view. Parasite nuclei were stained with Hoechst33342. Scale bar 5 μ m, DIC, differential interference contrast; merge, overlay of DIC, GFP and nuclei.

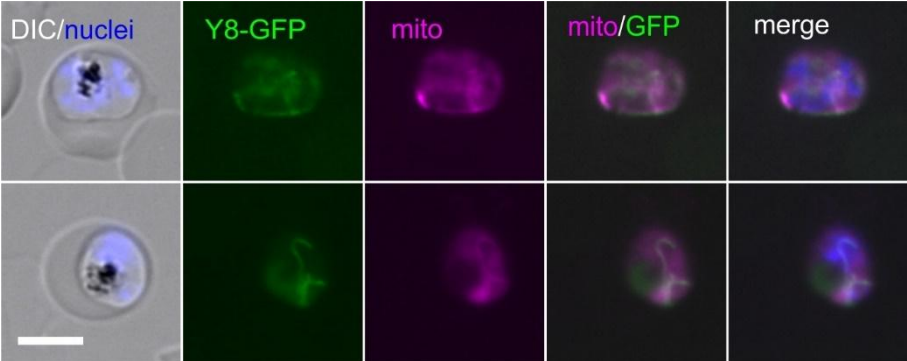


Figure 36. Fluorescence microscopy images of endogenously tagged Y8 (PF3D7_0406600) colocalized with and MitoTrackerTM Red CMXRos. Representative images of parasites expressing GFP-tagged Y8 (green), Representative images from 3 independent imaging sessions with at least 7 inspected fields of view. Parasite nuclei were stained with Hoechst33342. Scale bar 5 μm, DIC, differential interference contrast; merge, overlay of DIC, GFP and nuclei.

To assess the functional importance of Y8, we generated a knock sideways line by transfecting the Y8-2xFKBP-GFP-2xFKBP^{endo} cell line with an episomal plasmid expressing the NLS-FRB-mCherry mislocalizer, aiming to redirect the protein to the nucleus. Upon rapalog treatment, live-cell microscopy revealed no significant mislocalization of Y8-GFP, and the filamentous mitochondrial signal remained unchanged (Figure 37), indicating that mislocalization was unsuccessful. This indicates that either Y8 is very tightly anchored to the outside of the mitochondria or is transported into this organelle, which limits the accessibility to cytosolic mislocalizers. To further explore the essentiality of Y8, we constructed a conditional knockout plasmid using the DiCre/loxP system. However, due to time limitations, we were unable to obtain integrant lines in the course of this thesis. As a result, the functional relevance of Y8 remains unresolved and will require future investigation using alternative genetic approaches.

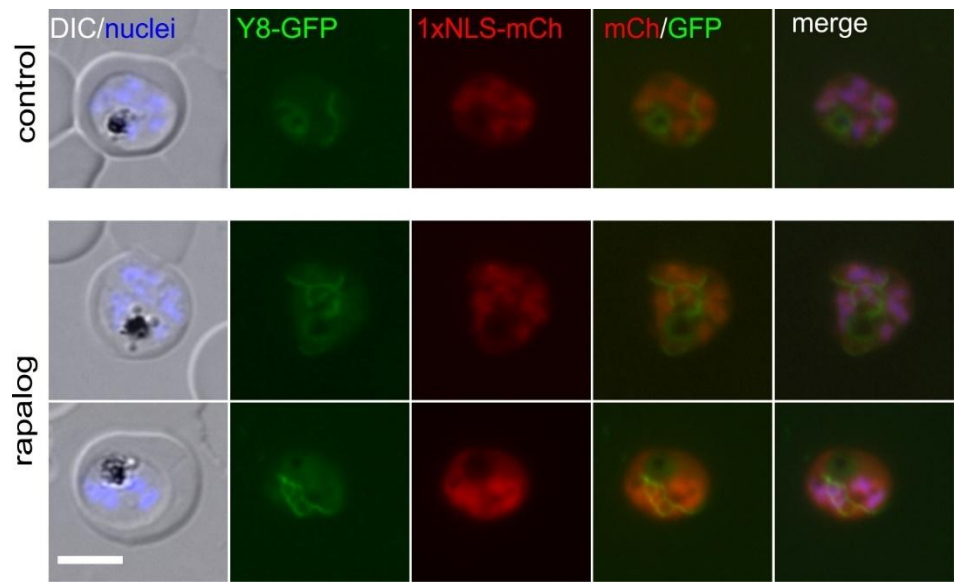


Figure 37. Knock sideways of endogenously tagged Y8 (PF3D7_0406600). Representative live cell images of knock-in cell line Y8-2xFKBP-GFP-2xFKBP ('GFP') with an episomally expressed NLS-FRB-mCherry mislocalizer. The cell culture was split into two dishes: one served as control without rapalog (control), and the other grown in the presence of 250 nM rapalog (rapalog). The samples for live cell imaging were taken 24 h post addition of rapalog. Representative images from 3 independent imaging sessions with at least 7 inspected fields of view. Parasite nuclei were stained with Hoechst33342. Scale bar, 5 μm, DIC, differential interference contrast, mCh, mCherry, merge, overlay of GFP, mCh

and nuclei. As no mislocalization was observed, no quantification of mislocalization efficiency was carried out.

3.10 Characterization of Y9 (PF3D7_0406700)

Y9 (Gene ID: PF3D7_0406700) is annotated in PlasmoDB as a putative KLRAQ domain-containing protein, although the KLRAQ domain itself is poorly characterized across organisms and lacks experimental validation. BLAST searches only retrieved homologous sequences from other *Plasmodium* species without functional annotation. In contrast, HHPred revealed a strong hit (probability: 100%; E-value: 3e-44) to the protein phosphatase 1 regulatory subunit 21, part of the human FERRY complex, which is known to associate with early endosomal RNA transport and ribosome interaction (Schuhmacher et al., 2023). The alignment covered 248 out of 847 amino acids of Y9. This prediction suggests a possible involvement in vesicle trafficking.

To study the localization and potential function of Y9, the endogenous gene was tagged using the SLI system (Birnbaum et al., 2017) to fuse it with the sequence encoding a 2xFKBP-GFP-2xFKBP tag at the C-terminus. Correct genomic integration was confirmed by PCR across the 5' and 3' integration junctions, as well as by loss of the wild-type locus (Figure 11). Live-cell fluorescence microscopy of Y9-2xFKBP-GFP-2xFKBPendo parasites revealed a punctate GFP signal in proximity to the nucleus, consistent with a Golgi-like distribution (Figure 38). The signal was detected in all stages except for the ring stage expression (Figure 38). Next, we performed colocalization experiments using two markers: GRASP (Golgi) and CLC (clathrin light chain, trans Golgi). Y9 showed partial overlap with GRASP (Figure 39), but the punctate morphology and distribution more closely resembled CLC marker (Figure 40), suggesting that Y9 may be located at the trans Golgi with a possible role in the trafficking of clathrin-coated vesicles. The plasmid used to mediate episomal expression of the mCherry tagged markers also contained a 1xNLS mislocalizer,

permitting inactivation of Y9 and assessing the marker after Y9 inactivation. Interestingly, after KS of Y9, the localization of neither GRASP nor CLC showed visible changes in their distribution or intensity (Figure 39 and Figure 40). This suggests that Y9 is not required for maintaining the structural integrity of the Golgi or clathrin vesicle network.

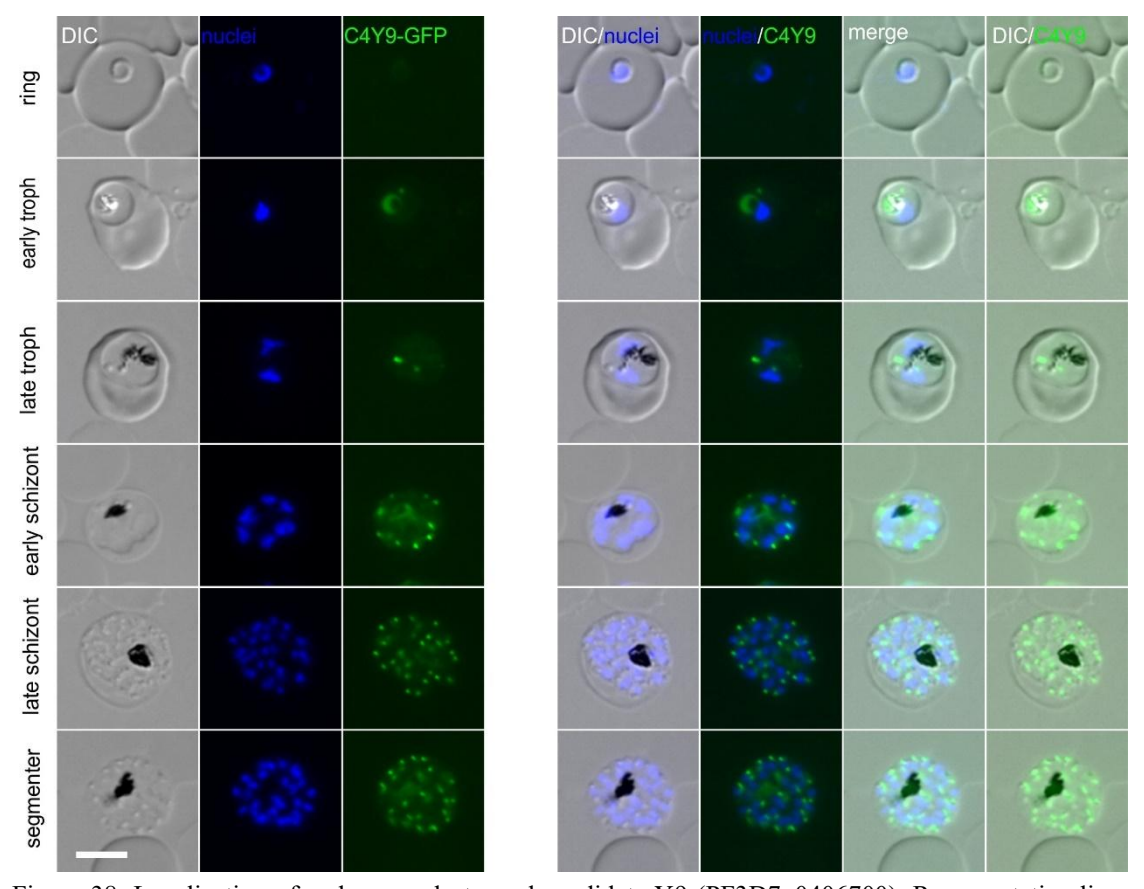


Figure 38. Localization of endogenously tagged candidate Y9 (PF3D7_0406700). Representative live cell fluorescence microscopy images of knock-in cell line Y9-2xFKBP-GFP-2xFKBP ('GFP'). The stages are indicated on the left of the panel. Representative images from 3 independent imaging sessions with at least 7 inspected fields of view. Parasite nuclei were stained with Hoechst33342. Scale bar 5 μ m, DIC, differential interference contrast; merge, overlay of DIC, GFP and nuclei.

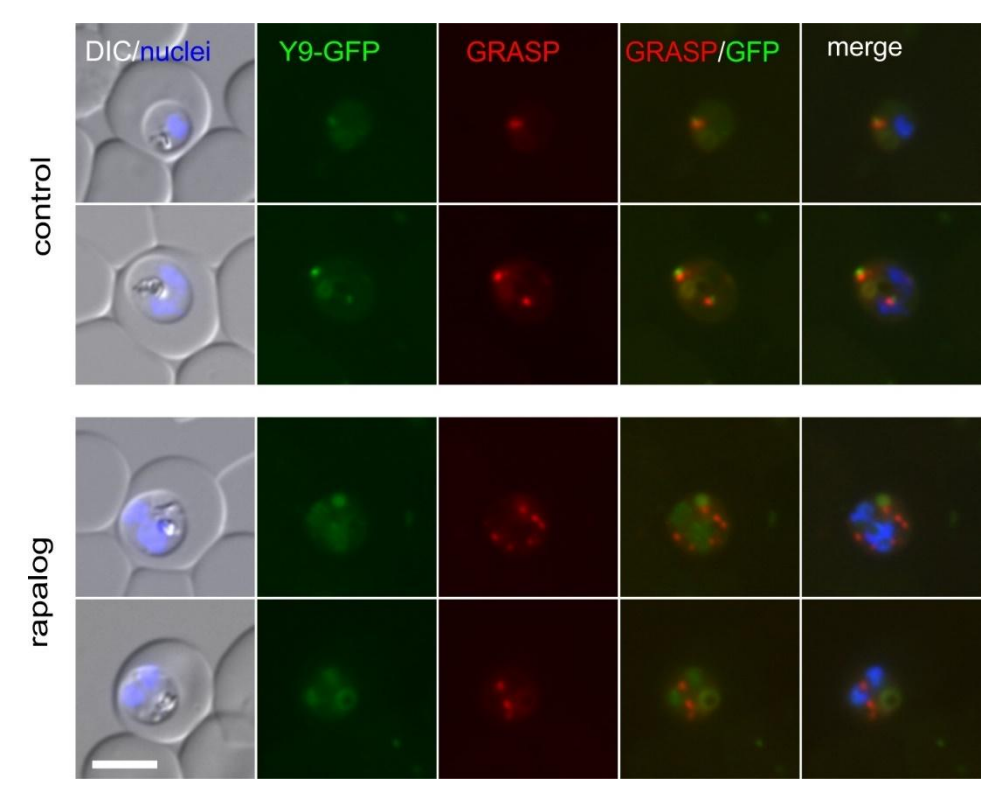


Figure 39. Y9 (PF3D7_0406700) co-localization with GRASP. Representative live cell images of knockin cell line of Y9-2xFKBP-GFP-2xFKBP (green) with episomally expressed GRASP-mCherry (red). The cell culture was split into two dishes: one served as control without rapalog (control), and the other grown in the presence of 250 nM rapalog (rapalog). The samples for live cell imaging were taken 24 h post addition of rapalog. Representative images from 3 independent imaging sessions with at least 7 inspected fields of view. Parasite nuclei were stained with Hoechst33342. Scale bar 5 μ m, DIC, differential interference contrast; merge, overlay of GRASP, GFP and nuclei.

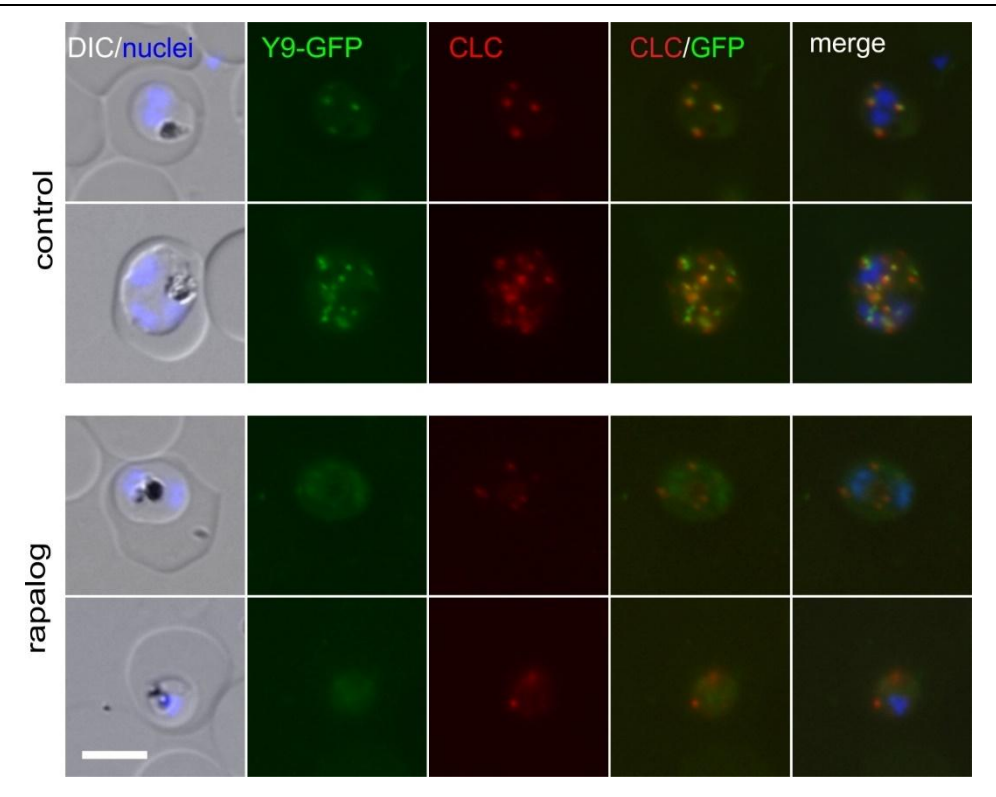


Figure 40. Y9 (PF3D7_0406700) co-localization with CLC. Representative live cell images of knock-in cell line of Y9-2xFKBP-GFP-2xFKBP (green) with episomally expressed CLC-mCherry (red). The cell culture was split into two dishes: one served as control without rapalog (control), and the other grown in the presence of 250 nM rapalog (rapalog). The samples for live cell imaging were taken 24 h post addition of rapalog. Representative images from 3 independent imaging sessions with at least 7 inspected fields of view. Parasite nuclei were stained with Hoechst33342. Scale bar 5 μ m, DIC, differential interference contrast; merge, overlay of CLC, GFP and nuclei.

To assess the functional importance of Y9, the Y9-2xFKBP-GFP-2xFKBP^{endo} cell line was transfected with an episomal plasmid expressing the NLS-FRB-mCherry mislocalizer, enabling conditional redirection of the protein to the nucleus. Upon rapalog treatment, live-cell microscopy revealed efficient mislocalization of Y9-GFP from its native perinuclear, punctate structures to the nucleus in the majority of parasites (Figure 41A). Quantification 24 hours post-induction showed that over 90% of parasites exhibited full mislocalization, with complete loss of the Golgi-like signal (Figure 41B).

Growth curve analysis demonstrated a strong and reduction in parasite proliferation following Y9 mislocalization, indicating that Y9 is essential for asexual blood-stage development (Figure 41C-E).

To investigate the stage Y9 is important in the intraerythrocytic developmental cycle of P. falciparum, we inactivated it by KS in synchronous parasites and monitored parasite growth using Giemsa smears (Figure 42). At 34-42 hpi, a small divergence in the stagedistribution was observed between the control and Y9-KS parasites. Notably, the proportion of early schizonts was lower in the Y9-KS group compared to the control, suggesting that Y9 inactivation slowed trophozoites to schizonts development. This developmental delay became more significant at 48-56 hpi—a time window for parasite egress and invasion—where parasitemia in the control group continued to increase while the Y9-KS parasites remained at a lower parasitemia, indicating a defect in completing schizogony and initiating the next replication cycle. At 58-66 hpi, although both groups displayed mainly ring-stage parasites, the overall parasitemia in the Y9-KS group was clearly reduced, implying that not all schizonts successfully generated progeny merozoites or that not all merozoites invaded new red blood cells. A similar but more distinct difference was observed at the equivlane time point in the second cycle at 96-104 hpi. Together, these results indicate that Y9 plays an importantl role in schizont development, parasite egress or subsequent merozoite invasion.

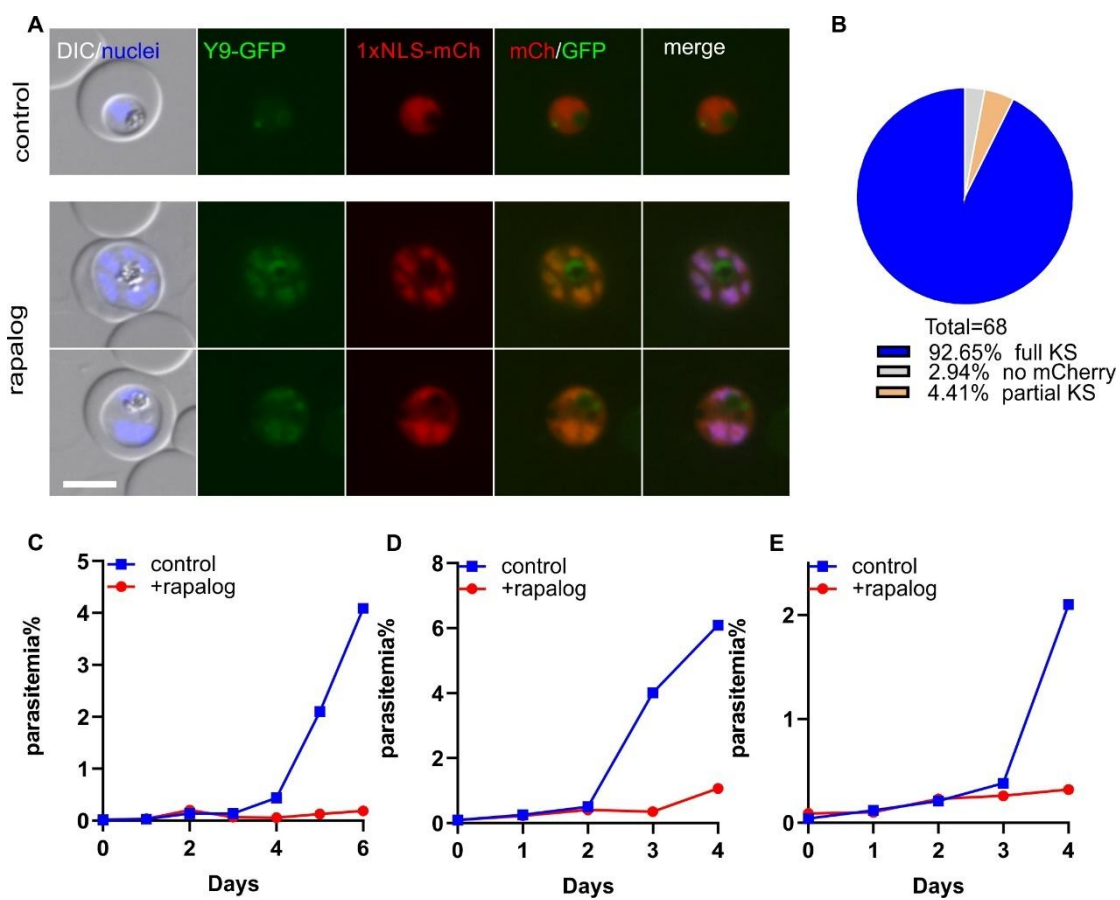


Figure 41. Knock sideways analysis of endogenous Y9 (PF3D7_0406700) tagged with 2xFKBP-GFP-2xFKBP. A) Representative live cell images of knock-in cell line Y9-2xFKBP-GFP-2xFKBP ('GFP') with an episomally expressed NLS-FRB-mCherry mislocalizer. Representative images from 3 independent imaging sessions with at least 7 inspected fields of view. Both rows show a parasite with full KS (complete GFP mislocalization, "full KS" in (B)). The cell culture was split into two dishes: one served as control without rapalog (control), and the other grown in the presence of 250 nM rapalog. The samples for live cell imaging were taken 24 h post addition of rapalog. Scale bar, 5 μm, DIC, differential interference contrast, mCh, mCherry, merge, overlay of GFP, mCh and nuclei. B) Pie chart shows quantification of knock sideways efficiency based on GFP localization following rapalog treatment. Quantification of knock sideways efficiency for Y9, based on the same experiments shown in (A). A total of 68 parasites were scored across 3 independent imaging sessions. KS status was evaluated 24 hours after rapalog addition. C-E) Growth curve of the Y9-NLS knock sideways. Parasite growth was assessed by flow cytometry in the presence (rapalog) or absence (control) of rapalog. Three independent replicates (all shown).

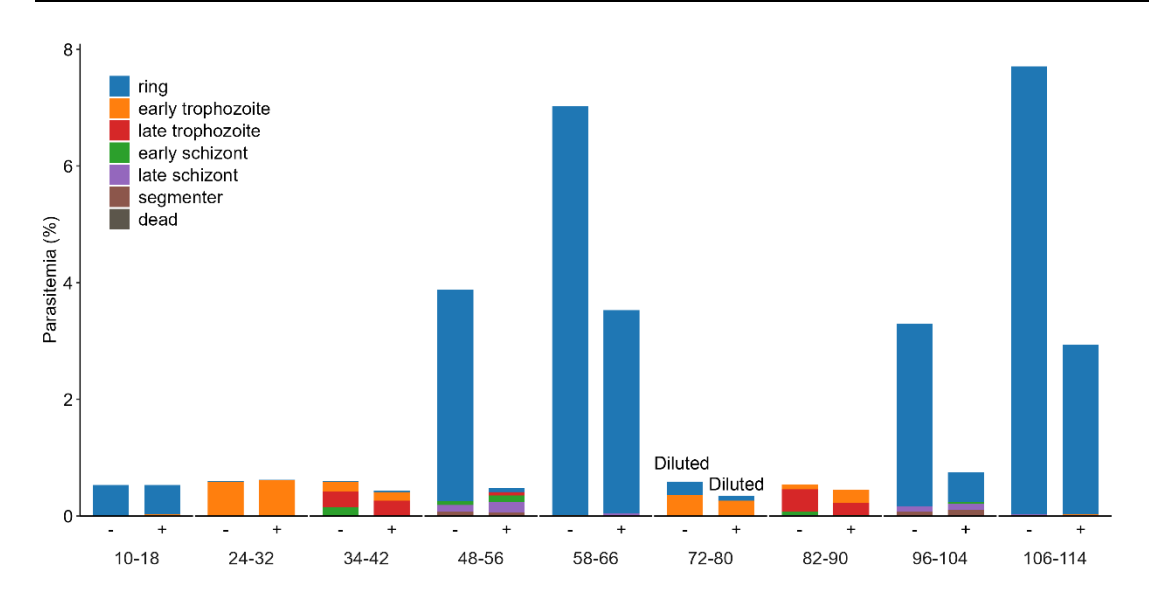


Figure 42. Stage specific impact of Y9-NLS knock sideways in synchronized *P. falciparum* parasites expressing a knock sideways version of Y9. Synchronized parasites (0-8 h age window based on two subsequent synchronisations 10 h apart) expressing a knock sideways version of Y9 were treated with rapalog whit the first synchronization and parasite stages were monitored every 10 or 14 hours in 5 days over two intraerythrocytic developmental cycles at the indicated parasite age. Diluted: the parasitemia shown is based on diluted samples (1:10), without extrapolation to original culture density. Parasitemia (%) and the distribution of parasite stages were quantified by Giemsa-stained blood smears. Data shown are representative of two independent biological replicates.

3.11 Characterization of Y11 (PF3D7 0407400)

Y11 (Gene ID: PF3D7_0407400) is annotated in PlasmoDB as a conserved Plasmodium protein of unknown function. BLAST, Motifscan and HHPred analysis did not show any similarity to known domains.

In order to localize and functionally analyze Y11, the corresponding gene was modified using SLI (Birnbaum et al., 2017) so that the endogenous Y11 becomes fused with the multipurpose sandwich tag (2xFKBP-GFP-2xFKBP). Correct integration into the genome was confirmed by PCR across the 5'- and 3'- integration junctions and by the absence of the original locus (Figure 11). Fluorescence microscopy with the Y11-2xFKBP-GFP-2xFKBP^{endo} parasites revealed that this protein localizes to a mitochondrion typical structure (Figure 43), forming a filamentous signal consistent

with mitochondrial morphology. Co-localization experiments with MitoTracker showed an overlap between the GFP signal and the mitochondrial marker, confirming the mitochondrial localization (Figure 44). Y11 expression was detectable throughout the asexual blood-stage cycle, with no obvious stage restriction.

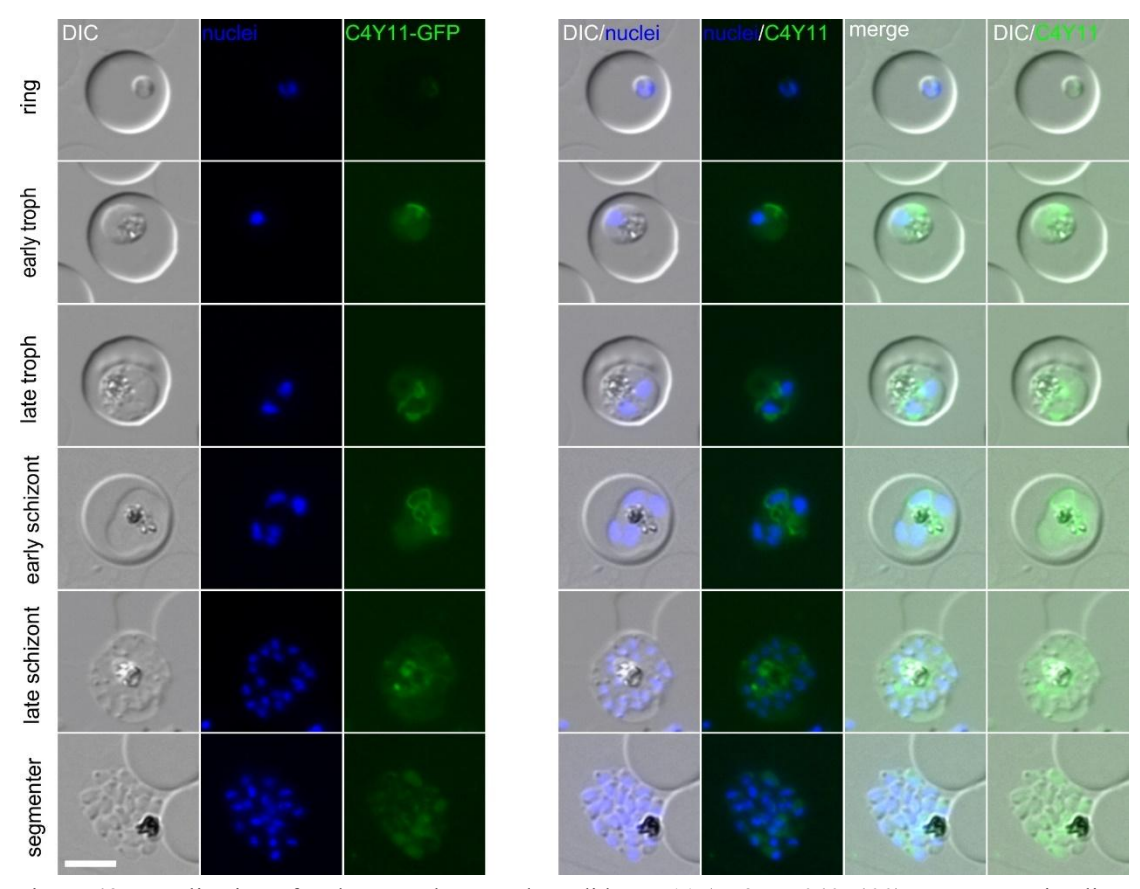


Figure 43. Localization of endogenously tagged candidate Y11 (PF3D7_0407400). Representative live cell fluorescence microscopy images of knock-in cell line Y11-2xFKBP-GFP-2xFKBP ('GFP'). The stages are indicated on the left of the panel. Representative images from 3 independent imaging sessions with at least 7 inspected fields of view. Parasite nuclei were stained with Hoechst33342. Scale bar 5 μ m, DIC, differential interference contrast; merge, overlay of DIC, GFP and nuclei.

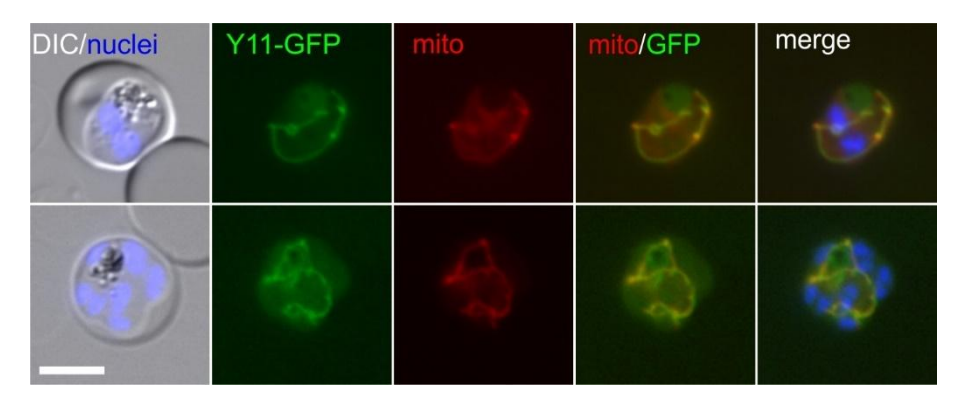


Figure 44. Fluorescence microscopy images of endogenously tagged Y11 (PF3D7_0407400) colocalized with MitoTrackerTM Red CMXRos. Representative images of fixed parasites expressing GFP-tagged Y11 (green). Representative images from 3 independent imaging sessions with at least 7 inspected fields of view. Parasite nuclei were stained with Hoechst33342. Scale bar 5 μm, DIC, differential interference contrast; merge, overlay of mito, GFP and nuclei.

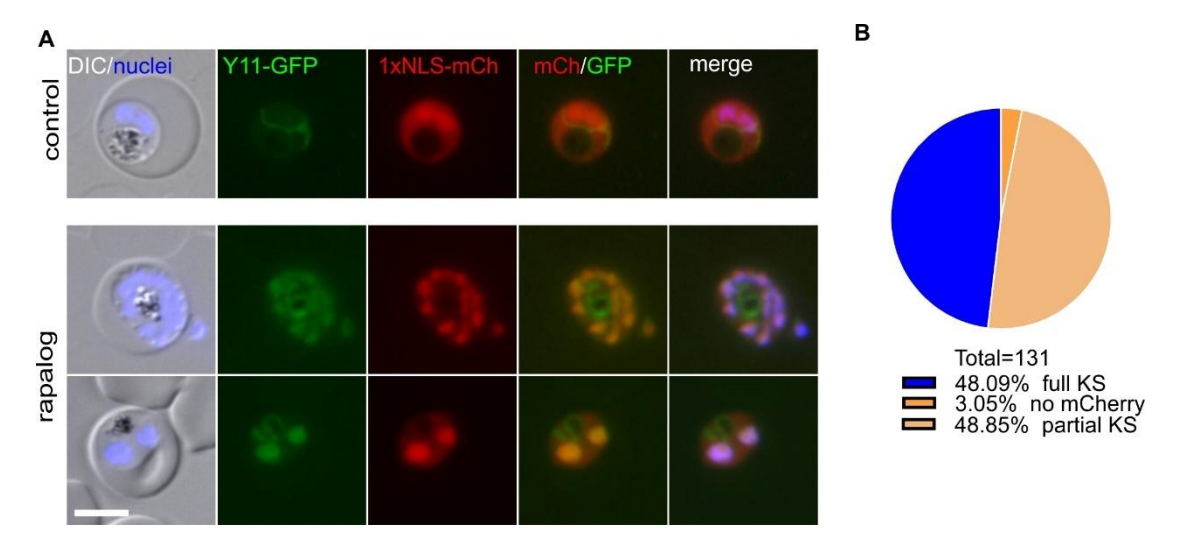


Figure 45. Knock sideways analysis of endogenous Y11 (PF3D7_0407400) tagged with 2xFKBP-GFP-2xFKBP. A) Representative live cell images of knock-in cell line Y11-2xFKBP-GFP-2xFKBP ('GFP') with an episomally expressed NLS-FRB-mCherry mislocalizer. Representative images from 3 independent imaging sessions with at least 7 inspected fields of view. The top row shows a parasite with full KS (complete GFP mislocalization, "full KS" in (B)), while the bottom row shows a parasite with partial KS (incomplete GFP mislocalization, "partial KS" in (B)). The cell culture was split into two dishes: one served as control without rapalog (control), and the other grown in the presence of 250 nM rapalog. The samples for live cell imaging were taken 24 h post addition of rapalog. Scale bar, 5 μm, DIC, differential interference contrast, mCh, mCherry, merge, overlay of GFP, mCh and nuclei. B) Pie chart shows quantification of knock sideways efficiency based on GFP localization following rapalog treatment. Quantification of knock sideways efficiency for Y11, based on the same experiments shown in (A). A total of 131 parasites were scored across 7 independent imaging sessions. KS status was evaluated 24 hours after rapalog addition.

In order to assess the importance of Y11, the Y11-2xFKBP-GFP-2xFKBP^{endo} cell line was transfected with an episomal plasmid expressing the NLS mislocalizer, permitting conditional inactivation using the knock sideways system. Representative live-cell microscopy confirmed that Y11-GFP was fully mislocalized to the nucleus upon rapalog treatment in about half of the parasites, while the remainder showed a partial knock sideways, indicating an overall good efficiency of the knock sideways (Figure 45).

Growth curve analysis revealed only subtle and variable differences between rapalog-treated (inactivated Y11) and control cultures. In several independent 5-day growth assays, the first, third, and fifth replicates showed a small reduction in parasitemia, while the second and fourth were identical to the control, suggesting inconsistency or a delayed onset of the growth defect (Figure 46). To further investigate this possibility, we performed an extended 7-day growth assay, in addition also comparing the Y11 knock sideways line to wild type 3D7 grown with and without rapalog. The 7-day curve revealed a mild but clearer reduction in growth in the Y11 line, suggesting a weak or cumulative effect over time of Y11 inactivation on parasite growth (Figure 47).

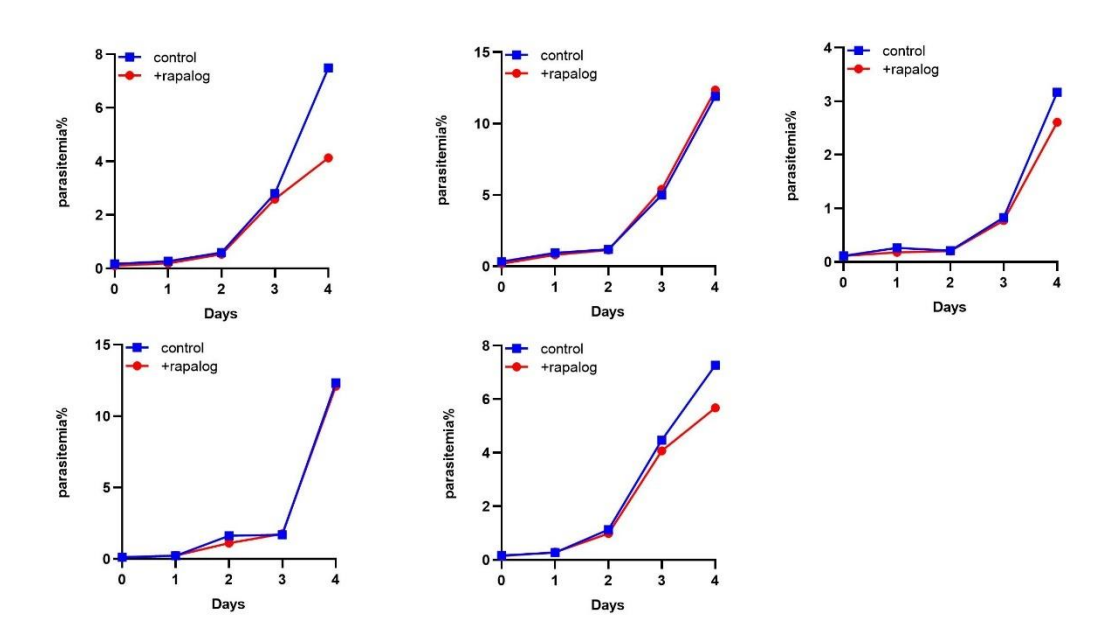


Figure 46. Growth curve of the Y11-NLS knock sideways. Parasite growth was assessed by flow cytometry in the presence (rapalog) or absence (control) of rapalog. Five independent replicates (all shown).

To assess whether this phenotype is stage-specific, we conducted growth assays with synchronized parasites starting from either ring or schizont stages. Parasites synchronized at the ring stage did not show a noticeable growth defect during the first cycle, but a slight reduction emerged after a second cycle (Figure 48). When starting

from schizont stage, a minor defect appeared earlier, by the second cycle, and became more pronounced by the third (day 4) (Figure 48).

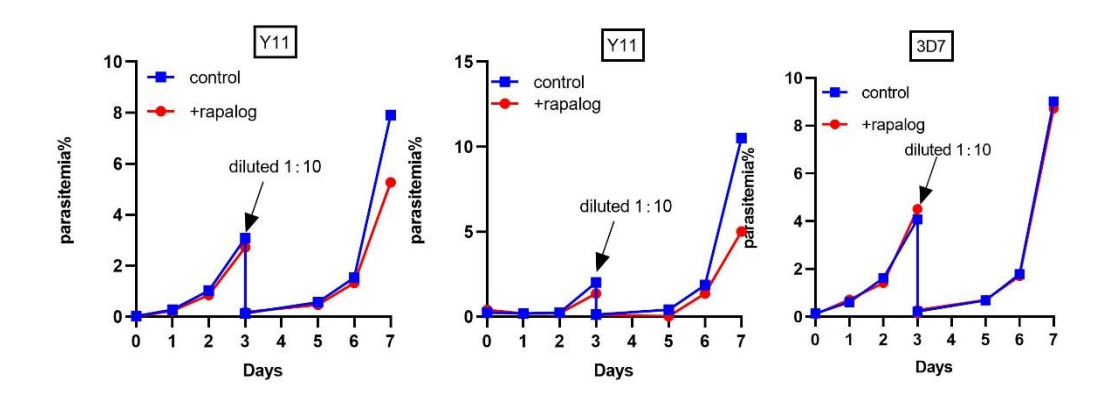


Figure 47. 7-Day Growth curve and the Y11 knock sideways with NLS compared with wild type parasites (3D7). Parasite growth was assessed by flow cytometry in the presence (rapalog) or absence (control) of rapalog.

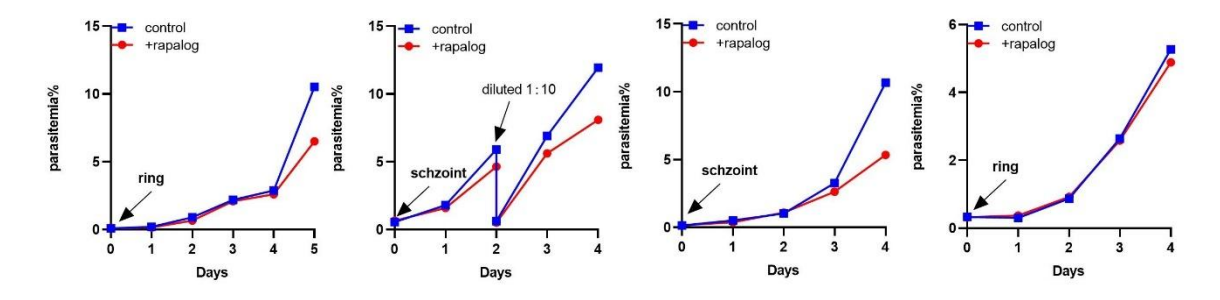


Figure 48. 7-Day Growth curve and the Y11 knock sideways with NLS using synchronous parasites starting with the stage indicated. Parasite growth was assessed by flow cytometry in the presence (rapalog) or absence (control) of rapalog.

In conclusion, although knock sideways of Y11 resulted in a mild partial growth reduction in some experiments or after extended assay times, the overall effect remained limited and inconsistent. These data suggest that Y11 is not an essential gene under standard asexual growth conditions, but it may contribute modestly to parasite fitness over multiple replication cycles.

3.12 Characterization of Y13 (PF3D7_0407700)

Y13 (Gene ID: PF3D7_0407700) is annotated in PlasmoDB as a putative TH1 domain-containing protein. TH1 domains have multiple functions and occur in a number of different proteins (Tyska et al., 2014) and the function of Y13 remains unclear in Plasmodium parasites.

BLAST searches did not yield any significant homologs or conserved domains outside *Plasmodium*. However, HHPred analysis revealed high-confidence matches of two separate regions (100% probability, E-value = 2.3e-44 and 278/784, amino acids aligned) to negative elongation factor D (NELF-D) from *homo sapiens*, which is part of the NELF complex involved in regulating transcription elongation by RNA polymerase II. This structural homology raises the possibility that Y13 may play a role in transcriptional control within the parasite nucleus.

In order to localize and functionally analyze Y13, the corresponding gene was modified using SLI (Birnbaum et al., 2017) so that the endogenous Y13 becomes fused with the multipurpose sandwich tag (2xFKBP-GFP-2xFKBP). Correct integration into the genome was confirmed by PCR across the 5'- and 3'- integration junctions and by the absence of the original locus (Figure 11). Fluorescence microscopy with the Y13-2xFKBP-GFP-2xFKBP^{endo} parasites revealed that this protein is localized in the nucleus (Figure 49), with a diffuse, partially focal, nuclear signal detectable across all asexual blood-stage forms. The signal was consistently observed in ring, trophozoite, and schizont stages, indicating constitutive nuclear expression without apparent stage restriction.

In order to assess the importance of Y13, the Y13-2xFKBP-GFP-2xFKBP^{endo} cell line was transfected with an episomal plasmid mediating expression of the Lyn mislocalizer, permitting conditional inactivation using knock sideways. Representative live-cell microscopy confirmed that Y13-GFP efficiently mislocalized to the parasite plasma

membrane upon rapalog treatment in the majority of parasites, consistent with full knock sideways (Figure 50A-B). Growth curve analysis revealed no significant difference between rapalog-treated (inactivated Y13) and control parasites (Figure 50 C-D). Taken together, these results indicate that Y13 mislocalization does not impair parasite growth under standard *in vitro* conditions, suggesting that Y13 is dispensable for asexual blood-stage development of the parasite.

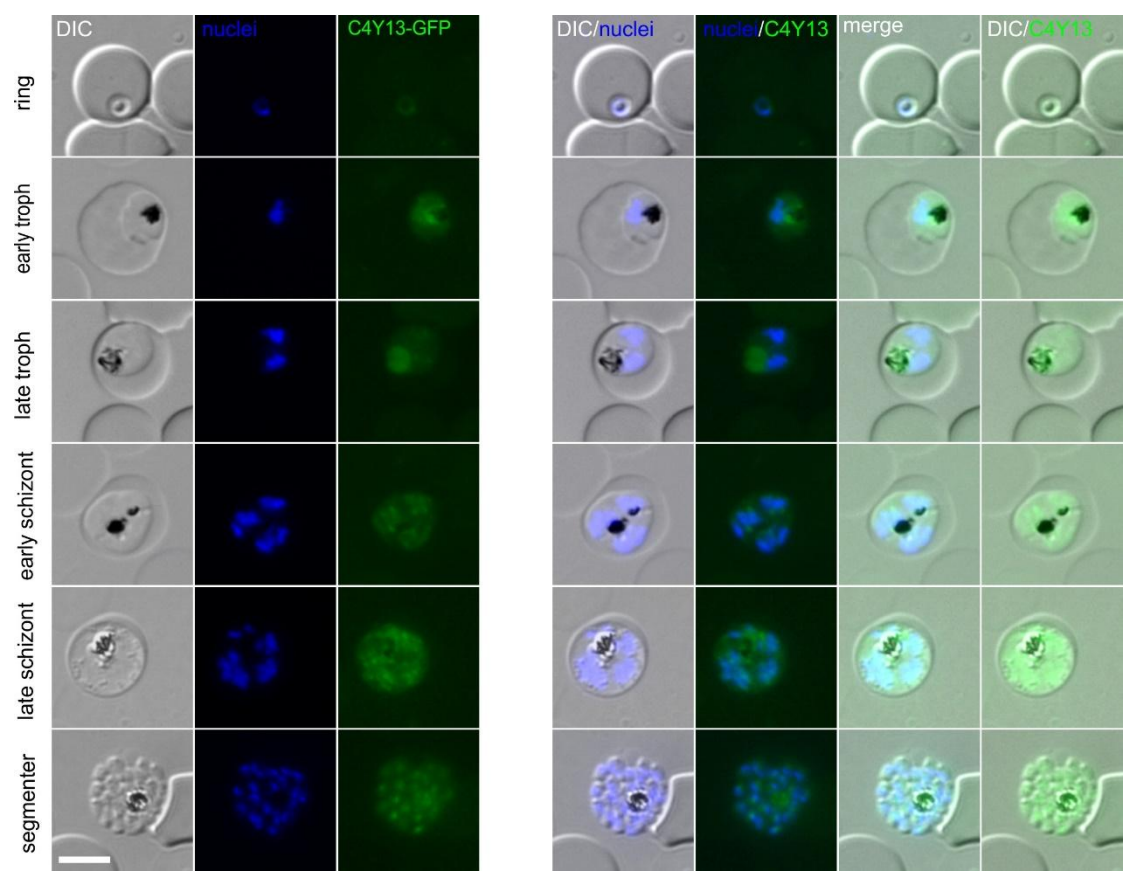


Figure 49. Localization of endogenously tagged candidate Y13 (PF3D7_0407700). Representative live cell fluorescence microscopy images of knock-in cell line Y13-2xFKBP-GFP-2xFKBP ('GFP'). The stages are indicated on the left of the panel. Representative images from 3 independent imaging sessions with at least 7 inspected fields of view. Parasite nuclei were stained with Hoechst33342. Scale bar 5 μ m, DIC, differential interference contrast; merge, overlay of DIC, GFP and nuclei.

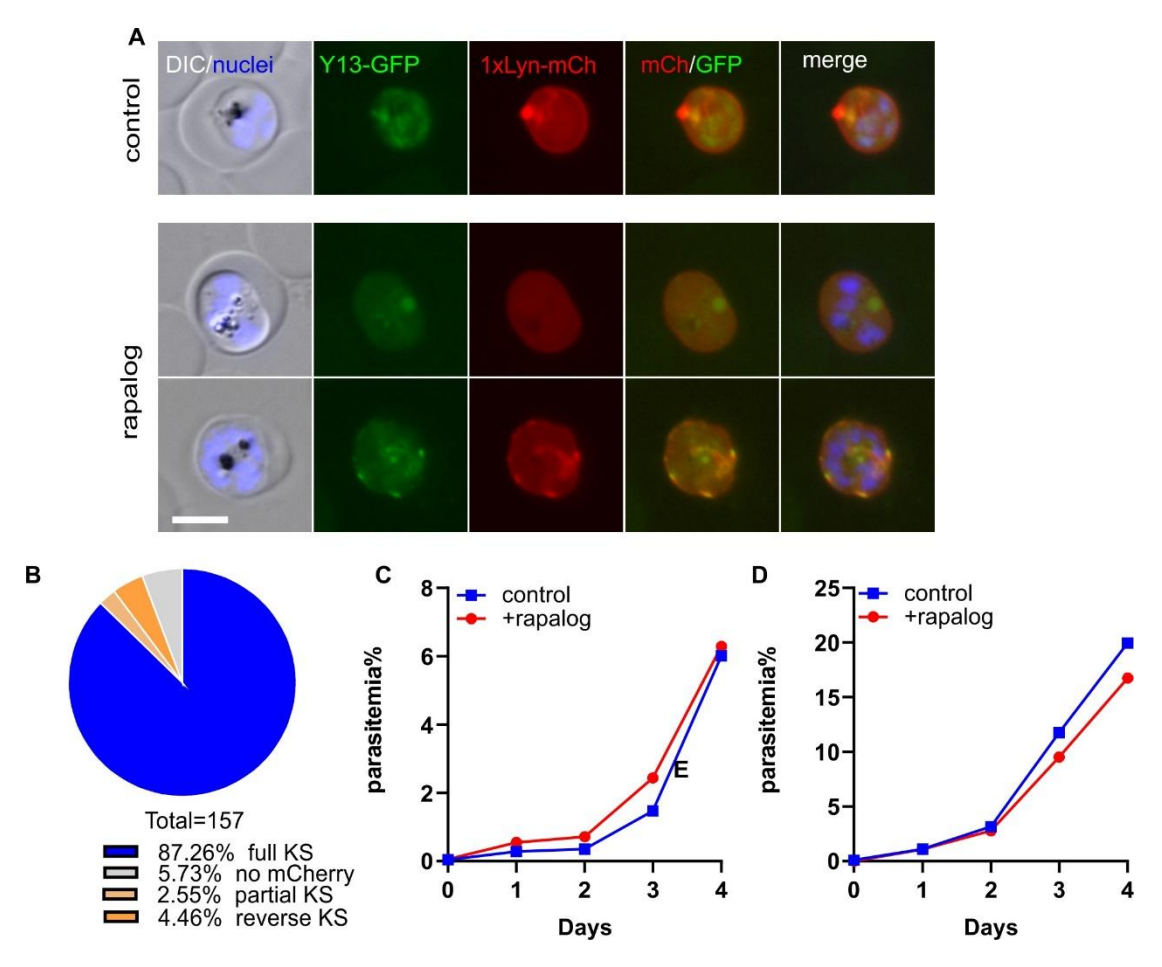


Figure 50. Knock sideways analysis of endogenous Y13 (PF3D7_0407700) tagged with 2xFKBP-GFP-2xFKBP. A) Representative live cell images of knock-in cell line Y13-2xFKBP-GFP-2xFKBP ('GFP') with an episomally expressed Lyn-FRB-mCherry mislocalizer. Representative images from 3 independent imaging sessions with at least 7 inspected fields of view. The top row shows a parasite with full KS (complete GFP mislocalization, "full KS" in (B)), while the bottom row shows a parasite with partial KS (incomplete GFP mislocalization"partial KS" in (B)). The cell culture was split into two dishes: one served as control without rapalog (control), and the other grown in the presence of 250 nM rapalog. The samples for live cell imaging were taken 24 h post addition of rapalog. Scale bar, 5 μm, DIC, differential interference contrast, mCh, mCherry, merge, overlay of GFP, mCh and nuclei. B) Pie chart shows quantification of knock sideways efficiency based on GFP localization following rapalog treatment. Quantification of knock sideways efficiency for Y13, based on the same experiments shown in (A). A total of 157 parasites were scored across 8 independent imaging sessions. KS status was evaluated 24 hours after rapalog addition. C-D) Growth curve of the Y13-Lyn knock sideways. Parasite growth was assessed by flow cytometry in the presence (rapalog) or absence (control) of rapalog. Two independent replicates (both shown).

3.13 Characterization of Y14 (PF3D7_0408000)

Y14 (Gene ID: PF3D7_0408000) is annotated in PlasmoDB as a conserved Plasmodium protein with unknown function. Functional predictions using BLAST, HHpred and MotifScan failed to detect any significant similarity to known proteins.

In order to localize and functionally analyze Y14, the corresponding gene was modified using SLI (Birnbaum et al., 2017) so that the endogenous Y14 becomes fused with the multipurpose sandwich tag (2xFKBP-GFP-2xFKBP). Correct integration into the genome was confirmed by PCR across the 5'- and 3'- integration junctions and by the absence of the original locus (Figure 11). Fluorescence microscopy with the Y14-2xFKBP-GFP-2xFKBP^{endo} parasites showed that this protein may localize to the mitochondrion (Figure 51), because the fluorescence showed a filamentous pattern that is typical of the branched mitochondrial structure in *Plasmodium* parasites. The GFP signal was detectable in late schizont and segmenter stages, showing stage-restricted expression. To verify the hypothesis that Y14 is a mitochondrial protein, we performed co-localization with MitoTracker, which confirmed that the GFP signal from Y14 overlapped with the mitochondrion (Figure 52).

In order to assess the importance of Y14, the Y14-2xFKBP-GFP-2xFKBP^{endo} cell line was transfected with an episomal plasmid mediating expression of the NLS mislocalizer, to attempt conditional inactivation via the knock sideways system. Upon rapalog treatment, fluorescence microscopy revealed that the mitochondrial localization of Y14-GFP remained unchanged (Figure 53), indicating that the mislocalization system was ineffective in pulling Y14 from the mitochondrion to nucleus. As a result, the functional essentiality of Y14 could not be assessed using the

knock sideways approach, and alternative strategies such as conditional knockouts will be required for further investigation.

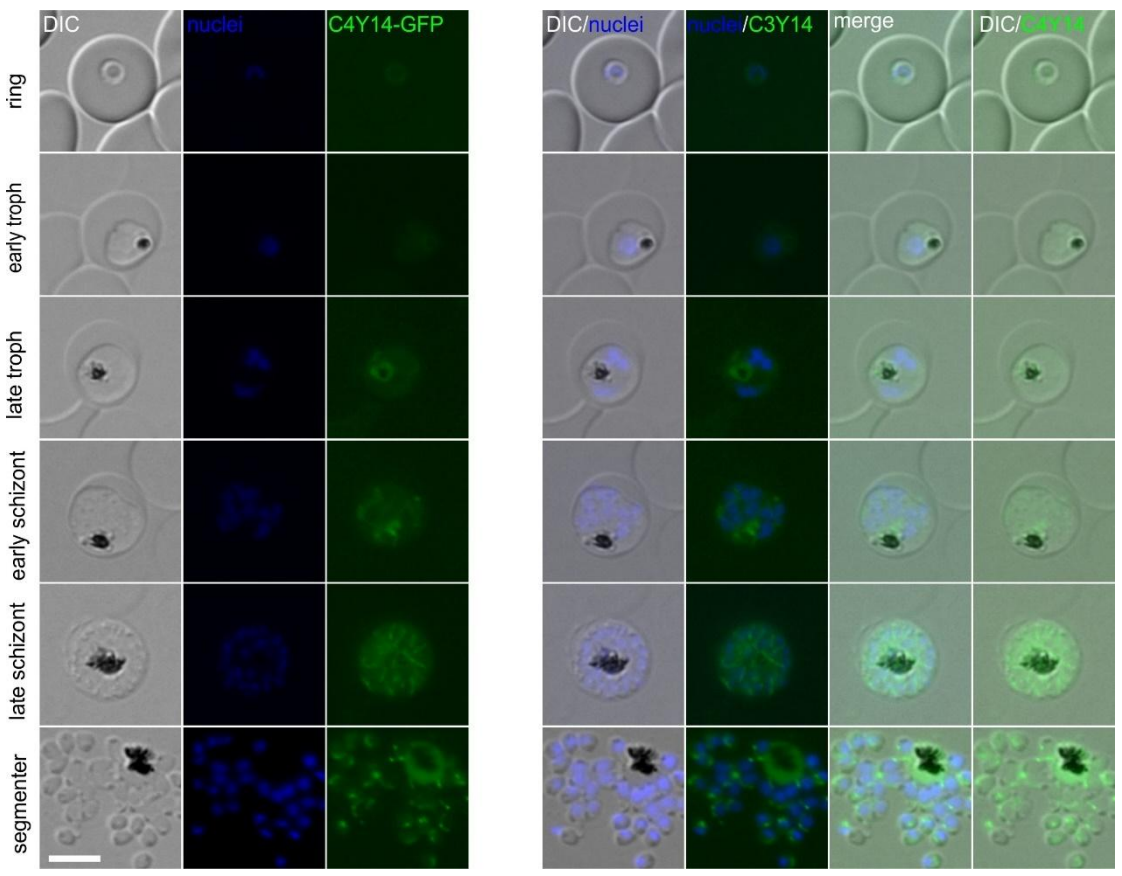


Figure 51. Localization of endogenously tagged candidate Y14 (PF3D7_0408000). Representative live cell fluorescence microscopy images of knock-in cell line Y14-2xFKBP-GFP-2xFKBP ('GFP'). The stages are indicated on the left of the panel. Representative images from 3 independent imaging sessions with at least 7 inspected fields of view. Parasite nuclei were stained with Hoechst33342. Scale bar 5 μ m, DIC, differential interference contrast; merge, overlay of DIC, GFP and nuclei.

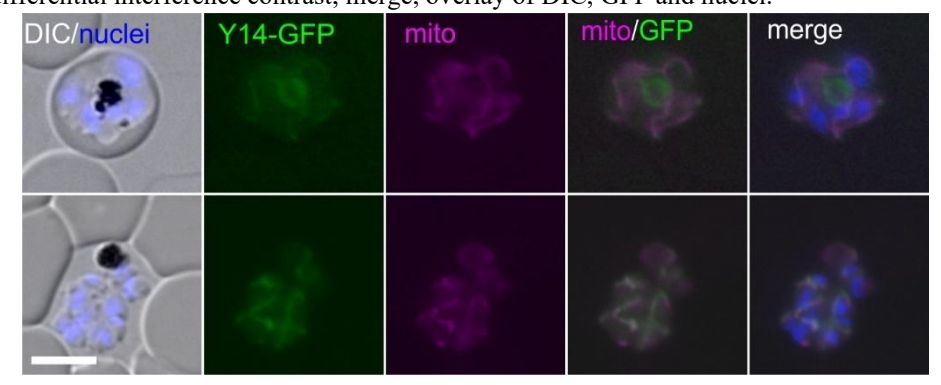


Figure 52. Fluorescence microscopy images of endogenously tagged Y14 (PF3D7_0408000) stained with MitoTrackerTM Red CMXRos. Representative images of fixed parasites expressing GFP-tagged Y14 (green), counterstained with Mitotracker (red). Representative images from 3 independent imaging sessions with at least 7 inspected fields of view. Parasite nuclei were stained with Hoechst33342. Scale bar 5 μm, DIC, differential interference contrast; merge, overlay of mito, GFP and nuclei.

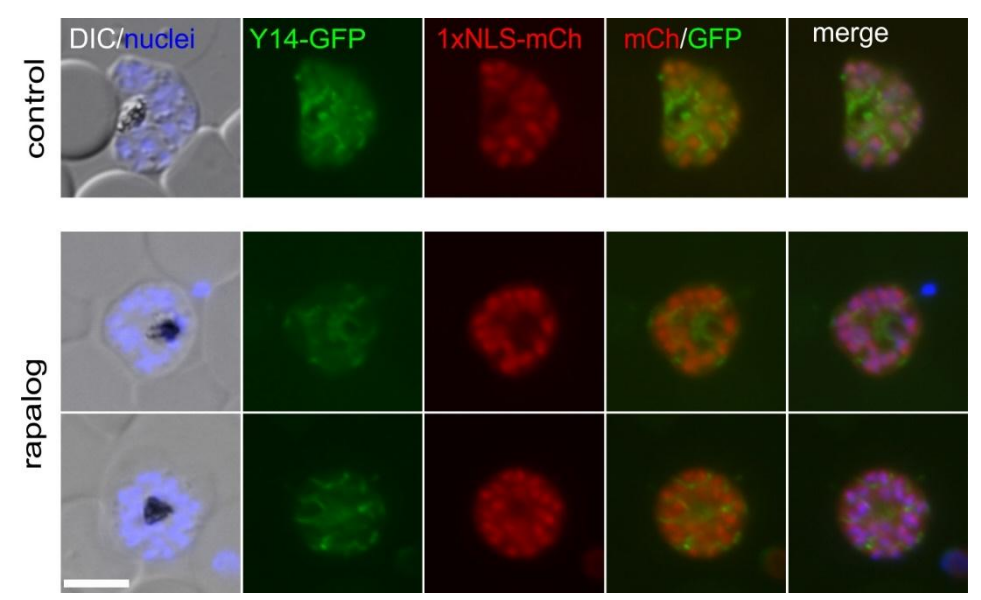


Figure 53. Knock sideways endogenously tagged Y14 (PF3D7_0408000). Representative live cell images of knock-in cell line Y14-2xFKBP-GFP-2xFKBP ('GFP') with an episomally expressed NLS-FRB-mCherry mislocalizer. The cell culture was split into two dishes: one served as control without rapalog (control), and the other grown in the presence of 250 nM rapalog (rapalog). The samples for live cell imaging were taken 24 h post addition of rapalog. Representative images from 3 independent imaging sessions with at least 7 inspected fields of view. Parasite nuclei were stained with Hoechst33342. Scale bar, 5 μ m, DIC, differential interference contrast, mCh, mCherry, merge, overlay of GFP, mCh and nuclei.

3.14 Characterization of Y15 (PF3D7_0408100)

Y15 (Gene ID: PF3D7_0408100) is annotated in PlasmoDB as a conserved Plasmodium protein with unknown function. Functional predictions using BLAST, HHPred, and MotifScan did not identify any significant similarity to known proteins or domains, indicating that Y15 may be a *Plasmodium*-specific protein with no characterized orthologs.

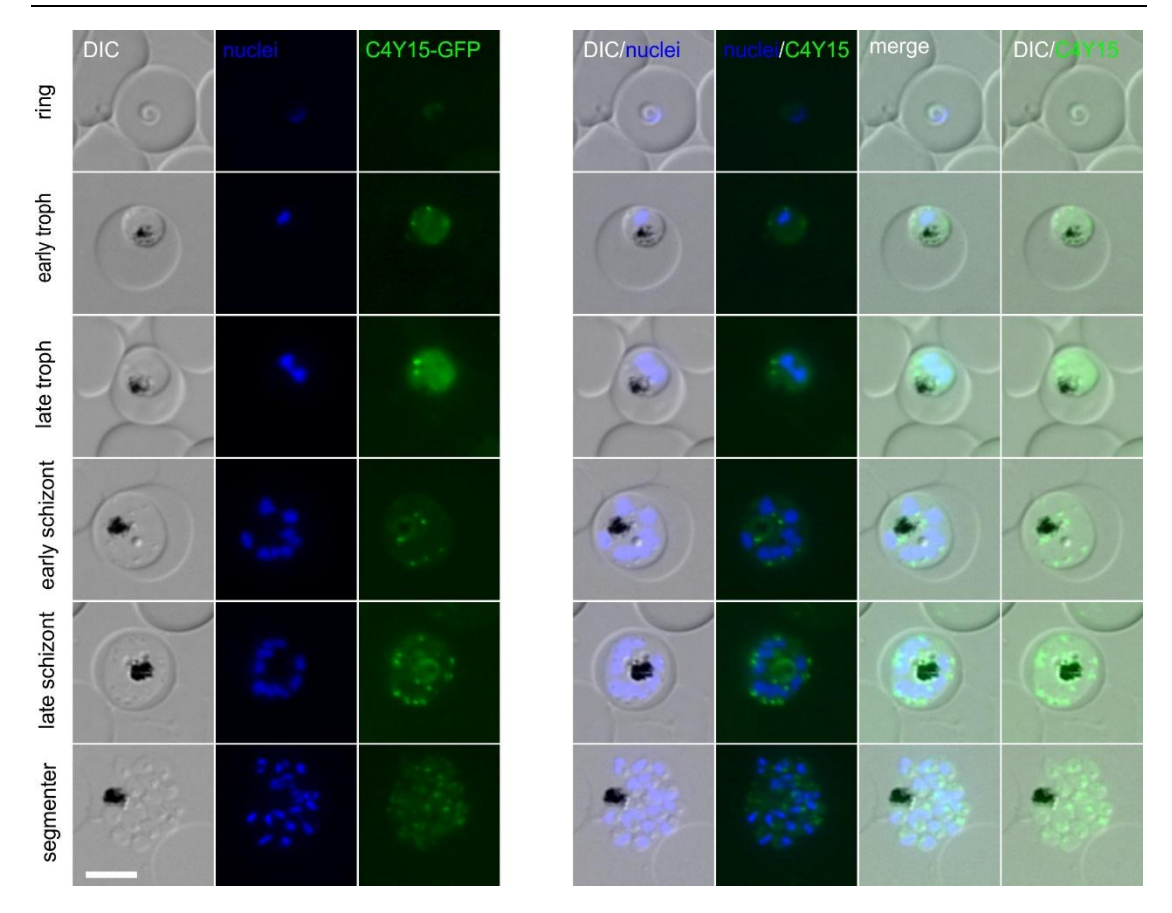


Figure 54. Localization of endogenously tagged candidate Y15 (PF3D7_0408100). Representative live cell fluorescence microscopy images of knock-in cell line Y15-2xFKBP-GFP-2xFKBP ('GFP'). The stages are indicated on the left of the panel. Representative images from 3 independent imaging sessions with at least 7 inspected fields of view. Parasite nuclei were stained with Hoechst33342. Scale bar 5 μ m, DIC, differential interference contrast; merge, overlay of DIC, GFP and nuclei.

In order to localize and functionally analyze Y15, the corresponding gene was modified using SLI (Birnbaum et al., 2017) so that the endogenous Y15 becomes fused with the multipurpose sandwich tag (2xFKBP-GFP-2xFKBP). Correct integration into the genome was confirmed by PCR across the 5'- and 3'- integration junctions and by the absence of the original locus (Figure 11). Fluorescence microscopy with the Y15-2xFKBP-GFP-2xFKBP^{endo} parasites showed that this protein localizes to the cytoplasm, with a punctate signal with some enrichment adjacent to the nucleus (Figure 54). This localization pattern raised the possibility of organellar association.

In order to assess the importance of Y15, the Y15-2xFKBP-GFP-2xFKBP^{endo} cell line was transfected with episomal plasmids mediating expression of either Lyn (Figure 55A) or NLS (Figure 56A) mislocalizers, with the aim of achieving conditional inactivation using knock sideways. Upon rapalog treatment, the Lyn-based system failed to mislocalize Y15 efficiently and quantification of 105 cells revealed that the majority of cells (92.38%) exhibiting a reverse KS phenotype—characterized by unexpected accumulation of GFP signal to the physiological site of Y15 (Figure 55B). In contrast, the NLS-based KS approach yielded efficient mislocalization. Among 118 parasites scored 24 hours post-rapalog induction, 92.37% exhibited full mislocalization of Y15-GFP to the nucleus, with only a small fraction showing partial KS (2.54%), reverse KS (0.85%), or no response (4.24%) (Figure 56B). The growth curve of the Y15-Lyn line remained comparable to the untreated control throughout the assay, which was expected given that the mislocalization was ineffective (Figure 55C-E). However, also the Y15-NLS line, upon rapalog-treatment, showed only a very moderate growth reduction of approximately 20% compared to the control. These results indicate that Y15 is dispensable for asexual blood-stage development under standard *in vitro* culture conditions (Figure 56C-E).

Next, we performed co-localization experiments with the Golgi marker GRASP to further investigate the subcellular localization of Y15. Co-localization experiments with GRASP-mCherry confirmed that the GFP signal from Y15 overlapped with the Golgi, indicating that Y15 is a Golgi-associated protein (Figure 57).

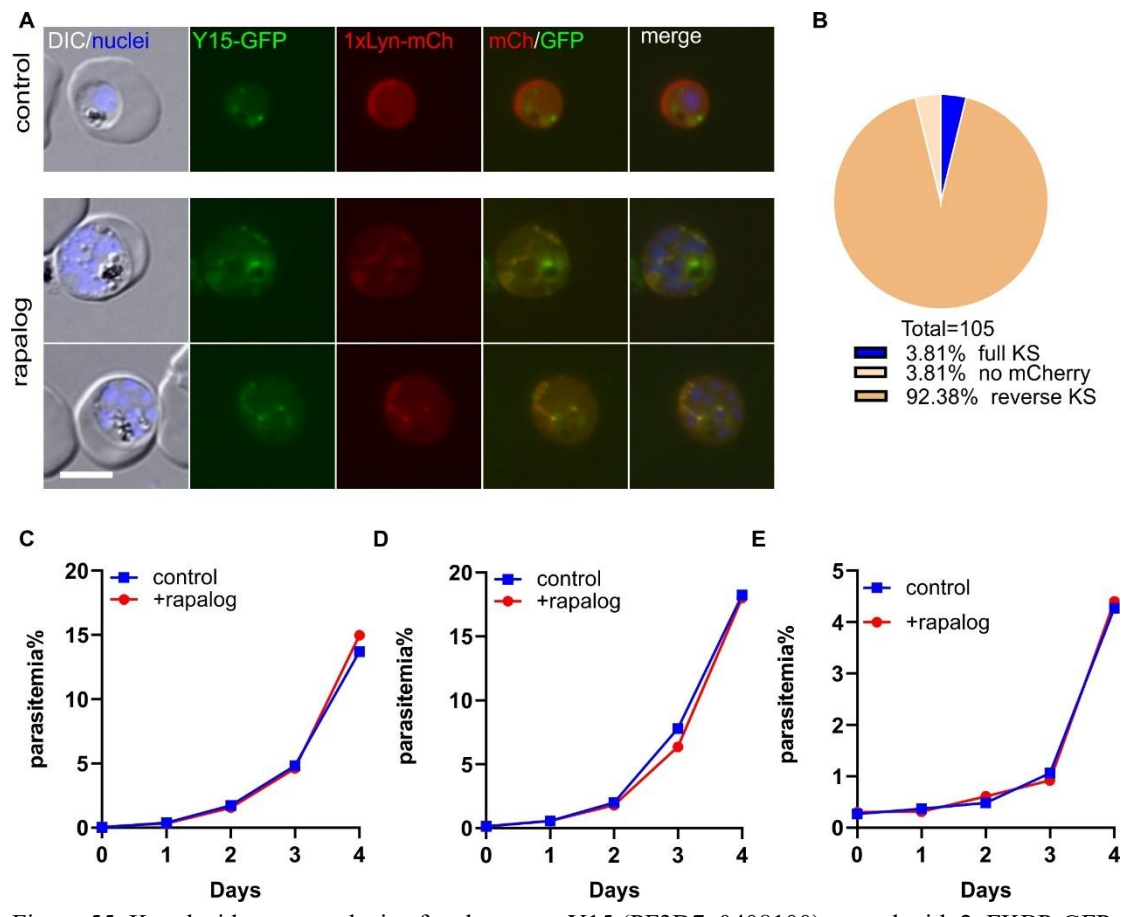


Figure 55. Knock sideways analysis of endogenous Y15 (PF3D7_0408100) tagged with 2xFKBP-GFP-2xFKBP. A) Representative live cell images of knock-in cell line Y15-2xFKBP-GFP-2xFKBP ('GFP') with an episomally expressed Lyn-FRB-mCherry mislocalizer. Representative images from 3 independent imaging sessions with at least 7 inspected fields of view. Both rows with rapalog show a parasite with full KS (mCh was recruited to the location of the GFP rather than causing its mislocalization "reverse KS" in (B)). The cell culture was split into two dishes: one served as control without rapalog (control), and the other grown in the presence of 250 nM rapalog. The samples for live cell imaging were taken 24 h post addition of rapalog. Scale bar, 5 μm, DIC, differential interference contrast, mCh, mCherry, merge, overlay of GFP, mCh and nuclei. B) Pie chart shows quantification of knock sideways efficiency based on GFP localization following rapalog treatment. Quantification of knock sideways efficiency for Y15, based on the same experiments shown in (A). C-E) A total of 105 parasites were scored across 4 independent imaging sessions. KS status was evaluated 24 hours after rapalog addition. Growth curve of the Y15-Lyn knock sideways. Parasite growth was assessed by flow cytometry in the presence (rapalog) or absence (control) of rapalog. Two independent replicates (both shown).

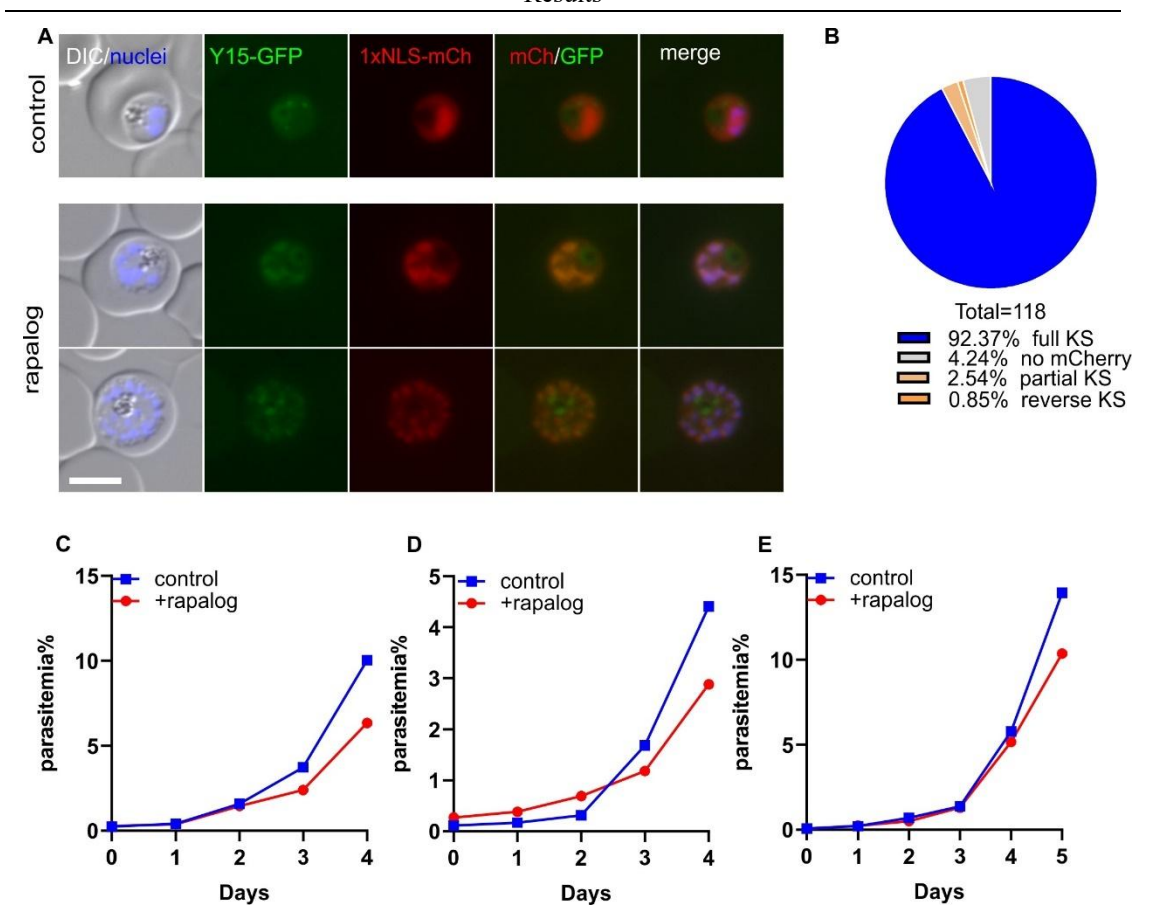


Figure 56. Knock sideways analysis of endogenous Y15 (PF3D7_0408100) tagged with 2xFKBP-GFP-2xFKBP. A) Representative live cell images of knock-in cell line Y15-2xFKBP-GFP-2xFKBP ('GFP') with an episomally expressed NLS-FRB-mCherry mislocalizer. Representative images from 3 independent imaging sessions with at least 7 inspected fields of view. Both rows with rapalog show a parasite with full KS (complete GFP mislocalization, "full KS" in (B)). The cell culture was split into two dishes: one served as control without rapalog (control), and the other grown in the presence of 250 nM rapalog. The samples for live cell imaging were taken 24 h post addition of rapalog. Scale bar, 5 μm, DIC, differential interference contrast, mCh, mCherry, merge, overlay of GFP, mCh and nuclei. B) Pie chart shows quantification of knock sideways efficiency based on GFP localization following rapalog treatment. Quantification of knock sideways efficiency for Y15, based on the same experiments shown in (A). A total of 118 parasites were scored across 5 independent imaging sessions. KS status was evaluated 24 hours after rapalog addition. C-E) Growth curve of the Y15-NLS knock sideways. CParasite growth was assessed by flow cytometry in the presence (rapalog) or absence (control) of rapalog. Three independent replicates (all shown).

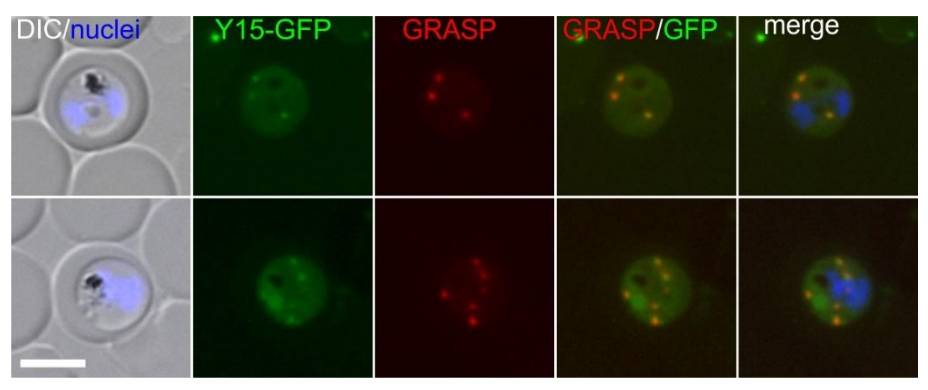


Figure 57. Y15 (PF3D7_0408100) co-localization with GRASP. Representative live cell images of knock-in cell line of Y15-2xFKBP-GFP-2xFKBP (green) with episomally expressed GRASP-mCherry (red). The cell culture was split into two dishes: one served as control without rapalog (control), and the other grown in the presence of 250 nM rapalog (rapalog). The samples for live cell imaging were taken 24 h post addition of rapalog. Representative images from 3 independent imaging sessions with at least 7 inspected fields of view. Parasite nuclei were stained with Hoechst33342. Scale bar 5 μm, DIC, differential interference contrast; merge, overlay of GRASP, GFP and nuclei.

3.15 Characterization of Y17 (PF3D7_0408300)

Y17 (Gene ID: PF3D7_0408300) is annotated as zinc finger Ran-binding domain-containing protein 2, putative. HHPred analysis revealed a high-confidence structural similarity (probability: 98.3%; E-value: 1e-6; cover: 75/344 aa) to a zinc finger Ran-binding domain-containing protein from *Dictyostelium discoideum*. Additional matches included RanBP2-type nuclear pore complex proteins, such as Nup153, further supporting the idea that Y17 may be involved in nuclear transport or RNA trafficking through the nuclear pore complex. Consistent with these predictions,

BLAST searches identified close homologs across multiple *Plasmodium* species, several of which are annotated as zinc finger, RAN-binding proteins.

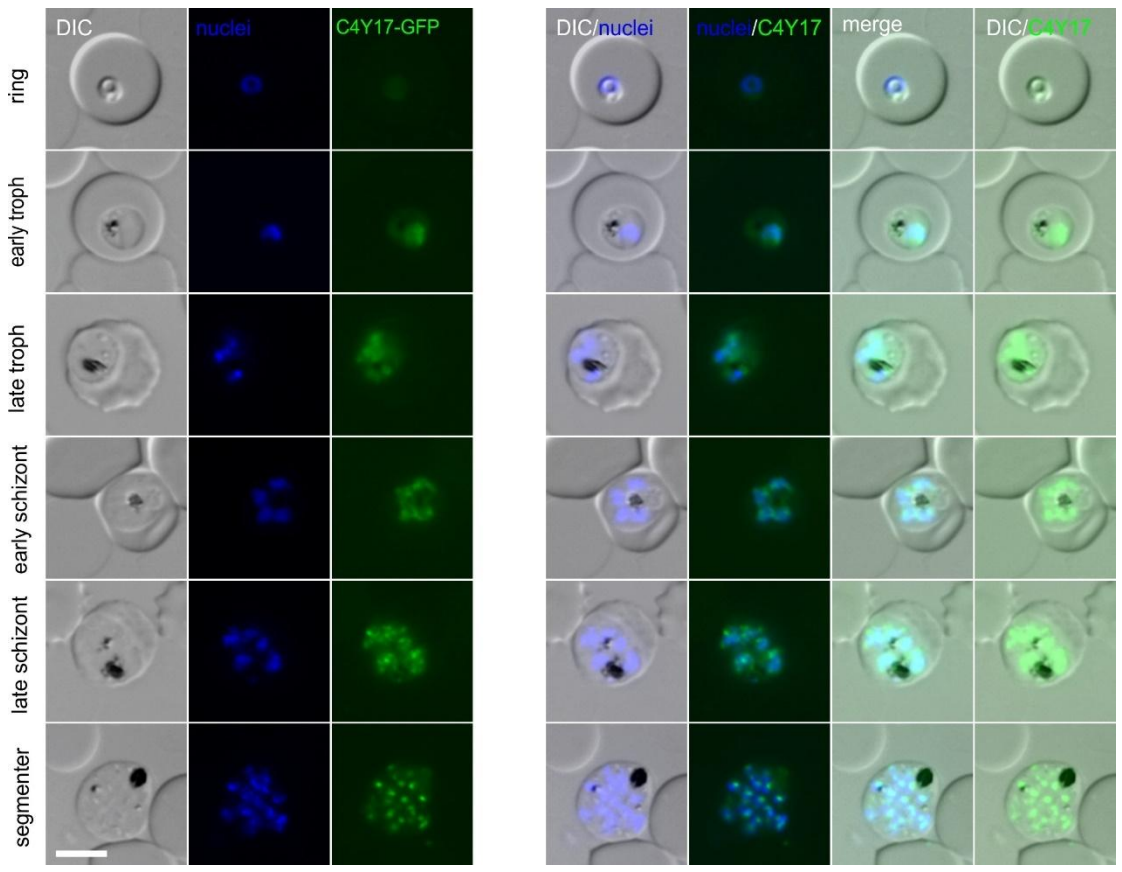


Figure 58. Localization of endogenously tagged candidate Y17 (PF3D7_0408300). Representative live cell fluorescence microscopy images of knock-in cell line Y17-2xFKBP-GFP-2xFKBP ('GFP'). The stages are indicated on the left of the panel. Representative images from 3 independent imaging sessions with at least 7 inspected fields of view. Parasite nuclei were stained with Hoechst33342. Scale bar 5 μ m, DIC, differential interference contrast; merge, overlay of DIC, GFP and nuclei.

In order to localize and functionally analyze Y17, the corresponding gene was modified using SLI (Birnbaum et al., 2017) so that the endogenous Y17 becomes fused with the multipurpose sandwich tag (2xFKBP-GFP-2xFKBP). Correct integration into the genome was confirmed by PCR across the 5'- and 3'- integration junctions and by the absence of the original locus (Figure 11). Fluorescence microscopy with the Y17-2xFKBP-GFP-2xFKBP^{endo} parasites revealed that the protein localizes to the nucleus, displaying a nuclear signal throughout the asexual blood-stage cycle (Figure 58).

Expression was detected in rings, trophozoites, and schizonts, suggesting constitutive nuclear localization across developmental stages.

In order to assess the importance of Y17, the Y17-2xFKBP-GFP-2xFKBP^{endo} cell line was transfected with an episomal plasmid expressing the Lyn mislocalizer, permitting conditional inactivation using the knock sideways system. Upon rapalog treatment, fluorescence microscopy showed only 1.95% showed full KS efficiency, and the majority (85.71%) exhibited mixed mislocalization patterns (Figure 59A-B). Growth curve analysis showed only a small reduction in the parasitemia of the rapalog-treated parasites compared to the control parasites (Figure 59C-E).

Taken together, these results indicate that Y17 may be a RAN-binding zinc finger protein that is almost fully dispensable during asexual blood-stage development, at least under *in vitro* conditions.

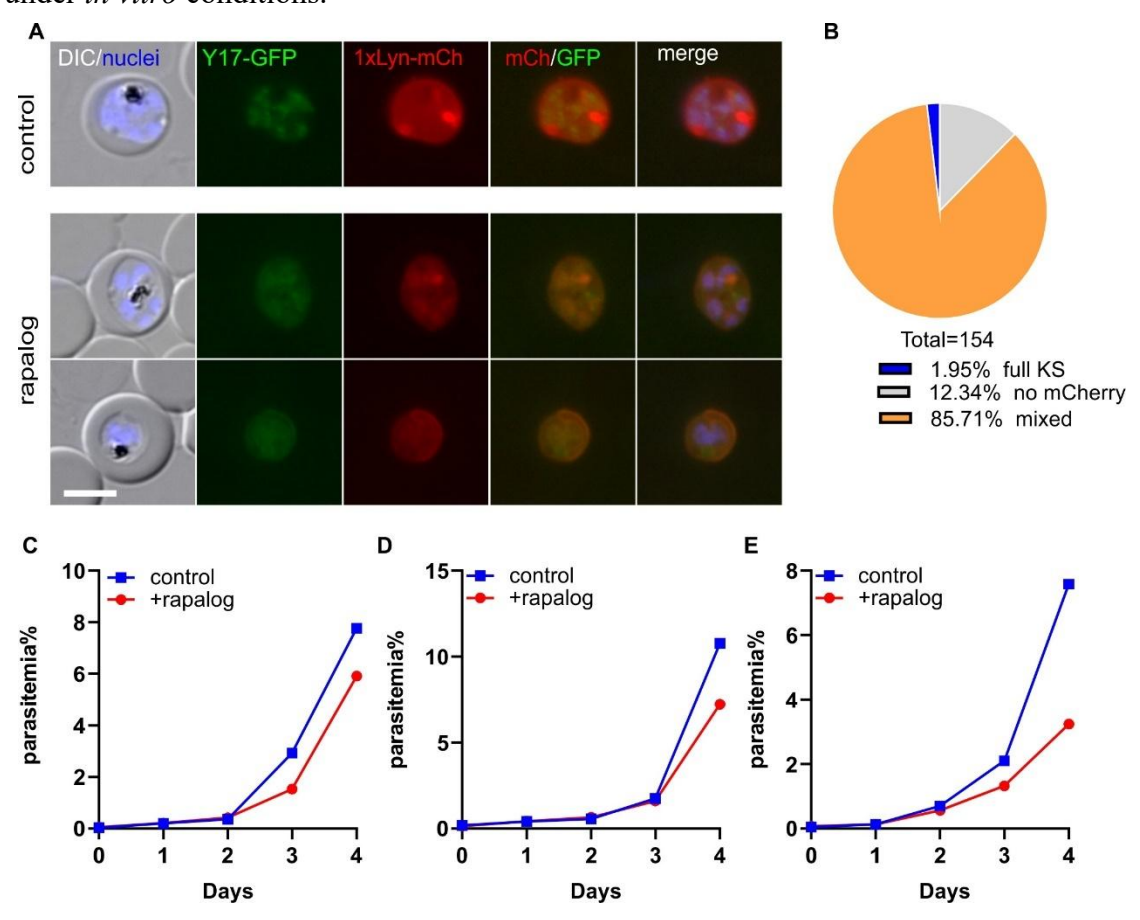


Figure 59. Knock sideways analysis of endogenous Y17 (PF3D7_0408300) tagged with 2xFKBP-GFP-2xFKBP. A) Representative live cell images of knock-in cell line Y17-2xFKBP-GFP-2xFKBP ('GFP') with an episomally expressed Lyn-FRB-mCherry mislocalizer. Representative images from 3 independent imaging sessions with at least 7 inspected fields of view. Both two rows show a parasite with mixed KS (incomplete and reverse GFP mislocalization. "mixed KS" in (B)). The cell culture was split into two dishes: one served as control without rapalog (control), and the other grown in the presence of 250 nM rapalog. The samples for live cell imaging were taken 24 h post addition of rapalog. Scale bar, 5 μm, DIC, differential interference contrast, mCh, mCherry, merge, overlay of GFP, mCh and nuclei. B) Pie chart shows quantification of knock sideways efficiency based on GFP localization following rapalog treatment. Quantification of knock sideways efficiency for Y17, based on the same experiments shown in (A). A total of 154 parasites were scored across 3 independent imaging sessions. KS status was evaluated 24 hours after rapalog addition. C-E) Growth curve of the Y17-Lyn knock sideways. Parasite growth was assessed by flow cytometry in the presence (rapalog) or absence (control) of rapalog. Three independent replicates (all shown).

3.16 Characterization of Y18 (PF3D7_0408400)

Y18 (Gene ID: PF3D7_0408400) is annotated in PlasmoDB as a conserved Plasmodium protein of unknown function. Similarity searches using BLAST and MotifScan did not yield any significant hits outside of the *Plasmodium* genus. However, HHPred analysis revealed a high-confidence match (probability: 100%, E-value: 2.1e–88) to a mitochondrial ribosomal protein mS145 from *T. gondii*.

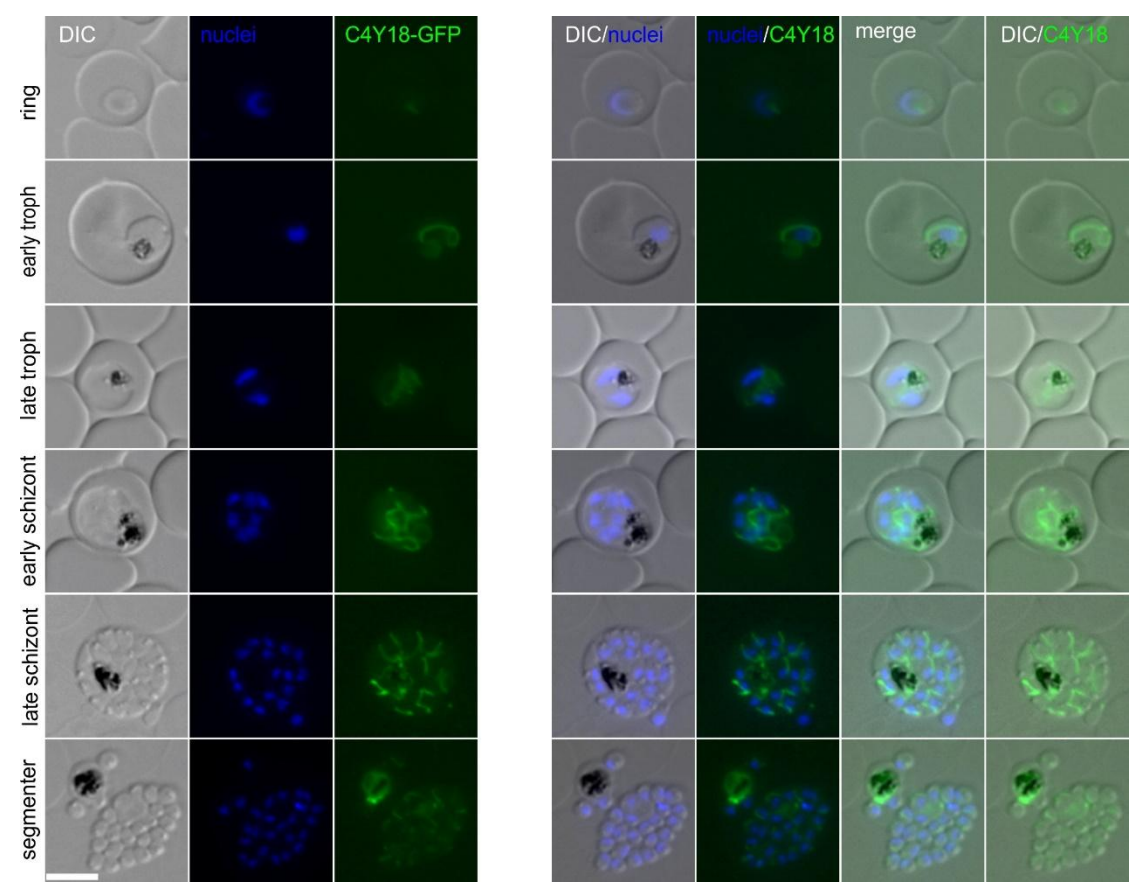


Figure 60. Localization of endogenously tagged candidate Y18 (PF3D7_0408400). Representative live cell fluorescence microscopy images of knock-in cell line Y18-2xFKBP-GFP-2xFKBP ('GFP'). The stages are indicated on the left of the panel. Representative images from 3 independent imaging sessions with at least 7 inspected fields of view. Parasite nuclei were stained with Hoechst33342. Scale bar 5 μ m, DIC, differential interference contrast; merge, overlay of DIC, GFP and nuclei.

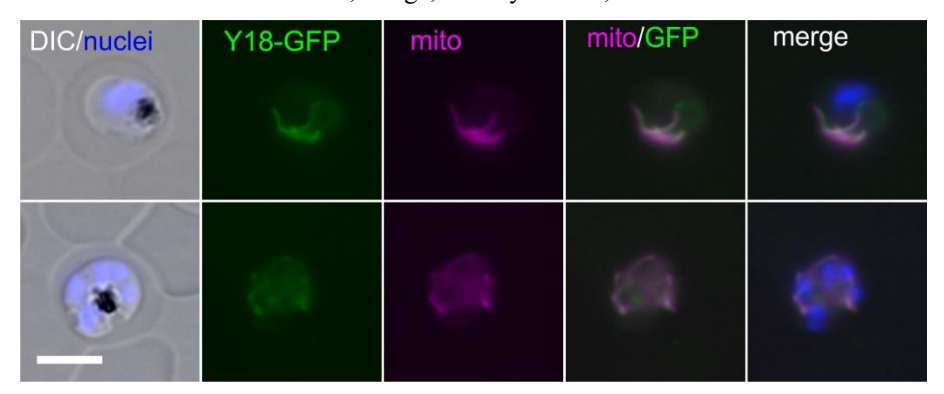


Figure 61. Fluorescence microscopy images of endogenously tagged Y18 (PF3D7_0408400) stained with MitoTrackerTM Red CMXRos. Representative images of fixed parasites expressing GFP-tagged Y18 (green), counterstained with Mitotracker (purple). Representative images from 3 independent imaging sessions with at least 7 inspected fields of view. Parasite nuclei were stained with Hoechst33342. Scale bar 5 µm, DIC, differential interference contrast; merge, overlay of mito, GFP and nuclei.

In order to localize and functionally analyze Y18, the corresponding gene was modified using SLI (Birnbaum et al., 2017) so that the endogenous Y18 becomes fused with the multipurpose sandwich tag (2xFKBP-GFP-2xFKBP). Correct integration into the genome was confirmed by PCR across the 5' and 3'-integration junctions and PCR showing absence of the original locus (Figure 11). Fluorescence microscopy with the Y18-2xFKBP-GFP-2xFKBP^{endo} parasites showed that this protein likely localizes to the mitochondrion (Figure 60), displaying a filamentous and branched pattern typical of the parasite's mitochondrium. Co-localization experiments with MitoTracker confirmed that the GFP signal overlapped with the mitochondrion (Figure 61). Expression was observed across all asexual stages, indicating constitutive presence in the mitochondrion.

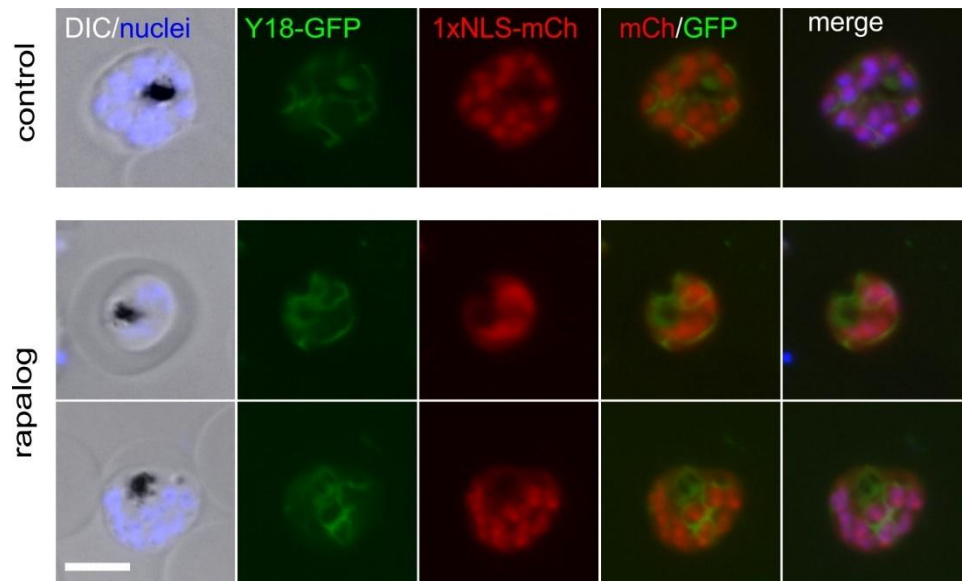


Figure 62. Knock sideways endogenously tagged Y18 (PF3D7_0408400). Representative live cell images of knock-in cell line Y18-2xFKBP-GFP-2xFKBP ('GFP') with an episomally expressed NLS-FRB-mCherry mislocalizer. The cell culture was split into two dishes: one served as control without rapalog (control), and the other grown in the presence of 250 nM rapalog (rapalog). The samples for live cell imaging were taken 24 h post addition of rapalog. Representative images from 3 independent imaging sessions with at least 7 inspected fields of view. Parasite nuclei were stained with Hoechst33342. Scale bar, 5 μm, DIC, differential interference contrast, mCh, mCherry, merge, overlay of GFP, mCh and nuclei.

In order to assess the importance of Y18, the Y18-2xFKBP-GFP-2xFKBP^{endo} cell line was transfected with an episomal plasmid expressing the NLS mislocalizer, to attempt conditional inactivation via the knock sideways system. Upon rapalog treatment, however, fluorescence microscopy revealed no detectable change in localization, and the mitochondrial GFP signal remained intact (Figure 62), indicating that mislocalization was unsuccessful. Consequently, the essentiality of Y18 could not be assessed using this method, and alternative approaches such as DiCre-mediated knockout will be required in future studies.

3.17 Characterization of Y20 (PF3D7 0410500)

Y20 (Gene ID: PF3D7_0410500) is annotated as a conserved Plasmodium protein with unknown function. BLAST, HHpred and MotifScan analyses failed to detect any meaningful domains or conserved features.

In order to localize and functionally analyze Y20, the corresponding gene was modified using SLI (Birnbaum et al., 2017) so that the endogenous Y20 becomes fused with the multipurpose sandwich tag (2xFKBP-GFP-2xFKBP). Correct integration into the genome was confirmed by PCR across the 5'- and 3'- integration junctions and by a PCR showing the absence of the original locus (Figure 11). Fluorescence microscopy with the Y20-2xFKBP-GFP-2xFKBP^{endo} parasites revealed accumulations of signal without clear organellar association (Figure 63). The GFP signal was detectable in the schizont and segmenter stage.

In order to assess the importance of Y20, the Y20-2xFKBP-GFP-2xFKBP^{endo} cell line was transfected with an episomal plasmid expressing the NLS mislocalizer, enabling conditional inactivation via the knock sideways system. Fluorescence microscopy revealed that, upon rapalog treatment, Y20-GFP was efficiently mislocalized to the

nucleus in the majority of parasites, indicating successful knock sideways (Figure 64A-B).

Growth curve analysis revealed no clearly difference in parasite proliferation between rapalog-treated and control groups (Figure 64C-D). These findings suggest that Y20 is dispensable for asexual blood-stage development under standard *in vitro* conditions.

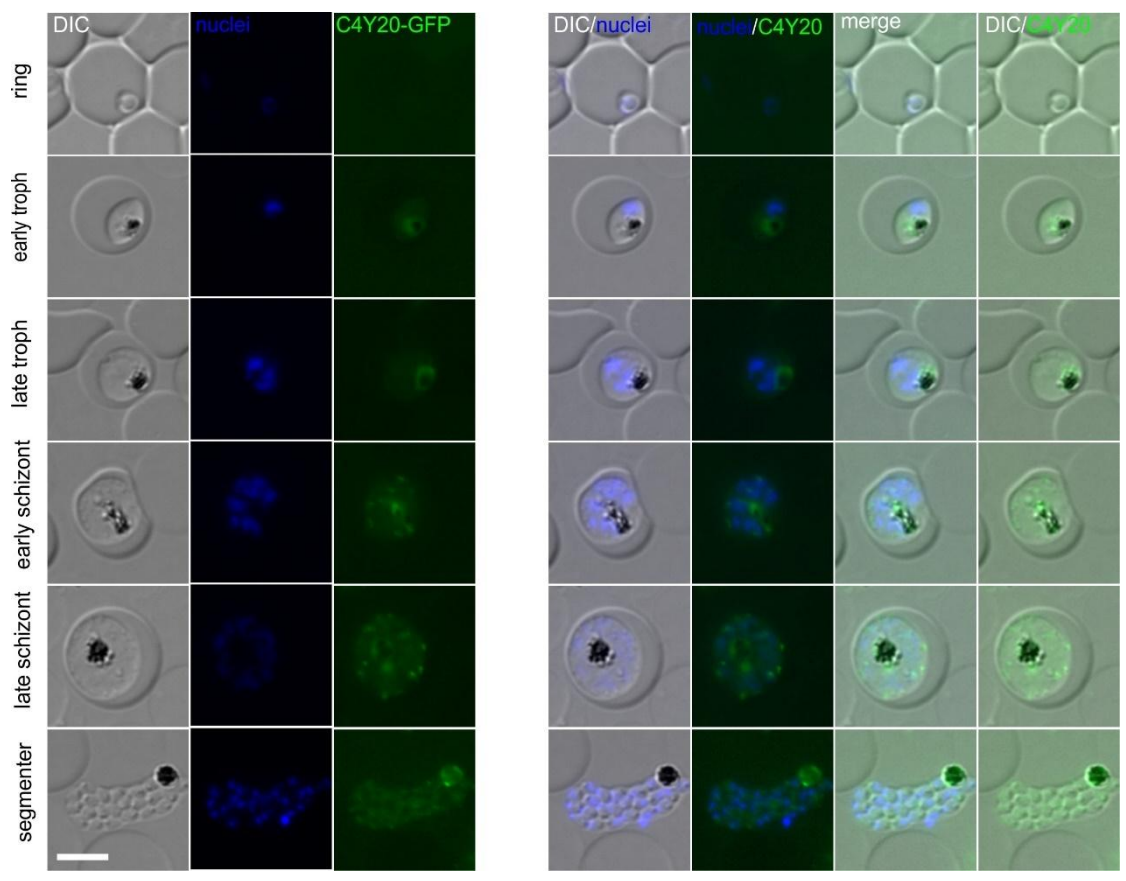


Figure 63. Localization of endogenously tagged candidate Y20 (PF3D7_0410500). Representative live cell fluorescence microscopy images of knock-in cell line Y20-2xFKBP-GFP-2xFKBP ('GFP'). The stages are indicated on the left of the panel. Representative images from 3 independent imaging sessions with at least 7 inspected fields of view. Parasite nuclei were stained with Hoechst33342. Scale bar 5 μ m, DIC, differential interference contrast; merge, overlay of DIC, GFP and nuclei.

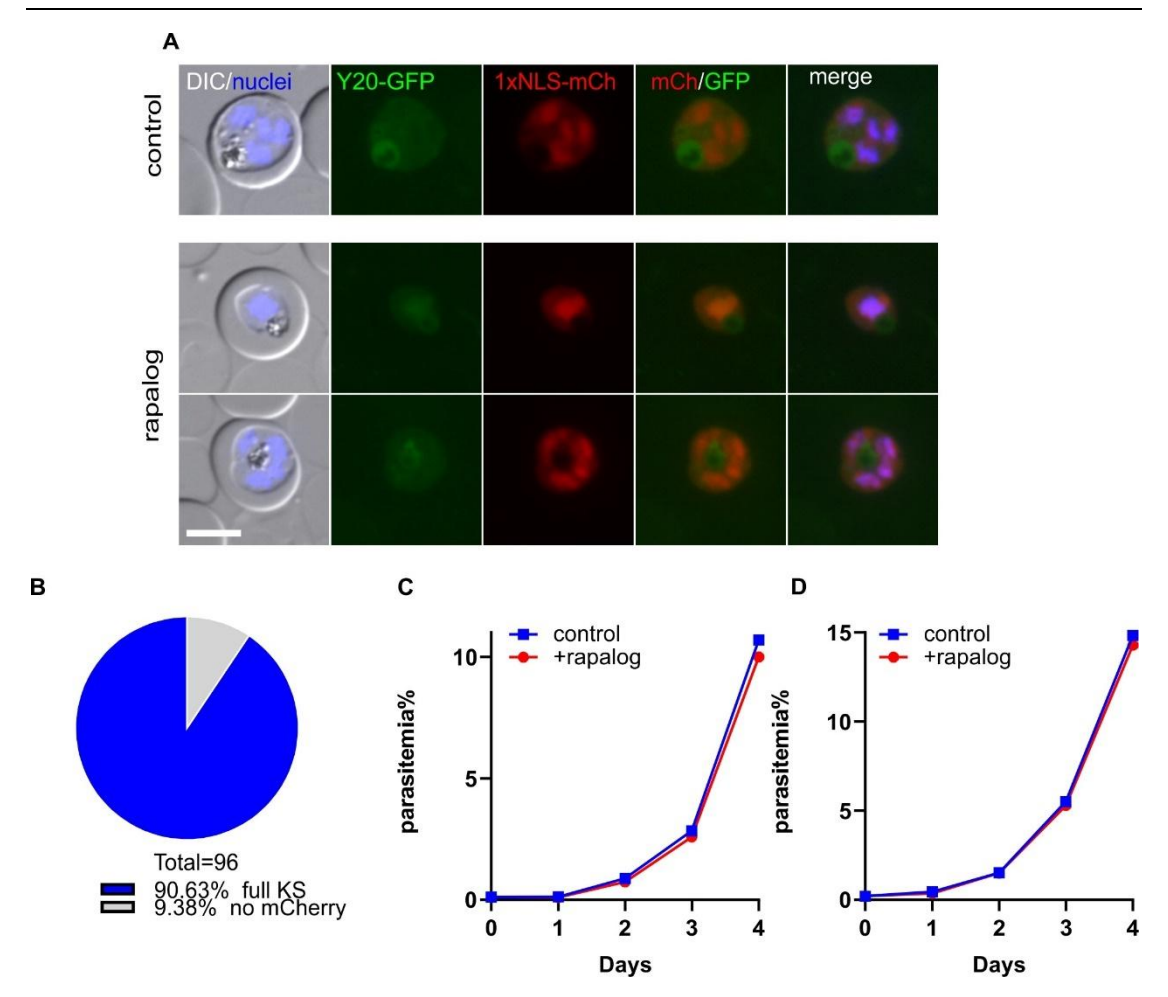


Figure 64. Knock sideways analysis of endogenous Y20 (PF3D7_0410500) tagged with 2xFKBP-GFP-2xFKBP. A) Representative live cell images of knock-in cell line Y20-2xFKBP-GFP-2xFKBP ('GFP') with an episomally expressed NLS-FRB-mCherry mislocalizer. Representative images from 3 independent imaging sessions with at least 7 inspected fields of view. Both two rows show a parasite with full KS (complete GFP mislocalization, "full KS" in (B)). The cell culture was split into two dishes: one served as control without rapalog (control), and the other grown in the presence of 250 nM rapalog. The samples for live cell imaging were taken 24 h post addition of rapalog. Scale bar, 5 μm, DIC, differential interference contrast, mCh, mCherry, merge, overlay of GFP, mCh and nuclei. B) Pie chart shows quantification of knock sideways efficiency based on GFP localization following rapalog treatment. Quantification of knock sideways efficiency for Y20, based on the same experiments shown in (A). A total of 118 parasites were scored across 5 independent imaging sessions. KS status was evaluated 24 hours after rapalog addition. C-D) Growth curve of the Y20-NLS knock sideways. Parasite growth was assessed by flow cytometry in the presence (rapalog) or absence (control) of rapalog. Three independent replicates (all shown).

3.18 Characterization of Y21 (PF3D7 0410800)

Y21 (Gene ID: PF3D7_0410800) is annotated in PlasmoDB as a putative apicomplexan kinetochore protein 3 (AKiT3). AKiT3 belongs to a group of recently described Apicomplexan-specific kinetochore proteins that are distinct from the canonical eukaryotic kinetochore components found in yeast and mammals that have been annotated after this work has started (Brousini et al., 2022). In *Toxoplasma gondii*, AKiT3 has been shown to associate with the mitotic spindle and centromeres, functioning as part of a divergent kinetochore complex that coordinates chromosome segregation during closed mitosis (Farrell and Gubbels, 2014). However, little is known about its function in *Plasmodium falciparum*.

In order to localize and functionally analyze Y21, the corresponding gene was modified using SLI (Birnbaum et al., 2017) so that the endogenous Y21 becomes fused with the multipurpose sandwich tag (2xFKBP-GFP-2xFKBP). Correct integration into the genome was confirmed by PCR across the 5'- and 3'- integration junctions and the absence of a PCR product for the original locus (Figure 11). Fluorescence microscopy with the Y21-2xFKBP-GFP-2xFKBP^{endo} parasites revealed that this protein localizes to the nucleus, showing a single focus per nucleus, often on the border of the Hoechst signal facing the parasite plasma membrane (Figure 65), typical for kinetochore proteins (see e.g. Kimmel et al., 2023). Co-localization with tubulin staining further confirmed that Y21 associates with the mitotic spindle, suggesting a role at the kinetochore during cell division (Figure 66).

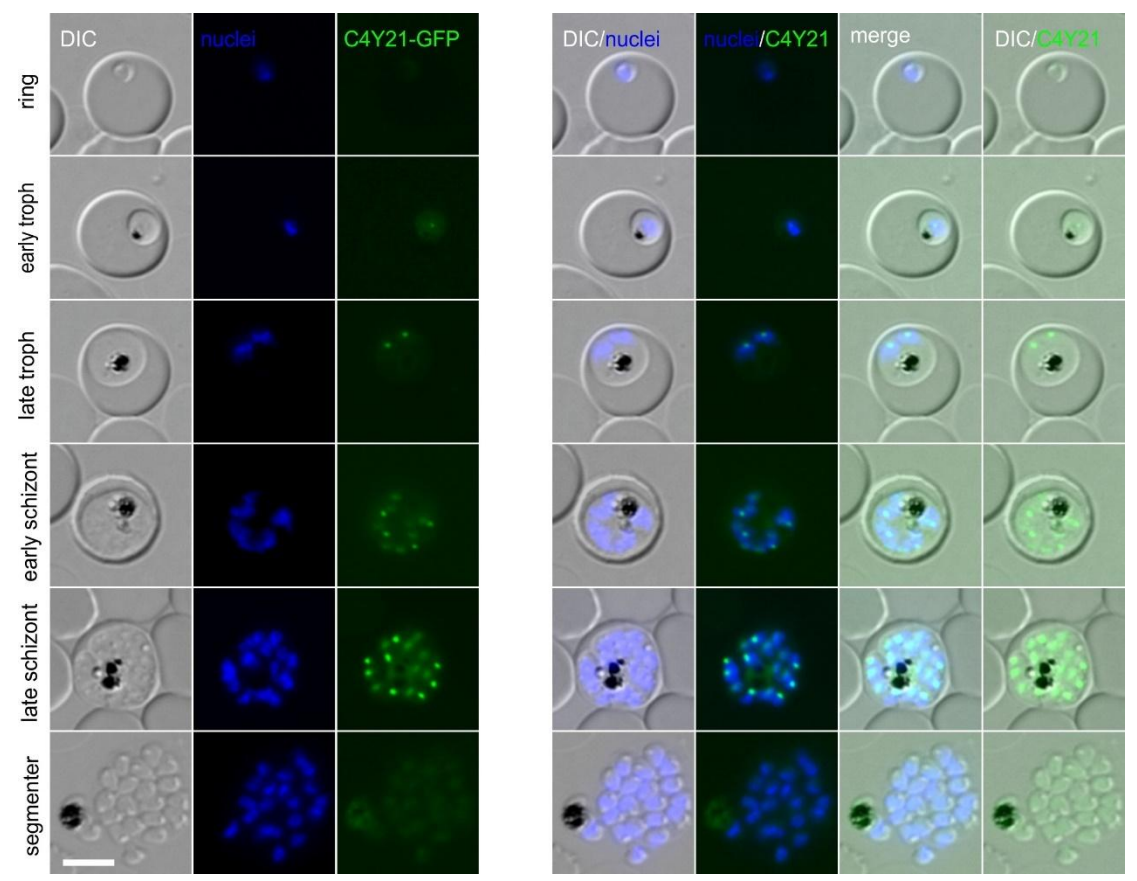


Figure 65. Localization of endogenously tagged candidate Y21 (PF3D7_0410800). Representative live cell fluorescence microscopy images of knock-in cell line Y21-2xFKBP-GFP-2xFKBP ('GFP'). The stages are indicated on the left of the panel. Representative images from 3 independent imaging sessions with at least 7 inspected fields of view. Parasite nuclei were stained with Hoechst33342. Scale bar 5 μ m, DIC, differential interference contrast; merge, overlay of DIC, GFP and nuclei.

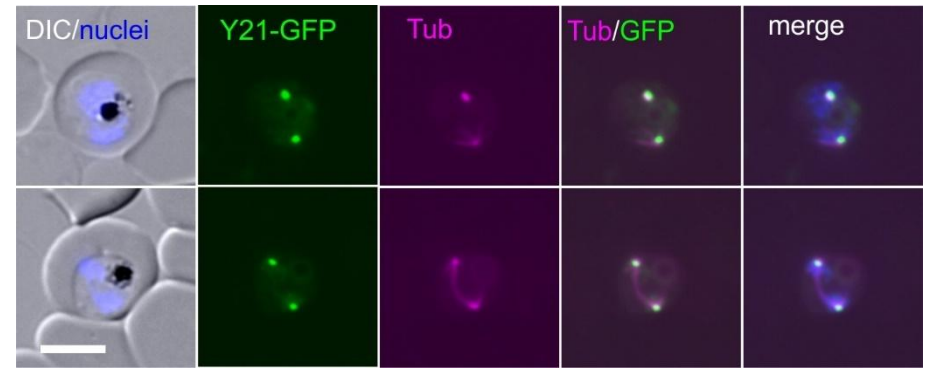


Figure 66. Y21 (PF3D7_0410800) co-localization with Tubulin. Representative live cell images of knock-in cell line of Y21-2xFKBP-GFP-2xFKBP (green) stained with TubulinTracker™ deep red (purple). Representative images from 3 independent imaging sessions with at least 7 inspected fields of

view. Parasite nuclei were stained with Hoechst33342. Scale bar 5 μ m, DIC, differential interference contrast; merge, overlay of Tub, GFP and nuclei.

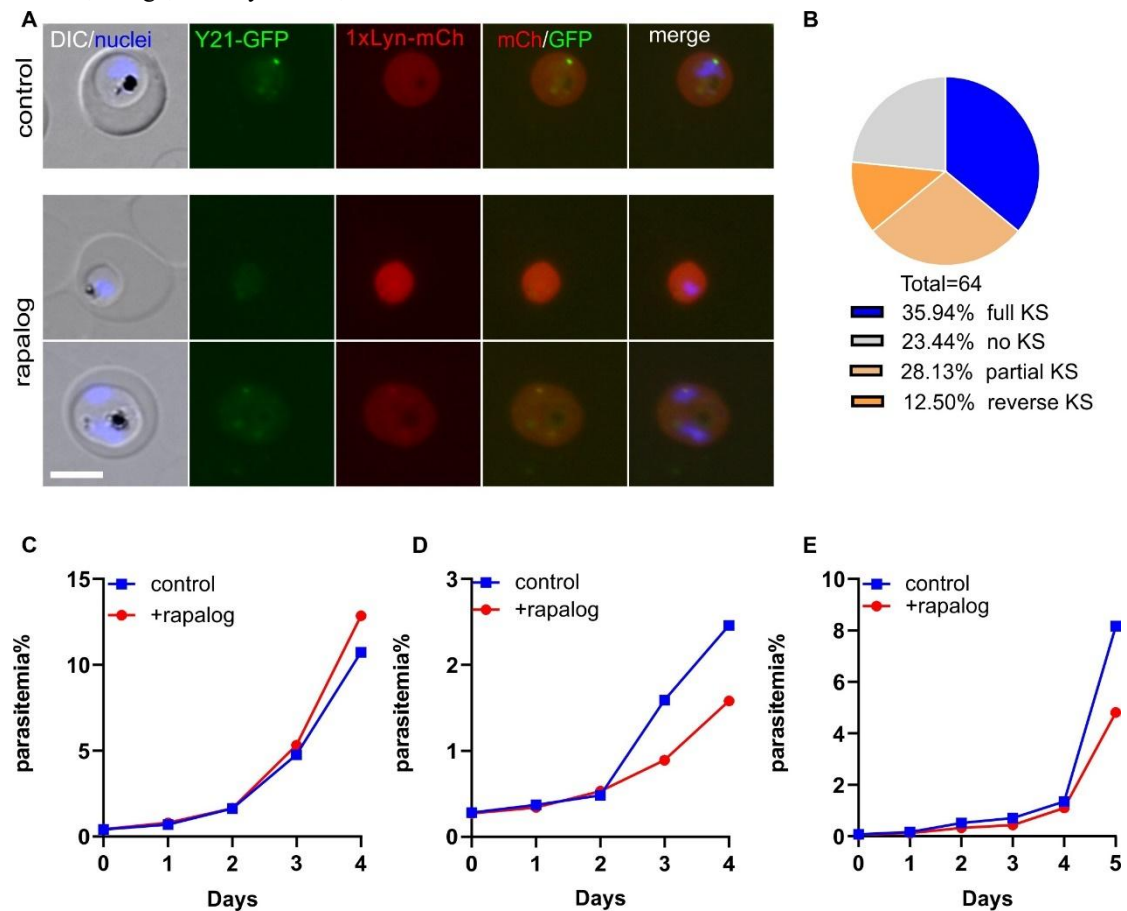


Figure 67. Knock sideways analysis of endogenous Y21 (PF3D7_0410800) tagged with 2xFKBP-GFP-2xFKBP. A) Representative live cell images of knock-in cell line Y21-2xFKBP-GFP-2xFKBP ('GFP') with an episomally expressed Lyn-FRB-mCherry mislocalizer. Representative images from 3 independent imaging sessions with at least 7 inspected fields of view. The top row shows a parasite with full KS (complete GFP mislocalization, "full KS" in (B)), while the bottom row shows a parasite with partial KS (incomplete GFP mislocalization. "partial KS" in (B)). The cell culture was split into two dishes: one served as control without rapalog (control), and the other was grown in the presence of 250 nM rapalog. The samples for live cell imaging were taken 24 h post addition of rapalog. Scale bar, 5 μm, DIC, differential interference contrast, mCh, mCherry, merge, overlay of GFP, mCh and nuclei. B) Pie chart shows quantification of knock sideways efficiency based on GFP localization following rapalog treatment. Quantification of knock sideways efficiency for Y21, based on the same experiments shown in (A). A total of 64 parasites were scored across 3 independent imaging sessions. KS status was evaluated 24 hours after rapalog addition. C-E) Growth curve of the Y21-Lyn knock sideways. Parasite growth was assessed by flow cytometry in the presence (rapalog) or absence (control) of rapalog. Three independent replicates (all shown).

In order to assess the importance of Y21, the Y21-2xFKBP-GFP-2xFKBP^{endo} cell line was transfected with an episomal plasmid expressing the Lyn mislocalizer, permitting conditional inactivation using the knock sideways system. Upon rapalog treatment, fluorescence microscopy revealed partial mislocalization of Y21-GFP from the nucleus to the plasma membrane (Figure 67A). Quantification of mislocalization efficiency indicated that 35% of parasites achieved full knock sideways, 25% exhibited partial mislocalization, 20% showed a reverse phenotype in which the FRB-anchor was recruited to the native nuclear location of Y21-GFP, and the remaining 20% showed no detectable mislocalization (Figure 67B). In all three independent biological replicates of growth curve, parasites treated with rapalog showed a consistent reduction in proliferation compared to controls (Figure 67C-E). On average, the final parasitemia on day 5 was reduced by approximately 50% relative to control conditions (Figure 67C-E). However, due to the limited efficiency of the knock sideways system and the frequent occurrence of reverse KS events, these results likely underestimate the true functional dependence of the parasite on Y21.

3.19 Characterization of Y22 (PF3D7_0410900)

Y22 (Gene ID: PF3D7_0410900) is annotated in PlasmoDB as a putative apicomplexan kinetochore protein 7 (AKiT7). Members of the AKiT family are unique to apicomplexans and have no clear orthologs in model eukaryotes (Brousini et al., 2022). In *Toxoplasma gondii*, AKiT7 has been proposed to associate with centromeric regions and function during mitosis, although its precise molecular role remains to be defined No conserved domains were detected by BLAST, HHpred or MotifScan.

In order to localize and functionally analyze Y22, the corresponding gene was modified using SLI (Birnbaum et al., 2017) so that the endogenous Y22 becomes fused with the multipurpose sandwich tag (2xFKBP-GFP-2xFKBP). Correct integration into the genome was confirmed by PCR across the 5'- and 3'- integration junctions and by the

absence of a PCR product for the original locus (Figure 11). Fluorescence microscopy with the Y22-2xFKBP-GFP-2xFKBP^{endo} parasites showed that this protein is localized in the nucleus, forming multiple discrete punctate foci per nucleus, either speaking against an association with mitotic structures like other AKiTs or Y22 shows additional foci in addition to the kinetochore (Figure 68). Co-localization analysis with tubulin revealed that some Y22-GFP foci overlapped with tubulin, suggesting partial association. However, the majority of Y22 signal appeared diffusely distributed throughout the nucleus and did not co-localize with tubulin. (Figure 69).

In order to assess the importance of Y22, the Y22-2xFKBP-GFP-2xFKBP^{endo} cell line was transfected with an episomal plasmid expressing the Lyn mislocalizer, enabling conditional inactivation via the knock sideways system. Upon rapalog treatment, fluorescence microscopy revealed only partial mislocalization of Y22-GFP from the nucleus to the plasma membrane (Figure 70A). Quantification of mislocalization efficiency indicated that 52% of parasites showed full knock sideways, 28% exhibited partial mislocalization, 8% showed a reverse phenotype—where the Lyn mislocalizer was recruited to the nuclear location of Y22-GFP—and the remaining 12% showed no detectable mislocalization (Figure 70B).

Growth curve analysis across three independent replicates consistently showed reduced proliferation compared to controls, with rapalog-treated groups reaching parasitemia levels that were approximately 50-80% lower than their corresponding controls by the end of the assay (Figure 70C-E). Due to the incomplete knock sideways efficiency, these results likely underestimate the true functional requirement of the parasite on Y22.

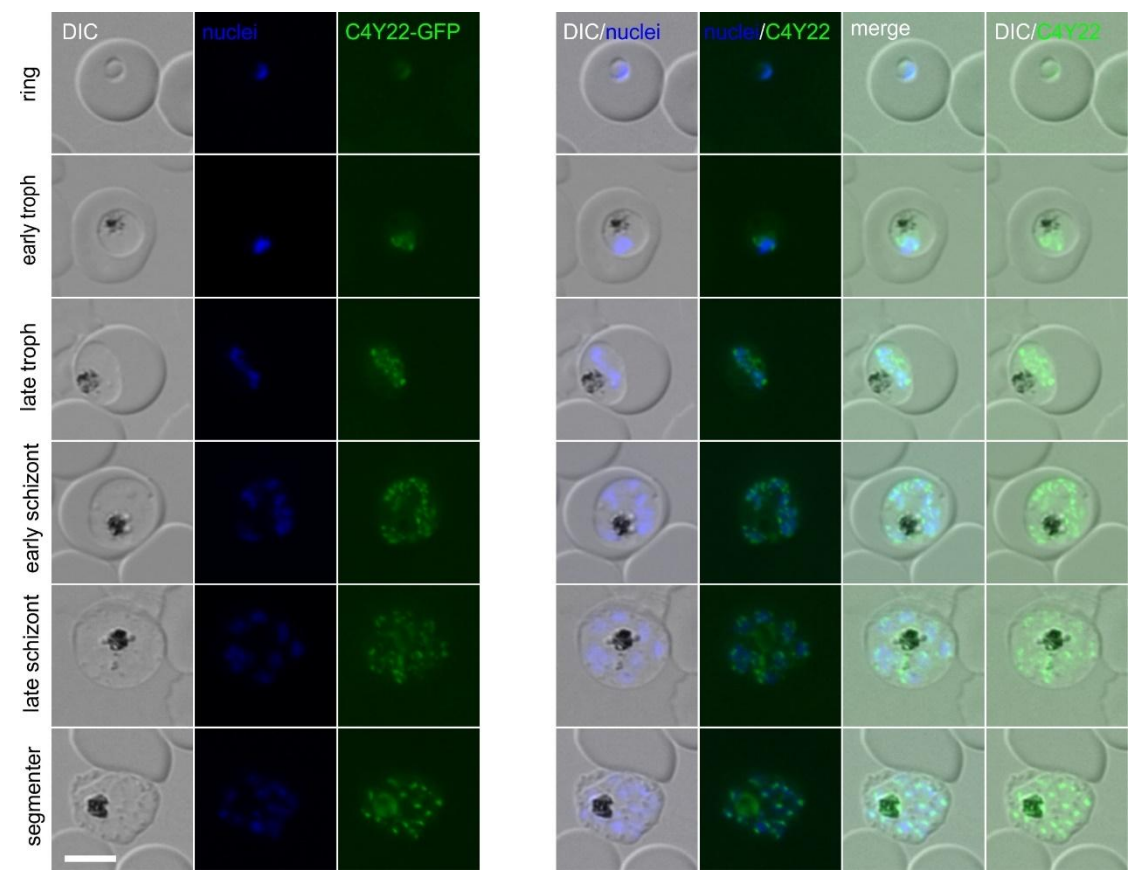


Figure 68. Localization of endogenously tagged candidate Y22 (PF3D7_0410900). Representative live cell fluorescence microscopy images of knock-in cell line Y22-2xFKBP-GFP-2xFKBP ('GFP'). The stages are indicated on the left of the panel. Representative images from 3 independent imaging sessions with at least 7 inspected fields of view. Parasite nuclei were stained with Hoechst33342. Scale bar 5 μ m, DIC, differential interference contrast; merge, overlay of DIC, GFP and nuclei.

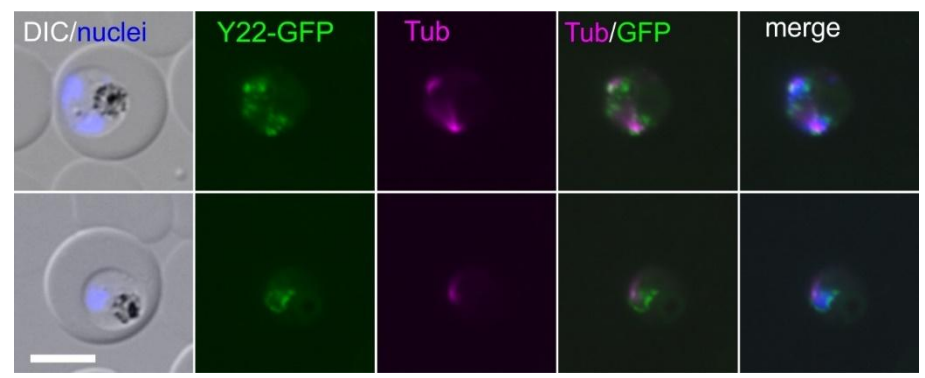


Figure 69. Y22 (PF3D7_0410900) co-localization with Tubulin. Representative live cell images of knock-in cell line of Y22-2xFKBP-GFP-2xFKBP (green) with staining TubulinTrackerTM deep red (purple). Representative images from 3 independent imaging sessions with at least 7 inspected fields of view. Parasite nuclei were stained with Hoechst33342. Scale bar 5 μm, DIC, differential interference contrast; merge, overlay of Tub, GFP and nuclei.

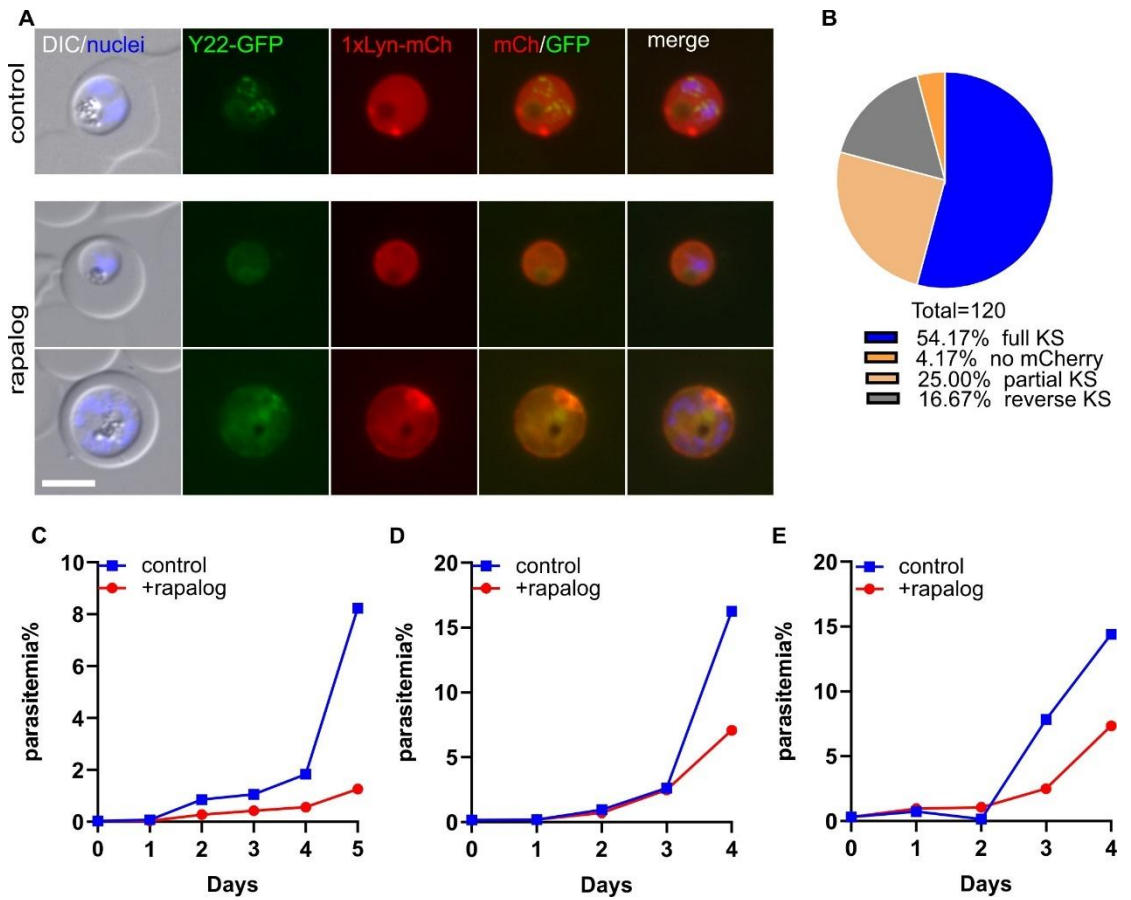


Figure 70. Knock sideways analysis of endogenous Y22 (PF3D7_0410900) tagged with 2xFKBP-GFP-2xFKBP. A) Representative live cell images of knock-in cell line Y22-2xFKBP-GFP-2xFKBP ('GFP') with an episomally expressed Lyn-FRB-mCherry mislocalizer. Representative images from 3 independent imaging sessions with at least 7 inspected fields of view. The top row shows a parasite with full KS (complete GFP mislocalization, "full KS" in (B)), while the bottom row shows a parasite with partial KS (incomplete GFP mislocalization. "partial KS" in (B)). The cell culture was split into two dishes: one served as control without rapalog (control), and the other grown in the presence of 250 nM rapalog. The samples for live cell imaging were taken 24 h post addition of rapalog. Scale bar, 5 μm, DIC, differential interference contrast, mCh, mCherry, merge, overlay of GFP, mCh and nuclei. B) Pie chart shows quantification of knock sideways efficiency based on GFP localization following rapalog treatment. Quantification of knock sideways efficiency for Y22, based on the same experiments shown in (A). A total of 64 parasites were scored across 3 independent imaging sessions. KS status was evaluated 24 hours after rapalog addition. C-E) Growth curve of the Y21-Lyn knock sideways. Parasite growth was assessed by flow cytometry in the presence (rapalog) or absence (control) of rapalog. Three independent replicates (all shown).

3.20 Characterization of Y23 (PF3D7_0411000)

Y23 (Gene ID: PF3D7_0411000) is annotated as a putative AP2 domain transcription factor AP2-Z, a member of the Apicomplexan AP2 family of transcriptional regulators. In other apicomplexans, AP2-Z is primarily associated with sexual development, particularly zygote and ookinete formation in the mosquito stage, and is thought to regulate stage-specific gene expression(Nishi et al., 2022) However, while AP2-Z is characterized in sexual development, its precise functions in the asexual blood stage of *Plasmodium falciparum* have not been fully defined, even though other ApiAP2 family members—such as *Pf*AP2-EXP2 and *Pf*AP2-G2—have been shown to regulate gene expression and proliferation during this stage (Shang et al., 2022; Singh et al., 2021).

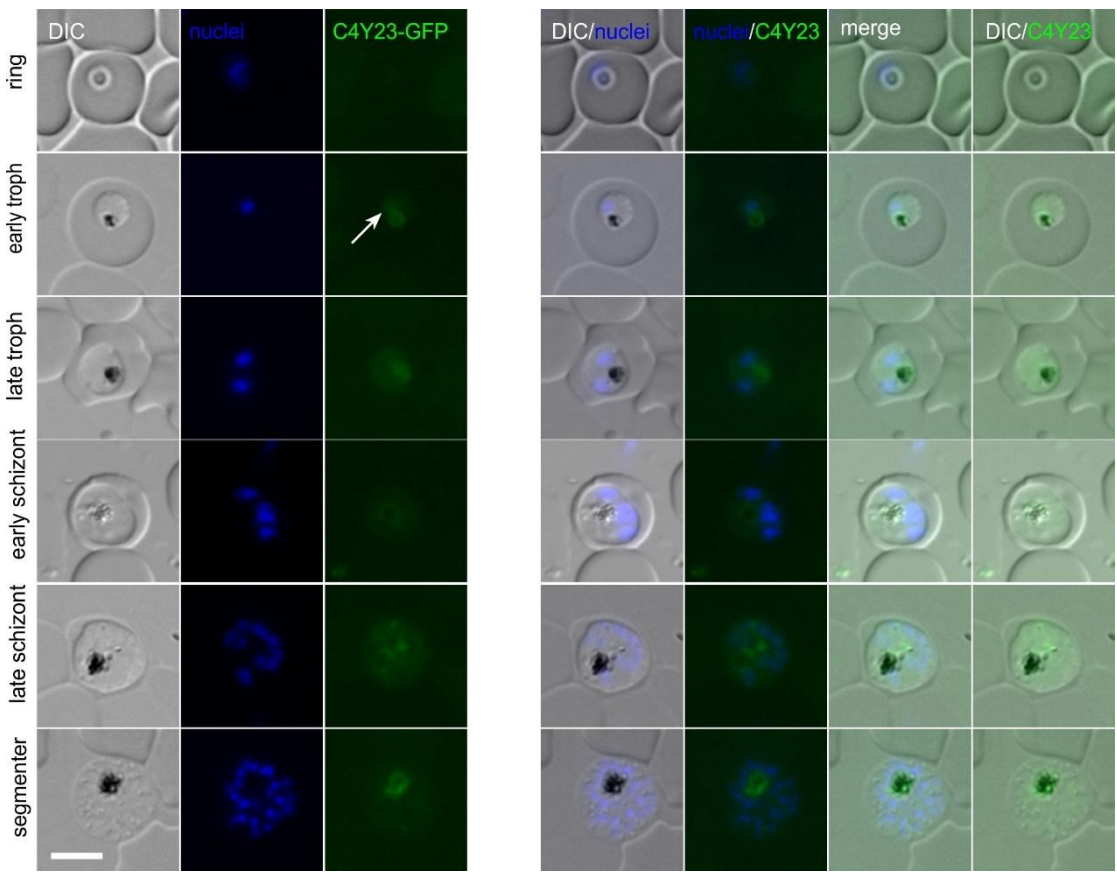


Figure 71. Localization of endogenously tagged candidate Y23 (PF3D7_0411000). Representative live cell fluorescence microscopy images of knock-in cell line Y23-2xFKBP-GFP-2xFKBP ('GFP'). The stages are indicated on the left of the panel. Representative images from 3 independent imaging sessions with at least 7 inspected fields of view. Parasite nuclei were stained with Hoechst33342. Scale bar 5 μm, DIC, differential interference contrast; merge, overlay of DIC, GFP and nuclei. Arrow shows faint signal in the nucleus in the early trophozoite.

In order to localize and functionally analyze Y23, the corresponding gene was modified using SLI (Birnbaum et al., 2017) so that the endogenous Y23 becomes fused with the multipurpose sandwich tag (2xFKBP-GFP-2xFKBP). Correct integration into the genome was confirmed by PCR across the 5'- and 3'- integration junctions and by the absence of a PCR product for the original locus (Figure 11). However, fluorescence microscopy of the Y23-2xFKBP-GFP-2xFKBP^{endo} parasite line failed to consistently detect any GFP signal across the asexual blood-stage cycle, suggesting very low expression (Figure 71). The possibility of limited cellular abundance of Y23 was also supported Transcriptomic data indicate that Y23 mRNA is expressed at low levels (Otto et al., 2010). However, in some cells a faint signal that appeared to be in the nucleus was detected (arrow, Figure 71).

In order to assess the importance of Y23, the Y23-2xFKBP-GFP-2xFKBP^{endo} cell line was transfected with episomal plasmids expressing either Lyn (Figure 72A) or NLS (Figure 73A) mislocalizers, enabling conditional inactivation using the knock sideways system. However, since Y23-GFP expression was undetectable in most cells by fluorescence microscopy under standard imaging conditions, we were unable to assess knock sideways efficiency or confirm successful mislocalization. Across three independent biological replicates, the Y23-Lyn line treated with rapalog consistently showed a modest reduction in growth compared to the control parasites. By the end of the assay, the parasitemia in the treated culture was approximately 20-50% lower than in the control culture (Figure 72B-D). By contrast, the Y23-NLS line did not result in any significant defect in parasite proliferation, with final parasitemia remaining comparable to control cultures in two biological replicates (Figure 73B-C). These findings are consistent with the signal of Y23 in the nucleus in some cells. The partial growth defect indicates that this AP2 protein also has some role in asexual stages.

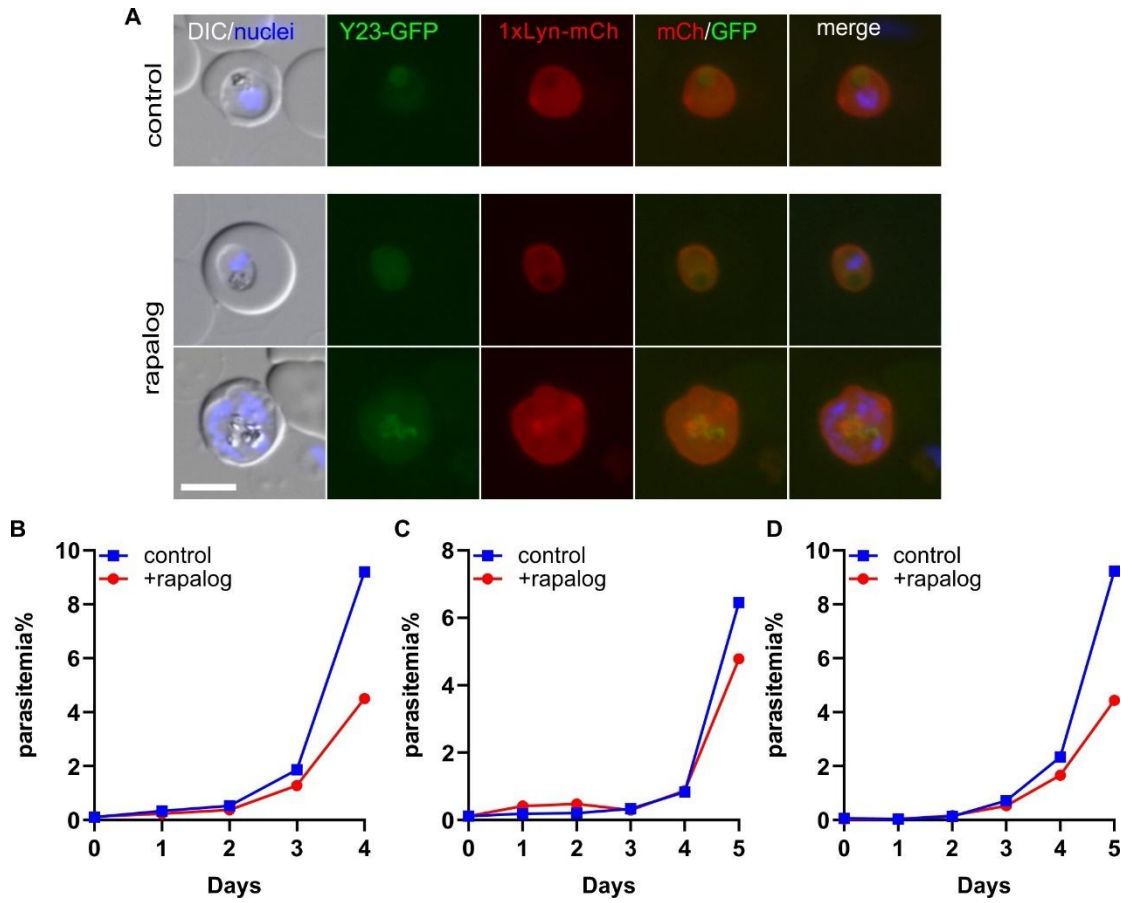


Figure 72. Knock sideways analysis of endogenous Y23 (PF3D7_0411000) tagged with 2xFKBP-GFP-2xFKBP. A) Representative live cell images of knock-in cell line Y23-2xFKBP-GFP-2xFKBP ('GFP') with an episomally expressed Lyn-FRB-mCherry mislocalizer. Representative images from 3 independent imaging sessions with at least 7 inspected fields of view. The cell culture was split into two dishes: one served as control without rapalog (control), and the other grown in the presence of 250 nM rapalog. The samples for live cell imaging were taken 24 h post addition of rapalog. Scale bar, 5 μm, DIC, differential interference contrast, mCh, mCherry, merge, overlay of GFP, mCh and nuclei. B-D) Growth curve of the Y23-Lyn knock sideways. Parasite growth was assessed by flow cytometry in the presence (rapalog) or absence (control) of rapalog. Three independent replicates (all shown).

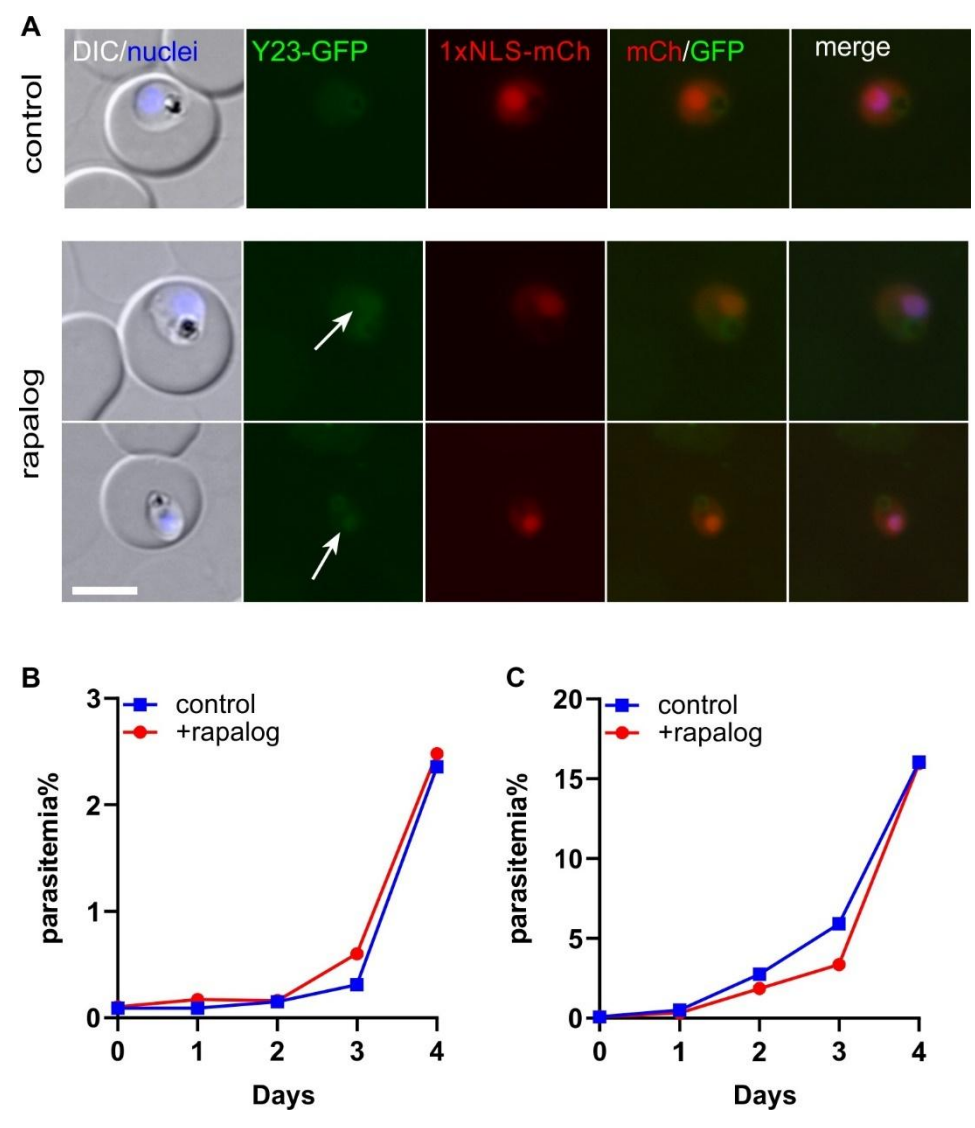


Figure 73. Knock sideways analysis of endogenous Y23 (PF3D7_0411000) tagged with 2xFKBP-GFP-2xFKBP. A) Representative live cell images of knock-in cell line Y23-2xFKBP-GFP-2xFKBP ('GFP') with an episomally expressed NLS-FRB-mCherry mislocalizer. Representative images from 3 independent imaging sessions with at least 7 inspected fields of view. The cell culture was split into two dishes: one served as control without rapalog (control), and the other grown in the presence of 250 nM rapalog. The samples for live cell imaging were taken 24 h post addition of rapalog. Scale bar, 5 μm, DIC, differential interference contrast, mCh, mCherry, merge, overlay of GFP, mCh and nuclei. B-C) Growth curve of the Y23-NLS knock sideways. Parasite growth was assessed by flow cytometry in the presence (rapalog) or absence (control) of rapalog. Two independent replicates (both shown).

3.21 Characterization of Y24 (PF3D7_0411300)

Y24 (Gene ID: PF3D7_0411300) is annotated in PlasmoDB as a golgin subfamily A member 6-like protein, putative. This annotation implies a Golgi-related localization or

function. However, no confident hits were obtained using BLAST, HHPred and MotifScan. To further probe into the PlasmoDB annotation, we aligned the Y24 amino acid sequence with that of Homo sapiens GOLGA6L2, the human protein it is putatively related to. The alignment revealed only 7 identical residues, indicating no meaningful sequence homology. We therefore classified Y24 as an unknown protein and proceeded to analyse it.

In order to localize and functionally analyze Y24, the corresponding gene was modified using SLI (Birnbaum et al., 2017) so that the endogenous Y24 becomes fused with the multipurpose sandwich tag (2xFKBP-GFP-2xFKBP). Correct integration into the genome was confirmed by PCR across the 5'- and 3'- integration junctions and by the absence of a PCR product for the original locus (Figure 11). Fluorescence microscopy with the Y24-2xFKBP-GFP-2xFKBP^{endo} parasite line revealed a punctate or diffuse signal near or overlapping with the Hoechst-stained nucleus (Figure 74). Due to the dispersed nature of the signal, it was not possible to conclusively determine whether Y24 was nuclear or cytoplasmic.

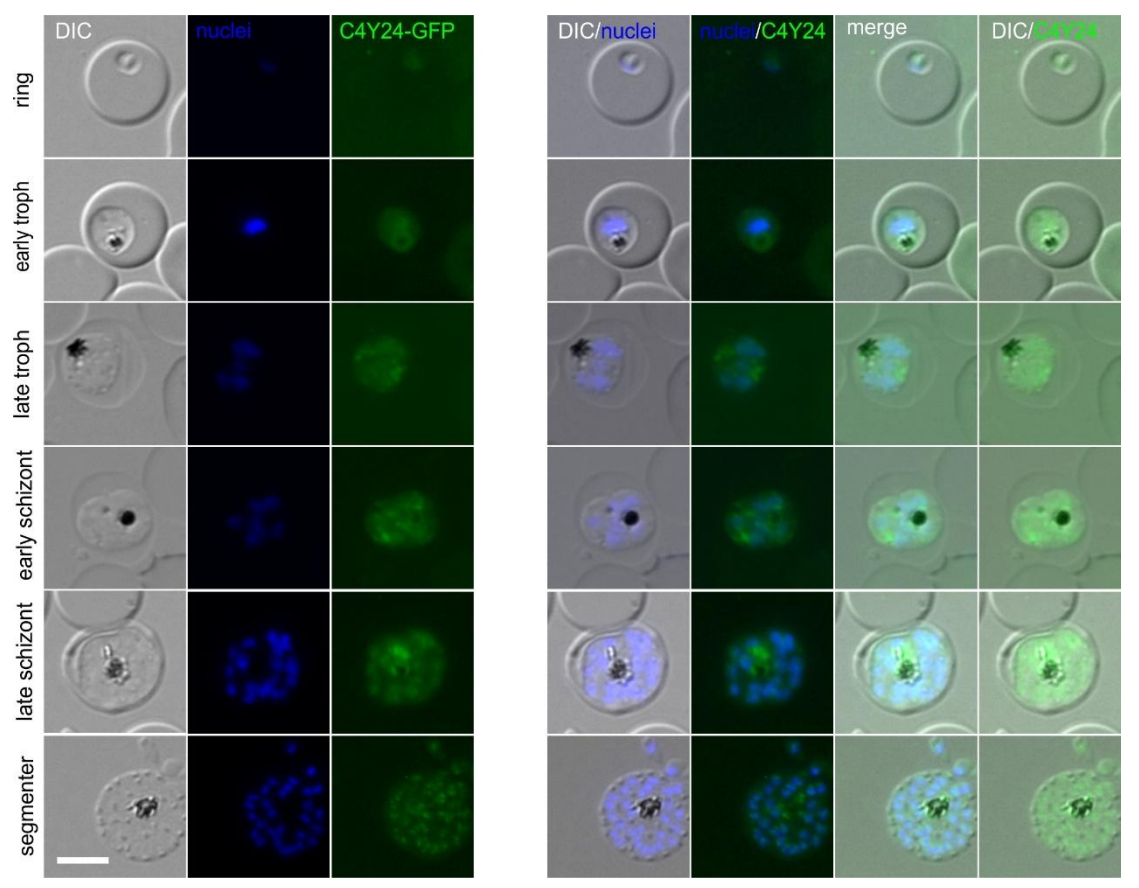


Figure 74. Localization of endogenously tagged candidate Y24 (PF3D7_0411300). Representative live cell fluorescence microscopy images of knock-in cell line Y24-2xFKBP-GFP-2xFKBP ('GFP'). The stages are indicated on the left of the panel. Representative images from 3 independent imaging sessions with at least 7 inspected fields of view. Parasite nuclei were stained with Hoechst33342. Scale bar 5 μ m, DIC, differential interference contrast; merge, overlay of DIC, GFP and nuclei.

To resolve this, we employed knock sideways assays using both, either Lyn (Figure 75) or NLS (Figure 76) mislocalizers. Imaging confirmed that both systems effectively altered Y24 localization upon rapalog treatment, although the Lyn-based mislocalization was considerably more efficient (~95% full mislocalization compared to ~47% full mislocalization, Figure 75B and 76B). Strikingly, only the Lyn-based mislocalization led to a strong growth defect (Figure 75C-E), whereas NLS-based mislocalization had only a small impact on parasite proliferation (Figure 76C-E). These results indicate that Y24 resides in the nucleus where it performs an important function. This observation stands in contrast to the annotation provided by PlasmoDB, which suggests a Golgi-associated role.

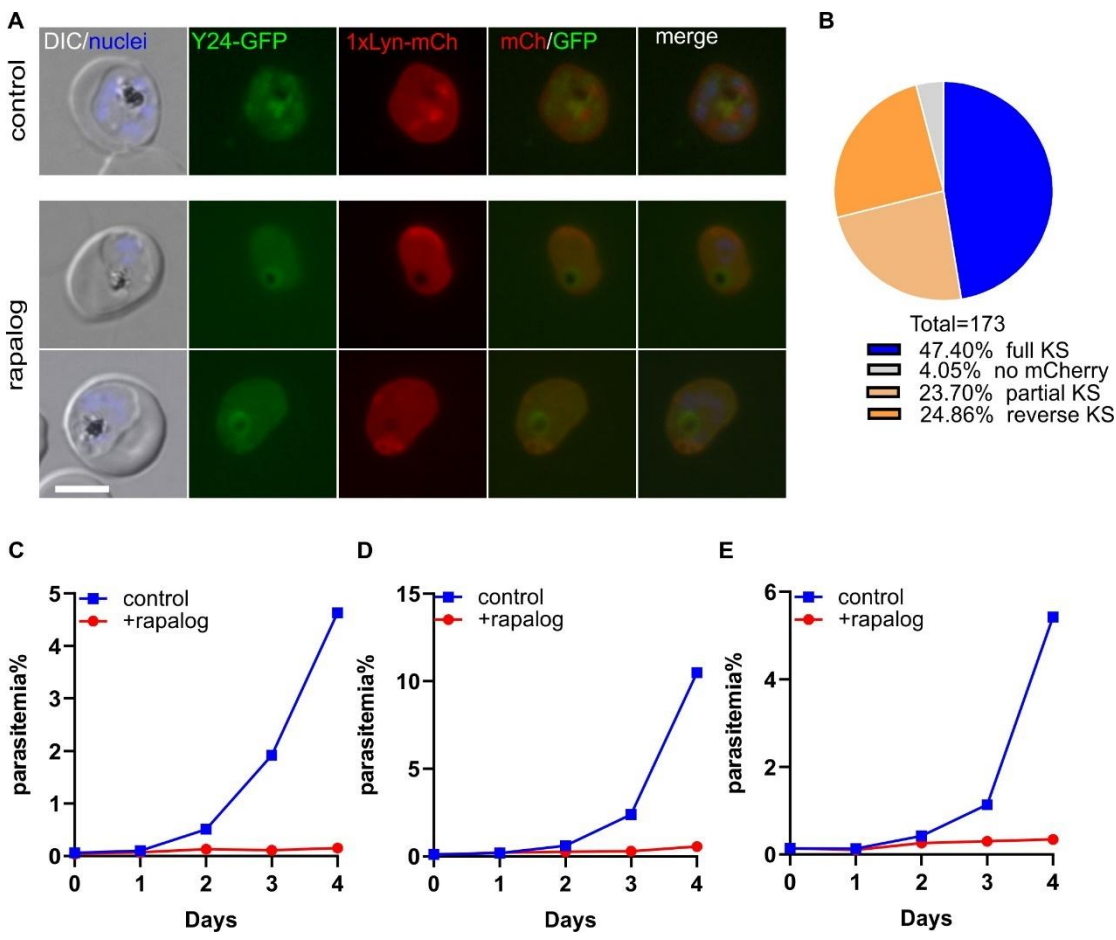


Figure 75. Knock sideways analysis of endogenous Y24 (PF3D7_0411300) tagged with 2xFKBP-GFP-2xFKBP. A) Representative live cell images of knock-in cell line Y24-2xFKBP-GFP-2xFKBP ('GFP') with an episomally expressed Lyn-FRB-mCherry mislocalizer. Representative images from 3 independent imaging sessions each with at least 7 inspected fields of view. Both two rows show a parasite with full KS (complete GFP mislocalization, "full KS" in (B)). The cell culture was split into two dishes: one served as control without rapalog (control), and the other grown in the presence of 250 nM rapalog. The samples for live cell imaging were taken 24 h post addition of rapalog. Scale bar, 5 μm, DIC, differential interference contrast, mCh, mCherry, merge, overlay of GFP, mCh and nuclei. B) Pie chart shows quantification of knock sideways efficiency based on GFP localization following rapalog treatment. Quantification of knock sideways efficiency for Y24, based on the same experiments shown in (A). A total of 157 parasites were scored across 8 independent imaging sessions. KS status was evaluated 24 hours after rapalog addition. C-E) Growth curve of the Y24-Lyn knock sideways. Parasite growth was assessed by flow cytometry in the presence (rapalog) or absence (control) of rapalog. Three independent replicates (all shown).

Next, we determined the stage Y24 is important during asexual blood stage development by carrying out knock sideways (using the Lyn mislocalier Y24 parasites) with synchronized parasites and monitoring parasite development across two

proliferation cycles. When Y24 was inactivated in ring stages, early development (10-32 hpi) was unaffected by rapalog treatment (Figure 77). From 34-42 hpi, the parasites grown in the presence of rapalog showed mildly delayed progression from late trophozoites to early schizonts and some drop in parasitemia. At 48-66 hpi, control parasites completed schizogony and produced ring-stage progeny, while the rapalog treated parasites exhibited lower overall parasitemia producing less than a third of the number of rings compared to controls and showed an accumulation of schizont and segmenter forms (Figure 77).

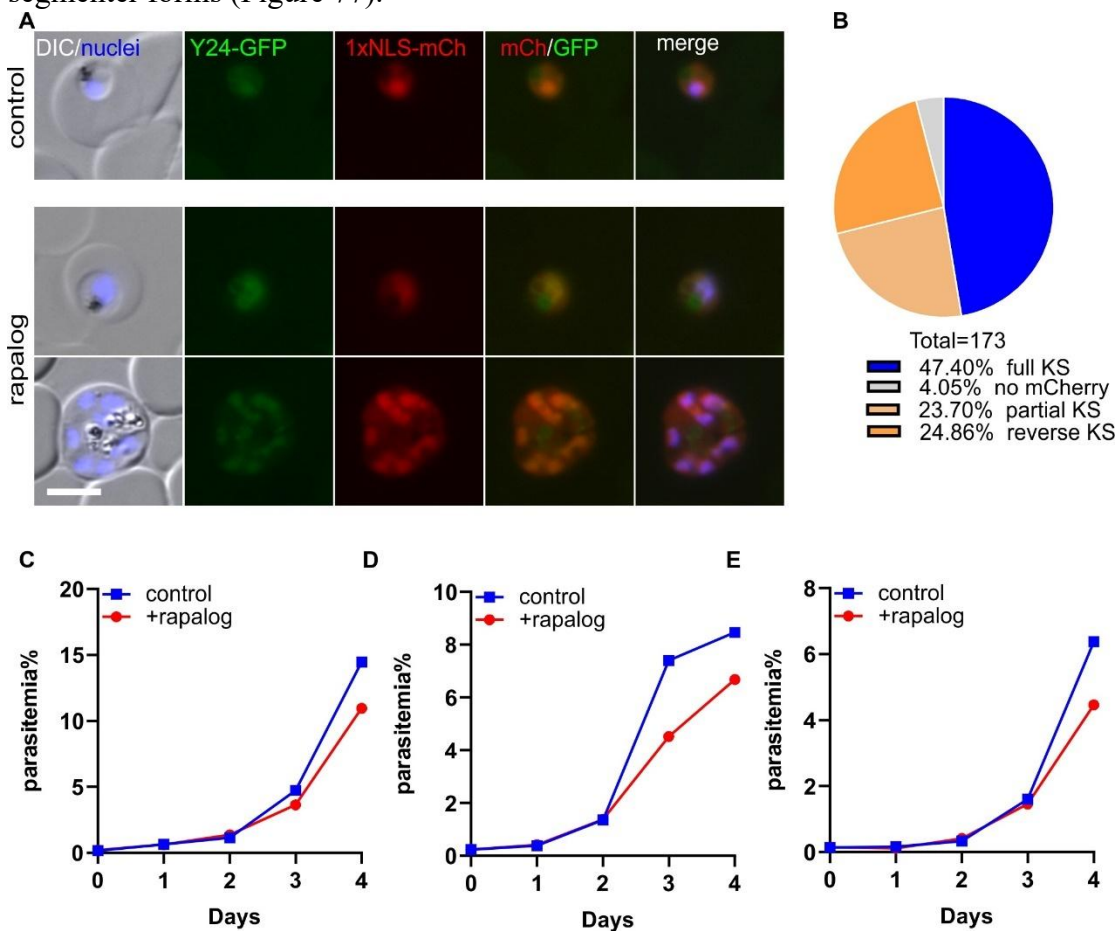


Figure 76. Knock sideways analysis of endogenous Y24 (PF3D7_0411300) tagged with 2xFKBP-GFP-2xFKBP. A) Representative live cell images of knock-in cell line Y24-2xFKBP-GFP-2xFKBP ('GFP') with an episomally expressed NLS-FRB-mCherry mislocalizer. Representative images from 3 independent imaging sessions with at least 7 inspected fields of view. The top row shows a parasite with full KS (complete GFP mislocalization, "full KS" in (B)), while the bottom row shows a parasite with partial KS (incomplete GFP mislocalization. "partial KS" in (B)). The cell culture was split into two dishes: one served as control without rapalog (control), and the other grown in the presence of 250 nM rapalog. The samples for live cell imaging were taken 24 h post addition of rapalog. Scale bar, 5 μ m,

DIC, differential interference contrast, mCh, mCherry, merge, overlay of GFP, mCh and nuclei. B) Pie chart shows quantification of knock sideways efficiency based on GFP localization following rapalog treatment. Quantification of knock sideways efficiency for Y24, based on the same experiments shown in (A). A total of 157 parasites were scored across 8 independent imaging sessions. KS status was evaluated 24 hours after rapalog addition. C-E) Growth curve of the Y24-NLS knock sideways. Parasite growth was assessed by flow cytometry in the presence (rapalog) or absence (control) of rapalog. Three independent replicates (all shown).

In the second cycle (72-114 hpi), the rapalog treated parasites continued to show lower parasitemia. At 72-90 hpi, both groups progressed to early schizont stages, but the rapalog-treated parasites showed a relative accumulation of trophozoites that remained until the end of the experiment, indicating a developmental arrest at that stage for many of the parasites. At 96-104 hpi, control parasites produced a strong second ring wave, while the KS parasites formed no rings (Figure 77).

In summary, our experimental data indicate that Y24 is a nuclear protein with no detectable similarity to Golgi proteins, and it plays an important role in asexual parasite development from the trophozoite to the schizont stage and either through this, or directly, in the formation of progeny, egress or invasion.

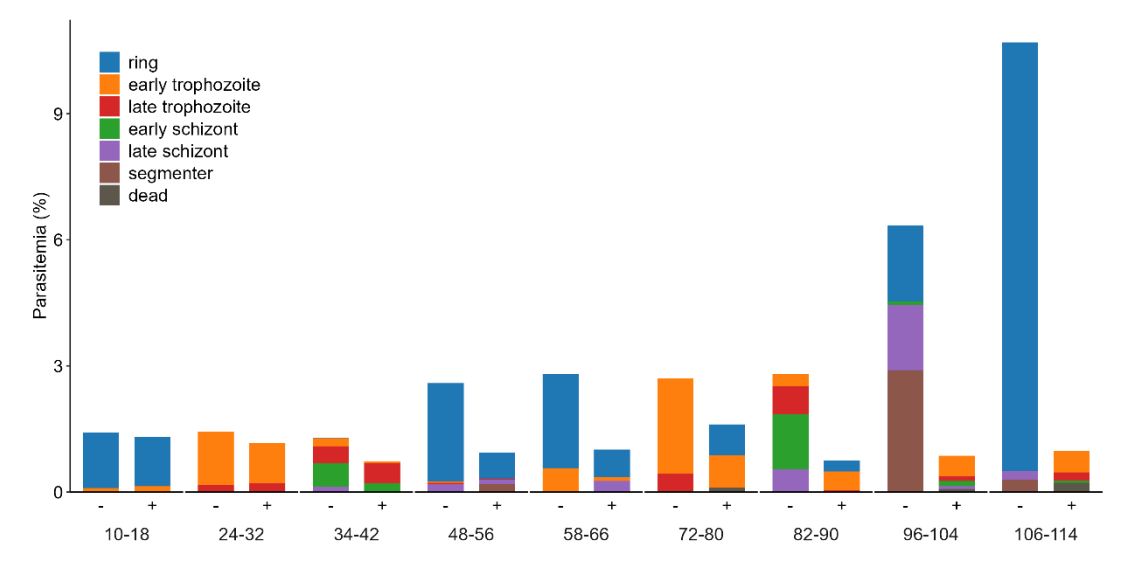


Figure 77. Stage assay of Y24-Lyn knock sideways parasites following rapalog treatment. Synchronized parasites expressing a knock sideways version of Y24-Lyn were treated with rapalog and parasite stages were monitored every 10/14 hours in 5 days over two intraerythrocytic developmental cycles. Diluted:

1:10. Parasitemia (%) and the distribution of parasite stages were quantified by Giemsa-stained blood smears. Data shown are representative of two independent biological replicates.

3.22 Characterization of Y25 (PF3D7_0411800)

Y25 (Gene ID: PF3D7_0411800) is annotated in PlasmoDB as a conserved Plasmodium protein with unknown function, and no meaningful homology or conserved domains were identified using BLAST, HHPred, or MotifScan.

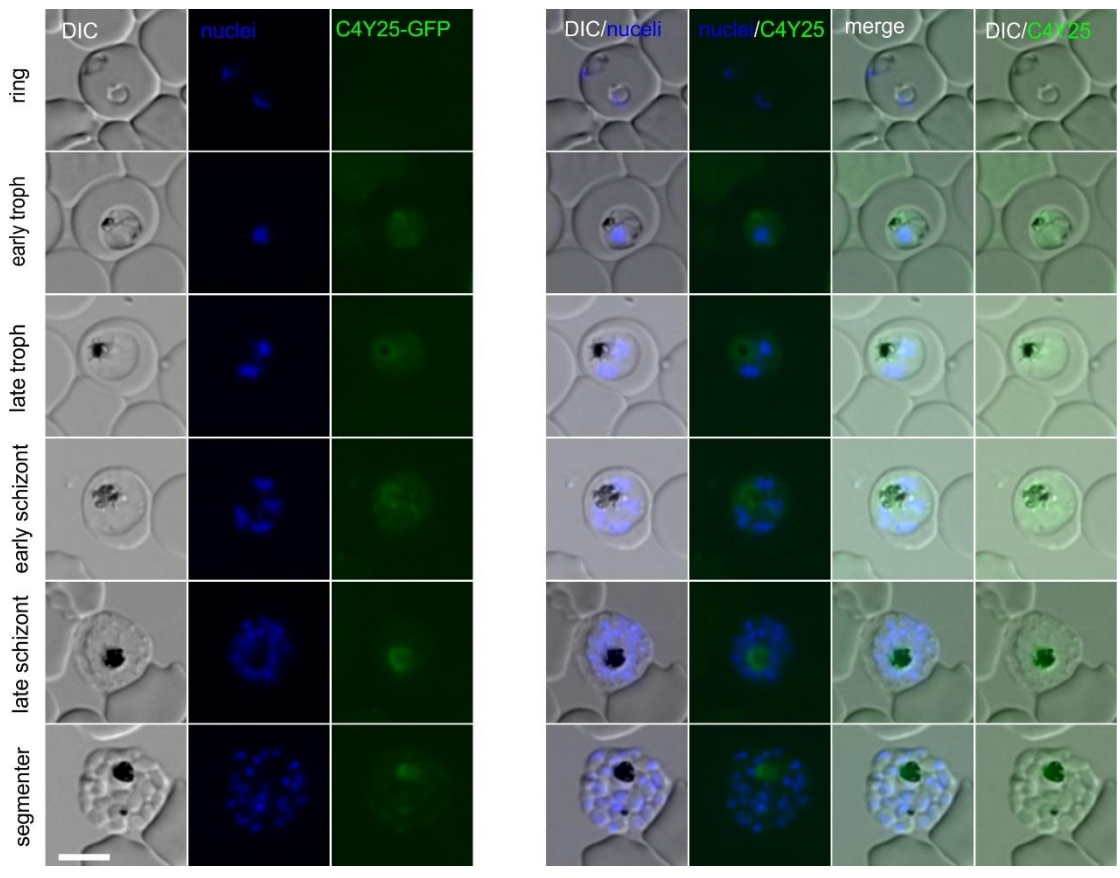


Figure 78. Localization of endogenously tagged candidate Y25 (PF3D7_0411800). Representative live cell fluorescence microscopy images of knock-in cell line Y25-2xFKBP-GFP-2xFKBP ('GFP'). The stages are indicated on the left of the panel. Representative images from 3 independent imaging sessions with at least 7 inspected fields of view. Parasite nuclei were stained with Hoechst33342. Scale bar 5 μm, DIC, differential interference contrast; merge, overlay of DIC, GFP and nuclei.

In order to localize Y25, the corresponding gene was modified using SLI (Birnbaum et al., 2017) so that the endogenous Y25 becomes fused with the multipurpose sandwich tag (2xFKBP-GFP-2xFKBP). Correct integration into the genome was confirmed by

PCR across the 5'- and 3'- integration junctions and by the absence of a PCR product for the original locus (Figure 11). Fluorescence microscopy of the Y25-2xFKBP-GFP-2xFKBP^{endo} parasite line revealed no detectable GFP signal across most asexual blood-stage parasites (Figure 78). Only very faint and inconsistent fluorescence was observed in some late-stage parasites, but the signal was close to background levels and not reproducible across imaging sessions. These results indicate that Y25 is expressed at very low levels during the asexual blood stage. Unfortunately, no KS line was obtained for this candidate in the course of this thesis and the importance of Y25 could therefore not be evaluated.

3.23 Characterization of Y28 (PF3D7_0415200)

Y28 (Gene ID: PF3D7_0415200) is annotated in PlasmoDB as a conserved Plasmodium protein with unknown function. Similarity searches using BLAST, HHPred, and MotifScan did not yield any significant hits or conserved domains.

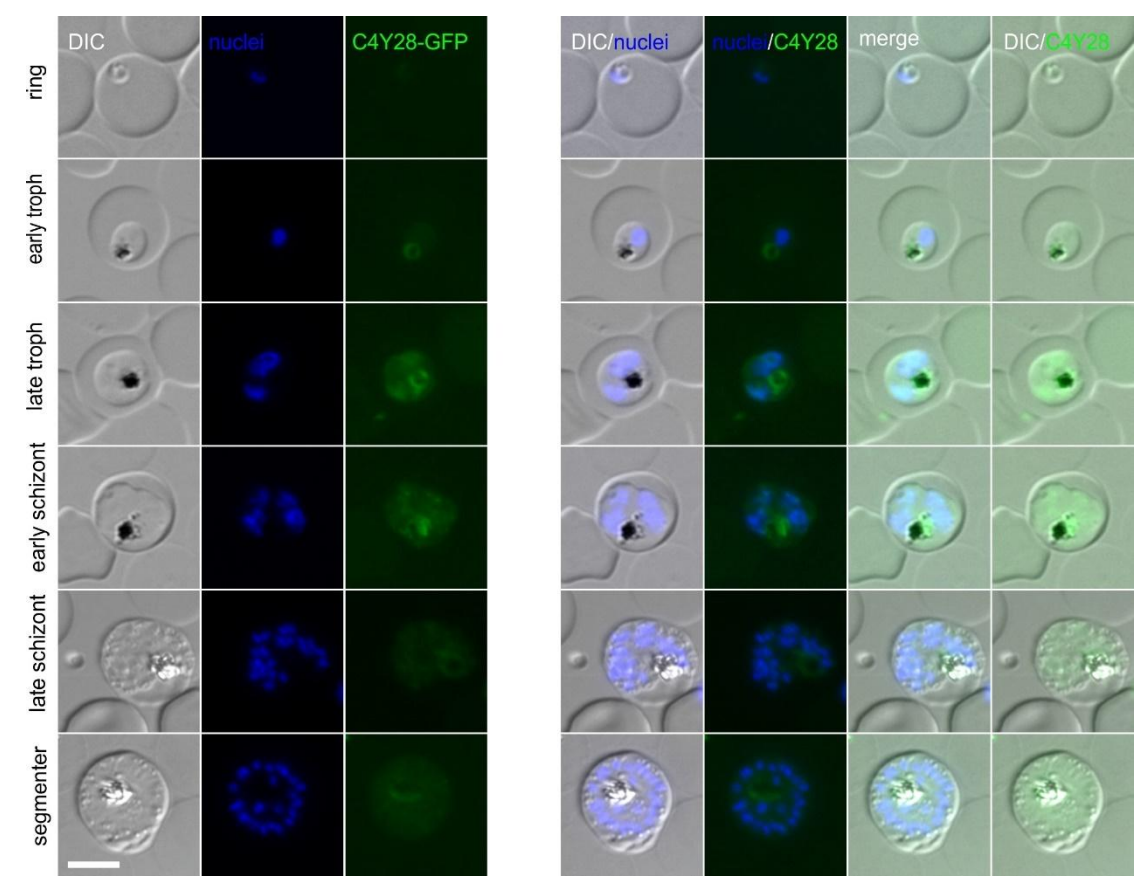


Figure 79. Localization of endogenously tagged candidate Y28 (PF3D7_0415200). Representative live cell fluorescence microscopy images of knock-in cell line Y28-2xFKBP-GFP-2xFKBP ('GFP'). The stages are indicated on the left of the panel. Representative images from 3 independent imaging sessions with at least 7 inspected fields of view. Parasite nuclei were stained with Hoechst33342. Scale bar 5 μ m, DIC, differential interference contrast; merge, overlay of DIC, GFP and nuclei.

In order to localize and functionally analyze Y28, the corresponding gene was modified using SLI (Birnbaum et al., 2017) so that the endogenous Y28 becomes fused with the multipurpose sandwich tag (2xFKBP-GFP-2xFKBP). Correct integration into the genome was confirmed by PCR across the 5'- and 3'- integration junctions and the absence of a PCR product for the original locus (Figure 11). Fluorescence microscopy of the Y28-2xFKBP-GFP-2xFKBP^{endo} cell line revealed a diffuse nuclear signal

(Figure 79). No signal was observed during the ring stage and the signal intensity declined during the schizont stage.

In order to assess the importance of Y28, the Y28-2xFKBP-GFP-2xFKBP^{endo} cell line was transfected with an episomal plasmid expressing the Lyn mislocalizer, enabling conditional inactivation via the knock sideways system. Upon rapalog treatment, fluorescence microscopy revealed efficient relocalization of Y28-GFP from the nucleus to the plasma membrane (Figure 80A). Quantification of the knock sideways efficiency showed that 80% of parasites achieved full mislocalization, 9% showed partial mislocalization, 1% exhibited a reverse phenotype (recruitment of the FRB anchor to the nuclear GFP), and the remaining 9% showed no detectable mCherry signal (Figure 80B).

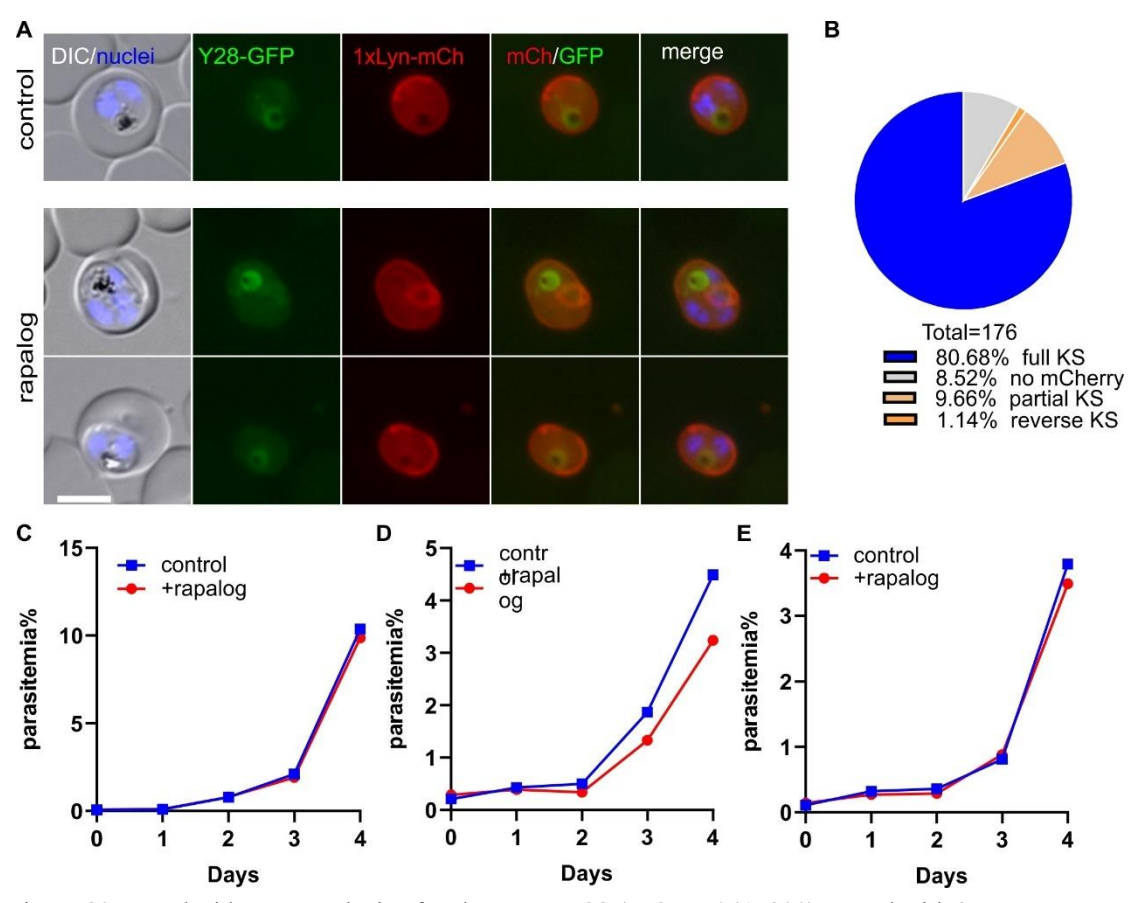


Figure 80. Knock sideways analysis of endogenous Y28 (PF3D7_0415200) tagged with 2xFKBP-GFP-2xFKBP. A) Representative live cell images of knock-in cell line Y28-2xFKBP-GFP-2xFKBP ('GFP') with an episomally expressed Lyn-FRB-mCherry mislocalizer. Representative images from 3

independent imaging sessions with at least 7 inspected fields of view. Both two rows show a parasite with full KS (complete GFP mislocalization, "full KS" in (B)). The cell culture was split into two dishes: one served as control without rapalog (control), and the other grown in the presence of 250 nM rapalog. The samples for live cell imaging were taken 24 h post addition of rapalog. Scale bar, 5 µm, DIC, differential interference contrast, mCh, mCherry, merge, overlay of GFP, mCh and nuclei. B) Pie chart shows quantification of knock sideways efficiency based on GFP localization following rapalog treatment. Quantification of knock sideways efficiency for Y28, based on the same experiments shown in (A). A total of 176 parasites were scored across 5 independent imaging sessions. KS status was evaluated 24 hours after rapalog addition. C-E) Growth curve of the Y28-Lyn knock sideways. Parasite growth was assessed by flow cytometry in the presence (rapalog) or absence (control) of rapalog. Three independent replicates (all shown).

Growth curve analysis across three independent replicates revealed no major growth defect upon Y28 inactivation. However, one of the three replicates showed a modest reduction in parasitemia following rapalog treatment compared to the control (Figure 80C-E). Despite this variability, the fact that the other two replicates exhibited near-identical proliferation to controls indicates that Y28 is likely dispensable for asexual blood-stage development under standard *in vitro* conditions. The observed fluctuation in one replicate may reflect biological variability rather than a true functional requirement of blood stage parasites on Y28.

3.24 Characterization of Y29 (PF3D7_0416900)

Y29 (Gene ID: PF3D7_0416900) is annotated in PlasmoDB as a conserved Plasmodium protein with unknown function. Bioinformatic predictions using BLAST, HHPred, and MotifScan did not identify any homologs or known domains.

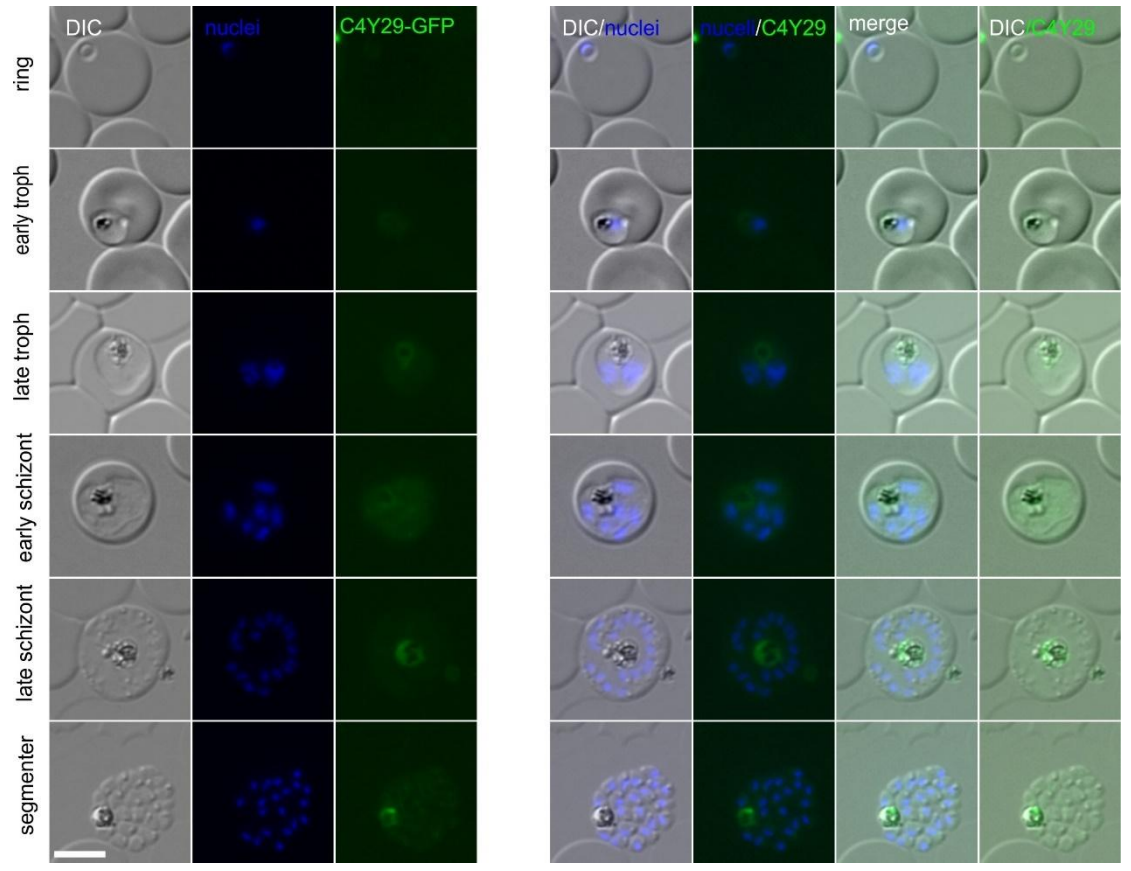


Figure 81. Localization of endogenously tagged candidate Y29 (PF3D7_0416900). Representative live cell fluorescence microscopy images of knock-in cell line Y29-2xFKBP-GFP-2xFKBP ('GFP'). The stages are indicated on the left of the panel. Representative images from 3 independent imaging sessions with at least 7 inspected fields of view. Parasite nuclei were stained with Hoechst33342. Scale bar 5 μ m, DIC, differential interference contrast; merge, overlay of DIC, GFP and nuclei.

In order to localize and functionally analyze Y29, the corresponding gene was modified using SLI (Birnbaum et al., 2017) so that the endogenous Y29 becomes fused with the multipurpose sandwich tag (2xFKBP-GFP-2xFKBP). Correct integration into the genome was confirmed by PCR across the 5'- and 3'- integration junctions and by the absence of a PCR product for the original locus (Figure 11). However, no GFP signal above background was detectable in the Y29-2xFKBP-GFP-2xFKBP^{endo} line by livecell fluorescence microscopy at any asexual stage (Figure 81), suggesting that the protein is expressed at very low levels.

To assess its functional importance, we performed knock sideways using the Lyn mislocalizer. However, since Y29-GFP expression was undetectable by fluorescence microscopy under standard imaging conditions, we were unable to assess knock sideways efficiency or confirm successful mislocalization (Figure 82A). Across three independent biological replicates, the Y29-Lyn parasite line treated with rapalog consistently showed a strong reduction in growth compared to the control group. By the end of the assay, parasitemia in the treated parasite culture was more than 90% lower than in controls (Figure 82B-D). These results indicate that Y29 is a nuclear protein and is essential for asexual blood-stage development.

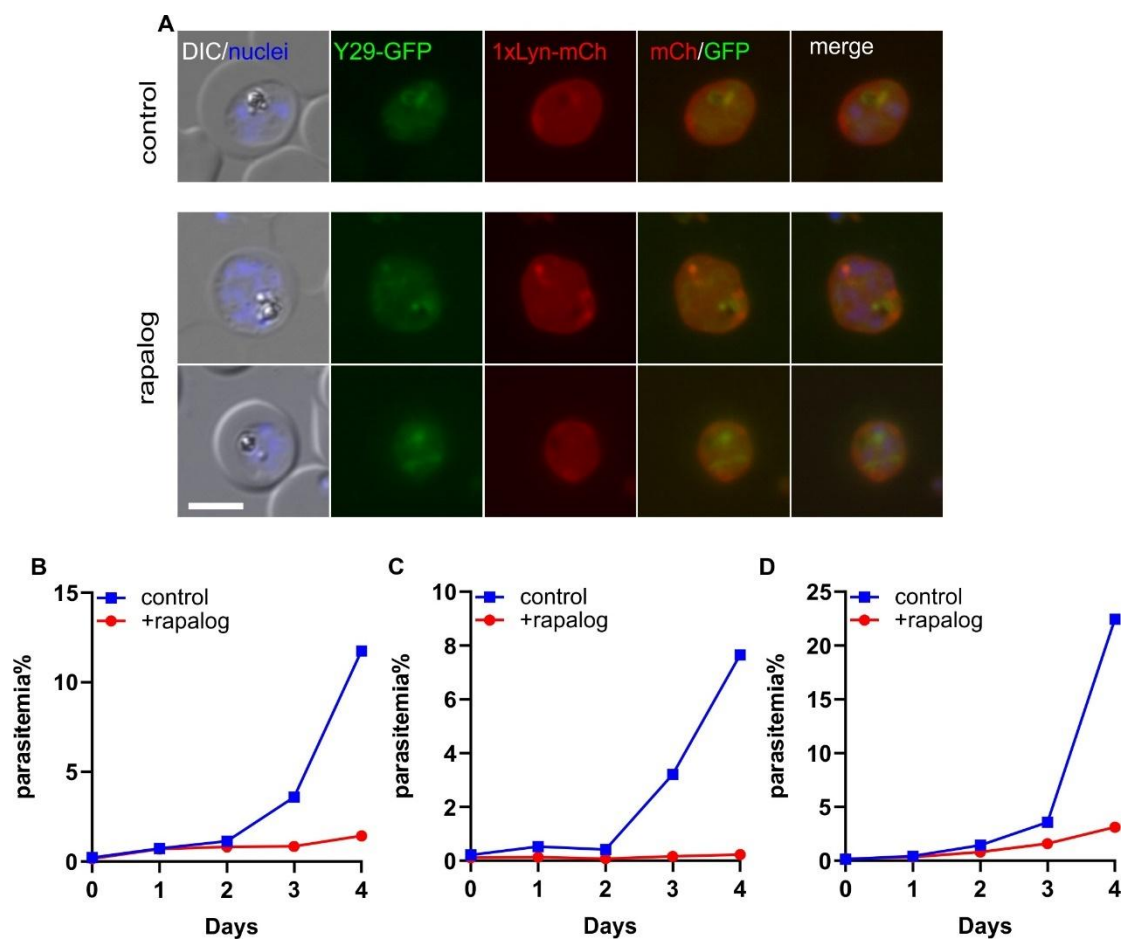


Figure 82. Knock sideways analysis of endogenous Y29 (PF3D7_0416900) tagged with 2xFKBP-GFP-2xFKBP. A) Representative live cell images of knock-in cell line Y29-2xFKBP-GFP-2xFKBP ('GFP') with an episomally expressed Lyn-FRB-mCherry mislocalizer. Representative images from 3 independent imaging sessions with at least 7 inspected fields of view. The cell culture was split into two dishes: one served as control without rapalog (control), and the other grown in the presence of 250 nM rapalog. The samples for live cell imaging were taken 24 h post addition of rapalog. Scale bar, 5 μm,

DIC, differential interference contrast, mCh, mCherry, merge, overlay of GFP, mCh and nuclei. B-D) Growth curve of the Y29-Lyn knock sideways. Parasite growth was assessed by flow cytometry in the presence (rapalog) or absence (control) of rapalog. Three independent replicates (all shown).

Given this strong phenotype, we sought to improve the detectability of Y29 by increasing GFP signal intensity. Immunofluorescence staining did not yield a visible signal, so we generated a parasite line expressing Y29 fused to a 7×GFP fragment of split GFP together with a separately expressed larger part of GFP (Feng et al., 2017; Kamiyama et al., 2016). This leads to increased fluorescence by reconstituting multiple GFPs on the target protein. This construct revealed a nuclear fluorescence pattern (Figure 83), consistent with the nuclear localization implied by the Lyn mislocalizer and supporting the conclusion that Y29 functions in the nucleus.

To identify in which stage Y29 is required, we induced the KS of Y29 in synchronous ring stage parasites and tracked parasite development using Giemsa smears (Figure 84). While overall parasitemia remained similar between control and rapalog-treated

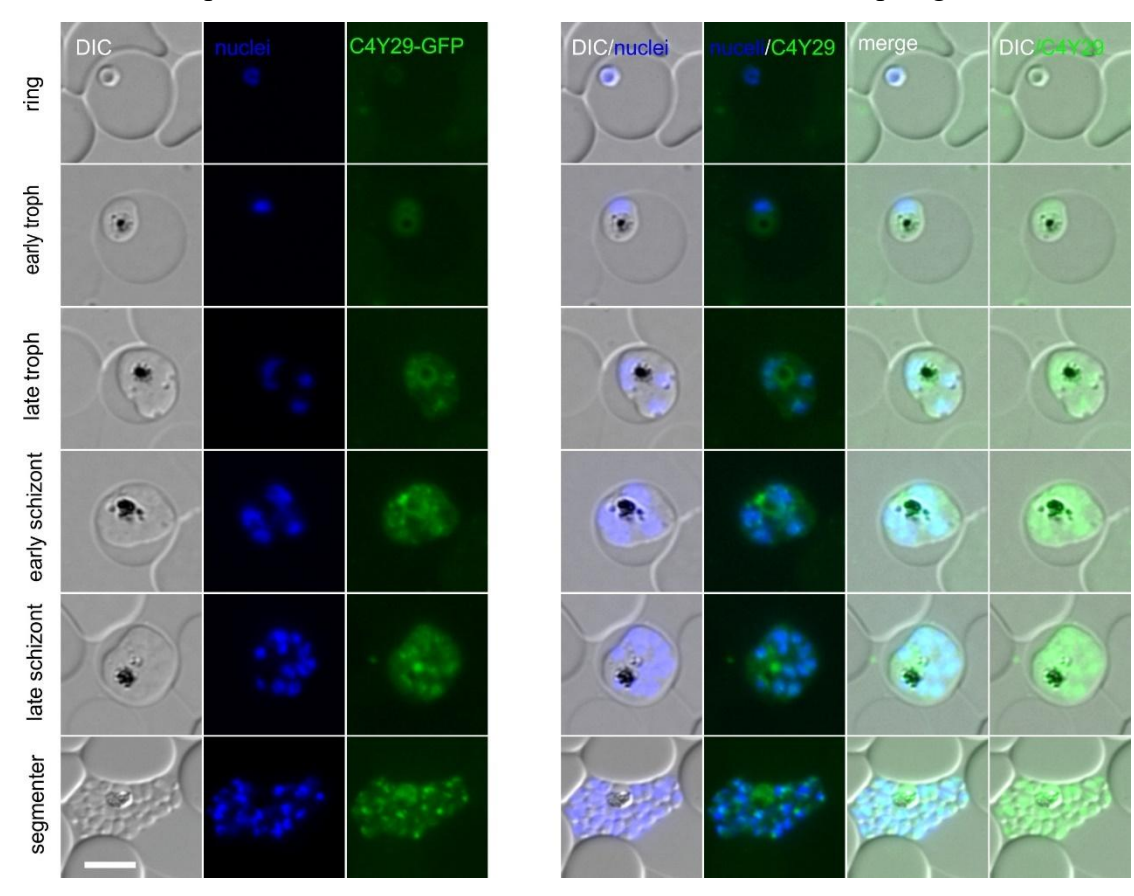


Figure 83. Localization of 7xGFP tagged candidate Y29 (PF3D7_0416900). Representative live cell fluorescence microscopy images of knock-in cell line Y29-7XGFP ('GFP'). The stages are indicated on the left of the panel. Representative images from 3 independent imaging sessions with at least 7 inspected fields of view. Parasite nuclei were stained with Hoechst33342. Scale bar 5 μ m, DIC, differential interference contrast; merge, overlay of DIC, GFP and nuclei.

parasites until ~72 hpi, we observed stage-specific delays in development in the rapalog treated parasites. This manifested as a delayed conversion already from ring to trophozoite, and further delayed transition from trophozoites to schizonts starting at 34-42 hpi. By 82 hpi, parasites began accumulating at the late schizont and segmenter stages with a considerable proportion of dead parasites and failed to form rings, suggesting impaired schizogony or reinvasion.

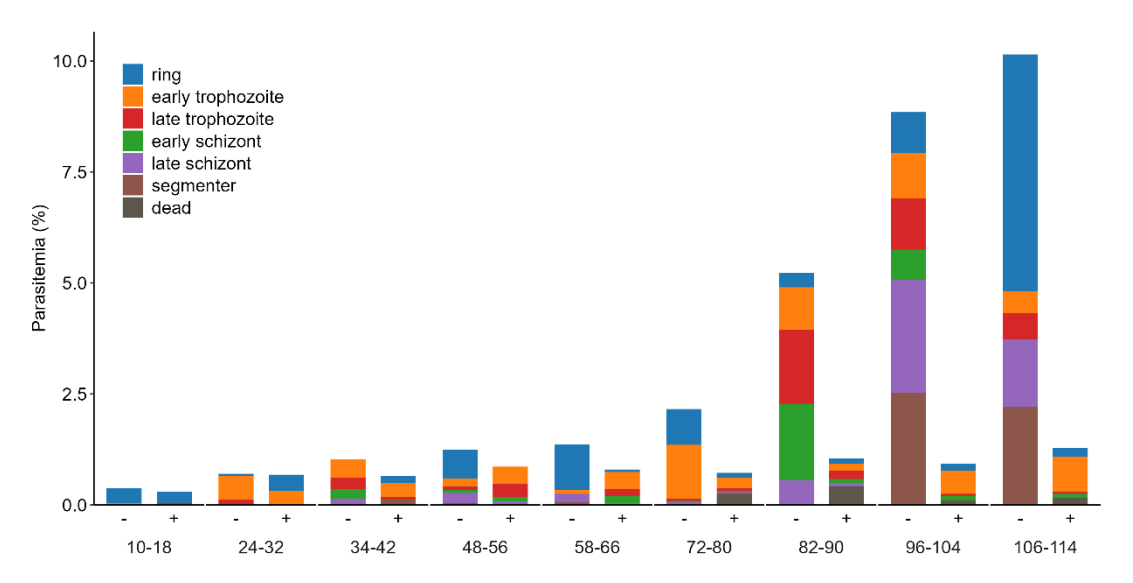


Figure 84. Stage assay of Y29-Lyn knock sideways parasites following rapalog treatment. Synchronized parasites expressing a knock sideways version of Y29-Lyn were treated with rapalog and parasite stages were monitored every 10/14 hours in 5 days over two intraerythrocytic developmental cycles. Diluted: 1:10. Parasitemia (%) and the distribution of parasite stages were quantified by Giemsa-stained blood smears. Data shown are representative of two independent biological replicates.

3.25 Characterization of Y30 (PF3D7_0417600)

Y30 (Gene ID: PF3D7_0417600) is annotated as a conserved Plasmodium protein with unknown function. Bioinformatic predictions using BLAST, HHPred, and MotifScan did not identify any homologs or known domains.

In order to localize Y30, the corresponding gene was modified using SLI (Birnbaum et al., 2017) so that the endogenous Y30 becomes fused with the multipurpose sandwich tag (2xFKBP-GFP-2xFKBP). Correct integration into the genome was confirmed by PCR across the 5'- and 3'- integration junctions and the absence of a PCR product for the original locus (Figure 11). Fluorescence microscopy of the Y30-2xFKBP-GFP-2xFKBP^{endo} cell line revealed an extremely weak GFP signal that was difficult to distinguish from background fluorescence at all asexual stages (Figure 85). As a result,

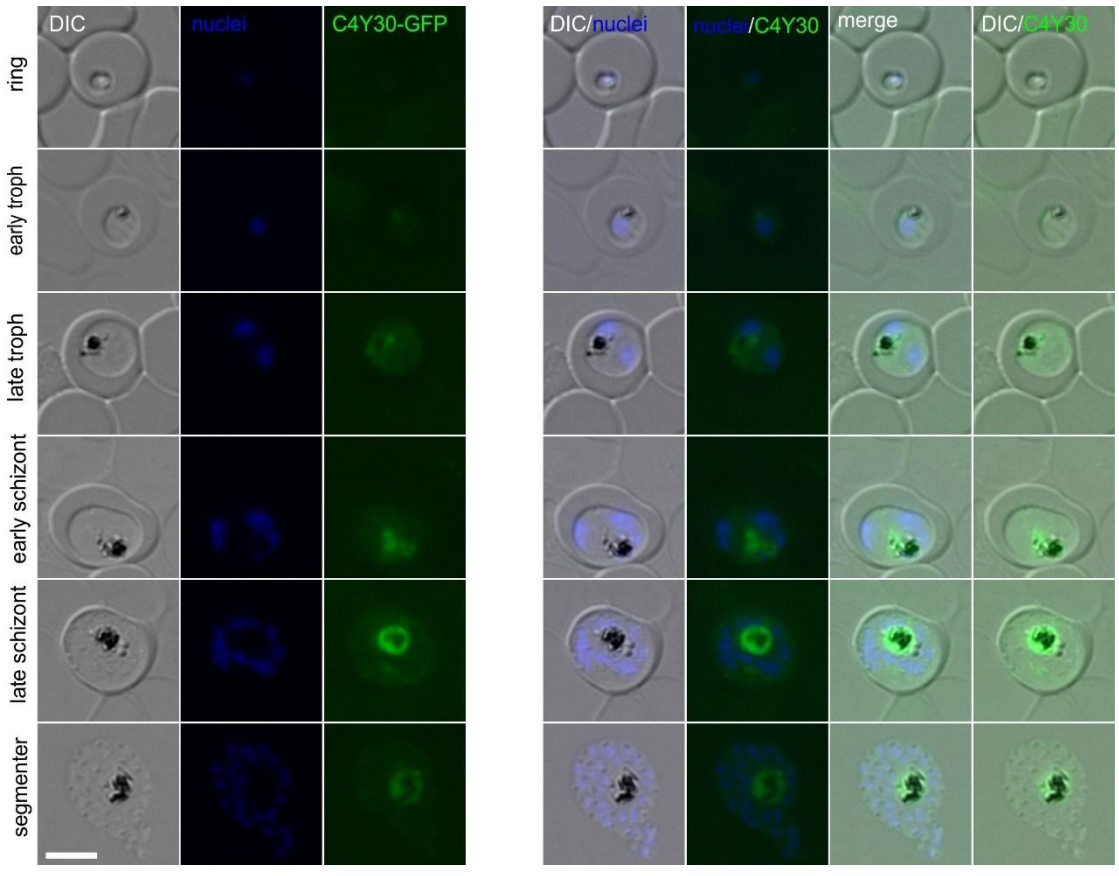


Figure 85. Localization of endogenously tagged candidate Y30 (PF3D7_0417600). Representative live cell fluorescence microscopy images of knock-in cell line Y30-2xFKBP-GFP-2xFKBP ('GFP'). The stages are indicated on the left of the panel. Representative images from 3 independent imaging sessions with at least 7 inspected fields of view. Parasite nuclei were stained with Hoechst33342. Scale bar 5 μ m, DIC, differential interference contrast; merge, overlay of DIC, GFP and nuclei.

it was not possible to confidently determine the subcellular localization of Y30 based on endogenous tagging. Due to time constraints, knock sideways cell lines were not obtained for this candidate and the importance of Y30 for parasite blood stages remains to be determined.

3.26 Characterization of Y32 (PF3D7 0417900)

Y32 (Gene ID: PF3D7_0417900) is annotated as a conserved Plasmodium protein of unknown function. Computational analyses using BLAST, HHPred, and MotifScan failed to detect any homologs or conserved domains.

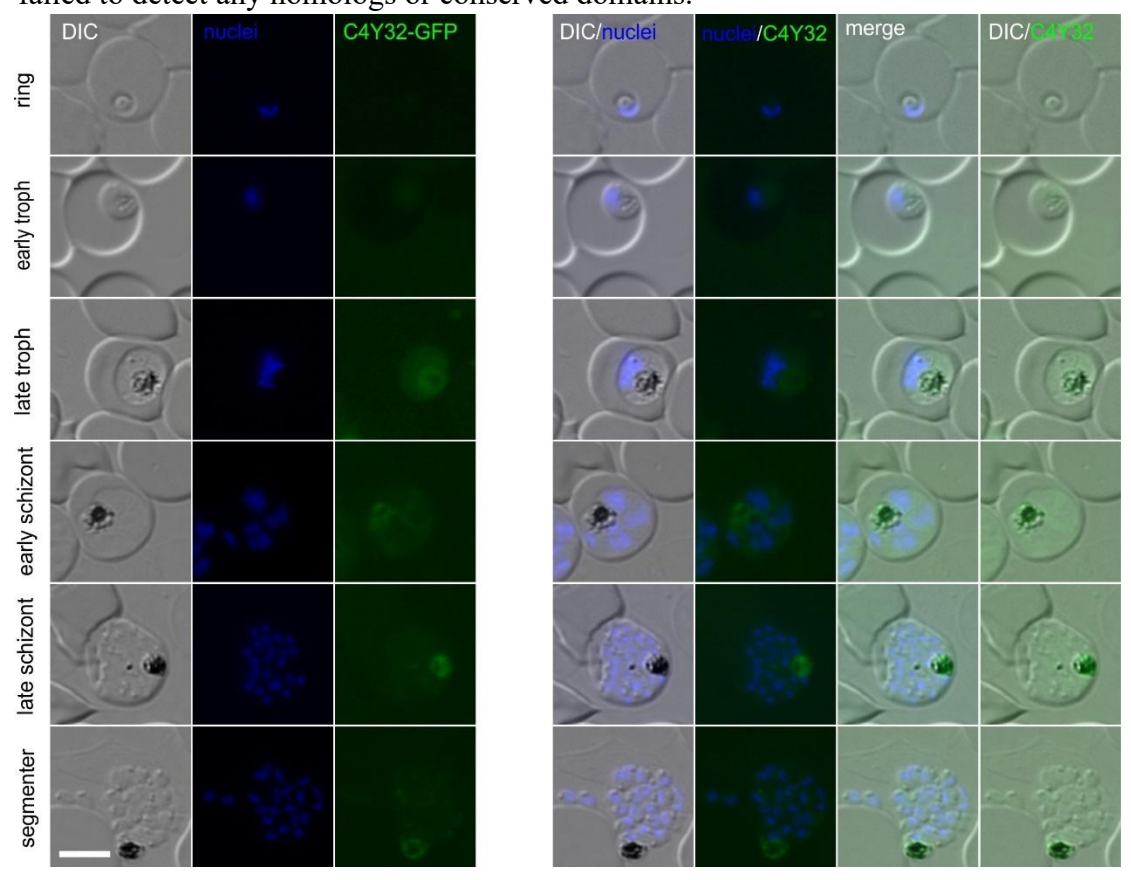


Figure 86. Localization of endogenously tagged candidate Y32 (PF3D7_0417900). Representative live cell fluorescence microscopy images of knock-in cell line Y32-2xFKBP-GFP-2xFKBP ('GFP'). The stages are indicated on the left of the panel. Representative images from 3 independent imaging sessions with at least 7 inspected fields of view. Parasite nuclei were stained with Hoechst33342. Scale bar 5 μ m, DIC, differential interference contrast; merge, overlay of DIC, GFP and nuclei.

In order to localize and functionally analyze Y32, the corresponding gene was modified using SLI (Birnbaum et al., 2017) so that the endogenous Y32 becomes fused with the multipurpose sandwich tag (2xFKBP-GFP-2xFKBP). Correct integration into the

genome was confirmed by PCR across the 5'- and 3'- integration junctions and by the absence of a PCR product for the original locus (Figure 11). Live-cell fluorescence microscopy revealed a very weak GFP signal in the Y32-2xFKBP-GFP-2xFKBP^{endo} line, but cytosolic fluorescence was detectable during the trophozoite stage (Figure 86), suggesting that Y32 is a low-abundance cytoplasmic protein.

In order to assess the importance of Y32, the Y32-2xFKBP-GFP-2xFKBP^{endo} cell line was transfected with an episomal plasmid mediating expression of the NLS mislocalizer, permitting conditional inactivation using knock sideways. Representative live-cell microscopy confirmed that Y32-GFP efficiently mislocalized to the nuclues

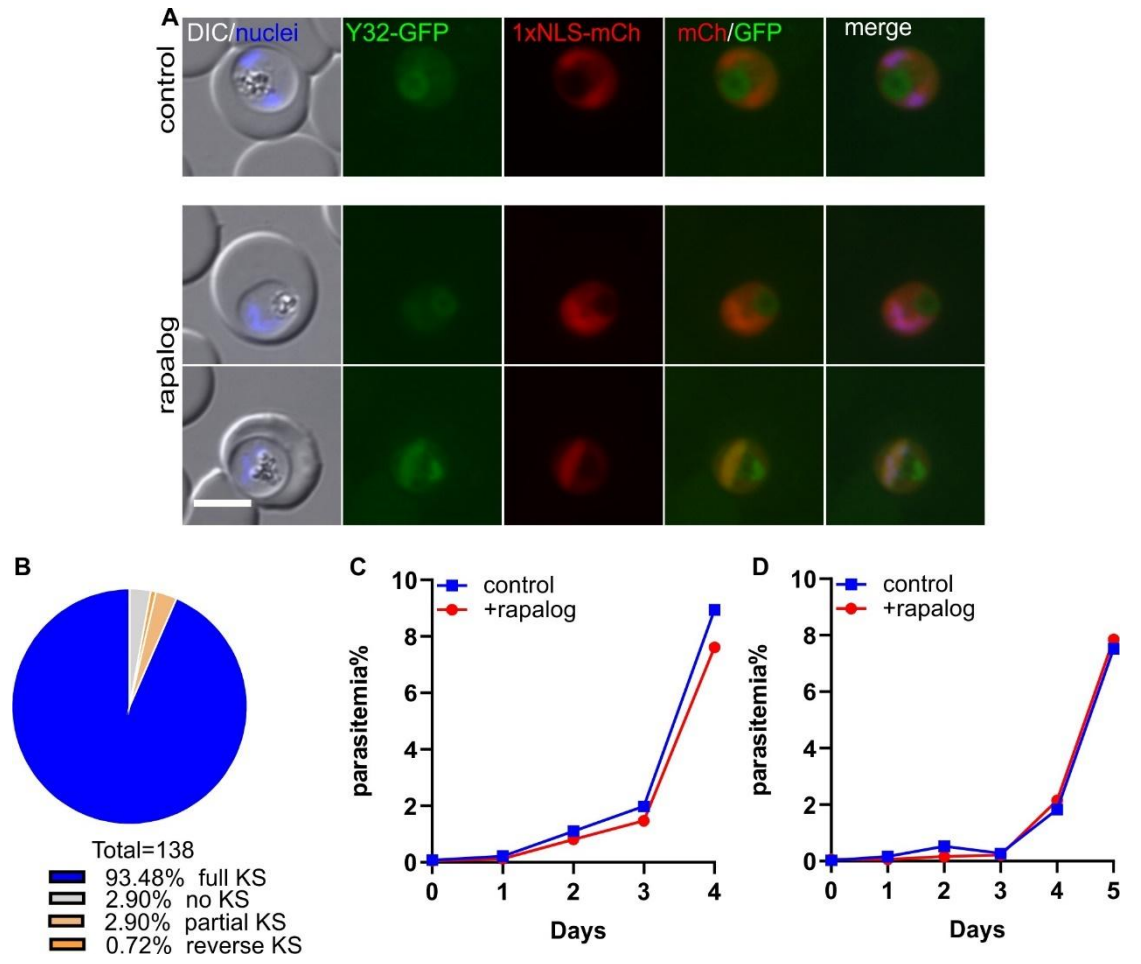


Figure 87. Knock sideways analysis of endogenous Y32 (PF3D7_0417900) tagged with 2xFKBP-GFP-2xFKBP. A) Representative live cell images of knock-in cell line Y32-2xFKBP-GFP-2xFKBP ('GFP') with an episomally expressed Lyn-FRB-mCherry mislocalizer. Representative images from 3 independent imaging sessions with at least 7 inspected fields of view. Both two rows show a parasite

with detectable GFP in the nucleus which was considered as full mislocalization ("full KS" in (B)). The cell culture was split into two dishes: one served as control without rapalog (control), and the other grown in the presence of 250 nM rapalog. The samples for live cell imaging were taken 24 h post addition of rapalog. Scale bar, 5 µm, DIC, differential interference contrast, mCh, mCherry, merge, overlay of GFP, mCh and nuclei. B) Pie chart shows quantification of knock sideways efficiency based on GFP localization following rapalog treatment. Quantification of knock sideways efficiency for Y32, based on the same experiments shown in (A). A total of 138 parasites were scored across 4 independent imaging sessions. KS status was evaluated 24 hours after rapalog addition. C-D) Growth curve of the Y32-NLS knock sideways. Parasite growth was assessed by flow cytometry in the presence (rapalog) or absence (control) of rapalog. Two independent replicates (both shown).

upon rapalog treatment (Figure 87A-B), supporting that the faint cytoplasmic signal shows the location of Y32-GFP. Growth curves revealed only minimal differences between rapalog-treated (inactivated Y32) and control parasites (Figure 87C-D), indicating that Y32 mislocalization does not affect parasite growth under standard *in vitro* conditions, and Y32 can therefore be considered dispensable for asexual blood stage development of the parasite.

3.27 Characterization of Y33 (PF3D7_0418300)

Y33 (Gene ID: PF3D7_0418300) is annotated in PlasmoDB as a conserved Plasmodium protein with unknown function. No significant sequence similarity or conserved domains were identified using BLAST, HHPred, or MotifScan.

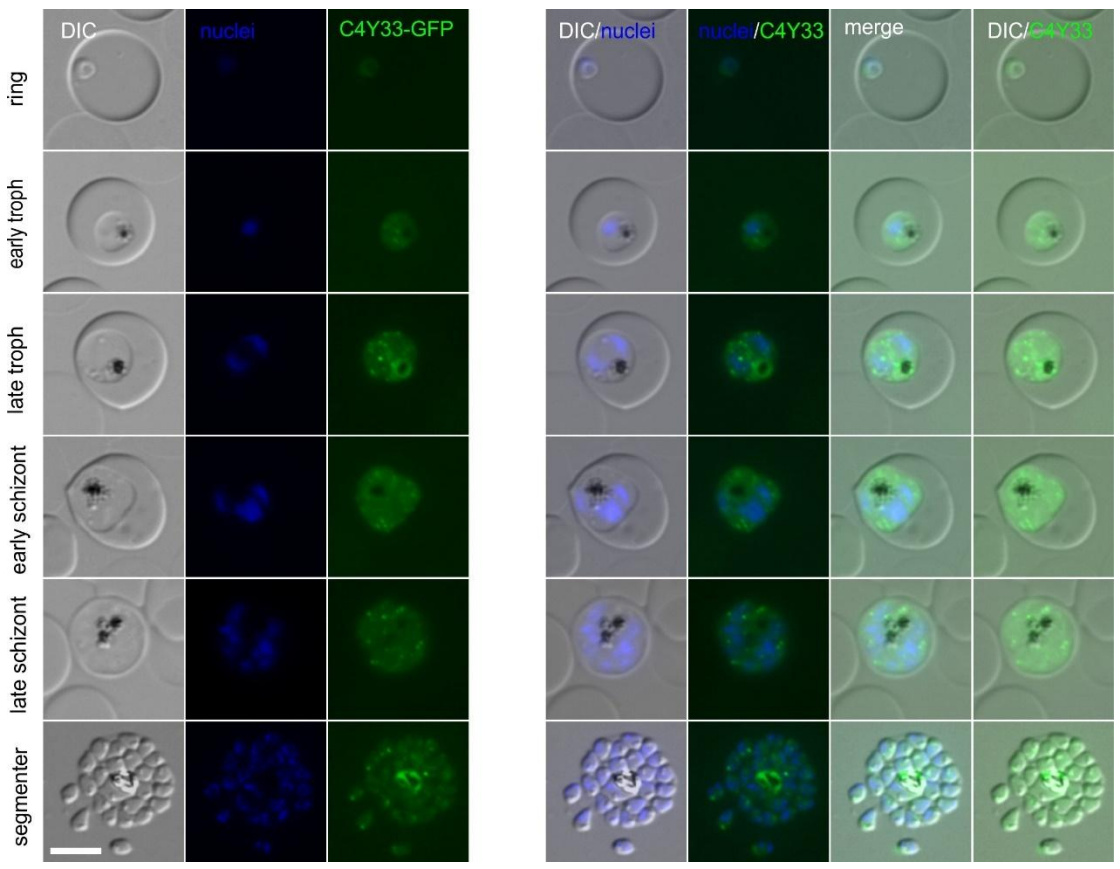


Figure 88. Localization of endogenously tagged candidate Y33 (PF3D7_0418300). Representative live cell fluorescence microscopy images of knock-in cell line Y33-2xFKBP-GFP-2xFKBP ('GFP'). The stages are indicated on the left of the panel. Representative images from 3 independent imaging sessions with at least 7 inspected fields of view. Parasite nuclei were stained with Hoechst33342. Scale bar 5 μ m, DIC, differential interference contrast; merge, overlay of DIC, GFP and nuclei.

In order to localize and functionally analyze Y33, the corresponding gene was modified using SLI (Birnbaum et al., 2017) so that the endogenous Y33 becomes fused with the multipurpose sandwich tag (2xFKBP-GFP-2xFKBP). Correct integration into the genome was confirmed by PCR across the 5'- and 3'- integration junctions and by PCR showing the absence of the original locus (Figure 11). Fluorescence microscopy of the Y33-2xFKBP-GFP-2xFKBP^{endo} parasite line revealed a punctate GFP signal in the

cytoplasm with an additional dispersed pool, consistent with localization to discrete cytoplasmic structures (Figure 88).

In order to assess the importance of Y33, the Y33-2xFKBP-GFP-2xFKBP^{endo} cell line was transfected with an episomal plasmid mediating expression of the NLS mislocalizer, permitting conditional inactivation using knock sideways. Representative live-cell microscopy confirmed that Y33-GFP efficiently mislocalized to nucleus upon rapalog treatment (Figure 89A). Mislocalization efficiency was determined by fluorescence microscopy 24 h after induction and indicated that >90% of cells showed full mislocalization of Y32 (no GFP fluorescence detected in the nucleus by microscopy) (Figure 89B). Growth assays revealed a moderate but consistent reduction in parasitemia (~50%) after knock sideways of Y33, indicating that Y33 contributes to efficient parasite growth, although it is not strictly essential for survival under standard *in vitro* conditions (Figure 89C-E).

We induced the knock sideways in synchronous ring stages to investigate the effect of Y33 inactivation during parasite development in asexual blood stages (Figure 90). We did not observe any difference between the parasites grown with rapalog and the control in the first cycle (10-48 hpi) but resulted in a mild reduction in the number of new rings generated. In the second cycle, the parasites again developed at similar rate until they reached the trophozoite stage, where the Y33 knock sideways parasites slowed in developmental (82 - 90 hpi) and again resulted in a lower parasitemia of progeny rings in the rapalog-treated parasites at 96-104 hpi and 106-114 hpi, but more profoundly than in the first cycle. It is not possible to determine whether the observed reduction in ring formation at later time points reflects a true defect in schizont egress or merozoite

invasion, or is simply a downstream consequence of impaired trophozoite development or formation of defective schizonts.

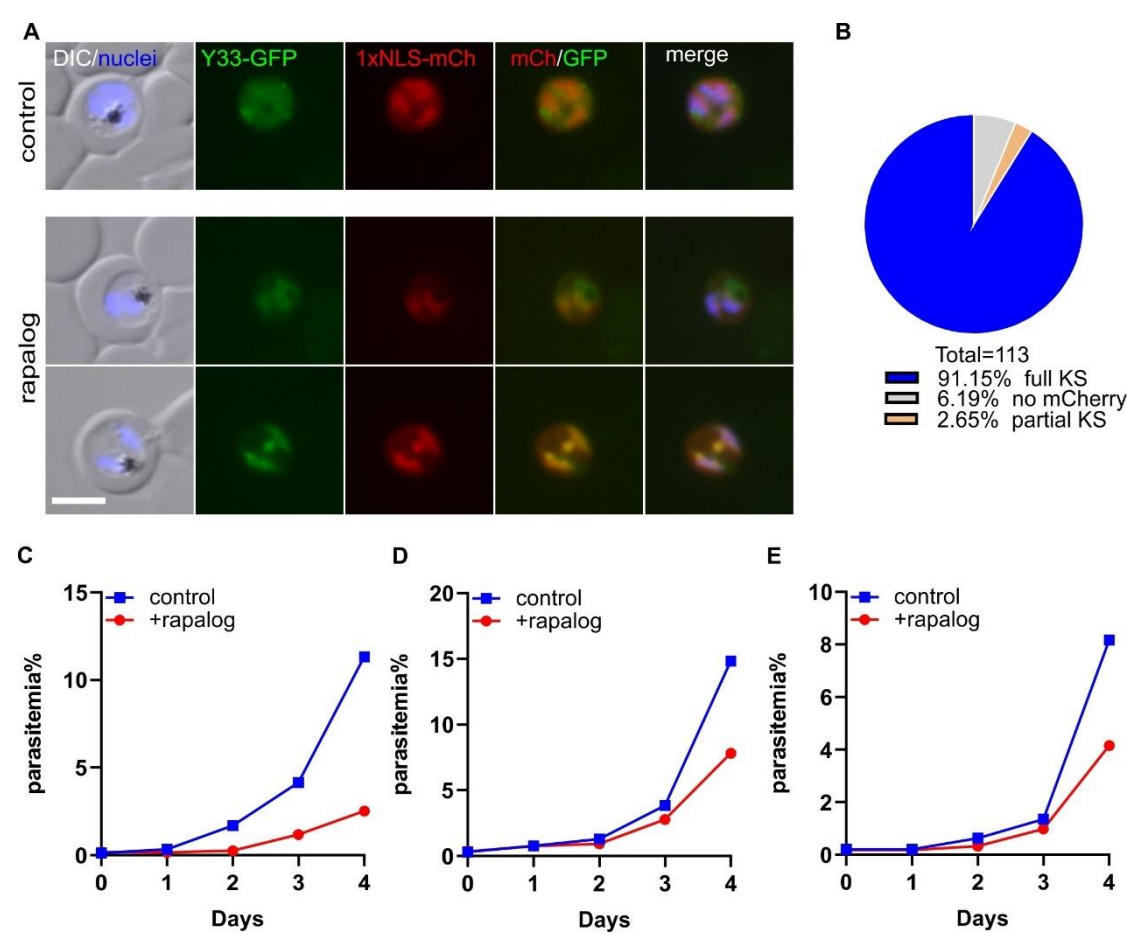


Figure 89. Knock sideways analysis of endogenous Y33 (PF3D7_0418300) tagged with 2xFKBP-GFP-2xFKBP. A) Representative live cell images of knock-in cell line Y33-2xFKBP-GFP-2xFKBP ('GFP') with an episomally expressed Lyn-FRB-mCherry mislocalizer. Representative images from 3 independent imaging sessions with at least 7 inspected fields of view. The bottom row shows a parasite with full KS (complete GFP mislocalization, "full KS" in (B)), while the top row shows a parasite with partial KS (incomplete GFP mislocalization. "partial KS" in (B)). The cell culture was split into two dishes: one served as control without rapalog (control), and the other grown in the presence of 250 nM rapalog. The samples for live cell imaging were taken 24 h post addition of rapalog. Scale bar, 5 μm, DIC, differential interference contrast, mCh, mCherry, merge, overlay of GFP, mCh and nuclei. B) Pie chart shows quantification of knock sideways efficiency based on GFP localization following rapalog treatment. Quantification of knock sideways efficiency for Y33, based on the same experiments shown in (A). A total of 113 parasites were scored across 4 independent imaging sessions. KS status was evaluated 24 hours after rapalog addition. C-E) Growth curve of the Y33-NLS knock sideways. Parasite growth was assessed by flow cytometry in the presence (rapalog) or absence (control) of rapalog. Two independent replicates (both shown).

In summary, Y33 is a cytoplasmic protein of unknown function that is important for parasite asexual development.

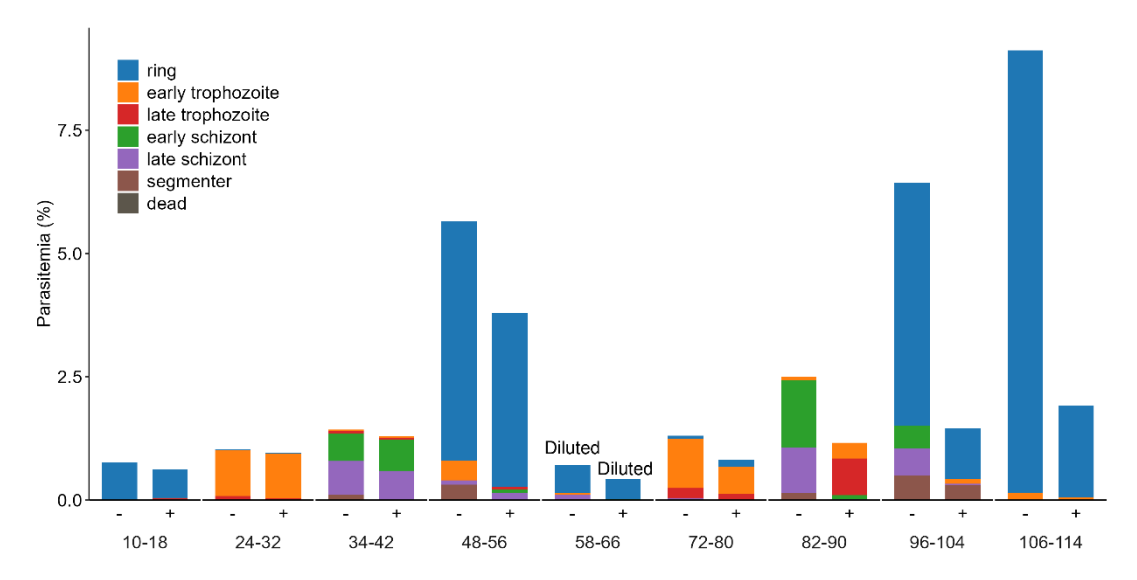


Figure 90. Stage assay of Y33-NLS knock sideways parasites following rapalog treatment. Synchronized parasites expressing a knock sideways version of Y33 were treated with rapalog and parasite stages were monitored every 10/14 hours in 5 days over two intraerythrocytic developmental cycles. Diluted: 1:10. Parasitemia (%) and the distribution of parasite stages were quantified by Giemsa-stained blood smears. Data shown are representative of two independent biological replicates.

3.28 Characterization of Y34 (PF3D7_0418900)

Y34 (Gene ID: PF3D7_0418900) is annotated as a conserved Plasmodium protein of unknown function. Similarity searches using BLAST, HHPred, and MotifScan did not identify any conserved domains or homologous proteins.

In order to localize and functionally analyze Y34, the corresponding gene was modified using SLI (Birnbaum et al., 2017) so that the endogenous Y34 becomes fused with the multipurpose sandwich tag (2xFKBP-GFP-2xFKBP). Correct integration into the genome was confirmed by PCR across the 5'- and 3'- integration junctions and by PCR showing absence of the original locus (Figure 11). Fluorescence microscopy of the Y34-2xFKBP-GFP-2xFKBP^{endo} parasite line revealed a cytoplasmic localization

pattern with some weak accumulations, with variable signal intensity between different parasites and across stages (Figure 91).

To assess its functional relevance, knock sideways was performed using the NLS mislocalizer. Upon rapalog treatment, Y34-GFP was successfully redirected to the nucleus (Figure 92A). Mislocalization efficiency was evaluated 24 h post-induction and showed that Y34-GFP was efficiently mislocalized to the nucleus in the majority of parasites (Figure 92B), indicating successful knock sideways. Growth curve analysis revealed approximately 40% reduction in parasite proliferation between rapalog-treated and control parasites (Figure 92C-E), indicating that Y34 is not essential for asexual blood-stage development under standard *in vitro* conditions.

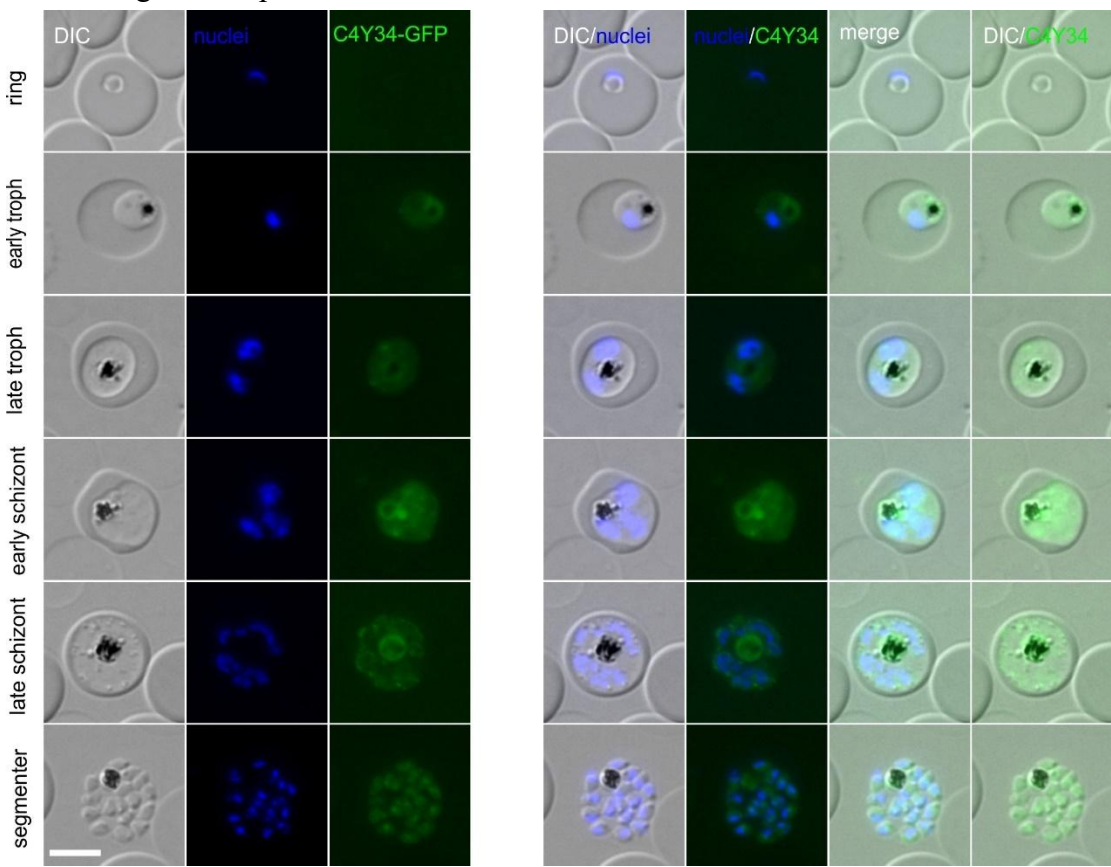


Figure 91. Localization of endogenously tagged candidate Y34 (PF3D7_0418900). Representative live cell fluorescence microscopy images of knock-in cell line Y34-2xFKBP-GFP-2xFKBP ('GFP'). The stages are indicated on the left of the panel. Representative images from 3 independent imaging sessions with at least 7 inspected fields of view. Parasite nuclei were stained with Hoechst33342. Scale bar 5 μ m, DIC, differential interference contrast; merge, overlay of DIC, GFP and nuclei.

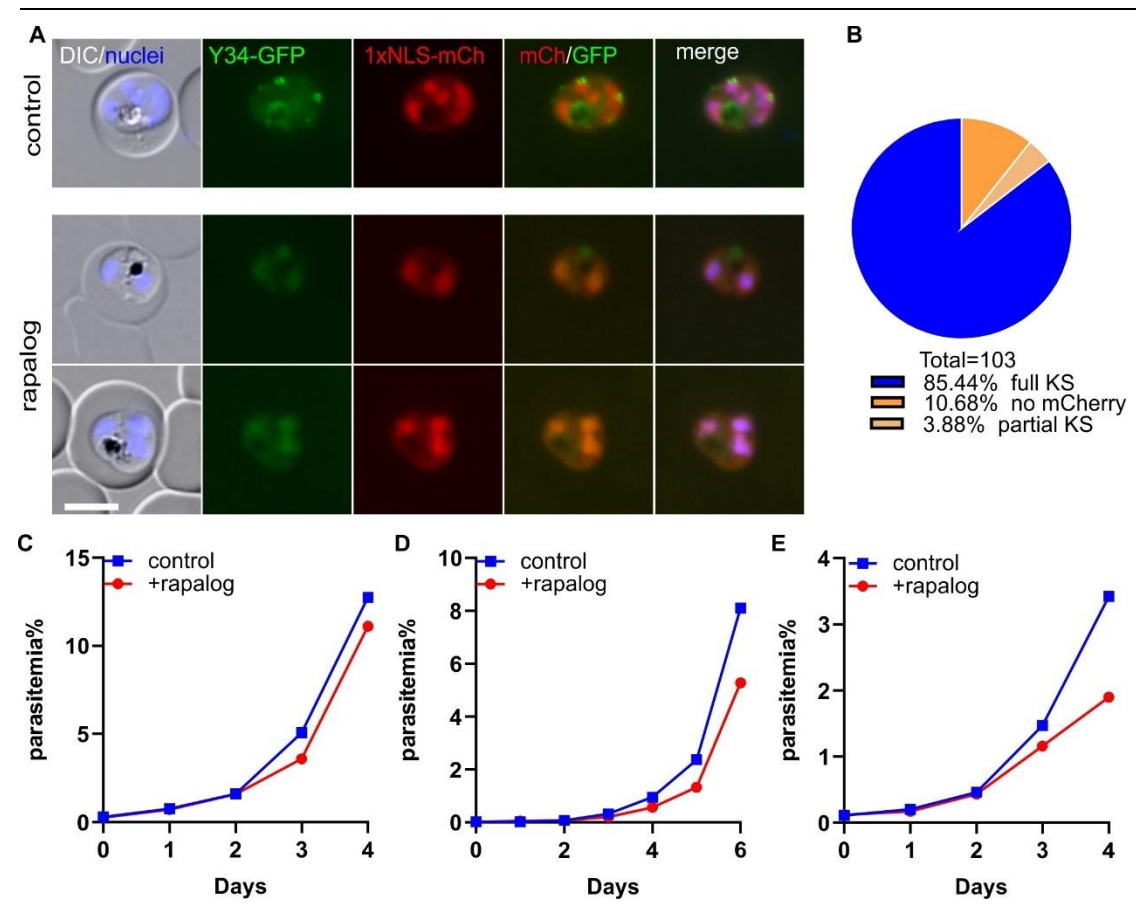


Figure 92. Knock sideways anlysis of endogenous Y34 (PF3D7_0418900) tagged with 2xFKBP-GFP-2xFKBP. A) Representative live cell images of knock-in cell line Y34-2xFKBP-GFP-2xFKBP ('GFP') with an episomally expressed Lyn-FRB-mCherry mislocalizer. Representative images from 3 independent imaging sessions with at least 7 inspected fields of view. The top row shows a parasite with full KS (complete GFP mislocalization, "full KS" in (B)), while the bottom row shows a parasite with partial KS (incomplete GFP mislocalization. "partial KS" in (B)). The cell culture was split into two dishes: one served as control without rapalog (control), and the other grown in the presence of 250 nM rapalog. The samples for live cell imaging were taken 24 h post addition of rapalog. Scale bar, 5 μm, DIC, differential interference contrast, mCh, mCherry, merge, overlay of GFP, mCh and nuclei. B) Pie chart shows quantification of knock sideways efficiency based on GFP localization following rapalog treatment. Quantification of knock sideways efficiency for Y34, based on the same experiments shown in (A). A total of 103 parasites were scored across 3 independent imaging sessions. KS status was evaluated 24 hours after rapalog addition. C-E) Growth curve of the Y34-NLS knock sideways. Parasite growth was assessed by flow cytometry in the presence (rapalog) or absence (control) of rapalog. Three independent replicates (all shown).

3.29 Characterization of Y35 (PF3D7 0419000)

Y35 (Gene ID: PF3D7_0419000) is annotated as a conserved Plasmodium protein of unknown function. Similarity searches using BLAST, HHPred, and MotifScan did not reveal any significant similarity to known proteins or domains.

In order to localize and functionally analyze Y35, the corresponding gene was modified using SLI (Birnbaum et al., 2017) so that the endogenous Y35 becomes fused with the multipurpose sandwich tag (2xFKBP-GFP-2xFKBP). Correct integration into the genome was confirmed by PCR across the 5'- and 3'- integration junctions and by a PCR showing the absence of the original locus (Figure 11). Despite successful genomic integration, no GFP signal was detected by live-cell fluorescence microscopy at any stage of the asexual blood cycle (Figure 93), suggesting that Y35 is expressed at very low levels.

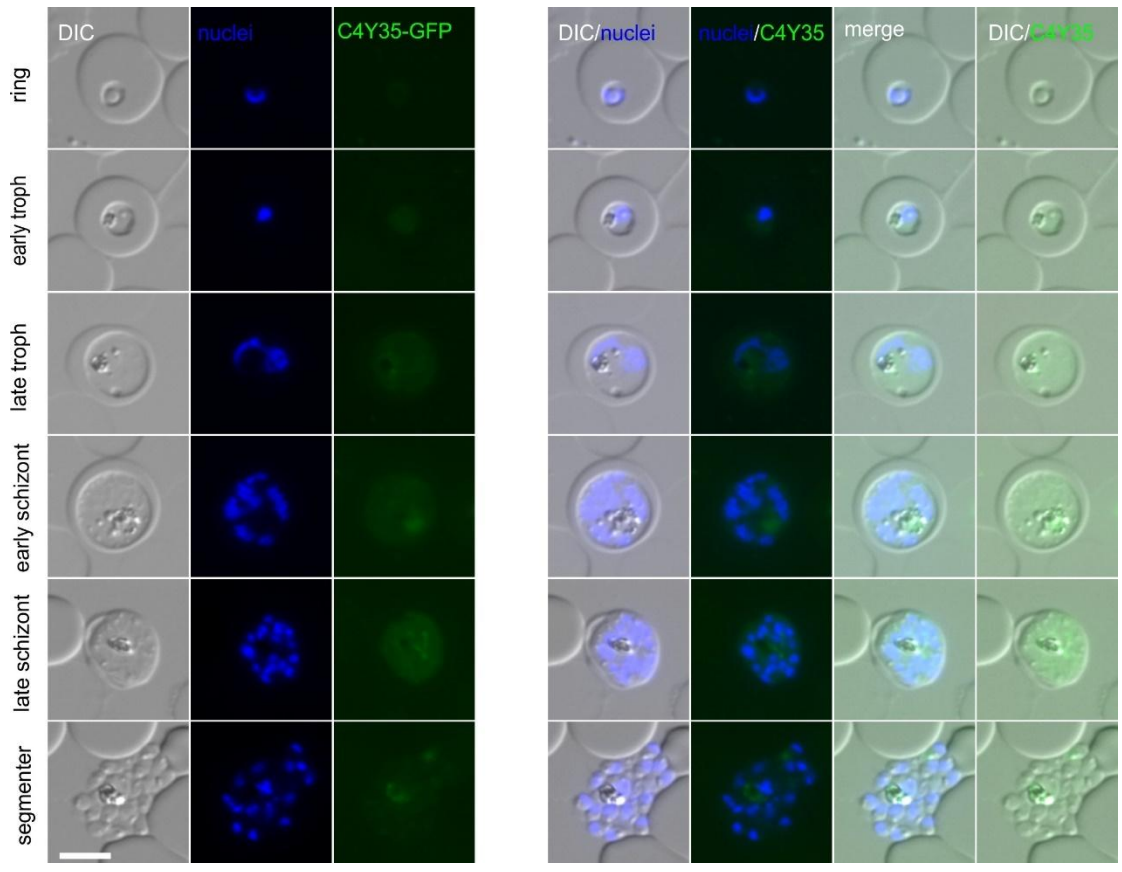


Figure 93. Localization of endogenously tagged candidate Y35 (PF3D7_0419000). Representative live cell fluorescence microscopy images of knock-in cell line Y35-2xFKBP-GFP-2xFKBP ('GFP'). The stages are indicated on the left of the panel. Representative images from 3 independent imaging sessions

with at least 7 inspected fields of view. Parasite nuclei were stained with Hoechst33342. Scale bar 5 μ m, DIC, differential interference contrast; merge, overlay of DIC, GFP and nuclei.

To assess whether Y35 is needed for parasite viability, we performed knock sideways using both, a cell line where the Lyn mislocalizer was used (Figure 94) and one where and the NLS mislocalizer was used (Figure 95). However, since Y35-GFP expression was undetectable by fluorescence microscopy under standard imaging conditions, we were unable to assess knock sideways efficiency or confirm successful mislocalization. However, interestingly a signal became apparent in the parasite nucleus after addition of rapalog to the cell line with the NLS mislocalizer, indicating that Y35 may under physiological conditions be distributed in the parasite cytoplasm (Figure 95 arrow). Across three independent biological replicates, the Y35-Lyn line treated with rapalog consistently showed a modest reduction in growth compared to the control parasites of about 40-60% to that of the controls at the end of the assay (Figure 94B-D). Interestingly, the Y35-NLS line showed a similar reduction with final parasitemia between 30 and 60% to that of the control cultures (Figure 95B-D). These findings indicate that both mislocalization to the nucleus and to the plasma membrane impair the function of Y35 and that Y35 is a low-abundance protein with a functional contributing to parasite growth under the tested conditions.

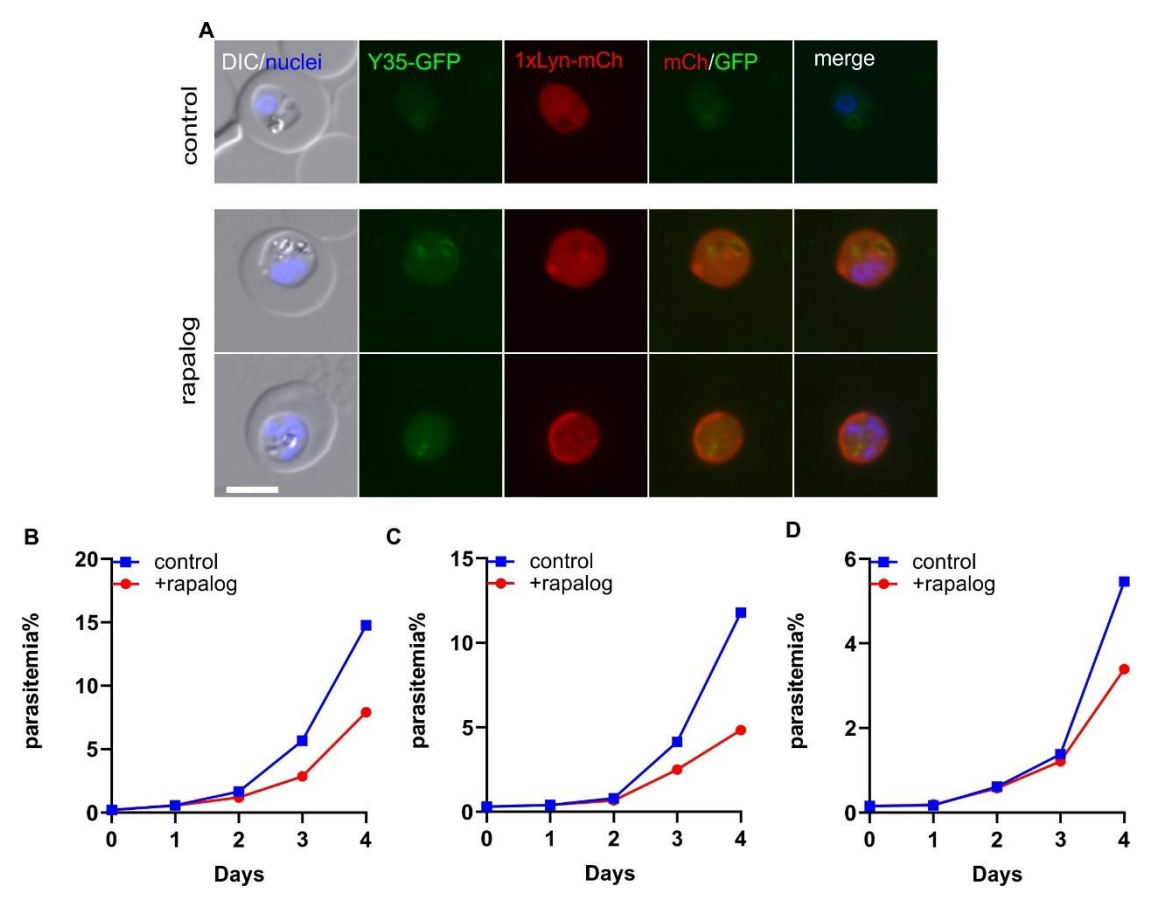


Figure 94. Knock sideways analysis of endogenous Y35 (PF3D7_0419000) tagged with 2xFKBP-GFP-2xFKBP. A) Representative live cell images of knock-in cell line Y35-2xFKBP-GFP-2xFKBP ('GFP') with an episomally expressed Lyn-FRB-mCherry mislocalizer. Representative images from 3 independent imaging sessions with at least 7 inspected fields of view. The cell culture was split into two dishes: one served as control without rapalog (control), and the other grown in the presence of 250 nM rapalog. The samples for live cell imaging were taken 24 h post addition of rapalog. Scale bar, 5 μ m, DIC, differential interference contrast, mCh, mCherry, merge, overlay of GFP, mCh and nuclei. Growth curve of the Y35-Lyn knock sideways. Parasite growth was assessed by flow cytometry in the presence (rapalog) or absence (control) of rapalog. Three independent replicates (all shown).

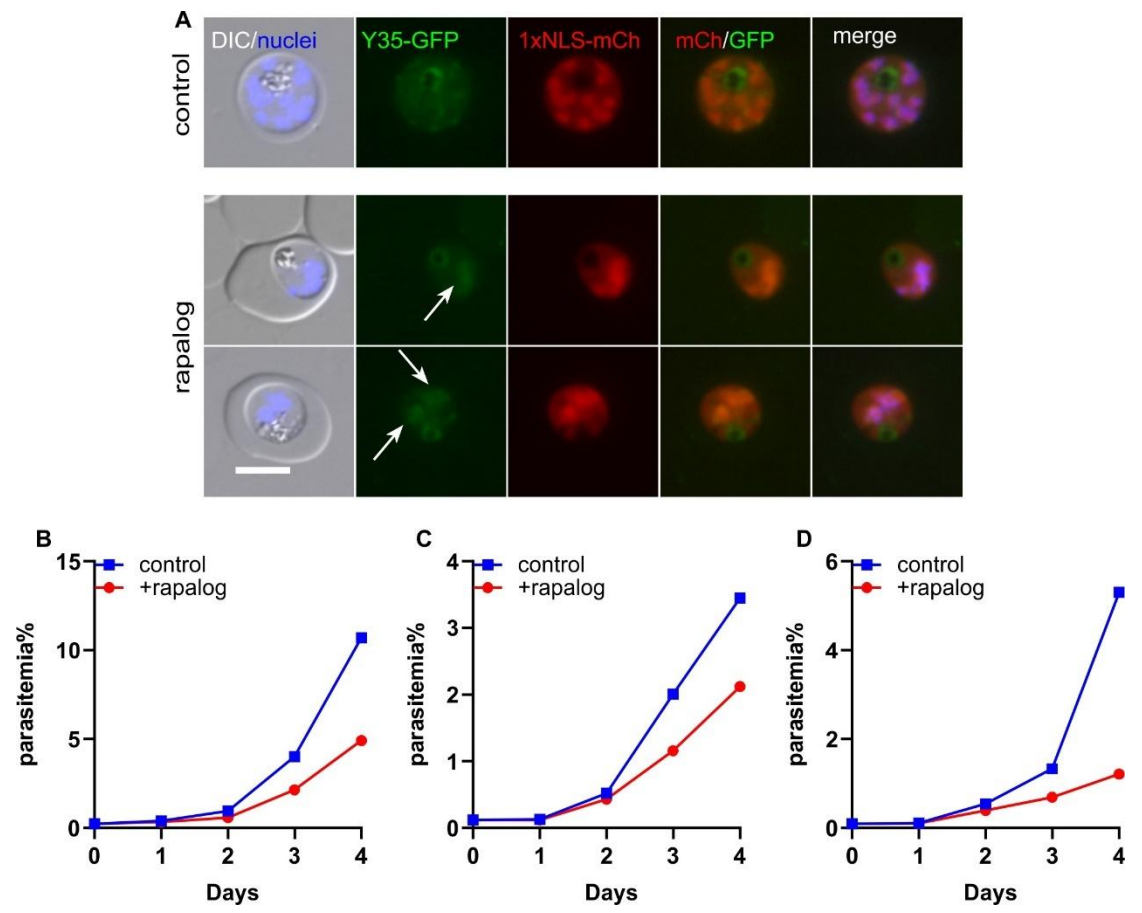


Figure 95. Knock sideways analysis of endogenous Y35 (PF3D7_0419000) tagged with 2xFKBP-GFP-2xFKBP. A) Representative live cell images of knock-in cell line Y35-2xFKBP-GFP-2xFKBP ('GFP') with an episomally expressed NLS-FRB-mCherry mislocalizer. Representative images from 3 independent imaging sessions with at least 7 inspected fields of view. The cell culture was split into two dishes: one served as control without rapalog (control), and the other grown in the presence of 250 nM rapalog. The samples for live cell imaging were taken 24 h post addition of rapalog. Scale bar, 5 μm, DIC, differential interference contrast, mCh, mCherry, merge, overlay of GFP, mCh and nuclei. Growth curve of the Y35-NLS knock sideways. Parasite growth was assessed by flow cytometry in the presence (rapalog) or absence (control) of rapalog. Three independent replicates (all shown).

3.30 Characterization of Y38 (PF3D7_0420600)

Y38 (Gene ID: PF3D7_0420600) is annotated in PlasmoDB as a putative apicomplexan kinetochore protein 6 (AKiT6). At the time of candidate selection, this gene had not yet been annotated as an AKiT. The AKiT family represents a group of Apicomplexa-specific kinetochore proteins that lack homology to canonical eukaryotic kinetochore components but are believed to perform analogous functions in chromosome

segregation during mitosis (Ishii and Akiyoshi, 2022). While it has since been studied in *P. berghei* (Brusini et al., 2022), no data are currently available for its function in *P. falciparum*, justifying its inclusion in our screen.

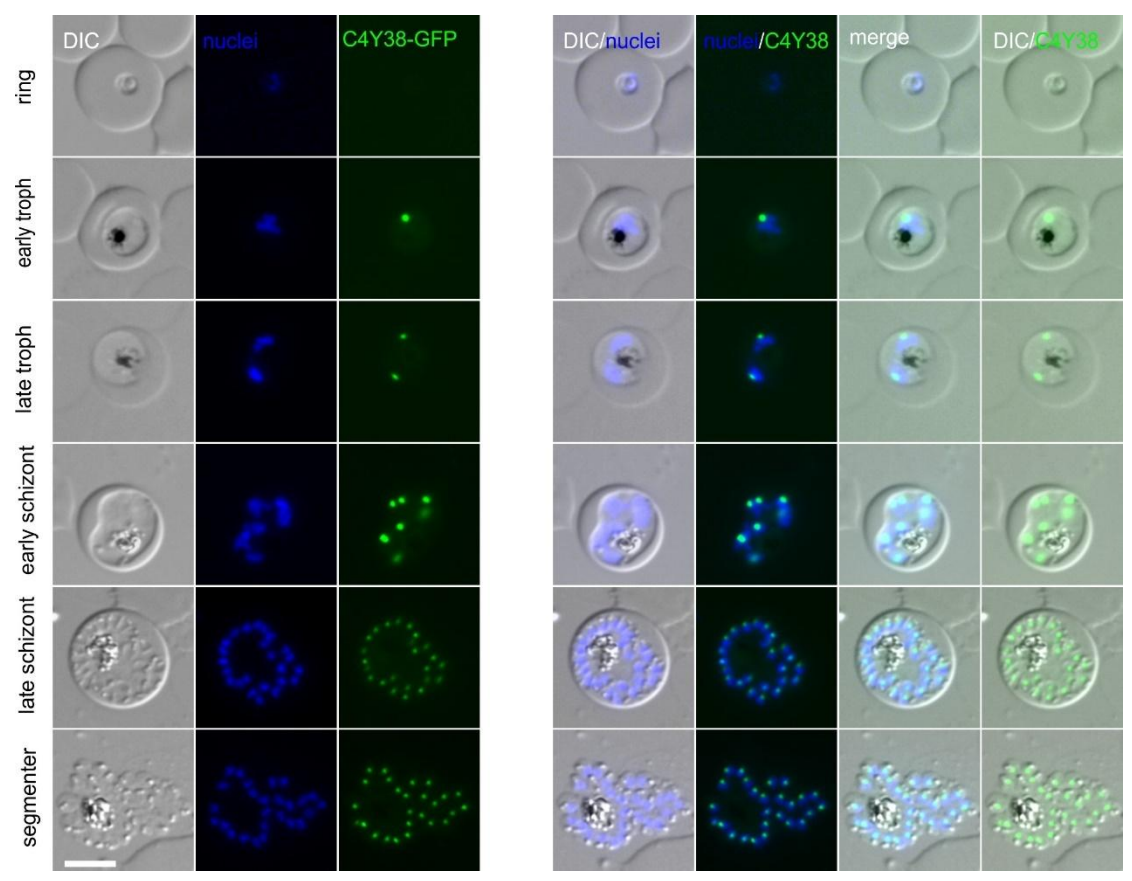


Figure 96. Localization of endogenously tagged candidate Y38 (PF3D7_0420600). Representative live cell fluorescence microscopy images of knock-in cell line Y38-2xFKBP-GFP-2xFKBP ('GFP'). The stages are indicated on the left of the panel. Representative images from 3 independent imaging sessions with at least 7 inspected fields of view. Parasite nuclei were stained with Hoechst33342. Scale bar 5 μm, DIC, differential interference contrast; merge, overlay of DIC, GFP and nuclei.

In order to localize and functionally analyze Y38, the corresponding gene was modified using SLI (Birnbaum et al., 2017) so that the endogenous Y38 becomes fused with the multipurpose sandwich tag (2xFKBP-GFP-2xFKBP). Correct integration into the genome was confirmed by PCR across the 5'- and 3'- integration junctions and the absence of the original locus (Figure 11). Live-cell fluorescence microscopy of the Y38-2xFKBP-GFP-2xFKBP^{endo} parasite line revealed distinct punctate nuclear foci,

typically one per nucleus on the plasma membrane facing side (Figure 96). This has been observed before for kinetochore proteins, e.g. SKA1/3 (Kimmel et al., 2023) and is consistent with Y38 being located in mitotic substructures. Co-localization with tubulin confirmed that Y38-GFP overlaps with mitotic spindle microtubules (Figure 97), supporting its proposed function as a kinetochore- or spindle pole-associated protein (Brusini et al., 2022).

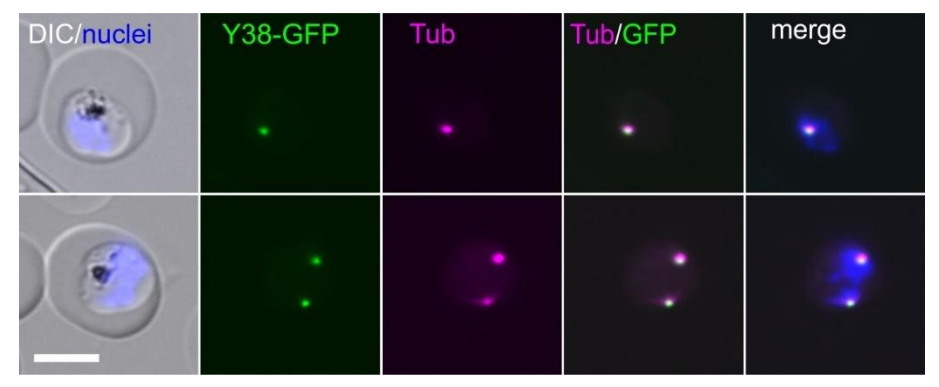


Figure 97. Y38 (PF3D7_0420600) co-localization with Tubulin. Representative live cell images of knock-in cell line of Y38-2xFKBP-GFP-2xFKBP (green) with staining TubulinTrackerTM deep red (purple). Representative images from 3 independent imaging sessions with at least 7 inspected fields of view. Parasite nuclei were stained with Hoechst33342. Scale bar 5 μm, DIC, differential interference contrast; merge, overlay of Tub, GFP and nuclei.

To assess the functional importance of Y38, we performed knock sideways using the Lyn mislocalizer. Upon rapalog treatment, Y38-GFP was partially redirected to the nucleus (Figure 98A). Microscopy-based classification of 51 rapalog-treated parasites revealed that 45.10% exhibited full KS, characterized by clear mislocalization of GFP signal to the parasite periphery (Figure 98B). Additionally, 35.29% showed partial KS, 15.69% displayed reverse KS, and 3.92% showed no mCherry signal (Figure 98B). The growth curve using the Lyn-based knock sideways system showed a very strong and consistent growth inhibition across three independent biological replicates in the rapalog treated parasites (Figure 98C-E), despite the imperfect knock sideways efficiency. While control parasites exhibited robust replication, parasitemia in the rapalog-treated cultures remained nearly static throughout the 4-day assay, indicating a

critical role for Y38 in parasite proliferation, suggesting that Y38 is essential for asexual blood-stage proliferation.

Taken together, our data confirm that Y38 is a nuclear, kinetochore-associated protein, whose localization and essentiality are fully consistent with its annotation as a putative apicomplexan kinetochore protein 6.

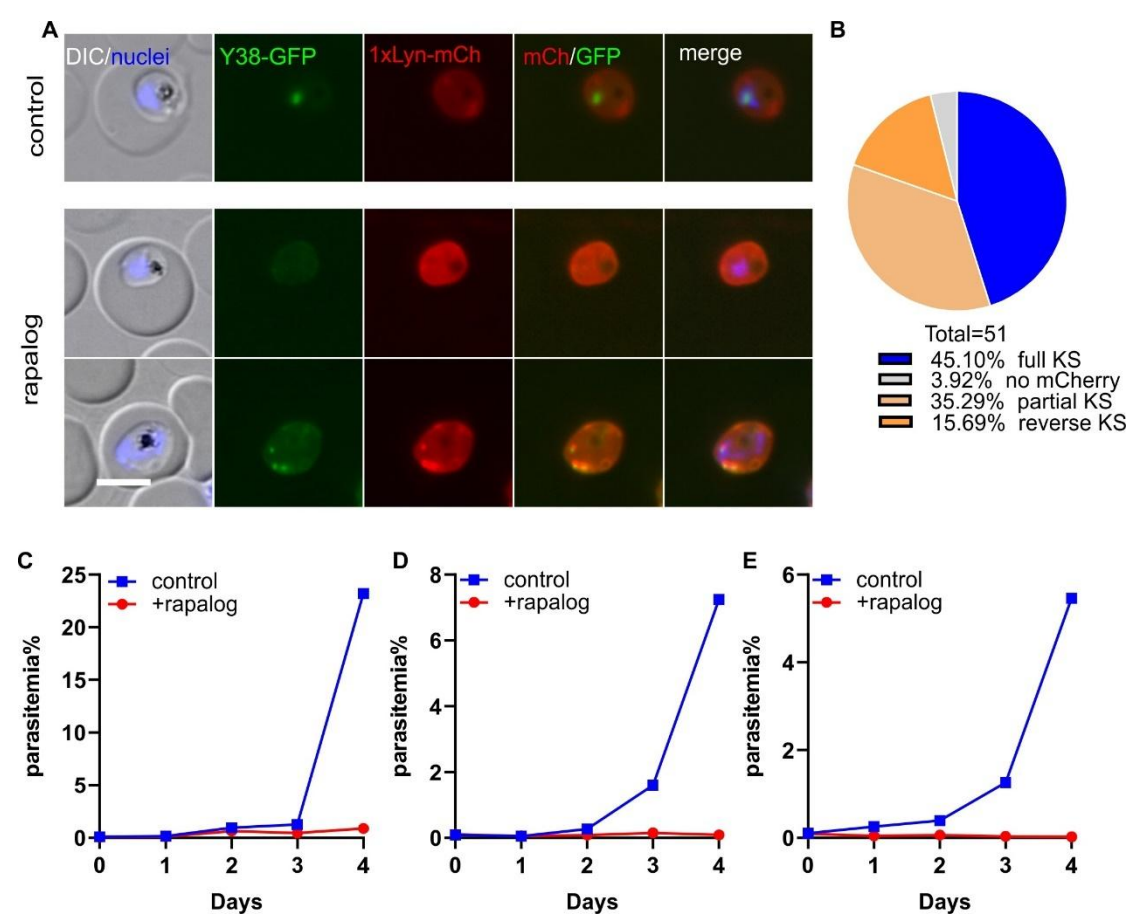


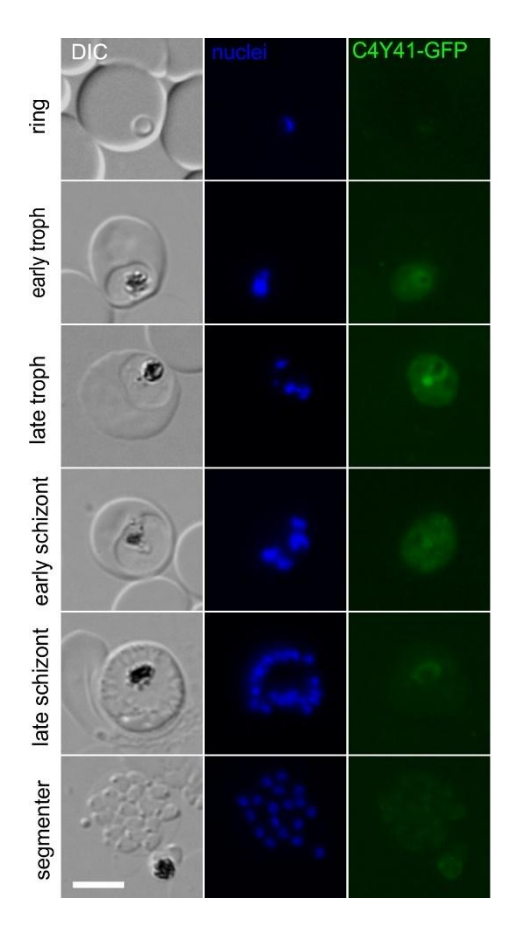
Figure 98. Knock sideways analysis of endogenous Y38 (PF3D7_0420600) tagged with 2xFKBP-GFP-2xFKBP. A) Representative live cell images of knock-in cell line Y38-2xFKBP-GFP-2xFKBP ('GFP') with an episomally expressed Lyn-FRB-mCherry mislocalizer. Representative images from 3 independent imaging sessions with at least 7 inspected fields of view. The top row shows a parasite with full KS (complete GFP mislocalization, "full KS" in (B)), while the bottom row shows a parasite with partial KS (incomplete GFP mislocalization. "partial KS" in (B)). The cell culture was split into two dishes: one served as control without rapalog (control), and the other grown in the presence of 250 nM rapalog. The samples for live cell imaging were taken 24 h post addition of rapalog. Scale bar, 5 μm, DIC, differential interference contrast, mCh, mCherry, merge, overlay of GFP, mCh and nuclei. B) Pie chart shows quantification of knock sideways efficiency based on GFP localization following rapalog treatment. Quantification of knock sideways efficiency for Y38, based on the same experiments shown

in (A). A total of 103 parasites were scored across 3 independent imaging sessions. KS status was evaluated 24 hours after rapalog addition. Growth curve of the Y38-Lyn knock sideways. Parasite growth was assessed by flow cytometry in the presence (rapalog) or absence (control) of rapalog. Three independent replicates (all shown).

3.31 Characterization of Y41 (PF3D7_0422600)

Y41 (Gene ID: PF3D7_0422600) is annotated in PlasmoDB as a conserved Plasmodium protein with unknown function. Similarity searches using BLAST, HHPred, and MotifScan did not identify any known domains or homologous proteins.

In order to localize and functionally analyze Y41, the corresponding gene was modified using SLI (Birnbaum et al., 2017) so that the endogenous Y41 becomes fused with the multipurpose sandwich tag (2xFKBP-GFP-2xFKBP). Correct integration into the genome was confirmed by PCR across the 5'- and 3'-integration junctions and by the absence of a PCR product for the original locus (Figure 11). Live-cell fluorescence



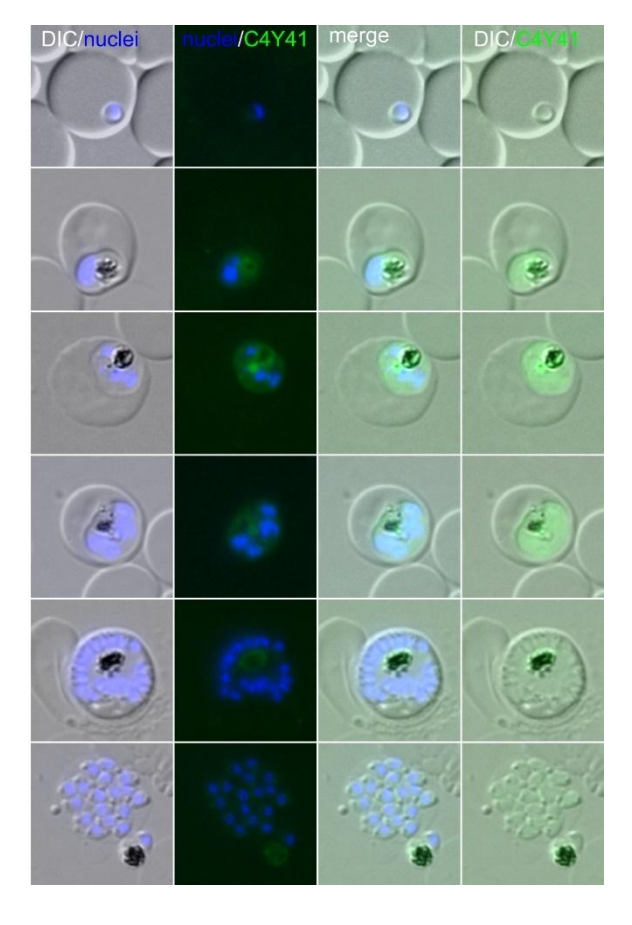


Figure 99. Localization of endogenously tagged candidate Y41 (PF3D7_0422600). Representative live cell fluorescence microscopy images of knock-in cell line Y41-2xFKBP-GFP-2xFKBP ('GFP'). The stages are indicated on the left of the panel. Representative images from 3 independent imaging sessions with at least 7 inspected fields of view. Parasite nuclei were stained with Hoechst33342. Scale bar 5 μ m, DIC, differential interference contrast; merge, overlay of DIC, GFP and nuclei.

microscopy of the Y41-2xFKBP-GFP-2xFKBP^{endo} line revealed a diffuse cytoplasmic localization with no apparent association with specific organelles or subcellular structures (Figure 99).

In order to assess the importance of Y41, the Y41-2xFKBP-GFP-2xFKBP^{endo} cell line was transfected with an episomal plasmid expressing the NLS mislocalizer, allowing conditional inactivation using the knock sideways system. Representative live-cell fluorescence microscopy showed that Y41-GFP efficiently mislocalized to the nucleus upon rapalog treatment (Figure 100A). Mislocalization efficiency was quantified 24 hours post-induction by microscopy, revealing that 96.27% of cells exhibited full nuclear mislocalization, while 3.73% showed no mCherry signal (Figure 100B).

Growth curve analysis following rapalog-induced mislocalization revealed no significant growth defect. Parasites treated with rapalog showed almost identical proliferation to untreated controls in two replicates (Figure 100C-D). These findings indicate that Y41 is dispensable for asexual blood-stage growth under standard *in vitro* conditions, and its function is not needed for parasite replication during this life cycle stage.

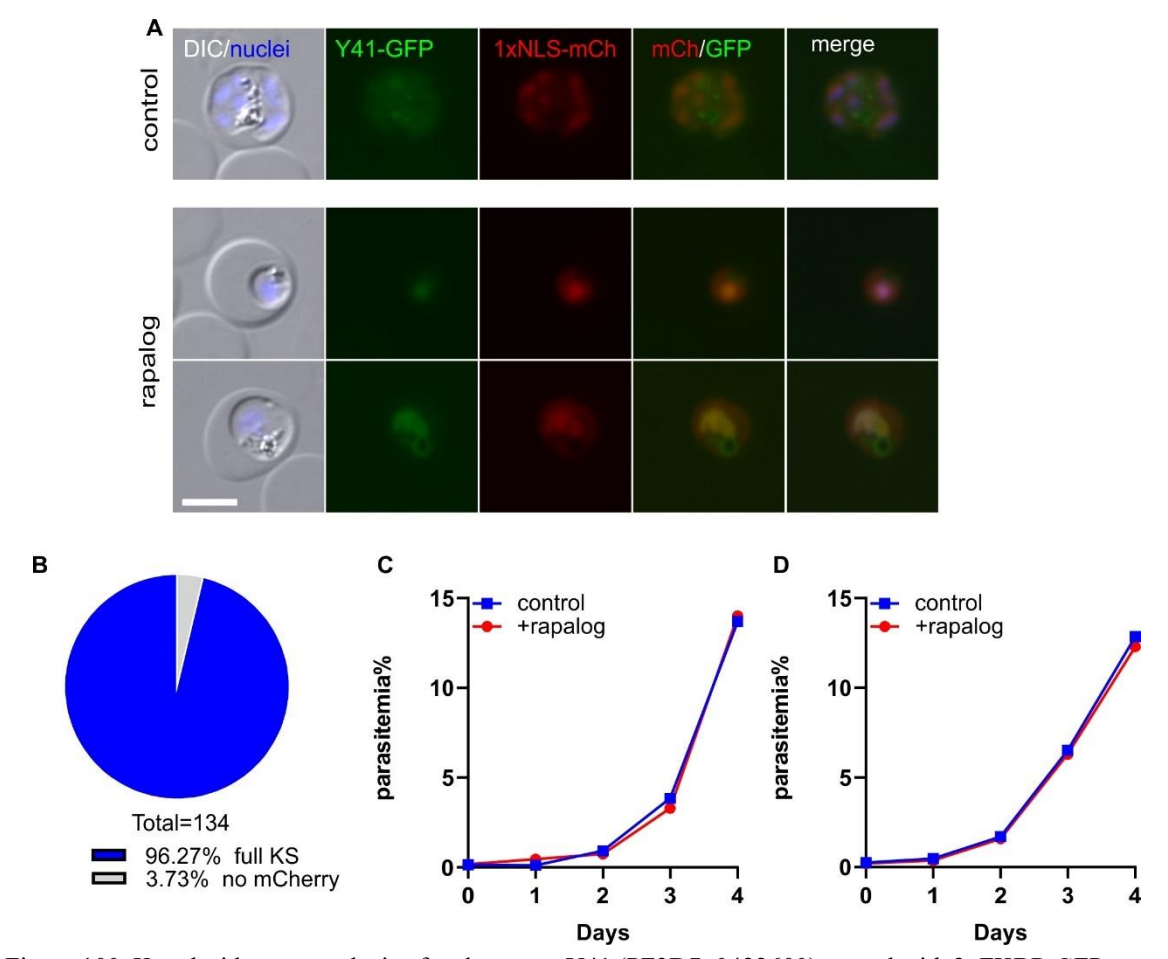


Figure 100. Knock sideways analysis of endogenous Y41 (PF3D7_0422600) tagged with 2xFKBP-GFP-2xFKBP. A) Representative live cell images of knock-in cell line Y41-2xFKBP-GFP-2xFKBP ('GFP') with an episomally expressed NLS-FRB-mCherry mislocalizer. Representative images from 3 independent imaging sessions with at least 7 inspected fields of view. Both two rows show a parasite with full KS (complete GFP mislocalization, "full KS" in (B)). The cell culture was split into two dishes: one served as control without rapalog (control), and the other grown in the presence of 250 nM rapalog. The samples for live cell imaging were taken 24 h post addition of rapalog. Scale bar, 5 μm, DIC, differential interference contrast, mCh, mCherry, merge, overlay of GFP, mCh and nuclei. B) Pie chart shows quantification of knock sideways efficiency based on GFP localization following rapalog treatment. Quantification of knock sideways efficiency for Y41, based on the same experiments shown

in (A). A total of 176 parasites were scored across 5 independent imaging sessions. KS status was evaluated 24 hours after rapalog addition. C-D) Growth curve of the Y41-NLS knock sideways. Parasite growth was assessed by flow cytometry in the presence (rapalog) or absence (control) of rapalog. Two independent replicates (both shown).

3.32 Characterization of Y42 (PF3D7 0423000)

Y42 (Gene ID: PF3D7_0423000) is annotated in PlasmoDB as a conserved Plasmodium protein of unknown function. Bioinformatic predictions using BLAST, HHPred, and MotifScan failed to identify any significant similarities with known homologs or conserved domains for Y42.

In order to localize and functionally analyze Y42, the corresponding gene was modified using SLI (Birnbaum et al., 2017) so that the endogenous Y42 becomes fused with the multipurpose sandwich tag (2xFKBP-GFP-2xFKBP). Correct integration into the genome was confirmed by PCR across the 5'- and 3'- integration junctions and by PCR showing absence of the original locus (Figure 11). Fluorescence microscopy of the Y42-2xFKBP-GFP-2xFKBP^{endo} parasite line revealed a strong nuclear GFP signal throughout the asexual cycle without apparent focal accumulations (Figure 101).

In order to assess the importance of Y42, the Y42-2xFKBP-GFP-2xFKBP^{endo} cell line was transfected with an episomal plasmid expressing the Lyn-FRB-mCherry mislocalizer, allowing conditional inactivation using the knock sideways system. Live-cell fluorescence microscopy showed that upon rapalog treatment, Y42-GFP displayed successful mislocalization (Figure 102A). Mislocalization efficiency was quantified 24 hours post-induction by microscopy, revealing that 87.26% of cells exhibited full mislocalization of Y42 to the nucleus (Figure 102B).

Growth curves revealed only minimal differences between rapalog-treated and control parasites in two independent replicates (Figure 102C-D), indicating that Y42 plays no important role during asexual blood-stage development.

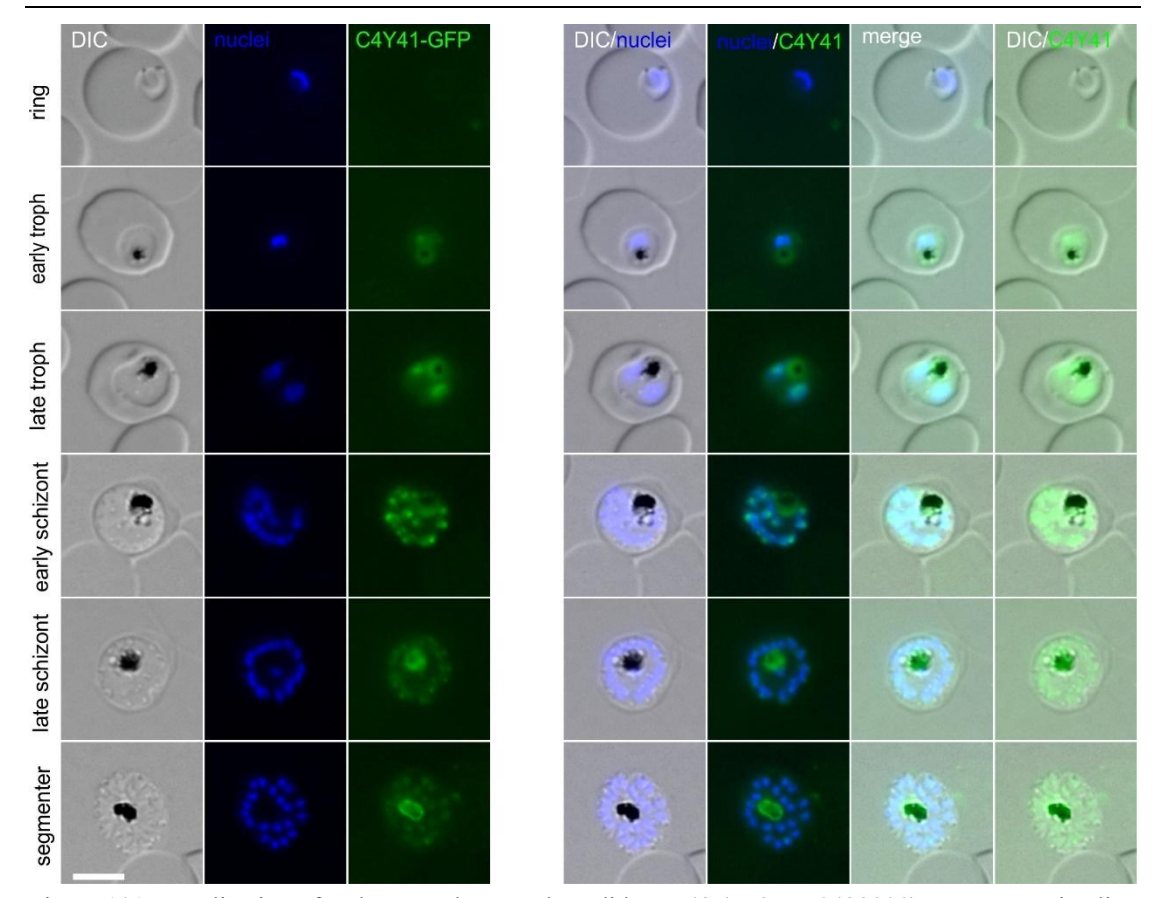


Figure 101. Localization of endogenously tagged candidate Y42 (PF3D7_0423000). Representative live cell fluorescence microscopy images of knock-in cell line Y42-2xFKBP-GFP-2xFKBP ('GFP'). The stages are indicated on the left of the panel. Representative images from 3 independent imaging sessions with at least 7 inspected fields of view. Parasite nuclei were stained with Hoechst33342. Scale bar 5 μ m, DIC, differential interference contrast; merge, overlay of DIC, GFP and nuclei.

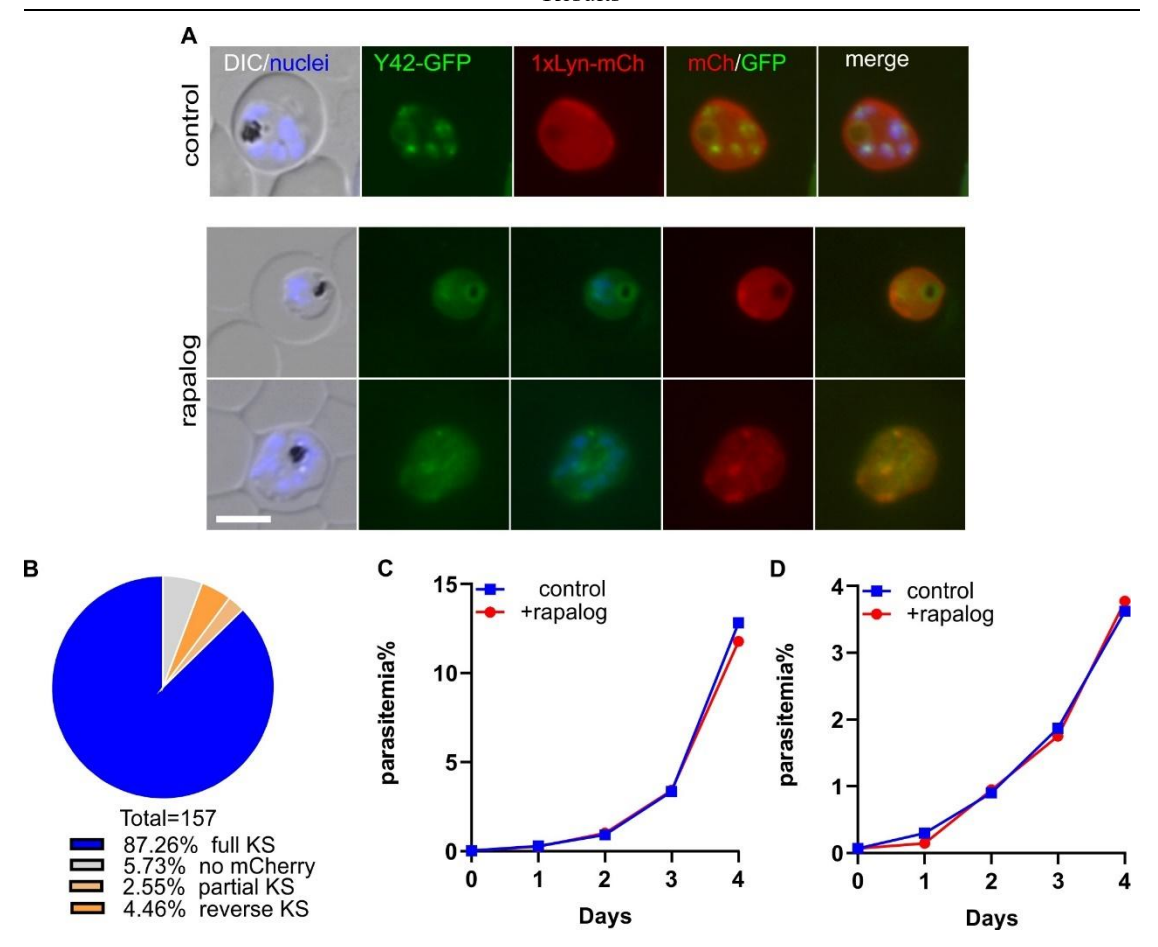


Figure 102. Knock sideways analysis of endogenous Y42 (PF3D7_0423000) tagged with 2xFKBP-GFP-2xFKBP. A) Representative live cell images of knock-in cell line Y42-2xFKBP-GFP-2xFKBP ('GFP') with an episomally expressed Lyn-FRB-mCherry mislocalizer. Representative images from 3 independent imaging sessions with at least 7 inspected fields of view. The top row shows a parasite with full KS (complete GFP mislocalization, "full KS" in (B)), while the bottom row shows a parasite with partial KS (incomplete GFP mislocalization. "partial KS" in (B)). The cell culture was split into two dishes: one served as control without rapalog (control), and the other grown in the presence of 250 nM rapalog. The samples for live cell imaging were taken 24 h post addition of rapalog. Scale bar, 5 μm, DIC, differential interference contrast, mCh, mCherry, merge, overlay of GFP, mCh and nuclei. B) Pie chart shows quantification of knock sideways efficiency based on GFP localization following rapalog treatment. Quantification of knock sideways efficiency for Y42, based on the same experiments shown in (A). A total of 103 parasites were scored across 3 independent imaging sessions. KS status was evaluated 24 hours after rapalog addition. C-D) Growth curve of the Y42-Lyn knock sideways. Parasite growth was assessed by flow cytometry in the presence (rapalog) or absence (control) of rapalog. Two independent replicates (both shown).

3.33 Characterization of Y43 (PF3D7_0423200)

Y43 (Gene ID: PF3D7_0423200) is annotated in PlasmoDB as a putative BSD-domain-containing protein. BSD domains (BTF2-like transcription factor, Synapse-associated protein, and DOS2) are α-helical structural motifs implicated in transcriptional regulation, RNA stability, and nuclear protein complex assembly in other eukaryotes (Doerks et al., 2002). However, their function in *Plasmodium* remains largely uncharacterized.

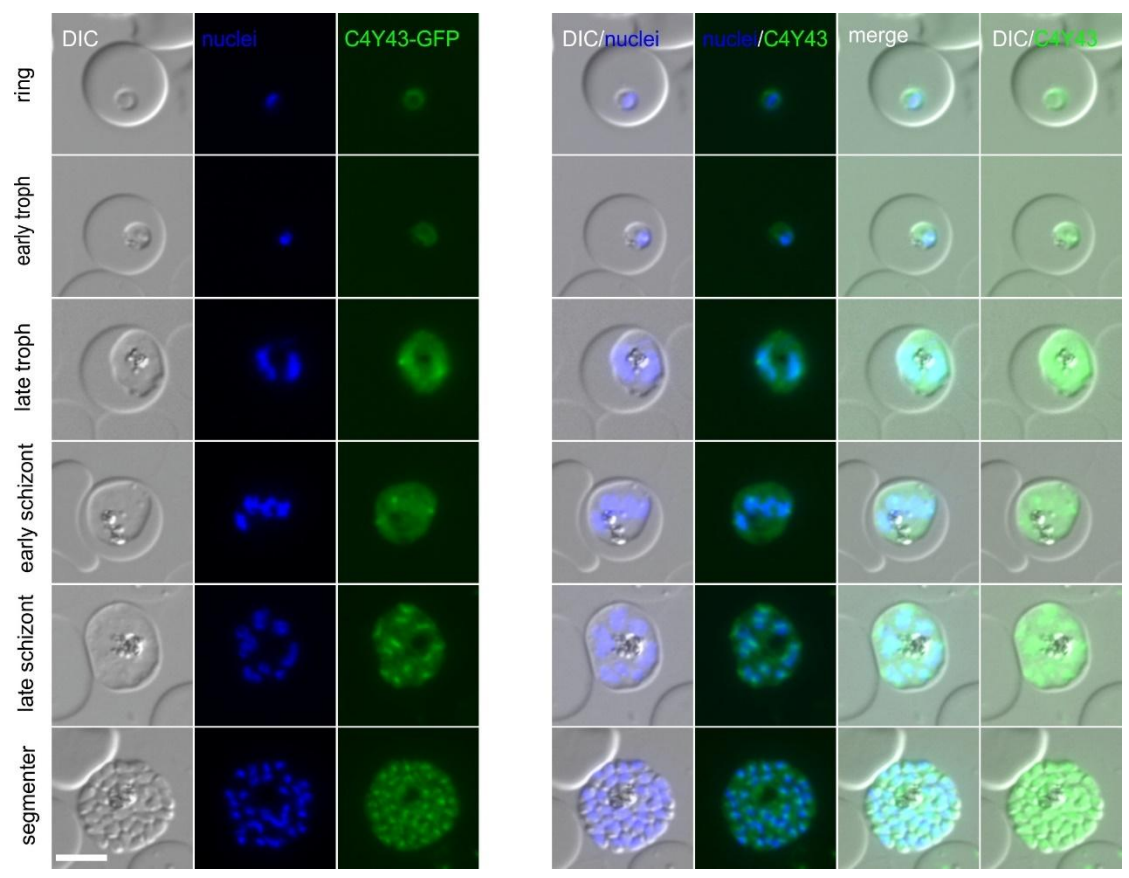


Figure 103. Localization of endogenously tagged candidate Y43 (PF3D7_0423200). Representative live cell fluorescence microscopy images of knock-in cell line Y43-2xFKBP-GFP-2xFKBP ('GFP'). The stages are indicated on the left of the panel. Representative images from 3 independent imaging sessions with at least 7 inspected fields of view. Parasite nuclei were stained with Hoechst33342. Scale bar 5 μ m, DIC, differential interference contrast; merge, overlay of DIC, GFP and nuclei.

HHPred analysis strongly supports the presence of a BSD domain in Y43, with high-confidence matches (probabilities: 99.2%, E-values: 4.6e-11). These hits span ~85-113 aligned residues and support a structural fold typical of BSD domains. Consistently, BLAST searches revealed close homologs across multiple *Plasmodium* species,

including *P. reichenowi* and *P. gaboni*, all with >95% sequence identity, indicating that Y43 is a highly conserved apicomplexan protein.

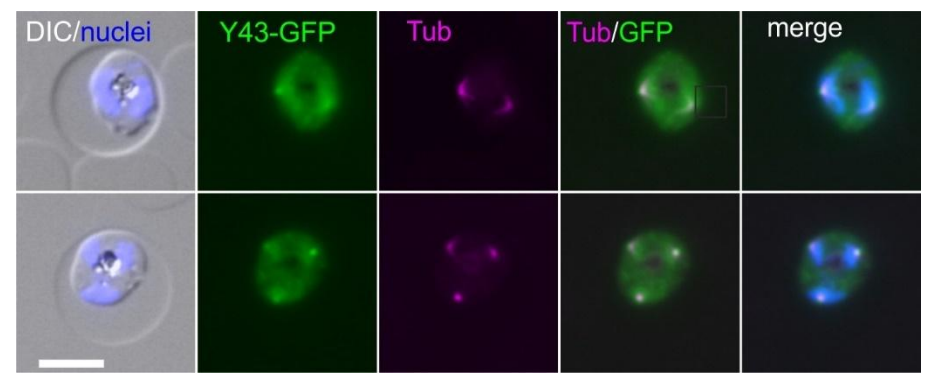


Figure 104. Y43 (PF3D7_0423200) co-localization with Tubulin. Representative live cell images of knock-in cell line of Y43-2xFKBP-GFP-2xFKBP (green) with staining TubulinTrackerTM deep red (purple). Parasites nuclei were stained with Hoechst33342 (blue). Scale bar, 5 μm, DIC, differential interference contrast.

In order to assess the importance of Y43, we first attempted to generate a C-terminal GFP fusion line, but this approach was unsuccessful. We therefore used SLI for N-terminal tagging (Birnbaum et al., 2017), which successfully produced a parasite line expressing GFP-tagged Y43. Fluorescence microscopy revealed that Y43 is present dispersed in the parasite cytoplasm and also localized to the nucleus, showing both diffuse nuclear fluorescence and a prominent punctate signal (Figure 103). The punctate structure resembled the distribution of the nuclear tubulin, prompting us to perform colocalization using fluorescent tubulin staining. The results confirmed that the punctate Y43 signal overlapped with tubulin, suggesting a potential association with nuclear microtubule organizing centers (Figure 104).

To functionally investigate Y43, the Y43-2xFKBP-GFP-2xFKBP^{endo} cell line was transfected with an episomal plasmid mediating expression of the Lyn mislocalizer, permitting conditional inactivation using knock sideways. Representative live-cell microscopy 24 h after rapalog treatment showed that Y43-GFP was only partially mislocalized in most cells, with residual signal still visible in the nucleus (Figure 105A).

Mislocalization efficiency was quantified across 80 parasites and revealed that 76.25% of cells exhibited partial KS, 15% full KS, and 8.75% no KS (Figure 105B).

Despite the predominance of partial knock sideways, we proceeded to assess the functional impact of Y43 mislocalization. Growth curves from two independent replicates revealed no significant difference between rapalog-treated and control groups (Figure 105C-D). However, due to the only partial mislocalization, it is unclear if this is indicative of dispensability of Y43. An alternative approach—such as DiCremediated conditional knockout—may be required to reveal its essentiality. While loxP sites were for conditional removal of Y43 with this approach in this parasite line, due to time constraints, the parasite line with the added DiCre could not be generated in this study.

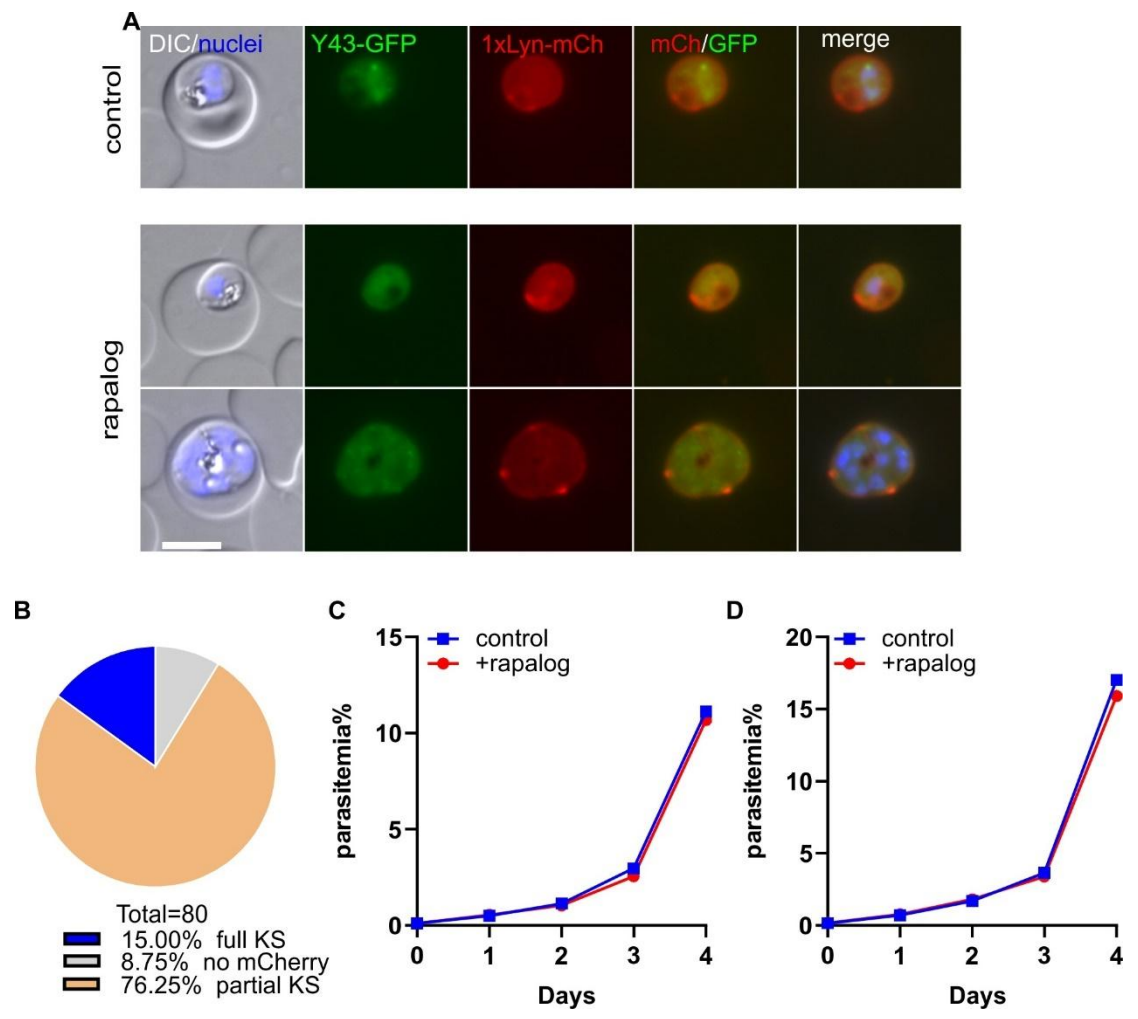


Figure 105. Knock sideways analysis of endogenous Y43 (PF3D7_0423200) tagged with 2xFKBP-GFP-2xFKBP. A) Representative live cell images of knock-in cell line Y43-2xFKBP-GFP-2xFKBP ('GFP') with an episomally expressed Lyn-FRB-mCherry mislocalizer. Representative images from 3 independent imaging sessions with at least 7 inspected fields of view. Both two rows show a parasite with partial KS (incomplete GFP mislocalization. "partial KS" in (B)). The cell culture was split into two dishes: one served as control without rapalog (control), and the other grown in the presence of 250 nM rapalog. The samples for live cell imaging were taken 24 h post addition of rapalog. Scale bar, 5 μm, DIC, differential interference contrast, mCh, mCherry, merge, overlay of GFP, mCh and nuclei. B) Pie chart shows quantification of knock sideways efficiency based on GFP localization following rapalog treatment. Quantification of knock sideways efficiency for Y43, based on the same experiments shown in (A). A total of 103 parasites were scored across 3 independent imaging sessions. KS status was evaluated 24 hours after rapalog addition. C-D) Growth curve of the Y43-Lyn knock sideways. Parasite growth was assessed by flow cytometry in the presence (rapalog) or absence (control) of rapalog. Two independent replicates (both shown)

3.34 Characterization of Y44 (PF3D7_0423600)

Y44 (Gene ID: PF3D7_0423600) is annotated in PlasmoDB as a conserved Plasmodium protein of unknown function. Similarity searches using BLAST, HHPred, and MotifScan did not reveal any known domains or significant homology to characterized proteins.

In order to localize and functionally analyze Y44, the corresponding gene was modified using SLI (Birnbaum et al., 2017) so that the endogenous Y44 becomes fused with the multipurpose sandwich tag (2xFKBP-GFP-2xFKBP). Correct integration into the genome was confirmed by PCR across the 5'- and 3'-integration junctions and by PCR showing the absence of the original locus (Figure 11). Live-cell fluorescence microscopy of the Y44-2xFKBP-GFP-2xFKBP^{endo} parasite line revealed a nuclear signal at all stages of the asexual cycle with accumulations in the nuclear periphery (Figure 106).

In order to assess the importance of Y44, the Y44-2xFKBP-GFP-2xFKBP^{endo} cell line was transfected with an episomal plasmid mediating expression of the Lyn mislocalizer, permitting conditional inactivation using knock sideways. Representative live-cell microscopy confirmed that Y44-GFP efficiently mislocalized to the parasite plasma membrane (Figure 107A). Mislocalization efficiency was determined by fluorescence microscopy 24 h after induction and indicated that 96.91% of cells showed full mislocalization of Y44 (no GFP fluorescence detected in the nucleus by microscopy) (Figure 107B). Growth curves revealed a profound difference between rapalog-treated (inactivated Y44) and control parasites, resulting in 13.37% 18.14% 21.26% growth compared to the control (Figure 107C-E).

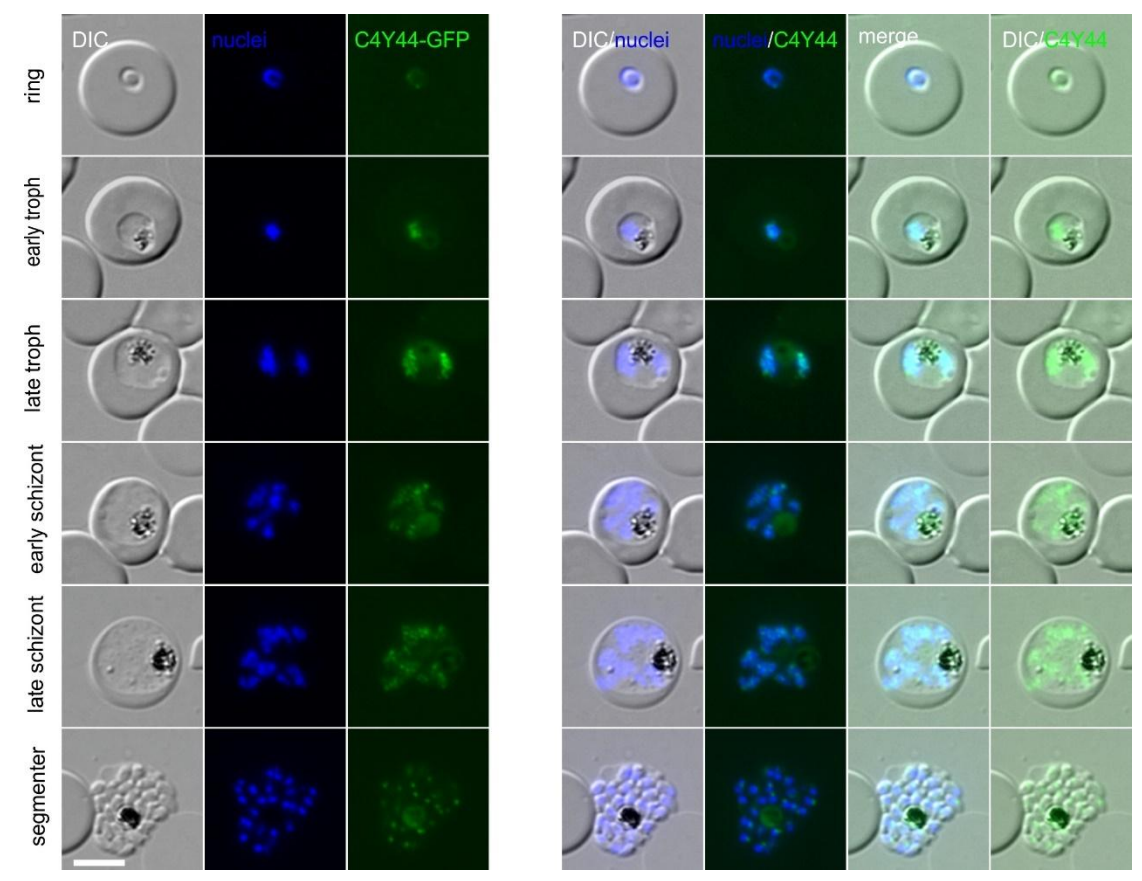


Figure 106. Localization of endogenously tagged candidate Y44 (PF3D7_0423600). Representative live cell fluorescence microscopy images of knock-in cell line Y44-2xFKBP-GFP-2xFKBP ('GFP'). The stages are indicated on the left of the panel. Representative images from 3 independent imaging sessions with at least 7 inspected fields of view. Parasite nuclei were stained with Hoechst33342. Scale bar 5 μ m, DIC, differential interference contrast; merge, overlay of DIC, GFP and nuclei.

Given the importance of Y44 for parasite growth, we performed KS in synchronous parasites to analysis its function in different parasite development stages. The outcome of the stage assay showed rapalog-treated parasites began to accumulate segmenters at the 34-42 hpi timepoint, and this resulted in a reduced number of ring stages, suggesting a failure to complete the developmental cycle. These defects became more pronounced during the second cycle, where the rapalog-treated parasites exhibited slowed development already during the trophozoite stage, arrested at late schizont stages and failed to generate new rings at 96-114 hpi (Figure 108).

Taken together, these results identify Y44 as a nuclear protein that is essential for the progression of asexual blood-stage development.

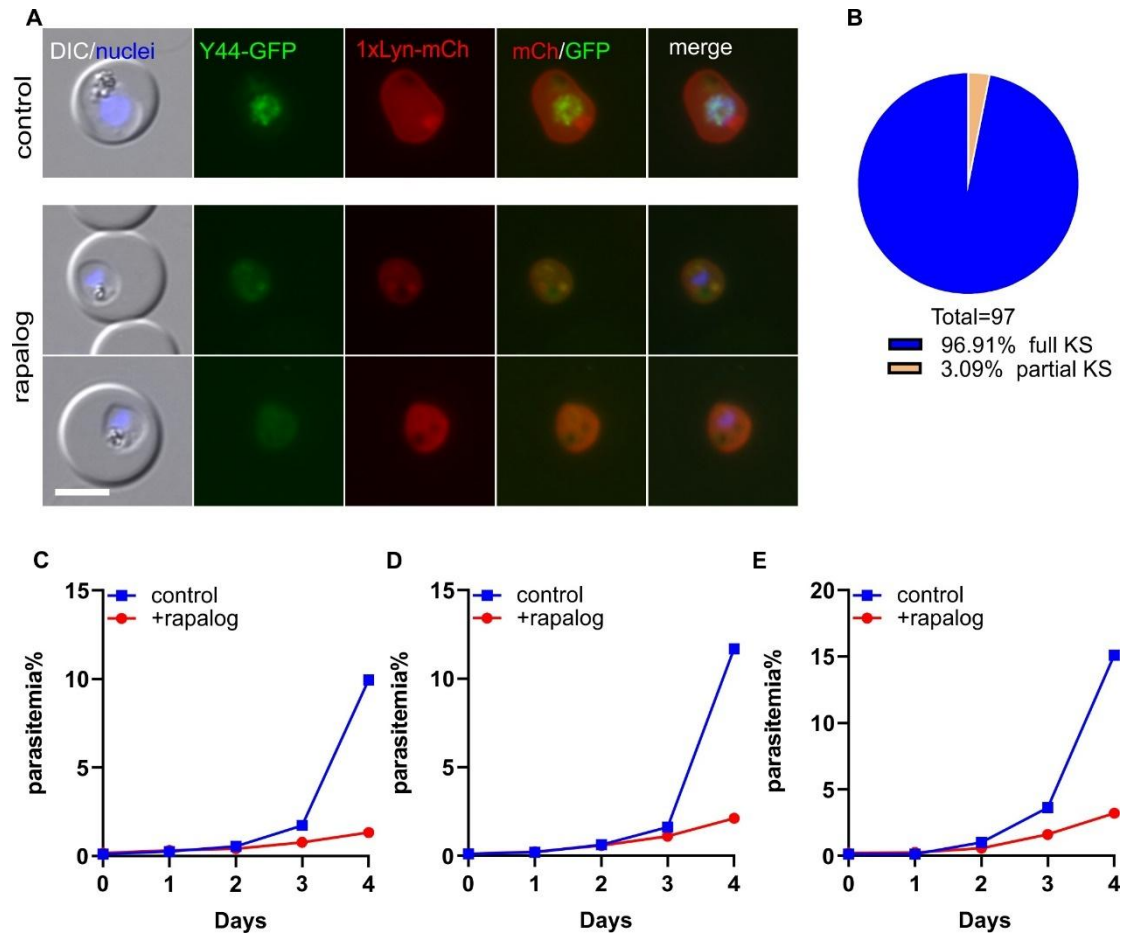


Figure 107. Knock sideways analysis of endogenous Y44 (PF3D7_0423600) tagged with 2xFKBP-GFP-2xFKBP. A) Representative live cell images of knock-in cell line Y44-2xFKBP-GFP-2xFKBP ('GFP') with an episomally expressed Lyn-FRB-mCherry mislocalizer. Representative images from 3 independent imaging sessions with at least 7 inspected fields of view. The top row shows a parasite with full KS (complete GFP mislocalization, "full KS" in (B)), while the bottom row shows a parasite with partial KS (incomplete GFP mislocalization. "partial KS" in (B)). The cell culture was split into two dishes: one served as control without rapalog (control), and the other grown in the presence of 250 nM rapalog. The samples for live cell imaging were taken 24 h post addition of rapalog. Scale bar, 5 μm, DIC, differential interference contrast, mCh, mCherry, merge, overlay of GFP, mCh and nuclei. B) Pie chart shows quantification of knock sideways efficiency based on GFP localization following rapalog treatment. Quantification of knock sideways efficiency for Y44, based on the same experiments shown in (A). A total of 103 parasites were scored across 3 independent imaging sessions. KS status was evaluated 24 hours after rapalog addition. C-E) Growth curve of the Y44-Lyn knock sideways. Parasite growth was assessed by flow cytometry in the presence (rapalog) or absence (control) of rapalog. Three independent replicates (all shown).

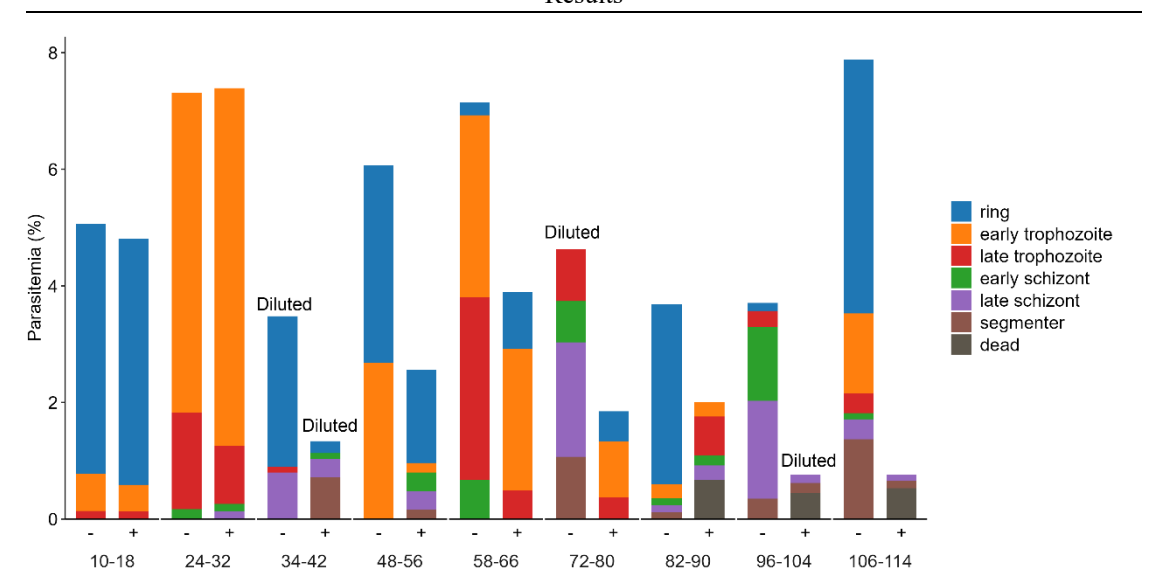


Figure 108. Stage assay of Y44-Lyn knock sideways parasites following rapalog treatment. Synchronized parasites expressing a knock sideways version of Y44 were treated with rapalog and parasite stages were monitored every 10/14 hours in 5 days over two intraerythrocytic developmental cycles. Diluted: 1:10. Parasitemia (%) and the distribution of parasite stages were quantified by Giemsa-stained blood smears. Data shown are representative of two independent biological replicates.

4. Discussion

4.1 Selection of candidates, localizations, function

In this study, we focused on the unknown genes from *Plasmodium falciparum* chromosome 4. At the beginning of the project, we selected 44 candidate genes which were annotated as "unknown protein" and "conserved Plasmodium protein" in PlasmoDB. We used three main tools — BLAST, MotifScan and HHPred — to predict the potential domains and structures in order to exclude candidates with likely functions. As a consequence, at that time, the candidate set contained proteins that did not have any significant hits or only showed very low similarity with known proteins. Hence, we started with the unknown non-secretory proteins of chromosome 4.

During the past four years, as more research and database updates occurred, several candidates were newly annotated or identified to show similarities to known domains. For example, Y21, Y22, and Y38 were in the meantime published as AKiT proteins, which are Apicomplexan-specific kinetochore components involved in mitosis (Brusini et al., 2022). Y3 showed some similarity to Ran-binding protein (Behrens et al., 2024). But up to now, none of these predictions have been validated clearly, and there are still no direct experimental reports showing the function or localization of these proteins in *Plasmodium falciparum* (discussed for AKiTs in section 4.2.1). Hence, these genes remain uncharacterized at the functional level, and their roles in the parasite life cycle are still unknown.

For all of the 43 selected candidate genes we successfully generated episomal constructs for C-terminal sandwich tagging. From these 33 integrant parasite lines were obtained after drug selection with the SLI drug and correct integration into the genome was confirmed by PCR. These integrants allowed us to investigate the subcellular

localization of each candidate protein by live-cell fluorescence microscopy. Analysis of GFP signal across parasite developmental stages revealed that the majority of our candidates exhibit expression either constitutively throughout the asexual cycle or with a peak in the trophozoite and schizont stages, as summarized in the expression map, although this could not be determined for six of the candidates as we did not detect any fluorescence (Figure 109).

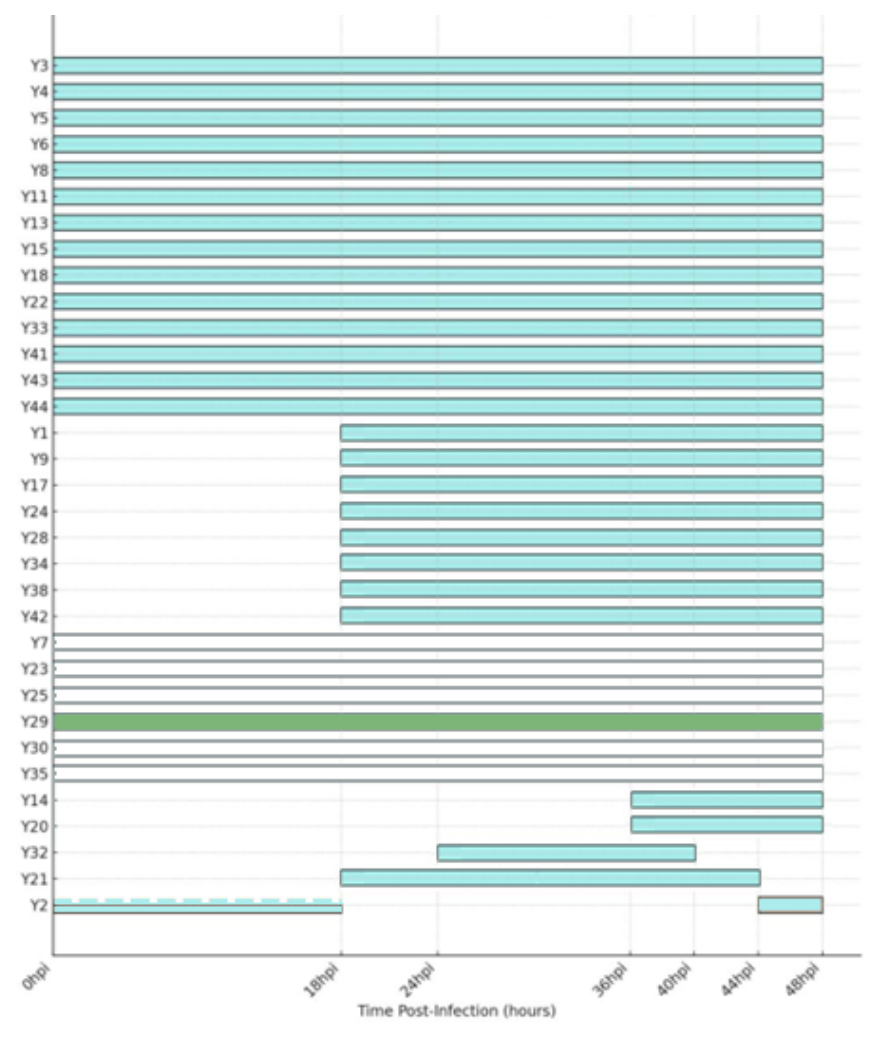


Figure 109. Temporal expression patterns of GFP-tagged candidate in the intraerythrocytic developmental cycle. Each horizontal bar represents one candidate expression period of an endogenously tagged candidate protein (Y1-Y44) as assessed by live-cell fluorescence microscopy. The X-axis denotes time post-infection (hpi), while the Y-axis lists individual candidate. Solid turquoise bars: GFP signal was consistently detectable in all observed parasites during the indicated time window. Dashed turquoise bars: GFP signal was detected only in a subset of the parasite population at that stage (e.g., partial expression of Y2 during 0-18 hpi). Dark green bar (Y29): GFP signal was detected only upon enhanced tagging using a 7×GFP tag, indicating that the standard 2×FKBP-GFP-2×FKBP tag failed to yield

detectable fluorescence. Gray bars: No GFP signal was detectable at any time point under standard live-cell imaging conditions.

Based on the GFP signals, we observed that 15 candidates are localized in the nucleus. Five candidates showed typical mitochondrial localization patterns, confirmed by colocalization with mitotracker (discussed in section 4.3). Two candidates were found in the Golgi apparatus. One protein showed a distribution consistent with the inner membrane complex (IMC), suggesting a possible structural function. Five other candidates were in unknown accumulations in the parasite cytoplasm, but since their knock sideways results indicated they are non-essential for parasite growth, we did not perform further analysis to determine their precise localization. Of six candidates, we were not able to detect any GFP signal under standard live fluorescence microscopy condition. However, in the case of Y29, we used a 7×GFP array to amplify the signal and were able to observe a nuclear localization (Figure 110). The reason this was done particularly for this candidate was that the KS had indicated it has an important function for parasite growth.

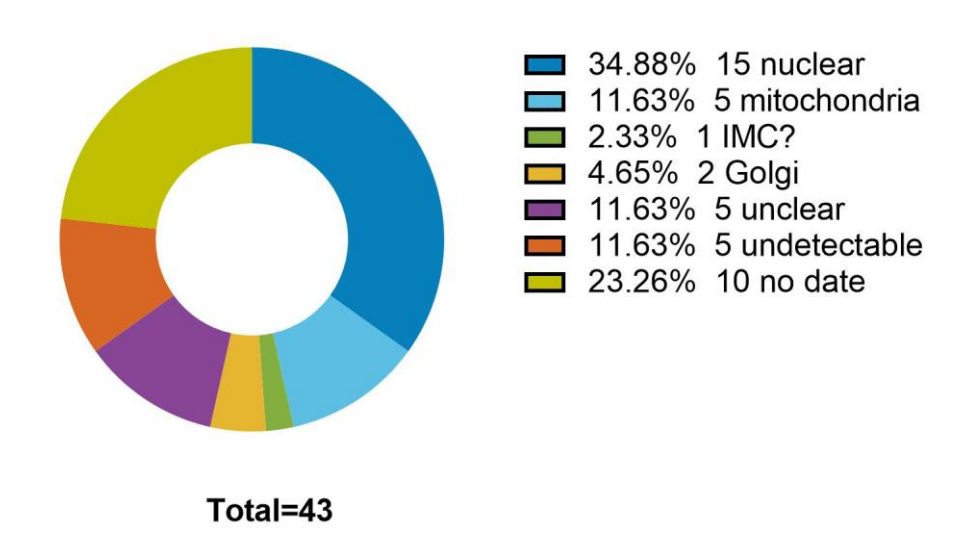


Figure 110. Pie chart displaying proportion of candidates with the indicated localisations. No data: no GFP-tagged cell lines were obtained.

For the remaining 10 candidates, we did not obtain C- terminal integrant lines. Likely this is due to functional inactivation of some of these with a C-terminal tag. Indeed, in the previous chromosome 3 screen, N-terminal tagging of two of the genes that could not be targeted with a C-terminal tag both proved important for parasite growth. This was here also attempted for five of the candidates that did not result in an integrant cell line (Y16, Y26, Y27, Y31, Y36). However, while episomal lines with some of these constructs have been obtained, we have not yet obtained the integrant lines due to time limitation. Y10, Y12, Y19 and Y39 were not attempted because they have very long coding sequences and N-terminal tagging requires recodonisation of the entire gene which would not have been cost-efficient in these cases. Y40 is a very short gene, only 84 amino acids, and it was not possible to design effective homology regions for N-terminal tagging.

To assess the functional importance of our candidate genes, we generated mislocalization (knock sideways) lines for 31 out of the 33 integrant parasite lines, Y25 and Y30, knock sideways cell lines have not yet been obtained. For most of them, the system worked well, and protein mislocalization could be induced effectively by rapalog treatment. Knock sideways of the majority of candidates resulted in varying degrees of growth inhibition (Figure 111). This was classified based on severity of phenotype: below 20% growth in a five-day growth assay was considered a severe growth defect (here defined as "essential"), below 50% as moderate growth defect, and below 80% as mild growth defect (Figure 111). Among these, six candidates were found to be essential for parasite survival, showing strong growth defects after knock sideways. Interestingly, among the essential group, four proteins are localized in the nucleus, one is localized in the Golgi, and one is likely associated with the IMC. Thirteen other candidates showed partial growth defects (3 moderate and 10 with mild growth defect), indicating that these proteins may play important but non-essential roles

or may be partially functionally redundant. The remaining seven candidates appeared to be dispensable, as knock sideways had no obvious effect on parasite growth under standard *in vitro* conditions (Figure 112).

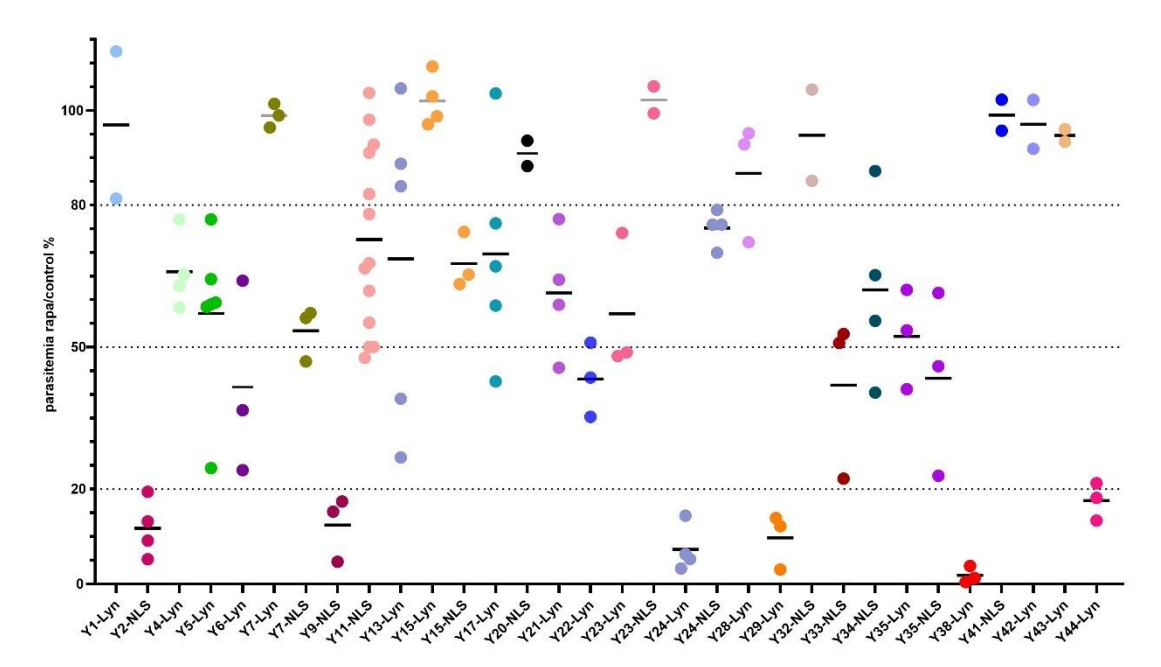


Figure 111. Summary of growth curve results for knock sideways lines. Each point represents an independent biological replicate. The Y-axis shows the parasitemia in rapalog-treated cultures normalized to that of the corresponding control (parasitemia on final day of assay (day 5)). Horizontal bars indicate the mean of replicates for each cell line. Dotted lines at 20%, 50%, and 80% highlight thresholds used to classify essential (<20%), moderate (20-50%), mild (50-80%), and dispensable (>80%) phenotypes. Each color represents a different candidate gene. When both Lyn- and NLS-based mislocalizers were used for a single candidate, only the more effective condition (i.e., the one with stronger phenotype) was considered in downstream classification. Different colors represent different candidate proteins.

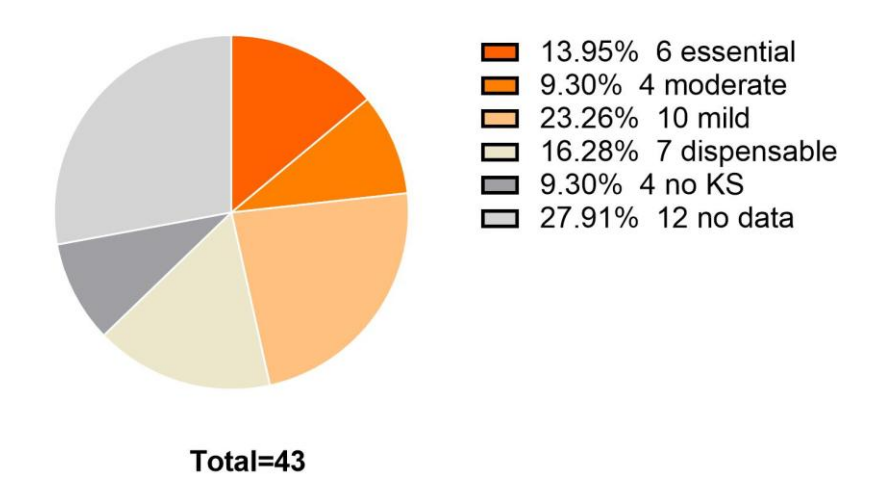


Figure 112. The essentiality of candidates based on knock sideways analysis. Candidates were categorized as essential (parasitemia <20% of control), medorate (20-50%), mild (50-80%) or dispensable (>80%), based on their normalized growth levels following rapalog-induced mislocalization. Candidates with failed knock sideways (no KS) and failed GFP-tag (no data).

However, we observed that four candidates — Y3, Y8, Y15, and Y18 — which are all localized in the mitochondrion, did not respond to the mislocalizer, possibly due to mitochondrial membrane structure or tag accessibility issues. These candidates were therefore not included in Figure 112 and their importance for parasite growth remains unknown (Figure 112, "no KS"). Additionally, the knock sideways system also did not perform very efficiently for Y43, where the mislocalization effect was weak and partial. To provide an overview of the screening outcomes, we compiled a summary table listing the tagging and knock sideways results for all 44 candidate genes (Table 13).

These results demonstrate that our screening strategy can efficiently reveal genes with essential functions in the parasite and that several previously uncharacterized nuclear proteins, one Golgi protein and one putative IMC protein are critical for the survival of blood-stage *Plasmodium falciparum* parasites. In addition, 4 further proteins (two located in the nucleus, one unclear and one undetectable) were important for parasite blood stage development.

Table 13. Summary of tagging and knock sideways results for the 43 candidate genes.

No.	Gene ID	episomal	SLI	Localization	KS
Y1	PF3D7_0403600	$\sqrt{}$	V	nuclear	V
Y2	PF3D7_0404000	\checkmark	$\sqrt{}$	IMC?	\checkmark
Y3	PF3D7_0404200	\checkmark	$\sqrt{}$	mitochondria	\checkmark
Y4	PF3D7_0404300	\checkmark	$\sqrt{}$	nuclear	\checkmark
Y5	PF3D7_0405500	\checkmark	$\sqrt{}$	nuclear	\checkmark
Y6	PF3D7_0406000	$\sqrt{}$	$\sqrt{}$	nuclear	\checkmark

Y7	PF3D7_0406500	$\sqrt{}$	V	unknown	
Y8	PF3D7_0406600	$\sqrt{}$	$\sqrt{}$	mitochondria	\checkmark
Y9	PF3D7_0406700	\checkmark	$\sqrt{}$	golgi	\checkmark
Y10	PF3D7_0406900	\checkmark	-	-	-
Y11	PF3D7_0407400	$\sqrt{}$	$\sqrt{}$	mitochondria	\checkmark
Y12	PF3D7_0407600	$\sqrt{}$	-	-	-
Y13	PF3D7_0407700	$\sqrt{}$	$\sqrt{}$	nuclear	\checkmark
Y14	PF3D7_0408000	\checkmark	$\sqrt{}$	mitochondria	\checkmark
Y15	PF3D7_0408100	\checkmark	$\sqrt{}$	golgi	\checkmark
Y16	PF3D7_0408200	$\sqrt{}$	-	-	-
Y17	PF3D7_0408300	$\sqrt{}$	$\sqrt{}$	nuclear	\checkmark
Y18	PF3D7_0408400	$\sqrt{}$	$\sqrt{}$	mitochondria	\checkmark
Y19	PF3D7_0409000	$\sqrt{}$	-	-	-
Y20	PF3D7_0410500	$\sqrt{}$	$\sqrt{}$	unclear	\checkmark
Y21	PF3D7_0410800	\checkmark	$\sqrt{}$	nuclear	\checkmark
Y22	PF3D7_0410900	\checkmark	$\sqrt{}$	nuclear	\checkmark
Y23	PF3D7_0411000	\checkmark	$\sqrt{}$	unknown	\checkmark
Y24	PF3D7_0411300	\checkmark	$\sqrt{}$	nuclear	\checkmark
Y25	PF3D7_0411800	$\sqrt{}$	$\sqrt{}$	unknown	-
Y26	PF3D7_0414400	\checkmark	-	-	-
Y27	PF3D7_0414800	\checkmark	-	-	-
Y28	PF3D7_0415200	\checkmark	$\sqrt{}$	nuclear	\checkmark
Y29	PF3D7_0416900	\checkmark	$\sqrt{}$	nuclear	\checkmark
Y30	PF3D7_0417600	\checkmark	$\sqrt{}$	unknown	-
Y31	PF3D7_0417700	\checkmark	-	-	-
Y32	PF3D7_0417900	\checkmark	$\sqrt{}$	unclear	\checkmark
Y33	PF3D7_0418300	\checkmark	\checkmark	unclear	\checkmark

Discussion

Y34	PF3D7_0418900	V	$\sqrt{}$	unclear	
Y35	PF3D7_0419000	$\sqrt{}$	\checkmark	unknown	\checkmark
Y36	PF3D7_0419100	$\sqrt{}$	-	-	-
Y38	PF3D7_0420600	$\sqrt{}$	\checkmark	nuclear	\checkmark
Y39	PF3D7_0421700	$\sqrt{}$	-	-	-
Y40	PF3D7_0421800	$\sqrt{}$	-	-	-
Y41	PF3D7_0422600	$\sqrt{}$	\checkmark	unclear	\checkmark
Y42	PF3D7_0423000	$\sqrt{}$	\checkmark	nuclear	\checkmark
Y43	PF3D7_0423200	0	0	nuclear	\circ
Y44	PF3D7_0423600	$\sqrt{}$	$\sqrt{}$	nuclear	\checkmark

Notes: "Episomal" indicates successful generation of parasite lines carrying the episomal GFP-tagging construct. "SLI" indicates successful genomic integration using the Selection-Linked Integration system."Localization" refers to the observed subcellular distribution of the GFP-tagged protein; "?" indicates unclear localization without direct experimental evidence, based on general appearance or expression pattern. "unclear" indicates the GFP signal was detectable, typically in the cytoplasm, but no precise subcellular structure could be assigned; "unknown" indicates no GFP signal was detectable under standard imaging conditions. "KS" shows whether a knock sideways line was successfully generated. "SLI" indicates whether a stable integrant parasite line was obtained for long-term experiments (e.g., phenotyping). " \checkmark " = successful or confirmed; "-" = not obtained; "×" = KS system did not work; " \circlearrowleft "=N-terminal tagged.

4.2 Nuclear-Localized Candidates

Among the 33 successfully localized candidates, 16 proteins showed a clear nuclear localization. This high proportion of nuclear-localized proteins is in line with previous systematic studies (Kimmel et al., 2023), which also found the nucleus to be the most common destination for unknown, non-secretory proteins. This previous screen analysed proteins encoded on chromosome 3, and found that 11 out of 33 candidates (33.3%) localized to the nucleus, while in our screen of chromosome 4, 15 out of 43 candidates (34.9%) showed a nuclear localization, further supporting the trend of nuclear proteins constituting a large proportion of the unknown non-secretory proteins.

This observation suggests that the nucleus of *Plasmodium falciparum* may serve as a hub for parasite-specific processes, particularly in gene regulation, DNA replication, and mitosis. The parasite nucleus is structurally and functionally different from that of model eukaryotes, lacking several canonical complexes and instead containing divergent or apicomplexan-specific components (Brusini et al., 2022). Therefore, many unknown proteins localizing to the nucleus may represent novel actors or regulators of these essential pathways.

In this study, the nuclear-localized proteins showed distinct localization patterns. Y1, Y4, and Y28 displayed a diffuse signal throughout the nucleus, suggesting involvement in general nuclear functions such as transcription or chromatin remodeling (Oehring et al., 2012). Similarly, Y13 and Y17 showed mostly diffuse nuclear distribution but with faint dot-like signals, which may point to a weak accumulation in sub-nuclear structures or dynamic complexes. In contrast, Y21, Y22, Y38, and Y43 were found to form one or several distinct foci within the nucleus. Foci in the nucleus can be indicative of different locations such as for instance the kinetochore (typically one or two foci per nucleus) (Cheeseman and Desai, 2008), heterochromatin (a few to several foci per nucleus) (Lopez-Rubio et al., 2009) or nuclear pores (several foci per nucleus) (Courjol et al., 2017).

4.2.1 AKiT-like Candidates

Apicomplexan Kinetochore (AKiT) proteins are a recently defined group of parasite-specific kinetochore components that are highly divergent from canonical eukaryotic kinetochore proteins (Brusini et al., 2022). Unlike model organisms, *Plasmodium falciparum* possesses highly divergent kinetochore architecture, and although homologs of core components such as NDC80, SPC24, or MIS12 have been identified, they often show low sequence conservation and may function in parasite-specific

complexes (Brusini et al., 2022; van Hooff et al., 2017; Zeeshan et al., 2020b). Instead, it relies on a set of lineage-specific proteins, termed AKiTs, to mediate chromosome segregation during mitosis (Brusini et al., 2022). In total, at least nine AKiTs (AKiT1-AKiT9) have been identified in *P. falciparum*, based on structural predictions, stage-specific expression, and co-localization with spindle markers (Brusini et al., 2022)

Among our nuclear candidates, Y21 (PF3D7_0410800), Y22 (PF3D7_0410900), and Y38 (PF3D7_0420600) were annotated as AKiT3, AKiT7, and AKiT6, respectively, in PlasmoDB. These annotations are based on isoform-level evidence inferred from *Plasmodium berghei*, and there is currently no direct experimental validation in *P. falciparum*. In our localization experiments, Y21 and Y38 formed distinct nuclear foci during schizogony, consistent with the typical pattern of mitotic kinetochore proteins. These puncta often duplicated and redistributed in dividing nuclei, further supporting their potential roles in chromosome segregation.

Unlike Y21 and Y38, which show bright and discrete nuclear foci characteristic of known Apicomplexan-specific kinetochore (AKiT) components, Y22-GFP presents more punctate per nucleus distributed throughout the nucleus across all asexual stages. While some foci overlap with spindle microtubules, as shown by partial co-localization with tubulin, the majority of the GFP signal does not associate with tubulin. This suggests that Y22 is unlikely to be exclusively a mitotic marker like canonical AKiT proteins.

Y22 knock sideways resulted in a growth reduction of approximately 60%, despite the fact that only about half of the parasites exhibited full mislocalization. This suggests that Y22 is likely important for parasite proliferation, and the observed phenotype may underestimate its true functional relevance. While we cannot entirely exclude that the C-terminal GFP tag may have affected localization or function, the robust phenotype

observed even with incomplete knock sideways argues strongly for an essential or nearessential role. However, the observed localization pattern was consistent across independent imaging sessions and reflected clear nuclear enrichment, suggesting that at least partial localization is preserved. Nonetheless, caution is warranted when interpreting its distinctive localization from other AKiTs.

Moreover, the annotation of Y22 as AKiT7 in PlasmoDB is based on inferred isoform data from *P. berghei* and not on direct experimental evidence in *P. falciparum*. Therefore, our results offer the first experimental localization of this protein in *P. falciparum*, and its non-canonical nuclear pattern may reflect either a divergent role or technical constraints that merit further investigation using orthogonal approaches. In our functional assays using knock sideways, Y38 (AKiT6) showed a clear growth defect upon rapalog treatment, indicating that it is essential for parasite survival. This agrees with a previous study (Brusini et al., 2022), which reported strong colocalization with tubulin and predicted AKiT6 as a microtubule-anchoring scaffold within the parasite kinetochore. In contrast, Y21 (AKiT3) did not exhibit as pronounced a growth defect upon mislocalization as observed for Y38. Although its localization pattern and structural prediction suggest a potential kinetochore role, our data indicate that Y21 is likely non-essential under standard culture conditions, or that the knock sideways system did not fully ablate its function.

In addition to these annotated AKiTs, we also observed that Y43 (PF3D7_0422800) displayed an evenly distributed cytoplasmic and nuclear signal with typically one accumulation per nucleus that appeared elongated during schizogony that turned into a larger round focus in segementers. The GFP tagged protein co-localized strongly with tubulin, suggesting a possible localization at the spindle poles or centrosome-like structures. Although Y43 did not show any similarity with AKiT proteins, its localization characteristics and co-occurrence with mitotic markers suggest a role in

microtubule organization during nuclear division. While its mislocalization phenotype was not clearly interpretable due to only partial knock sideways efficiency, Y43 represents a promising putative AKiT-like protein that warrants further investigation through orthogonal approaches such as DiCre-mediated knockout or proximity labeling.

4.2.2 Y24

One of the candidates with an essential function was Y24 (PF3D7 0411300). It is annotated in PlasmoDB as a Golgin subfamily A member 6-like protein, putative, implying a potential Golgi localization. This annotation was assigned by GeneDB based on the presence of the InterPro domain IPR026737, which corresponds to a coiled-coil region commonly found in Golgin A6 family proteins. To date, there is no experimental validation or functional characterization of this gene, and no phenotype-related information is available in Phenoplasm (Sanderson et al., 2017). BLAST searches retrieved only weak matches to hypothetical bacterial proteins such as DnaA-like replication initiators, with poor identity and low coverage. HHPred detected remote similarity to TATA-binding proteins (TBPs) and general transcription factors like TFIID subunits, but none of these predictions were confident. A direct alignment with human Golgin subfamily A member 6-like protein 2 (GOLGA6L2), the Golgi protein supposedly related to Y24, BLASTP comparison between Y24 (722 aa) and GOLGA6L2 (909 aa) identified a short region of weak sequence similarity, with 36.56% identity over 29% of the query sequence and an E-value of 6e-10. Despite this limited alignment, AlphaFold structural predictions revealed no meaningful similarity between the two proteins. GOLGA6L2 displays the typical elongated coiled-coil architecture of Golgi-tethering proteins, whereas Y24 adopts a more complex and modular structure with mixed α -helices and disordered regions, lacking any extended coiled-coil motifs. These results further indicate that the Golgi annotation likely resulted from weak sequence model inference (ISM) rather than true homology. Interestingly, the TDR

Targets database annotates Y24 with the Gene Ontology term "DNA binding" (GO:0003677), suggesting a potential nuclear role.

To investigate its actual localization, we endogenously tagged Y24 with GFP. The protein exhibited a punctate distribution adjacent to the Hoechst-stained nucleus, but the spatial resolution was not sufficient to clearly classify it as nuclear or cytoplasmic. We therefore performed knock sideways (KS) assays using both Lyn (plasma membrane) and NLS (nuclear retention) mislocalizers. Upon rapalog treatment, both systems efficiently mialocalized Y24. Strikingly, only Lyn-mediated mislocalization led to a strong growth defect, while NLS-based mislocalization had no effect. These results indicate that Y24 is a nuclear protein, and its function is specifically disrupted when mislocalized to the cytoplasm, confirming a critical nuclear role. This finding further supports the conclusion that this protein is not a Golgin.

To better understand the functional timing of Y24, we conducted stage assays across more than two intraerythrocytic development cycles. In the first cycle, rapalog-treated parasites progressed normally through early development (10-32 hpi) but showed a delay in the transition from late trophozoite to early schizont stages (34-42 hpi), and a subsequent accumulation of schizonts and segmenters (48-66 hpi), with fewer rings than control group emerging. In the next cycle (72-114 hpi), the rapalog group continued to show reduced parasitemia and a slight developmental lag, with fewer new rings produced. These results suggest that Y24 is particularly important for schizont maturation and merozoite formation, rather than early-stage development.

Altogether, our data indicate that Y24 is not a Golgin and its PlasmDB annotation may be incorrect. Rather it is an essential nuclear protein, playing a critical role during late asexual development.

4.2.3 Y6

Y6 (PF3D7_0408300) was initially tagged using a C-terminal sandwich plasmid. Diagnostic PCR confirmed correct genomic integration, but fluorescence microscopy revealed detectable GFP signal in only ~2% of the parasite population, localized to the nucleus.

Despite the limited visible signal, we proceeded to generate a knock sideways (KS) line using Lyn-FRB-mCherry as the mislocalizer. Upon rapalog treatment, flow cytometry revealed a ~40% reduction in parasite growth, indicating that functional inactivation of Y6 was at least partially achieved, and suggesting that GFP expression levels may have been underestimated by microscopy.

To improve expression consistency, we later re-cloned and re-transfected the Y6 tagging construct. The newly generated line showed robust nuclear GFP signal in all parasites, consistent with the localization observed in the initial line. Due to time constraints, however, knock sideways experiments have not yet been performed with this improved cell line.

Together, these results suggest that Y6 is a nuclear protein with possible functional relevance. While partial knock sideways results support a role for Y6 during asexual development, additional experiments using the optimized line are required to clarify its essentiality and subcellular dynamics under more controlled conditions.

4.3 Mitochondrial Candidates

In our screen, we identified five candidates localized to the mitochondrion, a notably higher number compared to the chromosome 3 screen, which reported only one mitochondrial protein (Kimmel et al., 2023). To understand whether this difference was

biologically meaningful or sampling bias, we compared the overall representation of mitochondrial proteins between chromosomes 3 and 4. Chromosome 3 contains 249 annotated genes, among which seven encode mitochondrial proteins based on data from PlasmoDB. Chromosome 4, with 261 genes, contains nine mitochondrial proteins. This suggests that the mitochondrial gene content is roughly balanced between the two chromosomes when considering the assignment from PlasmoDB which is based on release 68.

Interestingly, the expression patterns of the five mitochondrial candidates were not uniform. Y3, Y8, Y11 and Y18 showed GFP signal throughout all asexual blood stages, indicating constitutive expression and presence in the mitochondrion. In contrast, Y14 was only detectable in late stages, suggesting a stage-specific role during schizogony or merozoite maturation. Its late-stage restriction suggests a role in schizont-specific processes such as mitochondrial fission, organelle partitioning into daughter merozoites, or inner mitochondrial membrane remodeling (Van Dooren et al., 2006; Verhoef et al., 2024). These functions have been associated with several nuclear-encoded mitochondrial proteins in *P. falciparum*, including *Pf*OPA3, which supports inner membrane organization and electron transport chain integrity (Narwal et al., 2023), and *Pf*mRPL13, a mitochondrial ribosomal protein essential for maintaining mitochondrial structure and function during schizogony (Ke et al., 2018). Y14, given its expression timing in late stages, could for instance play a role in mitochondrial reorganization or partitioning during merozoite formation.

To assess their essentiality, we attempted knock sideways experiments for all five candidates using NLS mislocalization. However, we found that most mitochondrial proteins could not be effectively mislocalized from the mitochondrion. To further investigate whether the lack of FKBP-GFP mislocalization upon rapalog treatment was due to a failure in cytoplasmic access or due to genuine mitochondrial residence, we

assessed the presence of mitochondrial targeting signals using both classical (TargetP 2.0) and internal targeting sequence prediction tools (iMLP). For example, Y3 showed no predicted N-terminal mitochondrial transfer peptide according to TargetP (mTP score = 0.1934), but exhibited a strong iMTS signal at the N-terminus in the iMLP profile, suggesting a potential non-canonical targeting motif. In contrast, Y8 had a borderline mTP probability of 0.4863, close to the classical threshold (0.5), and also presented a strong N-terminal iMTS signal, supporting a possible import into the mitochondrial matrix. In support of its mitochondrial localization, Y8 was predicted by HHpred to be highly homologous to the mitochondrial ribosomal protein mS156 (9FIA B) from Toxoplasma gondii, with a 100% probability and an E-value of 6.4e-43. Given the known localization of mS156 to the mitochondrial matrix and its role in rRNA translation, it is highly plausible that Y8 also resides within the mitochondrial matrix. The failure to mislocalize it via the FKBP-FRB system may thus reflect physical inaccessibility due to the double membrane, rather than a lack of targeting or localization. Other candidates, such as Y11 and Y14, lacked predicted targeting signals in both tools, though iMLP still identified weak MTS-like features in Y11. Y18 lacked a predicted mitochondrial transfer peptide in TargetP (mTP score = 0.0894), and was classified as "Other" with high confidence. However, iMLP analysis revealed multiple discrete peaks throughout the protein sequence, suggesting the presence of internal MTS-like elements. As a result, we were unable to determine the functional importance of most candidates using KS. These observations indicate that the FKBP-FRB mislocalization strategy may not be optimal for proteins localized within mitochondrion, due to topological and steric constraints.

An exception was Y11 (PF3D7_0408700). This protein showed mitochondrial localization and was successfully mislocalized to the nucleus using the FKBP-FRB system, as upon rapalog treatment, the GFP signal shifted from the mitochondrial

pattern to the nucleus. This indicates it is a protein located at the outer face of the mitochondrion where it is accessible to the mislocalizer. Alternatively, mislocalization might have been efficient enough - or mitochondrial import slow enough - to permit mislocalization of this protein before it was imported into the mitochondrion. Despite the efficient KS only a weak growth defect was observed, suggesting that Y11 is not an essential mitochondrial protein. Overall, this confirms that KS can work for certain mitochondrial targets, likely depending on their membrane association, import efficiency, or topology.

As all of these mitochondrial proteins are nuclear encoded, they are amenable to a DiCre/loxP based gene excision strategy. To overcome the general failure of KS in mitochondrial proteins, we therefore also attempted to generate conditional knockouts using this system for those candidates. However, due to time limitations, we have not yet completed the integration and selection of these lines.

In summary, chromosome 4 appears to contain a normal proportion of mitochondrial proteins, but our sampling identified more of them than a previous screen with chromosome 3. Functional interrogation of mitochondrial candidates appears to be hampered by technical barriers for mislocalization, but our success with Y11 suggests that some proteins are still tractable. Further validation using DiCre systems will be essential to understand the roles of these mitochondrial candidates in parasite survival.

4.4 Golgi Candidates

Among the 33 successfully tagged candidates, two proteins—Y9 and Y15—were found to localize to perinuclear foci observed throughout the asexual blood-stage cycle that we suspected to correspond to the Golgi apparatus. To confirm this hypothesis, we conducted co-localization studies using established Golgi markers: GRASP, which marks cis- and medial-Golgi (Struck et al., 2008), and CLC, originally identified in a

BioID with the CHC (Birnbaum et al., 2020) and a marker for trans-Golgi and vesicle budding domains (Henrici Ryan et al., 2020). The results revealed distinct sub-Golgi localizations for the two proteins. Y9 displayed extensive co-localization with CLC but only limited overlap with GRASP, suggesting that Y9 is enriched at trans-Golgi domains or clathrin-coated vesicle formation sites, potentially involved in cargo sorting or trafficking toward the apical complex or plasma membrane (Krai et al., 2014; Pieperhoff et al., 2013). In contrast, Y15 showed overlap with GRASP, indicating that it resides in the cis-Golgi.

Functionally, knock sideways mislocalization of Y9 using NLS-FRB led to a pronounced growth defect, identifying it as essential for asexual proliferation. To further characterize the impact of Y9 mislocalization, we performed a growth assay with synchronized parasites to assess the stage-specific impact of the phenotype over two intraerythrocytic cycles. In the first cycle, parasites treated with rapalog began to show reduced progression at the late trophozoite stage (34-42 hpi), with a subsequent accumulation of early schizonts and segmenters 48-66 hpi. The number of ring-stages in the second cycle at 72-80 hpi was substantially diminished, and the parasites in the rapalog-treated group failed to fully propagate, as reflected by the drastic drop in parasitemia and skewed developmental profiles (Figure 42). This pattern is consistent with Golgi-dependent trafficking being crucial during late schizogony, when secretory organelles and membrane systems must be assembled and delivered to daughter merozoites (Breinich et al., 2009; Hallée et al., 2018; Struck et al., 2005).

In contrast, Y15 mislocalization caused a mild growth defect, while it showed successful mislocalization behavior under live-cell imaging, confirming that the FKBP-GFP construct responded to rapalog treatment. This indicates that Y15 plays a redundant role in Golgi integrity that is non-essential under standard culture conditions.

Interestingly, although Y9 is essential, it lacks clear functional annotation or characterized homologs in Apicomplexa. HHPred searches returned several high-probability hits (≥98%) to uncharacterized proteins or large scaffold-like molecules such as protein phosphatase 1 regulatory subunit 21 and disks large homologs, primarily from distant species like *Homo sapiens* and *Apis mellifera*. However, none of these hits provide a convincing functional link to Golgi trafficking, suggesting that Y9 may represent a *Plasmodium*-specific factor. Its essentiality, trans-Golgi enrichment, and stage-specific disruption strongly imply a role in vesicular cargo selection or fusion, processes central to egress and reinvasion. Given that few *P. falciparum* proteins with clathrin-like localization have been validated as essential (Henrici et al., 2020; Kaderi et al., 2015), Y9 represents a promising candidate for further mechanistic dissection and possible therapeutic targeting.

These findings also reinforce the need for multi-dimensional validation—combining localization, co-localization, conditional mislocalization, and temporal phenotyping—to interpret protein function, as localization alone is only a first step to determine a function.

4.5 Undetectable Candidates

Among the 33 successfully obtained tagging lines, six candidates (Y7, Y23, Y25, Y29, Y30, and Y35) showed no detectable GFP signal under standard live-cell imaging. This lack of fluorescence could result from extremely low expression levels, improper folding of the GFP tag, or localization environments that quench the signal. While we currently do not know which specific subcellular environment in the parasite could cause fluorescence quenching, one known example is the food vacuole, where the low pH can reduce GFP fluorescence (Patterson et al., 1997). However, our candidates are

not predicted to localize there, as they lack signal peptides or transmembrane domains typically associated with secretory trafficking.

To explore their expression dynamics, we examined transcriptional profiles across the asexual intraerythrocytic development cycle using RNA-seq data (Otto et al., 2010). Y23 showed a transcriptional peak during the trophozoite stage, reaching over 90 TPM, indicating a highly stage-specific expression pattern. For comparison, Y2 showed a stage specific expression profile with transcript levels during early ring stages (TPM ≈ 43 at 0 hpi), low expression during the trophozoite stage (TPM ≈ 19 at 24 hpi), and a strong peak in the late schizont stage, reaching 200 TPM at 48 hpi. Y29 and Y7 were moderately expressed across the IDC, suggesting low but constitutive transcription. Y30 exhibited a sharp increase in expression during the schizont stage, consistent with a role in late development. By contrast, Y25 and Y35 were expressed at very low levels throughout, indicating generally very low transcription (Table 14). Such cases may arise from extremely low protein abundance, unstable or poorly folded fusion proteins. (Pédelacq et al., 2006; Shaner et al., 2004; Snapp, 2005).

Table 14. mRNA Expression of Candidate Genes during 0-48 Hours Post-Infection (hpi) (Otto et al., 2010).

Candidate	0hpi	8hpi	16hpi	24hpi	32hpi	40hpi	48hpi
	(TPM)						
Y7	3.81	4.05	2.48	1.92	1.58	1.78	1.75
Y23	18.99	55.52	92.01	9.89	2.83	2.62	2.56
Y25	2.46	1.65	1.51	1.66	3.05	2.37	1.92
Y29	2.78	4.12	3.02	3.6	3.71	2.49	1.99
Y30	6.03	2.45	2.04	14.81	25.98	22.07	14.94
Y35	1.12	1.2	1.05	1.43	1.38	1.38	1.42

We assessed the essentiality of these candidates using knock sideways with both Lyn and NLS mislocalizers. KS lines were generated for Y7, Y23, Y29, and Y35. Among them, only Y29 knock sideways using the Lyn mislocalizer led to a strong growth defect, identifying it as essential for asexual proliferation. In contrast, Y7, Y23 and Y35 showed partial growth inhibition, indicating a moderate impact on parasite fitness. Interestingly, NLS-based KS rendered Y23 and Y35 visible in the nucleus, implying that these proteins are normally cytoplasmic and became detectable when accumulating in the nucleus.

Because of the strong phenotype of Y29, we re-engineered Y29 using a 7×GFP tandem tag, which led to successful detection of a fluorescence signal and revealed a nuclear localization pattern across all blood-stage forms, including ring, trophozoite, and schizont. This result mirrors observations in other *Plasmodium* nuclear regulators such

as *Pf*SIP2 and *Pf*AP2-HC, which are also expressed at low levels but govern essential chromatin dynamics (Carrington et al., 2021; Flueck et al., 2010).

The AlphaFold-predicted structure of Y29 revealed a surprisingly large and compact folded region containing extensive β -sheet networks and coiled-coil helices. Although no high-confidence hits emerged from BLAST or HHPred searches, structural similarity searches using DALI suggested weak resemblance to DNA-binding scaffolds and replication-associated factors. These predictions, combined with the nuclear localization and growth phenotype, imply that Y29 may act as a non-canonical chromatin-associated factor.

Functionally, knock sideways using Lyn mislocalizer produced a dramatic parasite growth defect, showing that Y29 is essential for asexual development. Further phenotyping by stage-resolved microscopy revealed that Y29 mislocalization severely affected the transition from late trophozoite to early schizont, as indicated by arrested development and accumulation of immature stages. In the second cycle, parasites failed to reach segmentation, and re-invasion efficiency was markedly reduced as judged by the number of new ring stages generated. This might indicate possible roles in replication licensing or nuclear reorganization, processes known to occur around 30-40 hpi and again during late schizogony (Francia et al., 2014; Gerald et al., 2011; Matthews et al., 2018).

Taken together, Y29 is a lowly-expressed, nuclear protein that is very important for the growth of *P. falciparum* asexual blood stages and its scarcity of expression does not correlate with a lack of importance for the parasite. Our broader screen showed that also the other tested low-expressing candidates are rather important for growth as inactivation of Y7, Y23 and Y35 resulted in a substantial growth defect of ~50% (Y7 NLS ~45%; Y23 Lyn ~40%, Y35 Lyn and NLS 45 - 55% growth defect, see Figure

111 and Figure 112). This contrasts with previous work where the undetectable candidates did not result in a phenotype when inactivated (Birnbaum et al., 2017; Kimmel et al., 2023; Schmidt, 2017). Interestingly Y35 now is now annotated as a dynein regulatory complex protein, suggesting cytoskeletal functions (Wirschell et al., 2013). The fact that both NLS and Lyn had a similar effect might indicate that both mislocalizers inactivated this protein. Y7 contains a NYN domain, typically linked to RNA processing and mRNA turnover (Anantharaman et al., 2006), which would be consistent with a function in the cytoplasm and an effect of the NLS rather than the Lyn miscloalizer.

In summary, all tested undetectable proteins were important for parasite growth. The case of Y29 underscores the critical importance of sensitive detection methods (e.g., 7xGFP), to localize such proteins, assess conditional inactivation, and expression timing to uncover the true roles of such elusive regulators. This also underscores the value of using enhanced tagging strategies and functional screens to uncover critical, easily overlooked (due to low expression) factors in *Plasmodium falciparum* biology.

4.6 Comparison of the results from this screen with published high throughput sets

To compare our findings with previous large-scale functional screens, we summarized the essentiality status of selected candidates based on our knock sideways results alongside data from five published high-throughput datasets: the *P. falciparum* PiggyBac mutagenesis screen (Zhang et al., 2018), the *P. berghei* PlasmoGEM CRISPR screen (Ghorbal et al., 2014), the *P. knowlesi* (Elsworth et al., 2025) pooled disruption screen, a secondary saturation screen (Oberstaller et al., 2025), and available orthologue data from *Toxoplasma gondii* (Barylyuk et al., 2020) including HyperLOPIT localization (Table 15).

Overall, there is a high level of agreement for many candidates. For example, Y13 and Y15 were classified as dispensable in our screen and consistently marked as dispensable across all referenced datasets. Conversely, Y9, Y21, Y24, Y29, Y38, and Y44 showed strong or moderate growth defects upon mislocalization in our screen, and were also consistently annotated as essential in PiggyBac and/or CRISPR-based screens. However, several candidates such as Y2 and Y29, which showed strong defects in our system, were assigned dispensable or middle scores in the plasmGEO screen.

However, certain discrepancies were observed. For instance, Y23 showed a moderate defect in our system but was classified as dispensable in the PiggyBac screen. In other cases (e.g., Y22, Y34), candidates with mild phenotypes in our screen fell into the "mild" or "moderate" categories in other datasets. A few cases, such as Y7 and Y15, showed near 100% growth in our assay despite being tagged and mislocalized, which could reflect biological redundancy.

Overall, this comparison illustrates the complementarity of different functional screening approaches. While pooled genome-scale methods provide powerful statistical breadth, targeted knock sideways strategies offer high spatial and temporal resolution, especially when combined with localization data. Integrating these approaches strengthens confidence in conserved essential genes and helps uncover context-dependent or subtle functions that might otherwise be overlooked.

Table 15. Comparison of gene essentiality across knock sideways and published datasets.

No.	our data	Piggbac	plasmGEM	Paper1	Paper2	ToxoDB
Y1-L	96.91%	dispensable (3490)	slow (0.44)	NF	NF	NF

Y2-N	11.74%	dispensable (5239)	essential (0.11)	essential (1906)	essential (0.16)	NF
Y4-L	65.92%	dispensable (4006)	ND	NF	NF	NF
Y5-L	57.11%	middle (2939)	ND	middle (3442)	dispensabl e (0.87)	NF
Y7-L/N	98.90%/ 53 . 54%	Dispensable (5427)	ND	dispensable (4746)	_	middle (5720)
Y9-N	12.43%	essential (27)	essential (0.04)	middle (2806)	dispensabl e (0.80)	middle (5760)
Y11-N	72.71%	dispensable (5429)	slow (0.79)	essential (936)	NF	NF
Y13-L	68.63%	dispensable (5257)	slow (0.90)	dispensable (4972)	dispenable (1)	dispenable (7470)
Y15-L/N		dispensable (5253)	_	_	_	NF
Y17-L	69.66%	dispensable (5254)	dispensabl e (0.99)	middle (2740)	dispenable (0.99)	middle (3856)
Y20-N	90.93%	essential (63)	dispensabl e (1.02)	middle (2640)	dispenable (0.77)	NF
Y21-L	61.46%	essential (999)	slow (0.56)	NF	NF	NF

Y22-L	43.27%	middle (3837)	slow (0.57)	dispensable (4212)	_	NF
Y23-L/N	57.04%/10 2.23%	dispensable (5132)	slow (0.54)	NF	NF	NF
Y24-L/N	7.29%/75.1 4%	essential (1353)	ND	essential (1456)	essential (0.16)	NF
Y28-L	86.71%	dispensable (5140)	essential (0.07)	dispensable (5820)	essential (0.07)	NF
Y29-L	9.70%	middle (2245)	ND	essential (942)	essential (0.30)	NF
Y32-N	94.76%	dispensable (5177)	ND	dispensable (4420)	•	middle (3129)
Y33-N	41.95%	dispensable (5149)	essential (0.08)	NF	NF	NF
Y34-N	62.09%	middle (2066)	dispensabl e (1.00)	middle (2964)	dispensabl e (0.73)	middle (2294)
Y35-L/N	52.25%/43. 42%	middle (2268)	ND	middle (3784)	dispensabl e (0.99)	middle (4014)
Y38-L	1.80%	essential (1350)	essential (0.09)	essential (529)	essential (0.16)	NF
Y41-N	98.99%	dispensable (5161)	ND	middle (2314)	middle (0.33)	NF

Y42-L	97.05%	middle (3276)	ND	NF	NF	NF
Y43-L	94.70%	dispensable (5163)	ND	middle (3497)	middle (0.49)	essential (294)
Y44-L	17.59%	essential (784)	ND	NF	NF	NF

Notes: This table compares the essentiality classification of selected candidate genes based on our knock sideways (KS) screen ("our data") and five published large-scale datasets: PiggyBac mutagenesis (Zhang et al., 2018), PlasmoGEM CRISPR screen (Ghorbal et al., 2014), paper1 is Elsworth et al., 2025, paper2 is Oberstaller et al., 2025. Red = Essential, Orange = Moderate phenotype, Blue = Mild phenotype, Green = Dispensable, L=Lyn, N=NLS, ND = Orthologue found, but no functional data available, NF = No orthologue found in the respective dataset.

4.7 Challenges

Although the SLI-based strategy combined with knock sideways mislocalization proved to be broadly effective for the functional analysis of unknown genes on chromosome 4, several limitations and uncertainties remain. For the ~10 candidates for which SLI integration failed, we were unable to identify a shared technical cause. However, likely these genes were refractory to C-terminal tagging, as attempts using standard SLI constructs were unsuccessful. This failure rate (~25%) is in a similar range to previous SLI-based screens — Birnbaum reported ~17% (Birnbaum et al., 2017) and Chr3 screen ~18% (Kimmel et al., 2023). This observation may indicate that these proteins possess functionally or structurally constrained C-termini, such that tagging interferes with proper folding, stability, or localization. Alternatively, the failure may reflect unique regulatory features or expression dynamics that are incompatible with the integration strategy. These genes will require alternative tagging or editing approaches. Extra efforts to study these genes (e.g. through N-terminal tagging) are

warranted, as these likely are essential genes. This idea is supported by the chromosome 3 screen where both of the tested genes found to be refractory to C-terminal tagging turned out to be important for parasite growth (Kimmel et al., 2023). An added advantage with the N-terminal tagging approach is also that it permits both, KS and diCre based gene excision and hence increases the likelihood of functional ablation. However, this approach has the drawback that the target gene needs to be synthesized in recodonized form, which adds cost and time.

In terms of functional assessment, knock sideways offers the advantage of rapid sustained inactivation of target proteins, providing an advantage to classical knockout or conditional knockout strategies for essential genes considering the rapid life cycle of the parasite. However, it is not always effective and the level of inactivation is not always easily determined. In some cases, the effect is also not straightforward to interpret. For instance, in the case of Y38, only low percentage protein mislocalization was achieved, yet the growth was severely impaired, indicating that even partial mislocalization can result in significant functional disruption. Conversely, candidates that showed no apparent phenotype after KS may not have been fully inactivated, raising concerns that residual protein activity could mask underlying essential functions. One such example is for instance Kelch13 which had been previously studied: incomplete (~90%) inactivation did not result in a growth defect but more efficient KS abolished growth (Birnbaum et al., 2017). It is technically difficult to confirm whether 100% of the target protein has been successfully mislocalized, as standard fluorescence microscopy might not detect low levels of residual protein in its native compartment. Thus, the degree of mislocalization and inactivation needs to be rigorously validated for each case. Moreover, due to the constraints of our tagging and mislocalization system, we preemptively excluded candidates containing predicted transmembrane domains or signal peptides, as these proteins are not amenable to mislocalization-based

inactivation with our system. While this decision improved technical feasibility, it also introduced a bias in target selection, omitting a biologically relevant class of membrane-associated or secretory proteins. However, at least the tagging approach would still be feasible for these proteins and again, this class could be targeted with diCre-based approaches. Due to the time and resource constraints (need for gene synthesis) this was omitted from this study.

5. Conclusion

In summary, our study provides a function and localization of proteins encoded by previously uncharacterized genes on *Plasmodium falciparum* chromosome 4 using a gene-by-gene screening strategy. Through the application of the SLI-mediated tagging system combined with knock sideways mislocalization, we successfully characterized 33 unknown genes, revealing novel protein localizations and potential roles in critical parasite processes. While our approach was constrained by the inherent limitations of genetic tools and prediction algorithms, it nonetheless expands the resource of validated tools and provides a platform and resources for deeper molecular dissection. The identification of nuclear- and organelle-localized proteins without similarity to proteins in other taxa, especially those potentially involved in important processes of the parasite's asexual life cycle, likely include unique parasite-specific mechanisms that warrant further investigation. These findings not only enrich our understanding of malaria parasite biology but also offer promising starting points for the development of new antimalarial targets, as targets not present in the human host have a better chance to be specifically targeted by chemotherapeutics.

6. References

Adjalley, S.H., Johnston, G.L., Li, T., Eastman, R.T., Ekland, E.H., Eappen, A.G., Richman, A., Sim, B.K.L., Lee, M.C.S., Hoffman, S.L., *et al.* (2011). Quantitative assessment of *Plasmodium falciparum* sexual development reveals potent transmission-blocking activity by methylene blue. Proceedings of the National Academy of Sciences *108*, E1214-E1223.

Agrawal, P., Manjithaya, R., & Surolia, N. (2020). Autophagy-related protein PfATG18 participates in food vacuole dynamics and autophagy-like pathway in *Plasmodium falciparum*. Molecular microbiology, *113(4)*, 766-782.

Aly, A.S.I., Vaughan, A.M., and Kappe, S.H.I. (2009). Malaria Parasite Development in the Mosquito and Infection of the Mammalian Host. Annual review of microbiology *63*, 195-221.

Amino, R., Thiberge, S., Blazquez, S., Baldacci, P., Renaud, O., Shorte, S., and Ménard, R. (2007). Imaging malaria sporozoites in the dermis of the mammalian host. Nature protocols *2*, 1705-1712.

Amrane, D., Arnold, C.S., Hutter, S., Sanz-Serrano, J., Collia, M., Azqueta, A., Paloque, L., Cohen, A., Amanzougaghene, N., Tajeri, S., *et al.* (2021). 2-Phenoxy-3-Trichloromethylquinoxalines Are Antiplasmodial Derivatives with Activity against the Apicoplast of *Plasmodium falciparum*. Pharmaceuticals *14*(8), 724.

Anantharaman, V., and Aravind, L. (2006). The NYN domains: novel predicted RNAses with a PIN domain-like fold. RNA biology *3*, 18-27.

Anwar, M.O., Islam, M.M., Thakur, V., and Mohmmed, A. (2022). Defining ERmitochondria contact dynamics in *Plasmodium falciparum* by targeting component of phospholipid synthesis pathway, phosphatidylserine synthase (*Pf*PSS). Mitochondrion 65, 124-138.

Arredondo, S.A., and Kappe, S.H.I. (2017). The s48/45 six-cysteine proteins: mediators of interaction throughout the Plasmodium life cycle. International journal for parasitology 47, 409-423.

Bachmann, A., Bruske, E., Krumkamp, R., Turner, L., Wichers, J.S., Petter, M., Held, J., Duffy, M.F., Sim, B.K.L., Hoffman, S.L., *et al.* (2019). Controlled human malaria infection with *Plasmodium falciparum* demonstrates impact of naturally acquired immunity on virulence gene expression. PLoS pathogens *15*, e1007906.

Bakar, N.A., Klonis, N., Hanssen, E., Chan, C., and Tilley, L. (2010). Digestive-vacuole genesis and endocytic processes in the early intraerythrocytic stages of *Plasmodium falciparum*. Journal of cell science *123*, 441-450.

Baker, D.A. (2010). Malaria gametocytogenesis. Molecular and biochemical parasitology 172, 57-65.

Banerjee, R., Liu, J., Beatty, W., Pelosof, L., Klemba, M., and Goldberg, D.E. (2002). Four plasmepsins are active in the *Plasmodium falciparum* food vacuole, including a protease with an active-site histidine. Proceedings of the National Academy of Sciences of the United States of America *99*, 990-995.

Bannister, L.H., Hopkins, J.M., Fowler, R.E., Krishna, S., and Mitchell, G.H. (2000). A Brief Illustrated Guide to the Ultrastructure of *Plasmodium falciparum* Asexual Blood Stages. Parasitology Today *16*, 427-433.

Baruch, D.I., Pasloske, B.L., Singh, H.B., Bi, X., Ma, X.C., Feldman, M., Taraschi, T.F., and Howard, R.J. (1995). Cloning the *P. falciparum* gene encoding *Pf*EMP1, a malarial variant antigen and adherence receptor on the surface of parasitized human erythrocytes. Cell *82*, 77-87.

Barylyuk, K., Koreny, L., Ke, H., Butterworth, S., Crook, O.M., Lassadi, I., Gupta, V., Tromer, E., Mourier, T., Stevens, T.J., *et al.* (2020). A Comprehensive Subcellular Atlas of the Toxoplasma Proteome via hyperLOPIT Provides Spatial Context for Protein Functions. Cell host & microbe 28, 752-766, e759.

Beck, J.R., and Ho, C.-M. (2021). Transport mechanisms at the malaria parasite-host cell interface. PLoS pathogens 17, e1009394.

Behrens, H. M., Schmidt, S., & Spielmann, T. (2021). The newly discovered role of endocytosis in artemisinin resistance. Medicinal Research Reviews, 41(6), 2998-3022.

Behrens, H.M., and Spielmann, T. (2024). Identification of domains in *Plasmodium falciparum* proteins of unknown function using DALI search on AlphaFold predictions. Scientific reports *14*, 10527.

Bertiaux, E., Balestra, A.C., Bournonville, L., Louvel, V., Maco, B., Soldati-Favre, D., Brochet, M., Guichard, P., and Hamel, V. (2021). Expansion microscopy provides new insights into the cytoskeleton of malaria parasites including the conservation of a conoid. PLoS biology *19*, e3001020.

Bhatt, S., Weiss, D.J., Cameron, E., Bisanzio, D., Mappin, B., Dalrymple, U., Battle, K.E., Moyes, C.L., Henry, A., Eckhoff, P.A., *et al.* (2015). The effect of malaria control on *Plasmodium falciparum* in Africa between 2000 and 2015. Nature *526*, 207-211.

Birnbaum, J., Flemming, S., Reichard, N., Soares, A.B., Mesen-Ramirez, P., Jonscher, E., Bergmann, B., and Spielmann, T. (2017). A genetic system to study *Plasmodium falciparum* protein function. Nature methods *14*, 450-456.

Birnbaum, J., Scharf, S., Schmidt, S., Jonscher, E., Hoeijmakers, W. A. M., Flemming, S., ... & Spielmann, T. (2020). A Kelch13-defined endocytosis pathway mediates artemisinin resistance in malaria parasites. Science, *367(6473)*, 51-59.

Bischoff, F.R., Krebber, H., Smirnova, E., Dong, W., and Ponstingl, H. (1995). Coactivation of RanGTPase and inhibition of GTP dissociation by Ran-GTP binding protein RanBP1. The EMBO Journal *14*, 705-715.

Bohórquez, E.B., Chua, M., and Meshnick, S.R. (2012). Quinine localizes to a non-acidic compartment within the food vacuole of the malaria parasite *Plasmodium* falciparum. Malaria journal 11, 350.

Bonifacino, J.S., and Glick, B.S. (2004). The mechanisms of vesicle budding and fusion. Cell *116*, 153-166.

Bozdech, Z., Llinás, M., Pulliam, B.L., Wong, E.D., Zhu, J., and DeRisi, J.L. (2003). The transcriptome of the intraerythrocytic developmental cycle of *Plasmodium falciparum*. PLoS biology *1*, E5.

Brancucci, N.M.B., Gerdt, J.P., Wang, C., De Niz, M., Philip, N., Adapa, S.R., Zhang, M., Hitz, E., Niederwieser, I., Boltryk, S.D., *et al.* (2017). Lysophosphatidylcholine Regulates Sexual Stage Differentiation in the Human Malaria Parasite *Plasmodium falciparum*. Cell *171*, 1532-1544, e1515.

Breinich, M.S., Ferguson, D.J.P., Foth, B.J., van Dooren, G.G., Lebrun, M., Quon, D.V., Striepen, B., Bradley, P.J., Frischknecht, F., Carruthers, V.B., *et al.* (2009). A Dynamin Is Required for the Biogenesis of Secretory Organelles in *Toxoplasma gondii*. Current Biology *19*, 277-286.

Bruce, M.C., Alano, P., Duthie, S., and Carter, R. (1990). Commitment of the malaria parasite *Plasmodium falciparum* to sexual and asexual development. Parasitology *100 Pt 2*, 191-200.

Brusini, L., Dos Santos Pacheco, N., Tromer, E. C., Soldati-Favre, D., & Brochet, M. (2022). Composition and organization of kinetochores show plasticity in apicomplexan chromosome segregation. Journal of Cell Biology, 221(9), e202111084.

Burrows, J.N., Duparc, S., Gutteridge, W.E., Hooft van Huijsduijnen, R., Kaszubska, W., Macintyre, F., Mazzuri, S., Möhrle, J.J., and Wells, T.N.C. (2017). New developments in anti-malarial target candidate and product profiles. Malaria journal *16*, 26.

Bushell, E., Gomes, A.R., Sanderson, T., Anar, B., Girling, G., Herd, C., Metcalf, T., Modrzynska, K., Schwach, F., Martin, R.E., *et al.* (2017). Functional Profiling of a Plasmodium Genome Reveals an Abundance of Essential Genes. Cell *170*, 260-272, e268.

Caminade, C., Kovats, S., Rocklov, J., Tompkins, A.M., Morse, A.P., Colón-González, F.J., Stenlund, H., Martens, P., and Lloyd, S.J. (2014). Impact of climate change on global malaria distribution. Proceedings of the National Academy of Sciences *111*, 3286-3291.

Cancino, J., Jung, J.E., and Luini, A. (2013). Regulation of Golgi signaling and trafficking by the KDEL receptor. Histochemistry and cell biology *140*, 395-405.

Carrington, E., Cooijmans, R.H.M., Keller, D., Toenhake, C.G., Bártfai, R., and Voss, T.S. (2021). The ApiAP2 factor PfAP2-HC is an integral component of heterochromatin in the malaria parasite *Plasmodium falciparum*. iScience *24*, 10244.

Carter, R., and Mendis, K.N. (2002). Evolutionary and historical aspects of the burden of malaria. Clinical microbiology reviews *15*, 564-594.

Cheeseman, I.M., and Desai, A. (2008). Molecular architecture of the kinetochore-microtubule interface. Nature Reviews Molecular Cell Biology *9*, 33-46.

Chen, A.L., Kim, E.W., Toh, J.Y., Vashisht, A.A., Rashoff, A.Q., Van, C., Huang, A.S., Moon, A.S., Bell, H.N., Bentolila, L.A., *et al.* (2015). Novel components of the Toxoplasma inner membrane complex revealed by BioID. mBio *6*, e02357-02314.

Cobbold, S.A., Vaughan, A.M., Lewis, I.A., Painter, H.J., Camargo, N., Perlman, D.H., Fishbaugher, M., Healer, J., Cowman, A.F., and Kappe, S.H. (2013). Kinetic flux profiling elucidates two independent acetyl-CoA biosynthetic pathways in *Plasmodium falciparum*. Journal of Biological Chemistry *288*, 36338-36350.

Conway, D. J. (2015). Paths to a malaria vaccine illuminated by parasite genomics. Trends in Genetics, 31(2), 97-107.

Cortes, A., & Deitsch, K. W. (2017). Malaria epigenetics. Cold Spring Harbor Perspectives in Medicine, 7(7), a025528.

Coulson, R.M., Hall, N., and Ouzounis, C.A. (2004). Comparative genomics of transcriptional control in the human malaria parasite *Plasmodium falciparum*. Genome research *14*, 1548-1554.

Courjol, F., Mouveaux, T., Lesage, K., Saliou, J.-M., Werkmeister, E., Bonabaud, M., Rohmer, M., Slomianny, C., Lafont, F., and Gissot, M. (2017). Characterization of a nuclear pore protein sheds light on the roles and composition of the *Toxoplasma gondii* nuclear pore complex. Cellular and Molecular Life Sciences *74*, 2107-2125.

Cowman, A.F., Healer, J., Marapana, D., and Marsh, K. (2016). Malaria: Biology and Disease. Cell *167*, 610-624.

Cowman, A.F., Tonkin, C.J., Tham, W.-H., and Duraisingh, M.T. (2017). The Molecular Basis of Erythrocyte Invasion by Malaria Parasites. Cell host & microbe 22, 232-245.

Cox, F.E.G. (2010). History of the discovery of the malaria parasites and their vectors. Parasites & vectors 3, 5.

Crabb, B.S., Cooke, B.M., Reeder, J.C., Waller, R.F., Caruana, S.R., Davern, K.M., Wickham, M.E., Brown, G.V., Coppel, R.L., and Cowman, A.F. (1997). Targeted Gene Disruption Shows That Knobs Enable Malaria-Infected Red Cells to Cytoadhere under Physiological Shear Stress. Cell *89*, 287-296.

Dahan-Pasternak, N., Nasereddin, A., Kolevzon, N., Pe'er, M., Wong, W., Shinder, V., Turnbull, L., Whitchurch, C.B., Elbaum, M., and Gilberger, T.W. (2013). *Pf*Sec13 is an unusual chromatin-associated nucleoporin of *Plasmodium falciparum* that is essential for parasite proliferation in human erythrocytes. Journal of cell science *126*, 3055-3069.

Dahl, E.L., and Rosenthal, P.J. (2008). Apicoplast translation, transcription and genome replication: targets for antimalarial antibiotics. Trends in parasitology *24*, 279-284.

Dahl Erica, L., Shock Jennifer, L., Shenai Bhaskar, R., Gut, J., DeRisi Joseph, L., and Rosenthal Philip, J. (2006). Tetracyclines Specifically Target the Apicoplast of the Malaria Parasite *Plasmodium falciparum*. Antimicrobial agents and chemotherapy *50*, 3124-3131.

Dearnley, M.K., Yeoman, J.A., Hanssen, E., Kenny, S., Turnbull, L., Whitchurch, C.B., Tilley, L., and Dixon, M.W.A. (2012). Origin, composition, organization and function of the inner membrane complex of *Plasmodium falciparum* gametocytes. Journal of cell science *125*, 2053-2063.

Doerks, T., Huber, S., Buchner, E., and Bork, P. (2002). BSD: a novel domain in transcription factors and synapse-associated proteins. Trends in Biochemical Sciences *27*, 168-170.

Draper, S.J., Sack, B.K., King, C.R., Nielsen, C.M., Rayner, J.C., Higgins, M.K., Long, C.A., and Seder, R.A. (2018). Malaria Vaccines: Recent Advances and New Horizons. Cell host & microbe *24*, 43-56.

Dvorin, J.D., Bei, A.K., Coleman, B.I., and Duraisingh, M.T. (2010). Functional diversification between two related *Plasmodium falciparum* merozoite invasion ligands

is determined by changes in the cytoplasmic domain. Molecular microbiology 75, 990-1006.

Ehlgen, F., Pham, J.S., de Koning-Ward, T., Cowman, A.F., and Ralph, S.A. (2012). Investigation of the *Plasmodium falciparum* Food Vacuole through Inducible Expression of the Chloroquine Resistance Transporter (*Pf*CRT). PloS one 7, e38781.

Elmendorf, H.G., and Haldar, K. (1993). Identification and localization of ERD2 in the malaria parasite *Plasmodium falciparum*: separation from sites of sphingomyelin synthesis and implications for organization of the Golgi. The EMBO journal *12*, 4763-4773.

Elsworth, B., Matthews, K., Nie, C.Q., Kalanon, M., Charnaud, S.C., Sanders, P.R., Chisholm, S.A., Counihan, N.A., Shaw, P.J., and Pino, P. (2014). PTEX is an essential nexus for protein export in malaria parasites. Nature *511*, 587-591.

Elsworth, B., Ye, S., Dass, S., Tennessen, J. A., Sultana, Q., Thommen, B. T., ... & Duraisingh, M. T. (2025). The essential genome of Plasmodium knowlesi reveals determinants of antimalarial susceptibility. Science, 387(6734), eadq6241.

Falekun, S., Sepulveda, J., Jami-Alahmadi, Y., Park, H., Wohlschlegel, J.A., and Sigala, P.A. (2021). Divergent acyl carrier protein decouples mitochondrial Fe-S cluster biogenesis from fatty acid synthesis in malaria parasites. eLife *10*, e71636.

Fang, H., Klages, N., Baechler, B., Hillner, E., Yu, L., Pardo, M., Choudhary, J., and Brochet, M. (2017). Multiple short windows of calcium-dependent protein kinase 4 activity coordinate distinct cell cycle events during Plasmodium gametogenesis. eLife 6, e26524.

Farrell, M., and Gubbels, M.J. (2014). The Toxoplasma gondii kinetochore is required for centrosome association with the centrocone (spindle pole). Cellular microbiology *16*, 78-94.

Feng, S., Sekine, S., Pessino, V., Li, H., Leonetti, M.D., and Huang, B. (2017). Improved split fluorescent proteins for endogenous protein labeling. Nature communications *8*, 370.

Fidock, D.A., Eastman, R.T., Ward, S.A., and Meshnick, S.R. (2008). Recent highlights in antimalarial drug resistance and chemotherapy research. Trends in parasitology *24*, 537-544.

Flammersfeld, A., Lang, C., Flieger, A., & Pradel, G. (2018). Phospholipases during membrane dynamics in malaria parasites. International Journal of Medical Microbiology, 308(1), 129-141.

Fidock, D.A., Nomura, T., Talley, A.K., Cooper, R.A., Dzekunov, S.M., Ferdig, M.T., Ursos, L.M.B., bir Singh Sidhu, A., Naudé, B., Deitsch, K.W., *et al.* (2000). Mutations in the *P. falciparum* Digestive Vacuole Transmembrane Protein PfCRT and Evidence for Their Role in Chloroquine Resistance. Molecular Cell *6*, 861-871.

Florens, L., Washburn, M.P., Raine, J.D., Anthony, R.M., Grainger, M., Haynes, J.D., Moch, J.K., Muster, N., Sacci, J.B., Tabb, D.L., *et al.* (2002). A proteomic view of the *Plasmodium falciparum* life cycle. Nature *419*, 520-526.

Flueck, C., Bartfai, R., Niederwieser, I., Witmer, K., Alako, B.T.F., Moes, S., Bozdech, Z., Jenoe, P., Stunnenberg, H.G., and Voss, T.S. (2010). A Major Role for the *Plasmodium falciparum* ApiAP2 Protein PfSIP2 in Chromosome End Biology. PLoS pathogens 6, e1000784.

Francia, M.E., and Striepen, B. (2014). Cell division in apicomplexan parasites. Nature reviews Microbiology *12*, 125-136.

Frischknecht, F., and Matuschewski, K. (2017). Plasmodium Sporozoite Biology. Cold Spring Harbor perspectives in medicine 7.

Galinski, M.R., Meyer, E.V., and Barnwell, J.W. (2013). Plasmodium vivax: modern strategies to study a persistent parasite's life cycle. Advances in parasitology *81*, 1-26.

Ganter, M., Goldberg, J.M., Dvorin, J.D., Paulo, J.A., King, J.G., Tripathi, A.K., Paul, A.S., Yang, J., Coppens, I., Jiang, R.H.Y., *et al.* (2017). *Plasmodium falciparum* CRK4 directs continuous rounds of DNA replication during schizogony. Nature Microbiology 2, 17017.

Gardner, M.J., Hall, N., Fung, E., White, O., Berriman, M., Hyman, R.W., Carlton, J.M., Pain, A., Nelson, K.E., Bowman, S., *et al.* (2002). Genome sequence of the human malaria parasite *Plasmodium falciparum*. Nature *419*, 498-511.

Gazzinelli, R.T., Kalantari, P., Fitzgerald, K.A., and Golenbock, D.T. (2014). Innate sensing of malaria parasites. Nature Reviews Immunology *14*, 744-757.

Gerald, N., Mahajan, B., and Kumar, S. (2011). Mitosis in the Human Malaria Parasite *Plasmodium falciparum*. Eukaryotic cell *10*, 474-482.

Ghorbal, M., Gorman, M., Macpherson, C.R., Martins, R.M., Scherf, A., and Lopez-Rubio, J.-J. (2014). Genome editing in the human malaria parasite *Plasmodium* falciparum using the CRISPR-Cas9 system. Nature Biotechnology *32*, 819-821.

Gluzman, I.Y., Francis, S.E., Oksman, A., Smith, C.E., Duffin, K.L., and Goldberg, D.E. (1994). Order and specificity of the *Plasmodium falciparum* hemoglobin degradation pathway. The Journal of clinical investigation *93*, 1602-1608.

Goldberg, D.E., Slater, A.F., Cerami, A., and Henderson, G.B. (1990). Hemoglobin degradation in the malaria parasite *Plasmodium falciparum*: an ordered process in a unique organelle. Proceedings of the National Academy of Sciences 87, 2931-2935.

Gomes, A.R., Marin-Menendez, A., Adjalley, S.H., Bardy, C., Cassan, C., Lee, M.C.S., and Talman, A.M. (2022). A transcriptional switch controls sex determination in *Plasmodium falciparum*. Nature *612*, 528-533.

Gould, S.B., Tham, W.-H., Cowman, A.F., McFadden, G.I., and Waller, R.F. (2008). Alveolins, a New Family of Cortical Proteins that Define the Protist Infrakingdom Alveolata. Molecular biology and evolution *25*, 1219-1230.

Grüring, C., Heiber, A., Kruse, F., Ungefehr, J., Gilberger, T.-W., and Spielmann, T. (2011). Development and host cell modifications of *Plasmodium falciparum* blood stages in four dimensions. Nature communications *2*, 165.

Guggisberg, A.M., Park, J., Edwards, R.L., Kelly, M.L., Hodge, D.M., Tolia, N.H., and Odom, A.R. (2014). A sugar phosphatase regulates the methylerythritol phosphate (MEP) pathway in malaria parasites. Nature communications *5*, 4467.

Gulati, S., Ekland, E.H., Ruggles, K.V., Chan, R.B., Jayabalasingham, B., Zhou, B., Mantel, P.-Y., Lee, M.C., Spottiswoode, N., and Coburn-Flynn, O. (2015). Profiling the essential nature of lipid metabolism in asexual blood and gametocyte stages of *Plasmodium falciparum*. Cell host & microbe *18*, 371-381.

Guttery, D.S., Holder, A.A., and Tewari, R. (2012). Sexual Development in Plasmodium: Lessons from Functional Analyses. PLoS pathogens 8, e1002404.

Hallée, S., Counihan, N.A., Matthews, K., de Koning-Ward, T.F., and Richard, D. (2018). The malaria parasite *Plasmodium falciparum* Sortilin is essential for merozoite formation and apical complex biogenesis. Cellular microbiology *20*, e12844.

Harding, C.R., Gow, M., Kang, J.H., Shortt, E., Manalis, S.R., Meissner, M., and Lourido, S. (2019). Alveolar proteins stabilize cortical microtubules in Toxoplasma gondii. Nature communications *10*, 401.

Harding, C.R., and Meissner, M. (2014). The inner membrane complex through development of Toxoplasma gondii and Plasmodium. Cellular microbiology *16*, 632-641.

Heinberg, A., Amit-Avraham, I., Mitesser, V., Simantov, K., Goyal, M., Nevo, Y., Kandelis-Shalev, S., Thompson, E., and Dzikowski, R. (2022). A nuclear redox sensor modulates gene activation and var switching in *Plasmodium falciparum*. Proceedings of the National Academy of Sciences of the United States of America *119*, e2201247119.

Hellerschmied, D., Serebrenik, Y.V., Shao, L., Burslem, G.M., and Crews, C.M. (2019). Protein folding state-dependent sorting at the Golgi apparatus. Molecular Biology of the Cell *30*, 2296-2308.

Hemingway, J., Ranson, H., Magill, A., Kolaczinski, J., Fornadel, C., Gimnig, J., Coetzee, M., Simard, F., Roch, D.K., Hinzoumbe, C.K., *et al.* (2016). Averting a malaria disaster: will insecticide resistance derail malaria control? The Lancet *387*, 1785-1788.

Henrici Ryan, C., Edwards Rachel, L., Zoltner, M., van Schalkwyk Donelly, A., Hart Melissa, N., Mohring, F., Moon Robert, W., Nofal Stephanie, D., Patel, A., Flueck, C., *et al.* (2020). The *Plasmodium falciparum* Artemisinin Susceptibility-Associated AP-2 Adaptin μ Subunit is Clathrin Independent and Essential for Schizont Maturation. mBio *11*, e02918-19

Hopp, C.S., Bowyer, P.W., and Baker, D.A. (2012). The role of cGMP signalling in regulating life cycle progression of Plasmodium. Microbes and infection 14, 831-837.

Hopp, C.S., Chiou, K., Ragheb, D.R., Salman, A.M., Khan, S.M., Liu, A.J., and Sinnis, P. (2015). Longitudinal analysis of Plasmodium sporozoite motility in the dermis reveals component of blood vessel recognition. eLife *4*, e07789.

Howes, R.E., Battle, K.E., Mendis, K.N., Smith, D.L., Cibulskis, R.E., Baird, J.K., and Hay, S.I. (2016). Global Epidemiology of Plasmodium vivax. The American Society of Tropical Medicine and Hygiene *95*, 15-34.

Ishii, M., and Akiyoshi, B. (2022). Plasticity in centromere organization and kinetochore composition: Lessons from diversity. Current opinion in cell biology 74, 47-54.

Joiner, K.A., and Roos, D.S. (2002). Secretory traffic in the eukaryotic parasite Toxoplasma gondii: less is more. The Journal of cell biology *157*, 557-563.

Kaderi Kibria, K.M., Rawat, K., Klinger, C.M., Datta, G., Panchal, M., Singh, S., Iyer, G.R., Kaur, I., Sharma, V., Dacks, J.B., *et al.* (2015). A role for adaptor protein complex 1 in protein targeting to rhoptry organelles in *Plasmodium falciparum*. Biochimica et Biophysica Acta (BBA) - Molecular Cell Research *1853*, 699-710.

Kamiyama, D., Sekine, S., Barsi-Rhyne, B., Hu, J., Chen, B., Gilbert, L.A., Ishikawa, H., Leonetti, M.D., Marshall, W.F., Weissman, J.S., *et al.* (2016). Versatile protein tagging in cells with split fluorescent protein. Nature communications 7, 11046.

Kaur, S., Nieto, N.S., McDonald, P., Beck, J.R., Honzatko, R.B., Roy, A., and Nelson, S.W. (2022). Discovery of small molecule inhibitors of *Plasmodium falciparum*

apicoplast DNA polymerase. Journal of enzyme inhibition and medicinal chemistry *37*, 1320-1326.

Ke, H., Dass, S., Morrisey, J.M., Mather, M.W., and Vaidya, A.B. (2018). The mitochondrial ribosomal protein L13 is critical for the structural and functional integrity of the mitochondrion in *Plasmodium falciparum*. Journal of Biological Chemistry 293, 8128-8137.

Kebaier, C., Voza, T., and Vanderberg, J. (2009). Kinetics of mosquito-injected Plasmodium sporozoites in mice: fewer sporozoites are injected into sporozoite-immunized mice. PLoS pathogens *5*, e1000399.

Kehrer, J., Kuss, C., Andres-Pons, A., Reustle, A., Dahan, N., Devos, D., Kudryashev, M., Beck, M., Mair, G.R., and Frischknecht, F. (2018). Nuclear Pore Complex Components in the Malaria Parasite Plasmodium berghei. Scientific reports 8, 11249.

Keleta, Y., Ramelow, J., Cui, L., and Li, J. (2021). Molecular interactions between parasite and mosquito during midgut invasion as targets to block malaria transmission. npj Vaccines *6*, 140.

Kenthirapalan, S., Waters, A.P., Matuschewski, K., and Kooij, T.W.A. (2016). Functional profiles of orphan membrane transporters in the life cycle of the malaria parasite. Nature communications *7*, 10519.

Kimmel, J. (2024). Functional characterisation of essential, nuclear *Plasmodium* falciparum proteins reveals conserved and unique roles in mitosis during blood-stage schizogony of malaria parasites. PhD thesis, University of Hamburg.

Kimmel, J., and Kehrer, J. (2022). Proximity-dependent biotinylation approaches to study apicomplexan biology. 117, 553-568.

Kimmel, J., Schmitt, M., Sinner, A., Jansen, P., Mainye, S., Ramón-Zamorano, G., Toenhake, C.G., Wichers-Misterek, J.S., Cronshagen, J., Sabitzki, R., *et al.* (2023). Gene-by-gene screen of the unknown proteins encoded on *Plasmodium falciparum* chromosome 3. Cell systems *14*, 9-23.e27.

Klaus, S., Binder, P., Kim, J., Machado, M., Funaya, C., Schaaf, V., Klaschka, D., Kudulyte, A., Cyrklaff, M., Laketa, V., *et al.* (2022). Asynchronous nuclear cycles in multinucleated *Plasmodium falciparum* facilitate rapid proliferation. Science Advances 8, eabj5362.

Klemba, M., Beatty, W., Gluzman, I., and Goldberg, D.E. (2004). Trafficking of plasmepsin II to the food vacuole of the malaria parasite *Plasmodium falciparum*. Journal of Cell Biology *164*, 47-56.

Kono, M., Herrmann, S., Loughran, N.B., Cabrera, A., Engelberg, K., Lehmann, C., Sinha, D., Prinz, B., Ruch, U., Heussler, V., *et al.* (2012). Evolution and Architecture of the Inner Membrane Complex in Asexual and Sexual Stages of the Malaria Parasite. Molecular biology and evolution *29*, 2113-2132.

Koyama, M., and Matsuura, Y. (2010). An allosteric mechanism to displace nuclear export cargo from CRM1 and RanGTP by RanBP1. The EMBO Journal *29*, 2002-2013-2013.

Kraemer, S.M., Kyes, S.A., Aggarwal, G., Springer, A.L., Nelson, S.O., Christodoulou, Z., Smith, L.M., Wang, W., Levin, E., Newbold, C.I., *et al.* (2007). Patterns of gene recombination shape var gene repertoires in *Plasmodium falciparum*: comparisons of geographically diverse isolates. BMC Genomics 8, 45.

Krai, P., Dalal, S., and Klemba, M. (2014). Evidence for a Golgi-to-endosome protein sorting pathway in *Plasmodium falciparum*. PloS one *9*, e89771.

Kumari, A., Yadav, A., and Lahiri, I. (2022). Transient State Kinetics of *Plasmodium falciparum* Apicoplast DNA Polymerase Suggests the Involvement of Accessory Factors for Efficient and Accurate DNA Synthesis. Biochemistry *61*, 2319-2333.

Kyes, S.A., Kraemer, S.M., and Smith, J.D. (2007). Antigenic variation in *Plasmodium falciparum*: gene organization and regulation of the var multigene family. Eukaryotic cell 6, 1511-1520.

Lal, M., and Kallar, N.A. (2009). Malaria morbidity in Sindh and the plasmodium species distribution. Pak J Med Sci July-September 25, 646-649.

LaMonte, G.M., Rocamora, F., Marapana, D.S., Gnädig, N.F., Ottilie, S., Luth, M.R., Worgall, T.S., Goldgof, G.M., Mohunlal, R., and Santha Kumar, T. (2020). Pan-active imidazolopiperazine antimalarials target the *Plasmodium falciparum* intracellular secretory pathway. Nature communications *11*, 1780.

Langhorne, J., Ndungu, F.M., Sponaas, A.-M., and Marsh, K. (2008). Immunity to malaria: more questions than answers. Nature Immunology *9*, 725-732.

Laurens, M.B. (2018). The Promise of a Malaria Vaccine—Are We Closer? Annual review of microbiology 72, 273-292.

Lavstsen, T., Turner, L., Saguti, F., Magistrado, P., Rask, T.S., Jespersen, J.S., Wang, C.W., Berger, S.S., Baraka, V., Marquard, A.M., *et al.* (2012). *Plasmodium falciparum* erythrocyte membrane protein 1 domain cassettes 8 and 13 are associated with severe malaria in children. Proceedings of the National Academy of Sciences of the United States of America *109*, E1791-1800.

Lemgruber, L., Kudryashev, M., Dekiwadia, C., Riglar, D.T., Baum, J., Stahlberg, H., Ralph, S.A., and Frischknecht, F. (2013). Cryo-electron tomography reveals four-membrane architecture of the Plasmodium apicoplast. Malaria journal *12*, 25.

Lopez-Rubio, J.-J., Mancio-Silva, L., and Scherf, A. (2009). Genome-wide Analysis of Heterochromatin Associates Clonally Variant Gene Regulation with Perinuclear Repressive Centers in Malaria Parasites. Cell host & microbe 5, 179-190.

MacRae, J.I., Dixon, M.W., Dearnley, M.K., Chua, H.H., Chambers, J.M., Kenny, S., Bottova, I., Tilley, L., and McConville, M.J. (2013). Mitochondrial metabolism of sexual and asexual blood stages of the malaria parasite *Plasmodium falciparum*. BMC biology *11*, 67.

Mamudu, C.O., Tebamifor, M.E., Sule, M.O., Dokunmu, T.M., Ogunlana, O.O., and Iheagwam, F.N. (2024). Apicoplast-Resident Processes: Exploiting the Chink in the Armour of *Plasmodium falciparum* Parasites. Advances in pharmacological and pharmaceutical sciences *2024*, 9940468.

Matthews, H., Duffy, C.W., and Merrick, C.J. (2018). Checks and balances? DNA replication and the cell cycle in Plasmodium. Parasites & vectors 11, 216.

McNamara, C.W., Lee, M.C., Lim, C.S., Lim, S.H., Roland, J., Nagle, A., Simon, O., Yeung, B.K., Chatterjee, A.K., and McCormack, S.L. (2013). Targeting Plasmodium PI (4) K to eliminate malaria. Nature *504*, 248-253.

McRobert, L., Taylor, C.J., Deng, W., Fivelman, Q.L., Cummings, R.M., Polley, S.D., Billker, O., and Baker, D.A. (2008). Gametogenesis in Malaria Parasites Is Mediated by the cGMP-Dependent Protein Kinase. PLoS biology *6*, e139.

Meibalan, E., and Marti, M. (2017). Biology of Malaria Transmission. Cold Spring Harbor perspectives in medicine 7.

Meissner, M., Ferguson, D.J.P., and Frischknecht, F. (2013). Invasion factors of apicomplexan parasites: essential or redundant? Current Opinion in Microbiology *16*, 438-444.

Mesen-Ramirez, J.P., Fuchs, G., Burmester, J., Farias, G.B., Alape-Flores, A.M., Singla, S., Alder, A., Cubillan-Marin, J., Castro-Pena, C., Lemcke, S., *et al.* (2025). HOPS/CORVET tethering complexes are critical for endocytosis and protein trafficking to invasion related organelles in malaria parasites. PLoS pathogens *21*, e1013053.

Miller, J.L., Sack, B.K., Baldwin, M., Vaughan, A.M., and Kappe, S.H.I. (2014). Interferon-mediated innate immune responses against malaria parasite liver stages. Cell reports *7*, 436-447.

Miller, L.H., Baruch, D.I., Marsh, K., and Doumbo, O.K. (2002). The pathogenic basis of malaria. Nature 415, 673-679.

Milner, D.A., Jr. (2018). Malaria Pathogenesis. Cold Spring Harbor perspectives in medicine 8.

Modrzynska, K., Pfander, C., Chappell, L., Yu, L., Suarez, C., Dundas, K., Gomes, A.R., Goulding, D., Rayner, J.C., Choudhary, J., *et al.* (2017). A Knockout Screen of ApiAP2 Genes Reveals Networks of Interacting Transcriptional Regulators Controlling the Plasmodium Life Cycle. Cell host & microbe *21*, 11-22.

Morano Alexander, A., Xu, W., Navarro Francesca, M., Shadija, N., Dvorin Jeffrey, D., and Ke, H. (2024). The dynamin-related protein PfDyn2 is essential for both apicoplast and mitochondrial fission in *Plasmodium falciparum*. mBio *16*, e03036-03024.

Mota, M.M., Pradel, G., Vanderberg, J.P., Hafalla, J.C., Frevert, U., Nussenzweig, R.S., Nussenzweig, V., and Rodríguez, A. (2001). Migration of Plasmodium sporozoites through cells before infection. Science *291*, 141-144.

Nacer, A., Walker, K., and Hurd, H. (2008). Localisation of laminin within Plasmodium berghei oocysts and the midgut epithelial cells of Anopheles stephensi. Parasites & vectors 1, 33.

Narwal, M., Jain, S., Rathore, S., and Mohmmed, A. (2023). *Plasmodium falciparum* OPA3-like protein (PfOPA3) is essential for maintenance of mitochondrial homeostasis and parasite proliferation. The FASEB Journal *37*, e23235.

Nishi, T., Kaneko, I., Iwanaga, S., and Yuda, M. (2022). Identification of a novel AP2 transcription factor in zygotes with an essential role in Plasmodium ookinete development. PLoS pathogens *18*, e1010510.

Oberstaller, J., Otto, T.D., Rayner, J.C., and Adams, J.H. (2021). Essential Genes of the Parasitic Apicomplexa. Trends in parasitology *37*, 304-316.

Oberstaller, J., Xu, S., Naskar, D., Zhang, M., Wang, C., Gibbons, J., Pires, C.V., Mayho, M., Otto, T.D., Rayner, J.C., *et al.* (2025). Supersaturation mutagenesis reveals adaptive rewiring of essential genes among malaria parasites. Science *387*, eadq7347.

Oehring, S.C., Woodcroft, B.J., Moes, S., Wetzel, J., Dietz, O., Pulfer, A., Dekiwadia, C., Maeser, P., Flueck, C., Witmer, K., *et al.* (2012). Organellar proteomics reveals hundreds of novel nuclear proteins in the malaria parasite *Plasmodium falciparum*. Genome biology *13*, R108.

Ostera, G., Tokumasu, F., Oliveira, F., Sa, J., Furuya, T., Teixeira, C., and Dvorak, J. (2008). *Plasmodium falciparum*: Food vacuole localization of nitric oxide-derived

species in intraerythrocytic stages of the malaria parasite. Experimental parasitology 120, 29-38.

Otto, T.D., Gilabert, A., Crellen, T., Böhme, U., Arnathau, C., Sanders, M., Oyola, S.O., Okouga, A.P., Boundenga, L., Willaume, E., *et al.* (2018). Genomes of all known members of a Plasmodium subgenus reveal paths to virulent human malaria. Nature Microbiology *3*, 687-697.

Otto, T.D., Wilinski, D., Assefa, S., Keane, T.M., Sarry, L.R., Böhme, U., Lemieux, J., Barrell, B., Pain, A., Berriman, M., *et al.* (2010). New insights into the blood-stage transcriptome of *Plasmodium falciparum* using RNA-Seq. Molecular microbiology *76*, 12-24.

Ovciarikova, J., Lemgruber, L., Stilger, K.L., Sullivan, W.J., and Sheiner, L. (2017). Mitochondrial behaviour throughout the lytic cycle of Toxoplasma gondii. Scientific reports 7, 42746.

Pédelacq, J.-D., Cabantous, S., Tran, T., Terwilliger, T.C., and Waldo, G.S. (2006). Engineering and characterization of a superfolder green fluorescent protein. Nature Biotechnology *24*, 79-88.

Patterson, G.H., Knobel, S.M., Sharif, W.D., Kain, S.R., and Piston, D.W. (1997). Use of the green fluorescent protein and its mutants in quantitative fluorescence microscopy. Biophysical Journal *73*, 2782-2790.

Phillips, M.A., Lotharius, J., Marsh, K., White, J., Dayan, A., White, K.L., Njoroge, J.W., El Mazouni, F., Lao, Y., and Kokkonda, S. (2015). A long-duration dihydroorotate dehydrogenase inhibitor (DSM265) for prevention and treatment of malaria. Science translational medicine 7, 296ra111-296ra111.

Pieperhoff, M.S., Schmitt, M., Ferguson, D.J.P., and Meissner, M. (2013). The Role of Clathrin in Post-Golgi Trafficking in Toxoplasma gondii. PloS one 8, e77620.

Prado, M., Eickel, N., De Niz, M., Heitmann, A., Agop-Nersesian, C., Wacker, R., Schmuckli-Maurer, J., Caldelari, R., Janse, C.J., Khan, S.M., *et al.* (2015). Long-term live imaging reveals cytosolic immune responses of host hepatocytes against Plasmodium infection and parasite escape mechanisms. Autophagy *11*, 1561-1579.

Przyborski, J., and Lanzer, M. (2005). Protein transport and trafficking in *Plasmodium falciparum*-infected erythrocytes. Parasitology *130*, 373-388.

Pulcini, S., Staines, H.M., Lee, A.H., Shafik, S.H., Bouyer, G., Moore, C.M., Daley, D.A., Hoke, M.J., Altenhofen, L.M., Painter, H.J., *et al.* (2015). Mutations in the *Plasmodium falciparum* chloroquine resistance transporter, PfCRT, enlarge the parasite's food vacuole and alter drug sensitivities. Scientific reports *5*, 14552.

Quevillon, E., Spielmann, T., Brahimi, K., Chattopadhyay, D., Yeramian, E., and Langsley, G. (2003). The *Plasmodium falciparum* family of Rab GTPases. Gene *306*, 13-25.

Ralph, S.A., van Dooren, G.G., Waller, R.F., Crawford, M.J., Fraunholz, M.J., Foth, B.J., Tonkin, C.J., Roos, D.S., and McFadden, G.I. (2004). Tropical infectious diseases: metabolic maps and functions of the *Plasmodium falciparum* apicoplast. Nature reviews Microbiology *2*, 203-216.

Ramesh, S., Cihalova, D., Rajendran, E., van Dooren, G., and Maier, A. (2023). Analysis of *Plasmodium falciparum* mitochondrial electron transport chain activity using seahorse XFe96 extracellular flux assays.

Rossati, A., Bargiacchi, O., Kroumova, V., Zaramella, M., Caputo, A., and Garavelli, P.L. (2016). Climate, environment and transmission of malaria. Le infezioni in medicina *24*, 93-104.

Rowe, J.A., Claessens, A., Corrigan, R.A., and Arman, M. (2009). Adhesion of *Plasmodium falciparum*-infected erythrocytes to human cells: molecular mechanisms and therapeutic implications. Expert reviews in molecular medicine 11, e16.

Sanderson, T., and Rayner, J.C. (2017). PhenoPlasm: a database of disruption phenotypes for malaria parasite genes. 2, 45.

Scherf, A., Lopez-Rubio, J.J., and Riviere, L. (2008). Antigenic Variation in *Plasmodium falciparum*. Annual review of microbiology *62*, 445-470.

Schmidt, S. (2017). Identification of essential parasite-specific genes in the human malaria parasite *Plasmodium falciparum*. Master's thesis, University of Tübingen.

Schmitt, M.F. (2020). Functional investigation of unknown malaria proteins in the human malaria parasite *Plasmodium falciparum*. PhD thesis, University of Hamburg.

Shaner, N.C., Campbell, R.E., Steinbach, P.A., Giepmans, B.N.G., Palmer, A.E., and Tsien, R.Y. (2004). Improved monomeric red, orange and yellow fluorescent proteins derived from Discosoma sp. red fluorescent protein. Nature Biotechnology *22*, 1567-1572.

Shang, X., Wang, C., Shen, L., Sheng, F., He, X., Wang, F., Fan, Y., He, X., and Jiang, M. (2022). PfAP2-EXP2, an Essential Transcription Factor for the Intraerythrocytic Development of *Plasmodium falciparum*. Frontiers in Cell and Developmental Biology *Volume 9 - 2021*.

Sherman, I.W. (1977). Amino acid metabolism and protein synthesis in malarial parasites. Bulletin of the World Health Organization *55*, 265-276.

- Shima, D.T., Scales, S.J., Kreis, T.E., and Pepperkok, R. (1999). Segregation of COPIrich and anterograde-cargo-rich domains in endoplasmic-reticulum-to-Golgi transport complexes. Current biology: CB *9*, 821-824.
- Sidhu, A.B.S., Verdier-Pinard, D., and Fidock, D.A. (2002). Chloroquine Resistance in *Plasmodium falciparum* Malaria Parasites Conferred by *pf*crtMutations. Science *298*, 210-213.
- Silvie, O., Rubinstein, E., Franetich, J.F., Prenant, M., Belnoue, E., Rénia, L., Hannoun, L., Eling, W., Levy, S., Boucheix, C., *et al.* (2003). Hepatocyte CD81 is required for *Plasmodium falciparum* and Plasmodium yoelii sporozoite infectivity. Nature medicine *9*, 93-96.
- Simon, C.S. (2022). Organization of microtubules and the atypical centrosome of *Plasmodium falciparum* during blood-stage schizogony. PhD thesis, Heidelberg University.
- Sinden, R., Canning, E.U., and Spain, B. (1976). Gametogenesis and fertilization in Plasmodium yoelii nigeriensis: a transmission electron microscope study. Proceedings of the Royal Society of London Series B Biological Sciences *193*, 55-76.
- Sinden, R.E., Canning, E.U., Bray, R.S., and Smalley, M.E. (1978). Gametocyte and gamete development in *Plasmodium falciparum*. Proceedings of the Royal Society of London Series B, Biological sciences *201*, 375-399.
- Singh, S., Santos, J.M., Orchard, L.M., Yamada, N., van Biljon, R., Painter, H.J., Mahony, S., and Llinás, M. (2021). The PfAP2-G2 transcription factor is a critical regulator of gametocyte maturation. Molecular microbiology *115*, 1005-1024.
- Smith, H.E., Mackenzie, A.M., Seddon, C., Mould, R., Kalampouka, I., Malakar, P., Needham, S.R., Beis, K., Bell, J.D., and Nunn, A. (2024). The use of NADH anisotropy to investigate mitochondrial cristae alignment. Scientific reports *14*, 5980.
- Smith, J.D., Rowe, J.A., Higgins, M.K., and Lavstsen, T. (2013). Malaria's deadly grip: cytoadhesion of *Plasmodium falciparum*-infected erythrocytes. Cellular microbiology *15*, 1976-1983.
- Snapp, E. (2005). Design and Use of Fluorescent Fusion Proteins in Cell Biology. Current Protocols in Cell Biology *27*, 21.4.21-21.4.13.
- Solebo, O., Ling, L., Nwankwo, I., Zhou, J., Fu, T.-M., and Ke, H. (2023). *Plasmodium falciparum* utilizes pyrophosphate to fuel an essential proton pump in the ring stage and the transition to trophozoite stage. PLoS pathogens *19*, e1011818.
- Spycher, C., Rug, M., Pachlatko, E., Hanssen, E., Ferguson, D., Cowman, A.F., Tilley, L., and Beck, H.P. (2008). The Maurer's cleft protein MAHRP1 is essential for

trafficking of PfEMP1 to the surface of *Plasmodium falciparum*-infected erythrocytes. Molecular microbiology *68*, 1300-1314.

Struck, N.S., de Souza Dias, S., Langer, C., Marti, M., Pearce, J.A., Cowman, A.F., and Gilberger, T.W. (2005). Re-defining the Golgi complex in *Plasmodium falciparum* using the novel Golgi marker Pf GRASP. Journal of cell science *118*, 5603-5613.

Struck, N.S., Herrmann, S., Schmuck-Barkmann, I., de Souza Dias, S., Haase, S., Cabrera, A.L., Treeck, M., Bruns, C., Langer, C., Cowman, A.F., *et al.* (2008). Spatial dissection of the cis- and trans-Golgi compartments in the malaria parasite *Plasmodium falciparum*. Molecular microbiology *67*, 1320-1330.

Sturm, A., Amino, R., van de Sand, C., Regen, T., Retzlaff, S., Rennenberg, A., Krueger, A., Pollok, J.M., Menard, R., and Heussler, V.T. (2006). Manipulation of host hepatocytes by the malaria parasite for delivery into liver sinusoids. Science *313*, 1287-1290.

Su, X.-z., Heatwole, V.M., Wertheimer, S.P., Guinet, F., Herrfeldt, J.A., Peterson, D.S., Ravetch, J.A., and Wellems, T.E. (1995). The large diverse gene family var encodes proteins involved in cytoadherence and antigenic variation of *Plasmodium falciparum*-infected erythrocytes. Cell *82*, 89-100.

Swift, R.P., Elahi, R., Rajaram, K., Liu, H.B., and Prigge, S.T. (2023). The *Plasmodium falciparum* apicoplast cysteine desulfurase provides sulfur for both iron-sulfur cluster assembly and tRNA modification. eLife *12*, e84491.

Talman, A.M., Blagborough, A.M., and Sinden, R.E. (2010). A *Plasmodium falciparum* Strain Expressing GFP throughout the Parasite's Life-Cycle. PloS one *5*, e9156.

Tawk, L., Dubremetz, J., Montcourrier, P., Chicanne, G., and Merezegue, F. (2011). Phosphatidylinositol 3-Monophosphate Is Involved in Toxoplasma. PLoS pathogens, *7*(*2*), e1001286

Tian, Y., Ye, R., Zhang, D., and Zhang, Y. (2024). The evolutionary history of *Plasmodium falciparum* from mitochondrial and apicoplast genomes of China-Myanmar border isolates. Parasites & vectors 17, 548.

Toenhake, C.G., Fraschka, S.A., Vijayabaskar, M.S., Westhead, D.R., van Heeringen, S.J., and Bártfai, R. (2018). Chromatin Accessibility-Based Characterization of the Gene Regulatory Network Underlying *Plasmodium falciparum* Blood-Stage Development. Cell host & microbe 23, 557-569, e559.

Travassos, M.A., Coulibaly, D., Bailey, J.A., Niangaly, A., Adams, M., Nyunt, M.M., Ouattara, A., Lyke, K.E., Laurens, M.B., Pablo, J., *et al.* (2015). Differential

recognition of terminal extracellular *Plasmodium falciparum* VAR2CSA domains by sera from multigravid, malaria-exposed Malian women. The American journal of tropical medicine and hygiene *92*, 1190-1194.

Vaidya, A.B. (2023). Inducing indigestion in malaria parasites: Genetic manipulations of a proton pump. Proceedings of the National Academy of Sciences *120*, e2310870120.

Vaidya, A.B., Painter, H.J., Morrisey, J.M., and Mather, M.W. (2008). The validity of mitochondrial dehydrogenases as antimalarial drug targets. Trends in parasitology *24*, 8-9.

Van Dooren, G.G., Marti, M., Tonkin, C.J., Stimmler, L.M., Cowman, A.F., and McFadden, G.I. (2005). Development of the endoplasmic reticulum, mitochondrion and apicoplast during the asexual life cycle of *Plasmodium falciparum*. Molecular microbiology *57*, 405-419.

Van Dooren, G.G., Stimmler, L.M., and McFadden, G.I. (2006). Metabolic maps and functions of the Plasmodium mitochondrion. FEMS Microbiology Reviews 30, 596-630.

Van Dooren, G.G., and Striepen, B. (2013). The Algal Past and Parasite Present of the Apicoplast. Annual review of microbiology *67*, 271-289.

van Esveld, S.L., Meerstein-Kessel, L., Boshoven, C., Baaij, J.F., Barylyuk, K., Coolen, J.P., van Strien, J., Duim, R.A., Dutilh, B.E., and Garza, D.R. (2021). A prioritized and validated resource of mitochondrial proteins in Plasmodium identifies unique biology. mSphere, 6(5), e0061421.

van Hooff, J.J.E., Tromer, E., van Wijk, L.M., Snel, B., and Kops, G.J.P.L. (2017). Evolutionary dynamics of the kinetochore network in eukaryotes as revealed by comparative genomics. EMBO reports *18*, 1559-1571.

Van Wye, J., Ghori, N., Webster, P., Mitschler, R.R., Elmendorf, H.G., and Haldar, K. (1996). Identification and localization of rab6, separation of rab6 from ERD2 and implications for an 'unstacked'Golgi, in *Plasmodium falciparum*. Molecular & Biochemical Parasitology 83, 107-120.

Verhoef, J.M., Boshoven, C., Evers, F., Akkerman, L.J., Gijsbrechts, B.C., van de Vegte-Bolmer, M., van Gemert, G.-J., Vaidya, A.B., and Kooij, T.W. (2024a). Detailing organelle division and segregation in *Plasmodium falciparum*. Journal of Cell Biology *223*, e202406064.

Verhoef, J.M.J., Boshoven, C., Evers, F., Akkerman, L.J., Gijsbrechts, B.C.A., van de Vegte-Bolmer, M., van Gemert, G.J., Vaidya, A.B., and Kooij, T.W.A. (2024b).

Detailing organelle division and segregation in *Plasmodium falciparum*. The Journal of cell biology, 223(12), e202406064.

White, M.T., Karl, S., Battle, K.E., Hay, S.I., Mueller, I., and Ghani, A.C. (2014). Modelling the contribution of the hypnozoite reservoir to *Plasmodium vivax* transmission. eLife *3*, e04692.

White, N.J. (2017). Malaria parasite clearance. Malaria journal 16, 88.

Wickham, M.E., Rug, M., Ralph, S.A., Klonis, N., McFadden, G.I., Tilley, L., and Cowman, A.F. (2001). Trafficking and assembly of the cytoadherence complex in *Plasmodium falciparum* infected human erythrocytes. The EMBO Journal *20*, 5636-5649-5649.

Wirschell, M., Olbrich, H., Werner, C., Tritschler, D., Bower, R., Sale, W.S., Loges, N.T., Pennekamp, P., Lindberg, S., Stenram, U., *et al.* (2013). The nexin-dynein regulatory complex subunit DRC1 is essential for motile cilia function in algae and humans. Nature Genetics *45*, 262-268.

Wittayacom, K., Uthaipibull, C., Kumpornsin, K., Tinikul, R., Kochakarn, T., Songprakhon, P., and Chookajorn, T. (2010). A nuclear targeting system in *Plasmodium falciparum*. Malaria journal 9, 126.

Yeh, E., and DeRisi, J.L. (2011). Chemical rescue of malaria parasites lacking an apicoplast defines organelle function in blood-stage *Plasmodium falciparum*. PLoS biology 9, e1001138.

Zeeshan, M., Brady, D., Stanway, R.R., Moores, C.A., Holder, A.A., and Tewari, R. (2020a). *Plasmodium berghei* kinesin-5 associates with the spindle apparatus during cell division and is important for efficient production of infectious sporozoites. Frontiers in cellular and infection microbiology *10*, 583812.

Zeeshan, M., and Pandey, R. (2020b). Real-time dynamics of Plasmodium NDC80 reveals unusual modes of chromosome segregation during parasite proliferation. Journal of cell science *134(5)*, jcs245753.

Zhang, M., Wang, C., and Otto, T.D. (2018). Uncovering the essential genes of the human malaria parasite *Plasmodium falciparum* by saturation mutagenesis. Science, 360(6388), eaap7847.

Appendix

Appendix 1 - Integration check Primers

No.	reverse primer	forward primer
Y1 int.	CCTAATATTCCTTCATTTCTACAAC	GTAATGAGCCTGTACAAAGTAATG
Y2 int.	CATACATATATATATGTGTGTGG	GTACTCTATGAGAAAATAATTCGTTC
Y3 int.	CCTTTTTATGATAAAATTACACC	GCTTCGATGTAAGATTAAAC
Y4 int.	CGTATTCTTTTCTTTTTTTTAATTC	CTTTACATTTAAAAGAAACGCC
Y5 int.	GTTGGATACTTTTTAATACCAGATG	CAAATATATTAAAGTATGAACG
Y6 int.	CTTCATAAAAAAAGGGGGGGGAGGTG	CAACATAGTTATACCAATGTTGATC
Y7 int.	GTTCCAGATTTGCATTGAGC	CTAATGGTAATAAGAAGTCC
Y8 int.	CTGAGATGTATATGAGAAAGGTG	GTGTAATAATTATGTATACCATGTG
Y9 int.	GGCCCAAACAATAAATGTAATAC	GCAGAGAAAATATACAACTTC
Y10 int.	GTAGCTTCTAATTTGTAGGGAC	CGTGCAACAAATTTGATGCG

Y11 int.	CAAAAGATGTACTACACACAAC	GATCCCCTTTGAGTAAAATCG
Y12 int.	GAAGATTTATATGAACCTTAAC	GATATTCAGTATGCATCCATTTATG
Y13 int.	GGTAAAATGGAAATGAAATAGGGTC	GAAAGAGTGGGATGATAATAAG
Y14 int.	CGTCAAGGACTAATATTTTAACC	CGAAGTGGCTGTGGGTATTGTTTAG
Y15 int.	CACGAATAATATTTCTATTTTG	GATGAATCAGATAATTATAAAGATG
Y16 int.	CCCAGAGACATGCCCCTAAGTATC	GACACAAGATTCGGATGATGAG
Y17 int.	GGGGCATGTCTCTGGGGGCATAACC	CGATGTAACCGAGTGAGACCCAAGAG
Y18 int.	CATAATCCTACTTATGTAATACTCC	GTTCTAGTCCTCGAAATATGAAAAAATC
Y19 int.	CTAAATTTAAGATCAAACGCTG	CGTCGGACACATTCTTATCTATG
Y20 int.	CATATAATGAACACACACACTCCTC	GTTGTGTTGATTTATAAAAACATG
Y21 int.	CCCCATGGTCGTTTATTAACAGAAC	CATAACACATCATGGTTTTGTATG
Y22 int.	GTTCTGTTAATAAACGACCATGGGG	GAATAATAACAAGAGTGATG
Y23 int.	CTTTTCTTTTATTATTTTCCC	CTGAGATAAGTCAACCAATGAAAG

Y24 int.	GGTTTTGCCTGTCATGGTCAG	GTGTAACAAACGAAACGGAC
Y25 int.	GCACACGCATACATATAATATGTCC	GGCGATCCTTTAGAAAATGTAG
Y26 int.	CACTTAAAATTATGGATTATATG	GGAATATCTCAGTTGTTAAACTCC
Y27 int.	GTATTTCTTATGTACCTCTTC	GAAATGTTCTCTTTAATGGTCC
Y28 int.	GGTAAAAACAATTCAAAGGAGCGGC	GAAAATAATGATGACAATAATAATG
Y29 int.	CACATACATTTTGCAGTCAAC	GAAAGTCCTATATGTTTTTGTC
Y30 int.	CAATTAAAAGCGTGTCATTTTTG	CCACAATTCGAAGAAGACATACTCC
Y31 int.	CTTTTAACAGTTCATAGTTTACAC	GTTTTGTAACTTTATCTGGC
Y32 int.	CGGCGATTATGCTTTATTTATGAAC	GACATACATAATCAGGATAC
Y33 int.	CCACTTCCAATTTAAAACACTCG	GAGTGATAACATAAATATGAGTG
Y34 int.	CGTGATGATATGTACTAAACGG	GCTATATCATTATGTCACACTGTG
Y35 int.	CATATAATATATTTTATGGAGATAC	GGATTCCGGAGGGATAGTTCACGC
Y36 int.	GCACCCTTCCGAACTACGCACA	GGATTCCGGAGGGATAGTTCACGC

Y38 int.	CAAACATATATAACAATTCTCACAC	GCCATTATTTATTCAATCTATTG
Y39 int.	CAAATTCTCATATCTAATATATGG	GAGATAGAATTAATTATTTGC
Y40 int.	GTTCATAATATTTTATATCTAGCC	GATGTCATAATAATTGAGTTTGG
Y41 int.	CTAATCAGACAAAAGAATAGAC	GGGGCTAACGGCAGACTATTCC
Y42 int.	GTGGTTCCTTGCATACGCTTCC	GTGTTTTTTTTCATGTAAACAAC
Y43 int.	GATCATGTTGATCATGTTGATG	GAAAAATTGTATAAGGTTACC
Y44 int.	CACCCATGTGGATATTATTACTACC	GTGTCCTATCTACCAAACATTCC

Appendix 2 - Homology Region Primers

No.	HR-FW	HR-RV
Y1	ATTTAGGTGACACTATAGAATACTCGCGGCCG CTGAGCTGGTTGTCATGTGGATAG	CAGCAGATCTTGATCTCAATCCTGACCTAGGT TTTGCCTTCCTCTTTGCTATATC
Y2	ATTTAGGTGACACTATAGAATACTCGCGGCCG CTAGGATAATAAGCAATACGAGAAAAAGAAG	CAGCAGATCTTGATCTCAATCCTGACCTAGG ATTTCTTGAATTATCCGATTTGATAG
Y3	ATTTAGGTGACACTATAGAATACTCGCGGCCG CTAAGATGTTTTGTTT	CAGCAGATCTTGATCTCAATCCTGACCTAGGT TTTTTAAAAAAAGTTATGGAGATATTC

Y4	ATTTAGGTGACACTATAGAATACTCGCGGCCG CTAAGATAACGAAAGTATTGCAAGTGATGC	CAGCAGATCTTGATCTCAATCCTGACCTAGG ATTTTCATCCTTCTTTGTAATATTTTTAATTTT ATTAAC
Y5	ATTTAGGTGACACTATAGAATACTCGCGGCCG CTAAGGAATTAAAATATTTCCAATAGAAAAAA CAGTATGCG	CAGCAGATCTTGATCTCAATCCTGACCTAGGT TTTTCACTCTTTAATTTTTTTTTAACAGG
Y6	ATTTAGGTGACACTATAGAATACTCGCGGCCG CTAAGAAGAAAAACAATTTTTAAAAGCAC	CAGCAGATCTTGATCTCAATCCTGACCTAGGT CGATCCATTTGCTTATTTGACCATACATG
Y7	ATTTAGGTGACACTATAGAATACTCGCGGCCG CTAAGGAGATAAAAATGGA G	CAGCAGATCTTGATCTCAATCCTGACCTAGG AACCTTTTGAAATAAGGCATTTAATATAAATT TTAAAGG
Y8	ATTTAGGTGACACTATAGAATACTCGCGGCCG CTGATATAGAAATATAAAATATTACTTTTTAAC	CAGCAGATCTTGATCTCAATCCTGACCTAGGT CACTTTTCCATCCTGATATAGTATGTG
Y9	ATTTAGGTGACACTATAGAATACTCGCGGCCG CTAACAGTTAATCGAAGCATATATCTCCTCTTG	CAGCAGATCTTGATCTCAATCCTGACCTAGGT TCATTCATAAAAAATAATGAAAGAATTACAC
Y10	ATTTAGGTGACACTATAGAATACTCGCGGCCG CTAAGGGTGAAAATAAAAAGAGGATAGAAGA AAAGG	GCAGCAGATCTTGATCTCAATCCTGACCTAG GTAATGTTCCAAGGATTATGGTACCTG

1		,
Y11	ATTTAGGTGACACTATAGAATACTCGCGGCCG CTAATATTCCTATATGCAGAGAAATATT	CAGCAGATCTTGATCTCAATCCTGACCTAGGT TTATGAACATCGGTACTATCTTTTTTTTG
Y12	ATTTAGGTGACACTATAGAATACTCGCGGCCG CTAAGAAAAAAAATAACTTATCTTAT	CAGCAGATCTTGATCTCAATCCTGACCTAGGT TTTATATTATCTGCATAAGTATCTGTATTAC
Y13	ATTTAGGTGACACTATAGAATACTCGCGGCCG CTAAGCCTTAGAGGAATATGTAGAATTAAGGG GG	CAGCAGATCTTGATCTCAATCCTGACCTAGG ACATGGTTGTGTTTCCATTTCTGATTGGATC
Y14	ATTTAGGTGACACTATAGAATACTCGCGGCCG CTAGAAGGAATATGAAAATTTCGACATG	CAGCAGATCTTGATCTCAATCCTGACCTAGG AAAGATATAAATATATATACTTCTATCTTC
Y15	ATTTAGGTGACACTATAGAATACTCGCGGCCG CTAAGAGAAATCCTATAATGAAGAGGG	CAGCAGATCTTGATCTCAATCCTGACCTAGGT TCGTCATCCTCACTATTATCAGAC
Y16	ATTTAGGTGACACTATAGAATACTCGCGGCCG CTGAGTTCGAAAAATAAATGTTAGTGGG	CAGCAGATCTTGATCTCAATCCTGACCTAGG GTCTTGCATAATTTTTTTGAATTCATTTG
Y17	ATTTAGGTGACACTATAGAATACTCGCGGCCG CTAAGACGACTGTGGTAATATTAACTGGGCC	CAGCAGATCTTGATCTCAATCCTGACCTAGG ATCCTTTCCATGCTTATTAGGTTTATC

Y18	ATTTAGGTGACACTATAGGATTCGCGCTAAAGAGTTGAT	CAGCAGATCTTGATCTCAATCCTGACCTAGGT
	CTAAGATACTTACGATTGCCCTAAAGAGTTGAT	TCTCTTTTAACTGTATTGTATATTTTC
	GAGG	
Y19	ATTTAGGTGACACTATAGAATACTCGCGGCCG	CAGCAGATCTTGATCTCAATCCTGACCTAGG
	CTAAGAAGGTAATTATATATATATGTAAAATT	GGTTTTGATAAAGGTACAGTTATCATTAATTA
	A	TAG
Y20	ATTTAGGTGACACTATAGAATACTCGCGGCCG	CAGCAGATCTTGATCTCAATCCTGACCTAGG
	CTAACTTAAGAAAAATAGAGAAGGTATAATTC	ATATTGGAAGCGCTTATCATCAGCTGTTG
	ATTC	
	Mile	
Y21	ATTTAGGTGACACTATAGAATACTCGCGGCCG	CAGCAGATCTTGATCTCAATCCTGACCTAGG
	CTAAGATTTTGATGGTATTAGTAAATTAC	GAAGTCCTCTAAAAACTCATCTACCC
Y22	ATTTAGGTGACACTATAGAATACTCGCGGCCG	CAGCAGATCTTGATCTCAATCCTGACCTAGGT
	CTGAGATCATATAAAAAATGACCATACAAATA	ATTTTGAATAACATACCTTTAAAGTTTTTAC
	TT	
Y23	ATTTAGGTGACACTATAGAATACTCGCGGCCG	CAGCAGATCTTGATCTCAATCCTGACCTAGG
	CTGAGGTAGTAATAATTATTATAGTAAAA	ATTATTCACATTACGATTGTAATTATTGAAAT
	TAAAT	G

Y24	ATTTAGGTGACACTATAGAATACTCGCGGCCG CTAGATTAAAAAAATTAAATGCGACGTTTGAAA	CAGCAGATCTTGATCTCAATCCTGACCTAGGT AAAATTATGTTATTATTTCTTTTGAGGGC
	ATTATG	AAAATTATOTTATTATTTCTTTTOAOOOC
Y25	ATTTAGGTGACACTATAGAATACTCGCGGCCG CTAAGGAGAATATGAAAGTTCATTAACAAATG	CAGCAGATCTTGATCTCAATCCTGACCTAGG ATTAAAATACAAATTAAAGAATAAATATTTT AG
Y26	ATTTAGGTGACACTATAGAATACTCGCGGCCG CTGAGATAAGGGTCCCACAAAAACAGTAGAGT TC	CAGCAGATCTTGATCTCAATCCTGACCTAGGT TTTACACAAAAAAAAAGAAAAATTTAGAATG
Y27	ATTTAGGTGACACTATAGAATACTCGCGGCCG CTAAATCCCAGAAATTGACGCTGGGTATAACG TTCAG	CAGCAGATCTTGATCTCAATCCTGACCTAGGT AAAAGCATTTTTTTAAATATATTATTAGG
Y28	ATTTAGGTGACACTATAGAATACTCGCGGCCG CTAAGGTAAGAGAAAAGTGTAAGGAAAATAGCT G	CAGCAGATCTTGATCTCAATCCTGACCTAGGT GCCCTTTTTTTTAGATTAAAAATTAACAAC
Y29	ATTTAGGTGACACTATAGAATACTCGCGGCCG CTAACAAATTGATGATGATGATAATGATGATA AT	CAGCAGATCTTGATCTCAATCCTGACCTAGG ATCATAAAAAAAGTACCTTTTCTCTATTTTTTTA AA

Y30	ATTTAGGTGACACTATAGAATACTCGCGGCCG CTAAGAGGGAGAAATAAAAGAGGTGGTACAA GAAGG	CAGCAGATCTTGATCTCAATCCTGACCTAGG ATAGTTCAAATTTTCCTTTTCCATATCTTC
Y31	ATTTAGGTGACACTATAGAATACTCGCGGCCG CTAAGAAAATAAAGAAAGCATAAACAACACA AC	CAGCAGATCTTGATCTCAATCCTGACCTAGGT TCTTTCGTTTTTTCAAATATATTATCCAC
Y32	ATTTAGGTGACACTATAGAATACTCGCGGCCG CTAAGGAAAAGAGGAAATAGAAGAATACAG	CAGCAGATCTTGATCTCAATCCTGACCTAGGT TCTAAACAGATATATACAGGTATTTTG
Y33	ATTTAGGTGACACTATAGAATACTCGCGGCCG CTGAGCTAGCCCCAGGTCGAAACCTGGATCAG G	CAGCAGATCTTGATCTCAATCCTGACCTAGG ATACACTGCTATCTTTATATCCTTCAAAAATT G
Y34	ATTTAGGTGACACTATAGAATACTCGCGGCCG CTAGACAGATCAACGTAATGACCCATCATCG	CAGCAGATCTTGATCTCAATCCTGACCTAGGT GAGAACCTACATAAAAAAAAAA
Y35	ATTTAGGTGACACTATAGAATACTCGCGGCCG CTAACAAAGGTTGATCGACATAACAACACATT C	CAGCAGATCTTGATCTCAATCCTGACCTAGG GGATGCTCTTATAACAAAATCTTCC

Y36	ATTTAGGTGACACTATAGAATACTCGCGGCCG CTAAGGGAAAATATTGGAGAAAGGGACAGAT G	CAGCAGATCTTGATCTCAATCCTGACCTAGGC ATTTCCTTGTTAAAAAAATAAATTTTTGATAAG
Y38	ATTTAGGTGACACTATAGAATACTCGCGGCCG CTAAGAACAGAAGTTGTTGTTAAATGGGGAAG AC	CAGCAGATCTTGATCTCAATCCTGACCTAGGT GTTTCGTTAAATACATCTTTTGCCAACATTG
Y39	ATTTAGGTGACACTATAGAATACTCGCGGCCG CTAAAGGGATGATAATCCTAATAGTATTACAA GAA	CAGCAGATCTTGATCTCAATCCTGACCTAGGC TCATAATATTTCCTGTTTATTTTTTTATCG
Y40	ATTTAGGTGACACTATAGAATACTCGCGGCCG CTAAAGTTGTAGTGATTATAGTAATAATTCCG	CAGCAGATCTTGATCTCAATCCTGACCTAGG AAAAATTTTCAGTTTTTTTTTT
Y41	ATTTAGGTGACACTATAGAATACTCGCGGCCG CTGAGAGGTACAAGATTCACCATCTTTGTACA G	CAGCAGATCTTGATCTCAATCCTGACCTAGGC TTTTTATTTATCGTATCATAATTAATGGTTTC
Y42	ATTTAGGTGACACTATAGAATACTCGCGGCCG CTAAGGAGATAATAAATATGAACAAAATAACC ATGG	CAGCAGATCTTGATCTCAATCCTGACCTAGGT AACATATAATATTCAACAAAATTGCAC

Y43	ATTTAGGTGACACTATAGAATACTCGCGGCCG CTAAGGAAATAAACATAATAAAAAAAAGTATG	CAGCAGATCTTGATCTCAATCCTGACCTAGG ATTCTGCATAGTTTCAAAGAAATTTTTTATTA
	AATTATG	TTATC
Y44	ATTTAGGTGACACTATAGAATACTCGCGGCCG CTAACAATCACCTGTACAAACGCTTATAAATAT	CAGCAGATCTTGATCTCAATCCTGACCTAGGT TTTATTTCGACATTTATAGGAAGATGTTCAGG
	С	

Appendix 3 - Y43 (PF3D7_0423200) recodonization

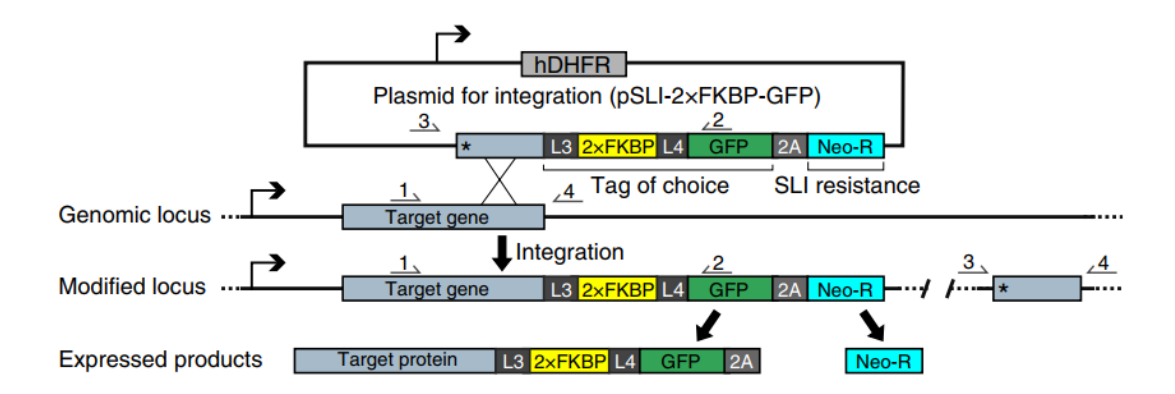
>Original sequence:

>Adjusted sequence:

ATGGGTAACAAGCACAACAAGAAGAAATACGAGCTTTGCGAGATACAGT
ATGAGGAGAAGGACTTCCAGCTTAAGTACCCTTGGAATGAGATAATTAAG
TGGGGATCAGATGACCTTAACGTAGACATTAACATTAAAATTGTTAAGAA

GGTTATAGAGGAGATAAAGGACATTACTCTTGACGAGGAGTCATTCTTCA
ACATAACTGAGGGAAAAGACATACAGAGTTTCCACTTCGAGGACAAATAC
GTATTGTGGGCTACTGCACTTCTTAAGGACATTCCAAACCTTAAGAAGAT
ACGTTACAACATAGTACCAAAGTACATAAATGAGAACGAGTTTTGGCTTC
GTTACTTCAGTAGCATTAAGATGATTATTATTAAGAACTTTTTCGAGACAA
TGCAAAACTAG

Appendix 4 - Schematic of SLI strategy.



L3 and L4 are linkers35; 2A, T2A skip peptide; Neo-R, neomycin-resistance gene; asterisks, stop codons; arrows, promoters; numbers, primers postion.

Acknowledgement

Time flies—it has already been four years since I arrived in Germany. I still clearly remember the first day I set foot in this harbor city: it was raining, and somehow it felt like the rain have to be endless. But I am lucky, because during these years, I met so many kind and wonderful people who made this journey special and wonderful.

As we known, there were times of exhaustion, confusion, and frustration—but also moments of real joy when an experiment finally worked or yeast disappeared. But in the end, I made it. I finished.

First and foremost, I want to express my deepest thanks to my supervisor, Dr. Tobias Spielmann, for giving me the chance to work in this exciting field. Tobi is one of the smartest and most precise scientists I've ever met. His way of thinking, his attention to detail, and his endless curiosity have deeply influenced how I do research. We have a saying in Chinese—"良师益友"—a good teacher and a loyal friend. That's exactly who Tobi has been to me. I know I'm not the talented or efficient PhD student, and I truly appreciate his patience and understanding along the way. These four years of supervising me must have cost him a lot of time and energy. I feel very lucky to have chosen him as my supervisor.

I am also very grateful to all my colleagues in the lab. You made the lab feel like a second home. Thank you for the long hours troubleshooting experiments, the beers we shared after work, and the casual chats that helped me feel less alone. A very special thank-you goes to Hannah Michaela Behrens. When I first arrived and knew almost nothing, Hannah was the one who patiently guided me through the protocols, answered all my questions, and helped me deal with everyday life in a new lab and a new country.

Acknowledgement

Most of all, I want to thank Meng Hongjun, my partner and closest companion during

these years. Thank you for being there through all the ups and downs. When I felt tired,

when I was stuck or lost, you always listened and gave me strength. Thank you for your

patience, for your encouragement, and for just staying with me.

I also want to thank myself. Thank you for not giving up, even when everything felt

uncertain and difficult. Thank you for showing up, again and again, and for believing

that things would get better.

To my family—thank you for your love and support. You never questioned my

decisions. You always said, "Just do what you want to do. Don't worry about us." That

meant so much to me, and I carried those words with me through the hardest times.

Finally, I sincerely thank the China Scholarship Council (CSC) for funding my doctoral

studies. Without this support, none of this would have been possible.

A PhD is not an end, but a new beginning. Very soon, I will leave Hamburg—a city

that witnessed some of the most intense years of my life. There may be no big farewell,

no special event. Just like this journey: a quiet storm, and then, a silent goodbye.

This is for everyone who helped me grow along the way. Thank you—for your guidance,

your support, and your belief in me. You made this journey meaningful.

Yangyang

July, Hamburg

239